Meso- and Neoarchaean Banded Iron Formations of the Slave Craton, NW Canada:
Seawater Chemistry, Source Characteristics, Depositional Setting and Age Constraints

by

Rasmus Haugaard Nielsen

A thesis submitted in partial fulfillment of the requirements for the degree of

Doctor of Philosophy

Department of Earth and Atmospheric Sciences
University of Alberta

Abstract

Banded iron formations (BIFs) are iron- and silica-rich chemical sedimentary rocks that have been widely used as a proxy for the chemical and redox composition of Achaean seawater. Within the Slave Craton (Northwest Territories, Canada), two different BIF deposits exist: (1) an ~ 2.85 Ga unit deposited in a continental rift basin, associated with fuchsitic quartzite, conglomerate and basement gneisses, and (2) an ~ 2.62 Ga unit deposited in an arc-type basin and found interbedded with extensive greywacke-mudstone turbidite sequences. The time frame within which these BIFs were deposited records major changes in global Archaean environmental conditions, such as mantle plume activity, continental assembly and changes in oceanic and atmospheric chemistry. Although these palaeoenvironmental factors can potentially be traced in BIFs, this study shows that these deposits tend to reflect phenomena that are strongly dependent on local-to-regional palaeoenvironmental conditions. This thesis presents new petrologic and geochemical insights into the deposition of these poorly studied Slave Craton BIF deposits. It interprets their geochemical seawater signature from a local-to-regional perspective as it relates to the ambient environment, and it provides a new understanding of the interplay of the dominant solute sources controlling seawater composition at the time.

Both BIF deposits display seawater derived shale-normalized rare earth elements + yttrium (REY) patterns enriched in heavy-REE relative to light-REE (HREE>LREE) and positive lanthanum (La) and yttrium (Y) anomalies. High-resolution, layer-by-layer geochemical and samarium-neodymium (Sm-Nd) isotope analyses further reveal that both BIF deposits were precipitated in a basin where seawater was a mixture of deep,

hydrothermal waters and surface waters with solutes sourced from land. The high silica contents (up to 20 wt.% SiO_2) in the iron bands and low iron contents (down to 4 wt. Fe_2O_3) in the silica bands show that background silica sedimentation within the water column was frequently interrupted by the convective upwelling of iron-rich water masses. In the older 2.85 Ga BIF, the iron-rich bands all have positive $\varepsilon_{Nd}(t)$ values which demonstrate that the dissolved REY in the source water during ferric iron precipitation was provided by deeper-marine hydrothermal fluids with relatively uniform $^{143}Nd/^{144}Nd$. The surface water, on the other hand, was heterogeneous and controlled by a wide range of REY sources all related to both radiogenic (positive $\varepsilon_{Nd}(t)$ values) and unradiogenic (negative $\varepsilon_{Nd}(t)$ values) continental landmasses. In the younger 2.62 Ga BIF, high germanium/silicon (Ge/Si) ratios in the iron bands, and low Ge/Si ratios in the silica bands are further evidence for the interplay between upper silica rich and deeper iron rich seawater during BIF formation. However, a difference between the ambient seawater behind deposition of the younger and older BIF deposits is the size of the hydrothermal contribution and the presence of a strong oxidant (e.g., O_2) in the 2.62 Ga BIF. During active rifting of the basement, a large excess of reduced europium (Eu^{2+}) from high-temperature hydrothermal fluids impacted the basin water and was incorporated in the precursor precipitate of the ca. 2.85 Ga BIF. The positive Eu anomaly is larger than in similarly-aged BIF deposits, as well as to the younger 2.62 Ga BIF in this study. Whereas the older BIF do not show any anomalies of cerium (Ce), parts of the younger BIF displays negative Ce anomalies, which indicate the presence of an oxidizing agent that was able to fractionate Ce^{3+} to Ce^{4+} in the 2.62 Ga seawater. These findings clearly indicate the importance of addressing each BIF within its own depositional context, as

they can reveal detectable changes in the evolution of relative water mass contributions in a particular depositional basin, over time.

The 2.62 Ga BIF is found interstratified with large volume of greywacke-mudstone turbidite deposits. As a modern analogue turbidites are deposited by density driven currents containing suspended debris. The extensive turbidite sedimentation associated with the BIF has noticeably impacted its elemental budget. As such, the slow chemical rainout of the precursor precipitates in this BIF likely took place on the basin floor adjacent to a steep submarine ramp. BIF deposition was episodically interrupted by turbidite currents and slump-generated debris flows sourced from the adjacent, tectonically active arc-terrain. Until now, the depositional timing of the 2.62 Ga BIF deposit has been based entirely on maximum depositional ages in detrital zircons from the associated turbidites. In this study we found a felsic-to-intermediate, ~3-cm-thick, tuff ash bed, interlayered within the turbidite-BIF sequence at Slemon Lake in the southwest part of the Slave Craton. The tuff yielded a single zircon age population with a U-Pb zircon crystallization age of 2620 ± 6 Ma. This crystallization age defines the age of these turbidite-BIF. The date defined by the tuff ash bed, together with maximum detrital zircon ages carried out on greywackes across the craton, separates the turbidite-BIF deposits into its own stratigraphic group, which we propose to be named the Slemon Group. The trace element signature of the tuff ash bed is reminiscent of arc-type volcanics, likely associated with the Defeat suite granitoids, thereby linking the younger turbidite-BIF basin to its overall tectonic environment.

Preface

This doctoral dissertation is original, independent work carried out by the author. Scientific collaboration and economical support was provided by the Northwest Territories Geoscience Office, while additional economic support was provided by NSERC Discovery Grants to Prof. Kurt Konhauser.

Chapter 2 of this thesis has been submitted as:

Haugaard, R., Ootes, L., Creaser, R. A., Konhauser, K., 2016. The nature of Mesoarchaean seawater and continental weathering in 2.85 Ga BIF, Slave craton, NW Canada. Geochimica et Cosmochimica Acta. In review.

R. Haugaard was responsible for fieldwork, sample collection, manuscript composition and financial support. L. Ootes was responsible for fieldwork, sample collection, edits and financial support. R.A. Creaser was responsible for obtaining Sm-Nd data and edits; K. Konhauser contributed with ideas, edits and financial support.

Chapter 3 of this thesis has been submitted as:

Haugaard, R., Ootes, L., Heaman, L. M., Hamilton, M., Shaulis, B., Konhauser, K., 2016. Depositional timing of Neoarchaean turbidites of the Slave craton - recommended nomenclature and type localities. Canadian Journal of Earth Sciences. Accepted manuscript.

R. Haugaard was responsible for fieldwork, sample collection, acquisition of data (except for the dating of the Burwash ash bed, which was done by M. Hamilton), manuscript composition and financial support; L. Ootes was responsible for fieldwork, sample collection, manuscript composition, edits and financial support; L.M. Heaman contributed with lab facilities and edits; M. Hamilton contributed with lab facilities and edits; B. Shaulis assisted with lab work; K. Konhauser contributed with financial support and edits.

Chapter 4 of this thesis has been submitted as:

Haugaard, R., Ootes, L., Konhauser, K., 2016. Neoarchaean BIF within a 2.62 Ga turbidite-dominated basin, Slave craton, NW Canada. Precambrian Research. In review.

R. Haugaard was responsible for fieldwork, sample collection and manuscript composition; L. Ootes were responsible for fieldwork, sample collection, edits and financial support; K. Konhauser contributed with manuscript edits and financial support.

Acknowledgements

This study has greatly benefitted from the help and expertise of several noteworthy people. First and foremost, I wish to thank Prof. Kurt Konhauser for his insight and advice throughout this project. My appreciation also goes to Luke Ootes from the NWT Geoscience Office for his steadfast curiosity, help and fruitful discussions on the Slave Craton. At University of Alberta, I would particularly emphasize the invaluable help of Mark Labbe and Martin Von Dollen in the thin section laboratory, and to Dr. Andrew Locock in the electron microprobe laboratory. Their assistance and good company during the many hours in the laboratory were indispensable to the successful completion of this thesis.

I also wish to thank Prof. Larry Heaman for insightful discussions on U-Pb systematics in zircons, to Prof. Tom Chacko for help with petrography and to Andrew DuFrane for his help and guidance on the LA-ICP-MS. Thanks also to Joshua Davies and Jesse Reimink for assistance during zircon separation procedures, and useful discussions on U-Pb dating in zircons. Thanks to Prof. Birger Rasmussen for fruitful discussions on BIF and good company in the field during sampling excursions to the Northwest Territories. Thanks to Igor Jacob for help with image scanning, and to Daniel Petrash for discussions on miscellaneous geological subjects. Thanks to Leslie Robbins for his technical assistance. Aleksandra Magdalena for help with thesis edits. Lastly, I also wish to thank the Polar Continental Shelf Program for granting me logistical support during field excursions to the Northwest Territories.

Table of Contents

List of Tables

List of Figures

1. Introduction

The Meso- to Neoarchaean (~3.0-2.5 Ga ago) marks an era in Earth's history when major changes in global surface conditions took place, including episodes of mantle plume activity and continent assembly (Eriksson, 1995; Condie, 2004; Barley et al., 2005), as well as changes in oceanic and atmospheric chemistry (Rye and Holland, 1998; Canfield, 2005). The latter, ultimately due to the evolution of cyanobacteria (Eigenbrode and Freeman, 2006), culminated in the oxygenation of the atmosphere and oceans, the so-called Great Oxidation Event, GOE (Holland, 2002; Bekker et al., 2004). As a result of the GOE, aerobic metabolisms were established on land (Konhauser et al., 2011). This, in turn, facilitated the onset of oxidative weathering reactions, and an increased flux of sulfate and redox-sensitive trace elements to the oceans (Canfield, 2005; Anbar et al., 2007; Bekker and Holland, 2012).

The plume breakouts and the growth of several granitoid-greenstone terrains record an episode of abundant juvenile crust formation (Eriksson et al., 2001, Taylor and McLennan, 2009). The opening and closure of marine basins were a natural process of the amalgamation and accretion of crustal nuclei (e.g., Barley et al., 2005). In these basins, various types of sedimentation took place from submarine volcanics, volcaniclastics, tuffs, epiclastics and chemical sedimentation; the latter including banded iron formation, BIF (Lowe, 1980; Erikkson et al., 2001).

1.1. BIF

Banded iron formations (BIFs) are iron- and silica-rich metasedimentary rocks that span much of the Archaean and early Palaeoproterozoic rock record. They are chemically pure, containing low concentrations of Al_2O_3 (<1 wt.%) and incompatible elements (e.g., Ti, Zr, Th, Hf and Sc <20 ppm), which indicates minimal detrital input. Because they precipitated out from seawater, their chemical compositions have been widely used as proxies for ancient seawater composition (Bjerrum and Canfied, 2002; Konhauser et al., 2009; Robbins et al., 2013; Swanner et al., 2013).

The majority of Archaean BIFs are made up of alternating bands of silica (SiO_2) and magnetite (Fe_3O_4) that together constitute >90% of the rock by weight (James, 1954; Trendall, 2004). The depositional conditions under which these rocks formed are still highly debated, due in part to their metamorphic overprinting, as well as the lack of modern analogues. The overall consensus is that the current BIF mineralogy is of secondary origin, and formed during both diagenetic and metamorphic processes. It is thought that the primary precipitates were likely amorphous silica ($Si(OH)_4$) and a ferric oxyhydroxide, such as ferrihydrite ($Fe(OH)_3$) (Klein, 2005; Bekker et al., 2010).

The major palaeoenvironmental changes that took place during the Meso- to Neoarchaean eras played a key role in shaping the late Archaean rock record (e.g., Eriksson et al, 2001), and can potentially be traced in 3.0 to 2.5 Ga BIF. For instance, the peak of BIF deposition during the late Archaean-earliest Palaeoproterozoic, best represented with the extensive Hamersley Group BIF from Western Australia (Haugaard et al., 2016), has been linked to major flood basalt events (Barley et al., 1997), while their sudden decrease between ca. 2.4–2.0 Ga, strongly support the GOE (e.g., Holland, 1999; Eriksson and Altermann, 2004).

1.2. BIF as a metamorphic rock

Defining the mineralogy and degree of metamorphic overprinting in BIF is fundamental to understanding the mechanisms underpinning the formation of these chemical sedimentary rocks. Detailed mineralogical studies on BIF have been carried out by numerous researchers (e.g., Trendall and Blockley, 1970; Klein, 1973, 1974, 2005; Ayres, 1972; Beukes, 1973; Gole, 1980a, 1980b; Gole and Klein, 1981a, 1980b; Klein and Gole, 1981; Ewers and Morris, 1981; Dymek and Klein, 1988; Webb et al., 2003; Rasmussen et al., 2013, 2014, 2015). Collectively, none of the BIF occurrences reported in these studies have preserved any of their original mineralogy. For instance, chert (microcrystalline quartz), hematite, magnetite, greenalite, minnesotaite, stilpnomelane and dolomite-ankerite are believed to be part of the late-diagenetic to low-grade metamorphic (sub-greenscist facies) assemblages (e.g., Trendall and Blockley, 1970; Ayres, 1972; Klein, 2005; Haugaard et al., 2016). During mid-to-moderate grade metamorphism (greenschist-amphibolite facies), chert/quartz, magnetite, grunerite, ferro-

actionolite, ferro-hornblende can predominate (Dymek and Klein, 1988; Klein, 2005, Haugaard et al., 2013). Under high-grade metamorphic conditions (upper amphibolite-granulite facies), quartz, magnetite, pyroxene and olivine appears (Gole and Klein, 1981; Fonarev et al., 2006). The low-grade mineral assemblages are only reported to exist in the well-studied Palaeoproterozoic BIF whereas the higher metamorphic mineral assemblages predominate in Archaean BIF. The proposed primary precursor minerals in BIF are ferric hydroxide, siderite and amorphous silica (Klein, 2005).

1.3. BIF and the Archaean seawater

1.3.1. The compositional banding

BIF is by definition a heterogeneous rock, with its alternating silica-rich and iron-rich bands. Throughout the years, the majority of studies attempting to resolve the nature of the Archaean seawater have used bulk (whole rock) geochemical BIF analysis (e.g., Bau and Dulski, 1996; Alexander et al., 2008, 2009; Kato et al., 1998, 2006). However, whole rock geochemical analyses can only provide a general picture of the ambient seawater, that is, bulk seawater conditions. That means shorter-term trends in the chemical fabric of the BIF record are not fully captured, and therefore, a more detailed method is required in order to resolve regional differences in ambient seawater conditions.

In this regard, the separation of BIF samples into individual silica-rich and iron-rich bands, and the analysis of the variations in their composition, has proven to be a useful technique to achieve a higher temporal resolution of changing seawater composition. Studies applying detailed petrographic and geochemical analyses on a layer-by-layer basis suggest that the banding in BIF reflects background silica precipitation from upper seawater that is occasionally interrupted by pulses of iron-rich bottom water (Hamade et al. 2003; Frei and Polat, 2007; Haugaard et al., 2013). These pioneering studies suggest that the interaction of two different water pools in the water column from which BIF precipitated is a likely model for the origin of the banding. However, additional studies of this type need to be carried out in order to confirm this hypothesis.

1.3.2. Rare earth elements + yttrium (REY)

The rare earth elements and yttrium (REY) has been widely used to trace the chemical signature of the contemporaneous seawater during BIF precipitation (Bau and Dulski, 1996; Bolhar et al., 2004). With a few exceptions, such as cerium (Ce) and europium (Eu), the shale-normalized REY distribution in BIF closely resembles the modern seawater REY pattern: low overall REY abundances, positive La- and Y-anomalies, and depleted light rare earth elements (LREE) relative to heavy rare earth elements (HREE). Unlike modern seawater, however, Archaean BIFs have positive Eu-anomalies and do not possess the characteristic strong negative Ce-anomalies of modern seawater. The positive Eu-anomalies are attributed to high-temperature (>350°C) hydrothermal fluids from mid-ocean ridges and back-arc spreading zones injecting solutes into anoxic bottom waters (Bau and Möller, 1993). The positive Eu anomaly is a result of enrichment of reduced Eu^{2+} in hot (>300°C) hydrothermal fluids flowing under reduced conditions through the oceanic crust at spreading ridges (Michard et al., 1983; Danielson et al., 1992). It has been proposed that the generally decrease in the size of the Eu anomaly in BIF throughout the Archaean is a result of decreasing upper mantle temperatures, which lowers the potential of preferential mobilization of Eu^{2+} in the fluids (e.g., Derry and Jacobsen, 1990; Danielson et al., 1992; Huston and Logan, 2004; Kato et al., 2006). Conversely, the absence of Ce anomalies is thought to reflect anoxic conditions (e.g., $<10^{-5}$ PAL or present day levels of O_2), which prevented the fractionation of redox-sensitive Ce^{3+} from neighbouring REEs (Bolhar et al., 2004).

1.3.3. Trace metals

The availability of essential nutrients, such as phosphorus, iron, chromium, nickel, molybdenum and vanadium, is a crucial component of the marine biosphere, and controls primary productivity. Indeed, the proliferation of microorganisms strongly depends on the relative flux of these bioessential metals into seawater. As pure authigenic chemical sedimentary rock (i.e., free of detrital contamination), it is thought that BIF effectively captures the evolving elemental (and isotopic) signatures of the seawater from which it precipitated. BIF can, therefore, be used to indirectly to track the plausibility of various microbial metabolisms throughout the Precambrian (Bjerrum and Canfield, 2002;

Konhauser et al., 2009).

The trace metal composition of BIF may also reflect changes in the redox state of the early atmosphere and oceans. For instance, an increase in Mo concentration in the ~2.5 Ga Mount McRae shale of Western Australia has been interpreted to reflect a 'whiff' of oxygen before the GOE (Anbar et al., 2007). This Mo was likely sourced from oxidative weathering of Mo-bearing sulfides in nearby continental crustal rocks. By contrast, Konhauser et al. (2009) found that post-2.7 Ga BIF incorporated less Ni as a result of decreased eruption of komatiitic lavas following the cooling of the upper mantle towards the Archaean-Proterozoic transition. Changing dissolved nickel input to the oceans would have had a profound effect on the proliferation of nickel-dependent methanogenic bacteria, and by extension, the redox state of the early atmosphere.

Based on Cr isotope values in BIF through time, Frei et al. (2009) proposed that cyanobacterial activity may already have been abundant by 2.8 Ga ago, and that the consequent production of free O_2 as a result of oxygenic photosynthesis may have led to the initial oxidative weathering of the continents several hundred millions years before the GOE. Conversely, Konhauser et al. (2011) suggested that oxidative weathering during the Mesoarchaean likely did not occur as suggested by the low authigenic Cr supply to the oceans. Collectively, these studies show a strong link between Archaean seawater composition (as reflected by BIF) and the composition of the coeval and adjacent crustal rocks.

1.4. The main sources of solutes for BIF precipitation

Seawater composition is mainly controlled by two processes: (1) submarine hydrothermal activity and (2) continental weathering. BIF potentially contain the chemical imprints from the mantle, oceanic and the continental reservoirs (e.g., Bekker et al., 2010; Haugaard et al., 2013). In modern seawater, the dominant contribution to solutes is from the erosion of the continents. Through the use of Nd isotopes, it is estimated that only ~2.5% of the modern ocean seawater chemistry is controlled by mid-ocean hydrothermal input (Goldstein and Jacobsen, 1987). It is thought that hydrothermal input into the oceans was up to an order of magnitude higher in the Archaean due to a higher heat-flux of the Archaean mantle (e.g., Nisbet et al., 1993). The best estimate of this flux is that it

was ~2-3 times higher than in the Phanerozoic (see Jacobsen and Pimentel-klose, 1988) and this was likely accommodated by higher submarine venting of hydrothermal fluids.

1.4.1. Silica and iron

The sources of silica and iron in BIF have been strongly disputed. It has been suggested that iron as Fe^{2+} could have been hydrothermally-sourced (e.g., Holland, 1973; Dymek and Klein, 1988) or as a result of continental weathering (Alibert and McCulloch, 1993). Similarly, a hydrothermal source for silica has been proposed by Steinhöfel et al. (2010), whereas continentally-sourced silica was proposed by Hamade et al. (2003).

One of the most reliable tools for tracing the relative continental and hydrothermal inputs in BIF are Sm-Nd isotope systematics (e.g., Miller and O'Nions, 1985). For instance, compiled $^{143}Nd/^{144}Nd$ data for pre-2.7 Ga BIF suggest that bulk anoxic Archaean seawater was dominated by high-temperature hydrothermal alteration of mantle-derived oceanic crust (Alexander et al., 2009). This alteration process was presumably also responsible for delivering the iron to BIF. In contrast, Frei and Polat (2007), Frei et al. (2008) and Haugaard et al. (2013) used the Nd signature in BIF to show that the silica in some BIF was sourced from continental landmasses and was decoupled from the iron source. One of the advantages of using Nd as a proxy for changes in seawater composition is that it behaves as a non-conservative element with a residence time in the (modern) oceans of 300-1000 years (much shorter than its mixing time) making it useful to track small timescale variations (e.g., Piepgras and Wasserburg, 1987; Eldersfield et al., 1990; Andersson et al., 1992).

1.5. BIF and the depositional environment

The origin of BIF is ambiguous, mostly because they are reported to have originated in various depositional environments, from rift-dominated continental margins, to back-arc and fore-arc volcanic dominated basins, as well as stable continental platforms (e.g., Gross, 1980, 1983). Thus, on a broader scale, these enigmatic rocks seem to be a natural part of diverse depositional environments controlled by various tectonic regimes. It seems, however, that high activity of submarine volcanism and hydrothermal alteration of

the basin floor (see above) played an active role in BIF deposition (Holland, 1983; Jacobsen and Pimentel-Klose, 1988; Isley, 1995; Isley and Abbott, 1999; Barley et al., 2005).

The marine depositional settings for Archaean BIF formation differed from Palaeoproterozoic marine settings. The relatively small depositional basins in the Archaean developed in relation to active arc-type tectonics and rapid thermal subsidence in environments that rarely were stable over extended periods of time (e.g., Gross, 1983). The BIF in Archaean basins are typically found associated with interbedded volcanic and volcaniclastic sedimentary rocks such as greywacke turbidites (e.g., Gross, 1983; Lowe and Tice, 2007; Haugaard et al., 2013). In contrast, the Palaeoproterozoic basins reflect a more stable style of sedimentation in extensive shallow marine basins along stable continental platforms (e.g., Gross, 1980, 1983; Taylor and McLennan, 1981; Eriksson et al., 2001; Condie, 2004; Barley et al., 2005; Haugaard et al., 2016). Although exceptions do exist (Alexander et al., 2008), the BIF deposited in the former setting are considered Algoma-type, whereas BIF formed in the latter setting are Superior-type. The latter includes the major BIF of the earliest Palaeoproterozoic, such as the Hamersley Group BIF (e.g., Gross, 1980; Haugaard et al., 2016).

1.6. Objectives

The Slave craton constitute ~200,000 km^2 of the northwestern part of the Canadian Shield and has a preserved Archaean rock record that is unique and extends deep in time from the Hadaen (≤4.03 Ga) to the very late Neoarchaean (2.55 Ga). The majority of the Slave craton is dominated by 2.68-2.58 Ga old granitoids and thick packages of metamorphosed greywacke-mudstone facies (e.g., Bleeker et al., 1999a; Bennett et al., 2005). The craton has been divided into a central-western part, the Central Slave Basement Complex (CSBC), and a younger arc-related eastern part, the eastern Slave domain, where no basement exposures has been reported (e.g., Isachsen and Bowring 1994). The CSBC is composed of a variety of polymetamorphic gneiss assemblages ranging from tonalitic, dioritic to granodioritic in composition, some of which are migmatized (Isachsen and Bowring, 1994).

Overlying these basement gneisses, a ca. 2.9-2.8 Ga regional unconformity marks the onset of an autochtonous supracrustal package (the Yellowknife Supergroup) beginning with a potentially metamorphosed weathering profile that is overlain by a widespread, but thin (2-200 m), basal sheet of quartzite-quartzarenites and BIF, the Central Slave Cover Group (CSCG). The detrital zircons from the quartzite show four main U-Pb age peaks at 3.40 Ga, 3.15 Ga, 2.95 Ga and 2.83 Ga (Sircombe et al., 2001).

The CSCG, in turn, is overlain by two volcanic-dominated sequences (e.g., Ketchum et al., 2004), which includes an older 2.74-2.7 Ga old rift-dominated massive to pillowed tholeiitic basalts (the Kam Group) and a younger sequences comprising a large abundance of arc-like felsic volcanic and volcaniclastic rocks, the ca. 2.69-2.66 Ga Banting Group bimodal volcanics (Bleeker et al., 1999b). One of the largest and best-preserved Archaean turbidite basins, the ca. 2.66 Ga (Ferguson et al., 2005) Burwash Basin, conformably overlies the volcanic dominated stratigraphy and covers a large part of the craton. These are the most abundant supracrustal rocks in the Slave craton and are composed of arc-related metamorphosed greywacke-mudstone turbidites (e.g., Ootes et al., 2009).

As opposed to many other cratons (e.g., Superior craton), and despite of the thick Kam Group mafic dominated rocks, the supracrustal rocks within the Slave craton mostly comprise sedimentary rather than volcanic lithofacies (e.g., Isachsen and Bowring, 1994). In fact, a sedimentary to volcanic rock ratio of almost 4:1 has been estimated by Padgham and Fyson (1992), which is sufficiently more than some of the volcanic provinces in the Superior craton (<20% sedimentary dominated). Of particular interest is the virtual absent of ultramafic komatiitic lavas from the supracrustal stratigraphy of the Slave craton, which typically is a tectonic and depositional important component of many Archaean greenstone belts (e.g., Windley, 1984; Padgham, 1992).

Within the Slave craton, BIF formation occurred in two different depositional environments: (1) ~2.9-2.8 Ga continental rift basin with BIF and quartzite deposited on the newly formed continental shelf, and (2) ~2.62 Ga arc-type basin with BIF and extensive deposition of greywacke and mudstone turbidites, locally with ash tuff beds.

The aim of this study is to characterize the seawater composition within these two Archaean depositional basins. This thesis provides a basic field observational and

petrographic framework for the BIFs in which context the geochemical data should be viewed. Importantly, the study of these BIFs will provide new insights into ocean chemistry and the depositional settings during one of the most important periods in the Earth history. To date, no geochemical data exists for these units. This is surprising given that such a study will provide vital information about the palaeo-seawater composition and evolution of the depositional basins, and in particular, the source inputs controlling the seawater over that time interval.

In this thesis, a detailed study of seawater patterns will be demonstrated by applying detailed layer-by-layer analysis of the BIF. Furthermore, the role of the associated supracrustal rocks in BIF deposition since they, unlike BIF, have modern analogues, will be examined. A fuller understanding of the seawater composition is then used to make inferences about the composition of local and regional terrestrial and hydrothermal sources. In addition to these two BIF chapters, a geochronology study of tuff beds and maximum deposition ages of the Neoarchaean BIF-turbidites is presented. The depositional ages of these, often homogenous, BIF-turbidites are poorly constrained and this chapter helps construct the timing of these important BIF deposits.

Furthermore, also presented are preliminary work on 1) the fuchsitic quartzite immediately underlying the 2.85 Ga BIF, and on 2) a possible metamorphosed weathering horizon preserved in the basement gneisses immediately underlying the fuchsitic quartzite (Appendices F and G). The latter is important since the main contributions to seawater composition is solutes and particles derived from continental weathering, and therefore, the preservation of a continental landmass that once was exposed for subaerial weathering is of key interest. In the former, I attempt to characterize the ultramafic contribution to the basin by analyzing the composition of the detrital chromite grains preserved in the fuchsitic quartzite.

References

Alexander, B. W., Bau, M., Andersson, P., 2009. Neodymium isotopes in Archean sea-water and implications for the marine Nd cycle in Earth's early oceans. Earth and Planetary Science Letters 283, 144–155.

Alexander, B. W., Bau, M., Andersson, P., Dulski, P., 2008. Continentally-derived solutes in shallow Archean seawater: rare earth element and Nd isotope evi- dence in iron formation from the 2.9Ga Pongola Supergroup, South Africa. Geochimica et Cosmochimica Acta 72, 378–394.

Alibert C., McCulloch M. T. M., 1993. Rare earth element and neodymium isotopic compositions of the banded iron-formations and associated shales from Hamersley, western Australia. Geochimica et Cosmochimica Acta 57, 1–18.

Anbar, A. D., Duan, Y., Lyons, T. W., Arnold, G. L., Kendall, B., Creaser, R. A., Kaufman, A. J., Gordon, G. W., Scott, C., Garvin, J., Buick, R., 2007. A whiff of oxygen before the Great Oxidation Event? Science 317 (5846), 1903–1906

Andersson, P. S., Wasserburg, G. J., Ingri, J., 1992. The sources and transport of Sr and Nd isotopes in the Baltic Sea. Earth and Planetary Science Letters, 113, 459–472.

Ayres, D., 1972. Genesis of Iron-bearing minerals in banded iron formation mesobands in The Dales Gorge Member, Hamersley Group, Western Australia. Economic Geology 67, 1214–1233.

Barley, M., Bekker, A., Krapez, B., 2005. Late Archean to Early Paleoproterozoic global tectonics, environmental change and the rise of atmospheric oxygen. Earth and Planetary Science Letters 238, 156–171.

Barley, M., Pickard, A., Sylvester, P., 1997. Emplacement of a large igneous province as a possible cause of banded iron formation 2.45 billion years ago. Nature 385, 1–4.

Bau, M., Möller, P., 1993. Rare earth element systematics of the chemically precipitated component in Early Precambrian iron formations and the evolution of the terrestrial atmosphere–hydrosphere–lithosphere system. Geochimica et Cosmochima Acta 57, 2239–2249.

Bau, M., Dulski, P., 1996. Distribution of yttrium and rare-earth elements in the Penge and Kurumanironformations, Transvaal Supergroup, South Africa. Precambrian Research 79, 37–55.

Bekker, A., Holland, H. D., Wang, P. -L., Rumble III, D., Stein, H. J., Hannah, J. L., Coetzee, L. L., Beukes, N. J., 2004. Dating the rise of atmospheric oxygen. Nature 427, 117–120

Bekker, A., Slack, J. F., Planavsky, N., Krapez, B., Hofmann, A., Konhauser, K. O., Rouxel, O. J., 2010. Iron formation: the sedimentary product of a complex interplay among mantle, tectonic, oceanic, and biospheric processes. Economical Geology 105, 467–508.

Bekker, A., Holland, H. D., 2012. Oxygen overshoot and recovery during the early Paleoproterozoic. Earth and Planetary Science Letters 317-318, 295-304.

Bennett, V., Jackson, V. A., Rivers, T., Relf, C., Horan, P., Tubrett, M., 2005. Geology and U–Pb geochronology of the Neoarchean Snare River terrane: tracking evolving tectonic regimes and crustal growth. Canadian Journal of Earth Science 934, 895–934.

Beukes, N., 1973. Precambrian iron-formations of southern Africa. Economical Geology 68, 960–1004.

Bjerrum, C. J., Canfield, D. E., 2002. Ocean productivity before about 1.9 Gyr ago limited by phosphorus adsorption onto iron oxides. Nature 417, 159-162.

Bleeker, W., Ketchum J. W. F., Jackson, V. A., Villeneuve, M. E., 1999a. The Central Slave Basement Complex, Part I: its structural topology and autochthonous cover. Canadian Journal of Earth Sciences 36, 1083-1109.

Bleeker, W., Ketchum, J. W., Davis, W. J., 1999b. The Central Slave Basement Complex, Part II: age and tectonic significance of high-strain zones along the basement-cover contact. Canadian Journal of Earth Sciences 36, 1111–1130.

Bolhar, R., Kamber, B. S., Moorbath, S., Fedo, C. M., Whitehouse, M. J., 2004. Characterisation of early Archaean chemical sediments by trace element signatures. Earth and Planetary Science Letters 222, 43–60.

Canfield, D. E., 2005. The early history of atmospheric oxygen: homage to Robert M. Garrels. Annual Review. Earth and Planetary Science 33, 1–36

Condie, K. C., 2004. Supercontinents and superplume events: distinguishing signals in the geologic record. Physics of the Earth and Planetary Interiors 146, 319–332.

Danielson, A., Möller, P., Dulski, P., 1992. The europium anomalies in banded iron formations and the thermal history of the oceanic crust. Chemical Geology 97, 1–12.

Derry, L. A., Jacobsen, S. B., 1990. The chemical evolution of Precambrian seawater: evidence from REEs in banded iron formations. Geochimica et Cosmochimica Acta 54, 2965–2977.

Dymek, R. F., Klein, C., 1988. Chemistry, petrology and origin of banded iron- formation lithologies from the 3800 MA isua supracrustal belt, West Greenland. Precambrian Research 39, 247–302.

Eigenbrode, J. L., Freeman, K. H., 2006. Late Archean rise of aerobic microbial

ecosystems. Proceedings of the National Academy of Sciences 103, 15759–15764.

Eriksson, K. A., 1995. Crustal growth, surface processes, and atmospheric evolution on the early Earth. Geological Society of London Special Publications 95, 11-25.

Eriksson, P. G., Altermann, W., 2004. Evolution of the Hydrosphere and Atmosphere. In: Eriksson P. G. et al. (eds.). The Precambrian Earth: Tempos and Events. Elsevier, Amsterdam. pp. 359-513.

Eriksson, P. G., Martins-Neto, M. A., Nelson, D. R., Aspler, L. B., Chiaranzelli, J. R., Catuneanu, O., Sakar, S., Altermann, W., Rautenbach, C. J., 2001. An introduction to Precambrian basins: their characteristics and genesis. Sedimentary Geology 141-142, 1–35.

Elderfield, H., Upstill-Goddard, R., Sholkovitz, E. R., 1990. The rare earth elements in rivers, estuaries, and coastal seas and their significance to the composition of ocean waters. Geochimica et Cosmochimica Acta 54, 971–991.

Ewers, W., Morris, R., 1981. Studies of the Dales Gorge Member of the Brockman iron formation, Western Australia. Economic Geology 76, 1929–1953.

Frei, R., Dahl, P. S., Duke, E. F., Frei, K. M., Hansen, T. R., Frandsson, M. M., Jensen, L. A., 2008. Trace element and isotopic characterization of Neoarchaean and Paleoproterozoic iron formations in the Black Hills (South Dakota, USA): assessment of chemical change during 2.9–1.9Ga deposition bracketing the 2.4–2.2Ga first rise of atmospheric oxygen. Precambrian Research 162, 441–474.

Frei, R., Gaucher, C., Poulton, S. W., Canfield, D. E., 2009. Fluctuations in Precambrian atmospheric oxygenation recorded by chromium isotopes. Nature 461, 250–253

Frei, R., Polat, A., 2007. Source heterogeneity for the major components of ~3.7Ga

Banded Iron Formations (Isua Greenstone Belt, Western Greenland): tracing the nature of interacting water masses in BIF formation. Earth and Planetary Science Letters 253, 266–281.

Goldstein S. J., Jacobsen S. B., 1987. The Nd and Sr isotopic systematics of river-water dissolved material - Implications for the sources of Nd and Sr in seawater. Chemical Geology 66, 245–272.

Gole, M. J. 1980a. Mineralogy and petrology of very low metamorphic grade Archaean banded iron-formations, Weld Range, Western Australia. American Mineralogist 66, 8-25.

Gole, M. J., 1980b. Low temperature retrograde minerals in metamorphosed Archean banded iron formations, western Australia. Canadian Mineralogist 18, 205–214.

Gole, M. J., Klein, C., 1981a. Banded Iron-Formation through much of Precambrian time. Journal of Geology 89, 169–183.

Gole, M. J., Klein, C., 1981b. High-grade metamorphic Archean banded iron-formations, Western Australia: Assemblages with coexisting pyroxenes ± fayalite. American Mineralogist 66, 87–99.

Gross, G., 1980. A classifiacation of iron formations based on depositional environments. Canadian Mineralogist 18, 215-222.

Gross G., 1983. Tectonic systems and the deposition of iron-formation. Precambrian Research 20, 171-187.

Haugaard, R., Frei R., Stendal, H., Konhauser, K., 2013. Petrology and geochemistry of the ~2.9 Ga Itilliarsuk banded iron formation and associated supracrustal rocks, West

Greenland: Source characteristics and depositional environment. Precambrian Research 229, 150–176.

Haugaard R., Pecoits E., Lalonde S., Rouxel O. and Konhauser K., 2016. The Joffre Banded Iron Formation, Hamersley Group, Western Australia: Assessing the Palaeoenvironment through detailed Petrology and Chemostratigraphy. Precambrian Research 273, 12–37.

Holland, H., 2002. Volcanic gases, black smokers, and the Great Oxidation Event. Geochimica et Cosmochimica Acta 66, 1-16.

Holland, H.D., 1999. When did the Earth's atmosphere become oxic? A reply. Geochemical News 100, 20–22.

Huston, D. L., Logan, G. A., 2004. Barite, BIFs and bugs: evidence for the evolution of the Earth's early hydrosphere. Earth and Planetary Science Letters 220, 41–55.

Isachsen, C. E., Bowring, S. A., 1994. Evolution of the Slave craton. Geology 22, 917-920.

Isley, A., Abbott, D., 1999. Plume-related mafic volcanism and the deposition of banded iron formation. Journal of Geophysical Research 104, 15461-15477.

Isley, A. E., 1995. Hydrothermal plumes and the delivery of iron to banded iron formation. Journal of Geology 103, 169–185.

Jacobsen, S., Pimentel-Klose, M., 1988. A Nd isotopic study of the Hamersley and Michipicoten banded iron formations: the source of REE and Fe in Archean oceans. Earth and Planetary Science Letters 87, 29–44.

James, H. L., 1954. Sedimentary facies of iron-formation. Economic Geology 49, 235–291.

Kato, Y., Ohta, I., Tsunematsu, T., 1998. Rare earth element variations in mid-Archean banded iron formations: Implications for the chemistry of ocean and continent and plate tectonics. Geochimica et Cosmochimica Acta 62, 1–23.

Kato, Y., Yamaguchi, K., Ohmoto, H., 2006. Rare earth elements in Precambrian banded iron formations: Secular changes of Ce and Eu anomalies and evolution of atmospheric oxygen. Geological Society of America Memoir 198, 269-289.

Ketchum, J. W. F., Bleeker, W., Stern, R. A., 2004. Evolution of an Archean basement complex and its autochthonous cover, southern Slave Province, Canada. Precambrian Research 135, 149–176.

Klein, C., 1973, Changes in mineral assemblages with metamorphism of some banded Precambrian iron-formations. Economic Geology 68, 1075-1088.

Klein, C., 1974. Greenalite, stilpnomelane, minnesotaite, crocidolite and carbonates in a very low grade metamorphic precambrian iron-formation. Canadian Mineralogist 12, 1–24.

Klein, C., 2005. Some Precambrian banded iron-formations (BIFs) from around the world: their age, geologic setting, mineralogy, metamorphism, geochemistry, and origins. American Mineralogist 90, 1473–1499.

Klein, C., Gole, M., 1981. Mineralogy and petrology of parts of the Marra Mamba Iron Formation, Hamersley Basin, Western Australia. American Mineralogist 66, 1–19.

Konhauser, K. O., Pecoits, E., Lalonde, S. V., Papineau, D., Nisbet, E. G., Barley, M. B., Arndt, N. T., Zahnle, K., Kamber, B. S., 2009. Oceanic nickel depletion and a methanogen famine before the Great Oxidation Event. Nature 458, 750–754.

Lowe, D.R., 1980. Archean sedimentation. Annual Reviews of Earth and Planetary Sciences 8, 145-167.

Lowe, D. R., Tice, M. M., 2007. Tectonic controls on atmospheric, climatic, and biological evolution 3.5–2.4 Ga. Precambrian Research 158, 177–197.

Michard, A., Albarbde, F., Michard, G., Minster, J. F., Charlou, J. L., 1983. Rare earth elements and uranium in high-temperature solutions from East Pacific Rise hydrothermal vent field (13~N). Nature 303, 795-797.

Miller, R. G., O'Nions, R. K., 1985. Source of Precambrian chemical and clastic sediments. Nature 314, 325–330.

Nisbet, E. G., Cheadle, M. J., Arndt, N. T., Bickle, M. J., 1993. Constraining the potential temperature of the Archean mantle — a review of the evidence from komatiites. Lithos 30, 291–307.

Ootes, L., Davis, W. J., Bleeker, W., Jackson, V. A., 2009. Two Distinct Ages of Neoarchean Turbidites in the Western Slave Craton: Further Evidence and Implications for a Possible Back-Arc Model. The Journal of Geology 117, 15–36.

Padgham, W., 1992. Mineral deposits in the Archean Slave Structural Province; lithological and tectonic setting. Precambrian Research 58, 1–24.

Padgham, W., Fyson, W., 1992. The Slave Province: a distinct Archean craton. Canadian Journal of Earth Sciences 29, 2072-2086.

Piepgras, D. J., Wasserburg, G. J. 1987. Rare earth element transport in the western North Atlantic inferred from Nd isotopic observations, Geochim. Cosmochim. Acta 51, 1257-1271

Rasmussen, B., Meier, D., Krapež, B., Muhling, J., 2013. Iron silicate microgranules as precursor sediments to 2.5-billion-year-old banded iron formations. Geology 41, 435–438.

Rasmussen, B., Krapež, B., Meier, D.B., 2014. Replacement origin for hematite in 2.5 Ga banded iron formation: evidence for postdepositional oxidation of iron- bearing minerals. Geological Society of America Bulletin 126 (3–4), 438–446.

Rasmussen, B., Krapež, B., Muhling, J.R., 2015. Seafloor silicification and hardground development during deposition of 2.5 Ga banded iron formations. Geology 43, 235–238.

Robbins,L. J., Lalonde, S. V., Saito, M. A., Planavsky, N. J., Mloszewska, M. A., Pecoits, E., Scott, C., Dupont, C. L., Kappler, A., Konhauser, K. O., 2013. Authigenic iron oxide proxies for marine zinc over geological time and implications for eukaryotic metallome evolution. Geobiology 11, 295-306.

Rye, R., Holland, H., 1998. Paleosols and the evolution of atmospheric oxygen: A critical review. American Society of London Special Publications 95, 11–25.

Taylor S. R., McLennan S. M., Armstrong R. L. and Tarney J., 1981. The Composition and Evolution of the Continental Crust: Rare Earth Element Evidence from Sedimentary Rocks. Philosphia Transaction of the Royal Society 301, 381–399.

Taylor, S. R., McLennan, S. M., 2009. Planetary Crusts: Their Composition, Origin and Evolution. Cambridge University Press, New York, pp. 378.

Trendall, A. F., Blockley, J. G., 1970. The Iron-Formations of the Precambrian Hamersley Group, Western Australia. Geological Survey Western Australia Bulletin 119.

Trendall, A. F., Blockley, J. G., 2004. Precambrian iron-formation. In: Eriksson, P.G., Altermann, W., Nelson, D.R., Mueller, W.U., Catuneanu, O. (Eds.), The Precam- brian

Earth: Tempos and Events. Developments in Precambrian Geology, vol. 12. Elsevier, Amsterdam, pp. 403–421.

Webb, A. D., Dickens, G. R., Oliver, N. H. S., 2003. From banded iron-formation to iron ore: geochemical and mineralogical constraints from across the Hamersley Province, Western Australia. Chemical Geology 197, 215–251.

Windley, B. F., 1984. The Evolving Continents. John Wiley and Sons Limited, 399 p.

2. The nature of Mesoarchaean seawater and continental weathering in 2.85 Ga BIF, Slave craton, NW Canada

2.1. Introduction

Banded iron formations (BIF) are iron-rich (15-40 wt.% Fe_2O_3) and siliceous (40-60 wt.% SiO_2) sedimentary deposits that precipitated from seawater throughout much of the Archaean. The mineralogy of Archaean BIF from the best-preserved successions is remarkably uniform, comprising mostly microcrystalline quartz (chert), magnetite, hematite, and Fe-rich silicate minerals (etc., actinolite, grunerite, hornblende). They typically contain low concentrations of Al_2O_3 (<1 wt.%) and incompatible elements (Ti < 50 ppm, Zr, Th, Nb, Hf and Sc <20 ppm), which indicates a deep-marine depositional setting with low input of epiclastic material (e.g., Trendall, 2002; Pickard et al., 2004). Based on their shale-normalized rare earth element and yttrium (REY) patterns, it is also now generally accepted that BIF captured the composition of bulk seawater. This observation has allowed for the chemical composition of BIF to be used as proxies not only for the source of solutes to the Precambrian oceans (e.g., Jacobsen and Pimentel-Klose, 1988; Derry and Jacobsen, 1990; Danielson et al., 1992; Alibert and McCulloch, 1993; Bau and Möller, 1993; Bau and Dulski, 1999; Hamade et al., 2003; Sreenivas and Murakami, 2005; Frei and Polat, 2007), but also as a means to estimate the bulk composition and redox-structure of ancient seawater (e.g., Bjerrum and Canfield, 2002; Ohmoto et al., 2006; Konhauser et al., 2009).

Some of the most compelling research into the environmental conditions of BIF deposition comes from the measurement of samarium (Sm) and neodymium (Nd) because (1) they share similar chemical affinities and have high resistance to fractionation in different geological processes (e.g., submarine hydrothermal alteration versus continental weathering), and (2) Nd is a non-conservative element with a residence time in the oceans of 300-1000 years (much shorter than its mixing time) making it useful to track small timescale variations (e.g., Piepgras and Wasserburg, 1987;

Eldersfield et al., 1990; Andersson et al., 1992). BIF older than ca. 2.7 Ga generally have relatively homogenous $\varepsilon_{Nd}(t)$ of +1 to +2 that are typical of the deep-waters dominated by hydrothermal fluids (Alexander et al., 2009). Deviation from these to more negative values down to $\varepsilon_{Nd}(t)$ of -3 indicate the influence of older terrestrial sources in BIF deposition (e.g., Miller and O'Nions, 1985; Alexander et al., 2008).

Recent studies, however, have shown that some BIF do not conform to the canonical view of chemical sedimentary rock reflecting bulk ocean water conditions. For instance, Alexander et al. (2008) demonstrated that the 2.9 Ga Pongola BIF in South Africa was deposited in a near-shore environment with interbedded and intermixed epiclastic detritus sourced from emergent continental crustal sources. Similarly, Haugaard et al. (2013) showed the existence of shaley-BIF with mixed chemical and siliciclastic components within the 2.9 Ga Itilliarsuk BIF in West Greenland. Collectively, the $\varepsilon_{Nd}(t)$ values in both BIF units were partly inherited by local-to-regional crustal sources. As such, some BIF reflect local seawater variations as a function of the specific tectonic and depositional environment. In this regard, one of the main issues pertaining to using BIF as palaeo-proxies is that much of the existing dataset is based on bulk rock analyses, meaning that short-term trends in the chemical fabric of the sedimentary rock record are not fully captured.

In this work, we present new field, petrologic, and geochemical data from the ca. 2.85 Ga BIF from the Central Slave Cover Group, Slave craton, northwestern Canada that were initially reported by Bleeker et al. (1999a). The BIF were deposited alongside shelf- and shoreline-type deposits, such as quartz pebble-conglomerate and fuchsitic quartzite, and it is one of the first documented Mesoarchaean BIF deposited in a near-shore setting. This novelty allows for a determination of the relative importance of hydrothermal versus continental sourcing of the elemental constituents during the time span of deposition. On a layer-by-layer basis, we demonstrate that these BIF are complex sedimentary units that provide important clues about internal seawater variations and the nature of local-to-regional landmasses.

2.2. The Slave craton: the basement and the cover sequence

The Slave craton constitutes ~200,000 km^2 of the northwestern part of the Canadian Shield (Fig. 2.1A) and has a preserved Archaean rock record that extend deep in time from the Hadaean ($\leq$4050 Ma) to the very late Neoarchaean (2550 Ma). In the west and central Slave craton, basement rocks form a block, the Central Slave Basement Complex (CSBC) that is composed of a variety of polymetamorphic gneiss assemblages ranging from tonalitic, dioritic to granodioritic in composition, some of which are migmatized and mylonitized (Isachsen and Bowring, 1994, 1997; Bleeker et al., 1999a,b; Ketchum et al., 2004; Reimink et al., 2014). Apart from the minor and ancient Hadaean to Eoarchaean tonalitic to gabbroic Acasta gneisses, the majority of the CSBC ranges between 3300-2900 Ma (Bleeker et al., 1999b; Ketchum et al., 2004).

On the top of these basement gneisses occurs a ca. 2900-2800 Ma (Isachsen and Bowring, 1997) regional unconformity that marks the onset of an autochtonous supracrustal package, the Central Slave Cover Group (CSBC; Bleeker et al., 1999a). It begins with a conglomerate that is overlain by a widespread, but thin (2-200 m) fuchsitic quartzite-quartz arenites, BIF and minor occurrence of felsic tuffs and pelites. (Fig. 2.1B; Bleeker et al., 1999a). These, in turn, are overlain by the volcanic dominated Yellowknife Supergroup, in particular the Kam Group mafic volcanic rocks and its correlatives (Fig. 2.1B; Bleeker et al., 1999a). Within the Kam Group, intercalated thin beds of felsic tuffs contain inherited 2860 Ma zircon grains that were likely derived from the underlying CSCG (Isachsen and Bowring, 1997), pointing toward a coherent autochthonous stratigraphy of the Yellowknife Supergroup relative to the CSBC and CSCG (Bleeker, 2002). The Kam Group consists of the 2738-2697 Ma old massive-to-pillowed, up to 6 km thick, tholeiitic basalts (Cousens, 2002). Up section, the abundance of arc-like felsic volcanic and volcaniclastic rocks increases exemplified by the deposition of the ca. 2660 Ma Banting Group bimodal volcanic rocks (Isachsen et al., 1991; Cousens et al., 2002). The Slave craton is relatively unique amongst Archaean cratons (Superior, Kapvaal, etc.) in that >70% of the supracrustal rocks are dominated by <2660 Ma greywacke-mudstone turbidites of the Duncan Lake Group, and that ultramafic komatiitic lavas are virtually absent in the stratigraphy (e.g., Padgham, 1992; Isachsen and Bowring, 1997; Yamashita et al., 1999; Bleeker, 2002; Ootes et al., 2009).

The CSCG is believed to represent an early continental rifting of the CSBC with subsequent erosion and deposition of mature sediments on the newly formed inner shelf (Sircombe et al., 2001). The CSCG can be regionally correlated over distances of hundreds of kilometers throughout the central and western part of the Slave craton (Fig. 2.1A). A detrital U-Pb zircon study by Sircombe et al. (2001) shows that the dominating provenance of the detrital sediment in the basal fuchsitic quartzite contains felsic contribution from crust, with three major age populations at ~2960 Ma, ~3150 Ma and a broad grouping of 3600-3300 Ma. Collectively, this shows localized variations in the sediment provenance that contributed to the CSCG basin. Important depositional age constraints have been carried out at Dwyer Lake and Bell Lake, where a rhyolitic tuffaceaous rock between the quartzite and BIF yielded crystallization ages of 2853+2/-1 Ma and 2826±1.5 Ma, respectively (Ketchum and Bleeker, 2000; Ketchum et al., 2004. Fig. 2.1B). Another ash flow tuff was dated at Bell Lake by Isachsen and Bowring (1997) and yielded an age of 2835±4 Ma.

2.3. Samples and analytical methods

Two thin section slabs were polished and carbon coated for electron microprobe (EMP) analyses on a JEOL Microprobe 8900 at the University of Alberta. The current was set to ~20 nA and the probe beam diameter was set to 10 microns. Counting time for quantitative analysis was 20 seconds on peak, and 10 seconds on background position. Dwell time was 10 ms. Standardization to minerals with known element concentration was completed on hematite, chromite, kaersutite, and diopside.

Individual BIF bands were physically separated with a micro saw from a ca. 7 kg fresh sample collected from Dwyer Lake, with the purpose of conducting geochemical analysis on a layer-by-layer basis. This resulted in seven quartz and seven magnetite band separates. The separates were crushed in an agate mortar, and the rock powders dissolved with HF+HNO3 and analyzed using a PerkinElmer Elan6000 Quad-ICPMS (quadrupole inductively coupled plasma mass spectrometer) for trace elements at the University of Alberta. Accuracy and precision of the analytical protocol was verified with the use of the well-established international whole-rock basalt standard (CRPG Nancy). The accuracy on the measured concentrations for all elements on the standard is less than

±10%. For major element oxides, the powders were analyzed by Code 4C Whole Rock Analysis-XRF at Activation Laboratories Limited.

Shale normalization of the REY uses the North American Shale Composite (NASC), as reported by McLennan (1989), while chondrite normalization values are from Anders and Grevasse (1989), and primitive mantle values are after Sun and McDonough (1989). Since Gd often show variable stabilities in solution and surface complexation (e.g., Kim et al., 1991), the shale-normalized Eu anomaly is quantified as $(Eu/Eu^*)_{SN} = [Eu/(0.67Sm+0.33Tb)]_{SN}$. Due to positive $(La/La^*)_{SN}$ anomalies, any fractionation between LREE and HREE is quantified by $(Pr/Yb)_{SN}$. The procedure for obtaining potential anomalies of $(La/La^*)_{SN}$ and $(Ce/Ce^*)_{SN}$ can be found in Bau and Dulski (1996).

For Sm-Nd isotopes, rock powders were weighed and totally spiked with a known amount of mixed ^{150}Nd-^{149}Sm tracer solution - this tracer is calibrated directly against the Caltech mixed Sm/Nd normal described by Wasserburg et al. (1981). For magnetite-rich samples, an initial dissolution step in 6N HCl occurred for 48 hours at $120\,^{o}C$ in sealed Teflon PFA vessels, followed by dissolution in mixed 24N HF + 16N HNO_3 media at $160\,^{o}C$ for 5 days. Silica-rich samples only received the latter dissolution step. The fluoride residue is converted to chloride with HCl, and Nd and Sm are separated by conventional cation and HDEHP-based chromatography. Chemical processing blanks are < 200 picograms of either Sm or Nd, and are insignificant relative to the amount of Sm or Nd analyzed for any rock sample. Further details can be found in Creaser et al. (1997) and Unterschutz et al. (2002).

The isotopic composition of Nd is analyzed in static mode by Multi-Collector ICP-Mass Spectrometry (Schmidberger et al., 2007). All isotope ratios are normalized for variable mass fractionation to a value of $^{146}Nd/^{144}Nd = 0.7219$ using the exponential fractionation law. The $^{143}Nd / ^{144}Nd$ ratio of samples is presented here relative to a value of 0.511850 for the La Jolla Nd isotopic standard, monitored by use of an in-house Alfa Nd isotopic standard for each analytical session. Sm isotopic abundances are also measured in static mode by Multi-Collector ICP- Mass Spectrometry, and are normalized for variable mass fractionation to a value of 1.17537 for $^{152}Sm/^{154}Sm$ also using the exponential law. Using the same isotopic analysis and normalization procedures above,

we analyze the Nd isotope standard "Shin Etsu: J-Ndi-1" (Tanaka et al., 2000) which has a $^{143}Nd/^{144}Nd$ value of 0.512107 ± 7 relative to a La Jolla $^{143}Nd/^{144}Nd$ value of 0.511850. The value of $^{143}Nd/^{144}Nd$ determined for JNdi-1 conducted during the analysis of the samples reported here was 0.512100 ± 7 (2SE); the long-term average value is 0.512098 ± 11 (1SD, n=67, past 6 years).

2.4. The BIF of the CSCG

2.4.1. Field relations

Field observations and sampling was conducted at five different CSCG localities (Dwyer Lake, Bell Lake, Patterson Lake, Brown Lake and Emile River, Fig. 2.1A). The detailed outcrop transects at the sample sites are illustrated in Fig. 2.2, with locations of samples analyzed shown. The bulk of the CSCG is composed of lower amphibolite grade oxide and silicate BIF underlain by grey to greenish quartzite and quartzarenite (Fig. 2.3A). The latter often contains chromium-rich mica (fuchsite) with minute seams of detrital black chromite grains. Along the contact the CSCG is highly discontinuous ranging from <1 m and up to -40 m in thickness and can be traced laterally for 100-150 m.

A well-exposed profile of the CSCG (Fig. 2.3A) shows gradation from mature fuchsitic quartzite to semipelite with interbedded BIF, and into a more homogenous BIF package on top. In many places, later intrusion of mafic dykes and sills complicate the exposure of the original sedimentary succession (Fig. 2.3A). In addition, intense shearing has locally modified the CSBC-CSCG preserved by a high degree of mylonitization.

The majority of the BIF outcrop is unfolded and well-banded with micro- to meso-bands of quartz alternating with bands of magnetite (Figs. 2.3B-E). Green amphiboles are occasionally developed within the bands (Figs. 2.3C and 2.3D). At few places, the silica bands have undergone intense recrystallization into coarser-grained quartz bands (Fig. 2.3E). During stretching, the more competent quartz bands have been deformed into a boudinage structure, while later compression has resulted in formation of cm-scale microfolds. Further up section at Bell Lake, the BIF is intermixed with cm-scale detrital beds that are rusty in outcrop and contain fine-grained metamorphic hornblende, mica and garnet (Fig. 2.3F). Locally, beds of pebble conglomerate and pebble-bearing

sedimentary rocks are present in association with units of semi-pelites, impure quartzite and BIF (Fig. 2.3G).

2.4.2. Petrography and mineralogy

In general, the BIF comprises alternating bands of microcrystalline quartz and magnetite, ranging from <1 mm and up to 1 cm in thickness (Fig. 2.4A-C). Single magnetite grains vary from 25 mm to 0.5 mm, whereas quartz ranges from microcrystalline (<25 mm) to 1 mm in diameter. Fine-grained (0.025-0.25 mm) pale-green ferro-actinolite occurs on the quartz-magnetite interface (Figs. 2.4B and 2.4C). Some of these crystals crosscut the original bedding planes, illustrating their metamorphic origin. In places, 0.5 cm thick bands of colorless-to-pale brown grunerite appear as 50 to 0.5 mm crystals (Figs. 2.4C-E). Electron micro-probe analysis (Fig. 2.4F and Table 2.1) confirms that the two dominant amphiboles in the BIF are ferro-actinolite and grunerite. In a few samples, a network of both grunerite and dark green hornblende is developed alongside quartz and magnetite, but with only sparse amount of actinolite. The 0.5-2 cm thick pelitic beds in the upper section of the BIF at Bell Lake show dense growth of pleochroitic Fe-rich hornblende in association with dark brown biotite and randomly distributed 0.2-1 mm garnets (Figs. 2.4G and 2.4H). The dark green euhedral hornblende occurs both as up to 1.5 mm tabular crystals with a diamond shaped cross-section, and as up to 2-3 mm long prismatic crystals. The hornblende-biotite-garnet beds are interbedded with a more pure BIF type quartz-magnetite mineralogy but the beds are commonly bounded below and above by a finer-grained layer of grunerite (see Fig. 2.4H). The BIF is also found in adjacent to pebble-bearing sedimentary rock that comprises angular-to subangular K-feldspar pebbles reaching 3 mm in size and are set in a matrix of smaller grains of quartz and very fine-lamina (0.1-0.2 mm) of biotite (Figs. 2.4I and 2.4J).

2.5. Geochemistry and Sm-Nd isotopes

2.5.1. Bulk BIF and silica and iron bands

2.5.1.1. Major and trace elements

Whole rock major- and trace-elements of the bulk BIF (see Table 2.2) shows that SiO_2 and Fe_2O_3 contents range between 39.8 to 77.2 wt.% and 6.9 to 51.6 wt.%, respectively. The Al_2O_3 contents vary, but are generally <2 wt.%. The concentration of Al_2O_3 within all the bulk BIF samples are positive correlated to other insoluble elements, such as TiO_2, Zr, Nb, Hf and Th, but also more soluble elements, such as K_2O and Na_2O and MgO (not shown). Only within the Bell Lake samples, which contain fine-scale pelitic beds (see Figs. 2.4G and 2.4H), does the Al_2O_3 content reaches ~10 wt.% alongside higher abundances of insoluble elements.

High-resolution geochemical analysis of the individual silica and iron bands (Table 2.2 and Figs. 2.5 and 2.6) shows that the silica bands contain up to 96 wt.% SiO_2 (average 88 wt.%), whereas the iron bands have up to 82 wt.% Fe_2O_3 (average 75 wt.%.). The average amount of Fe_2O_3 in the silica bands is 8.7 wt.% and the average amount of SiO_2 in the iron bands is 19.4 wt.% (Figs. 2.5A, 2.6A and 2.6B). In all the bands, Al_2O_3 is < 1 wt.% with less in the silica bands (average 0.12 wt.%) relative to the iron bands (average 0.41 wt.%). Low concentrations of insoluble trace elements, such as Th, Nb, Zr, and Ti demonstrate low clastic contamination in the samples. In general, however, there is a consistently higher concentration of Al, K, Ti, Zr and Cr in the iron bands, relative to the silica bands (Figs. 2.5B, 2.6C-F). The only exception is silica 'band H', which has the same Al, K, Ti, Zr and Cr concentrations as the iron bands. All trace metals, including Ni, are very low in concentration. The average Ni content in the iron bands is only ~1 ppm, whereas in the silica bands the Ni is below detection limit (<0.06 ppm). The amount of CaO and MgO varies systematically between each individual silica- and iron-band, with the overall highest content in the iron bands. This variation is likely a function of the variation of the modal content of amphiboles, which is highest in the iron bands (Fig. 2.5C).

2.5.1.2. Rare Earth Elements

For the majority of the bulk BIF samples, the total REE ($\sum$REE) vary from 4.80 to 27.79 ppm (average 14.69 ppm, Table 2.2). The shale-normalized REY patterns (Fig. 2.7A) show an enrichment of HREE relative to LREE with $(Pr/Yb_{SN})<<1$. The Eu anomaly ranges from 1.19-3.18 (average 2.08). Less pronounced is the fractionation of Y where the average $(Y/Ho)_{SN}$ is 1.22. The Bell Lake samples with intermixed detritus are exceptions, where both the $\sum$REE and the $(Pr/Yb)_{SN}$ ratio of 0.99 and 0.86, are higher than the other BIF samples, and with no developed Y anomaly $((Y/Ho)_{SN} \sim 1$, Fig. 2.7A and Table 2.2). Still these Bell Lake samples display an average positive Eu anomaly of 2.3 (Table 2.2).

In the separated silica and iron bands, the $\sum$REE vary systematically (Figs. 2.5D and 2.6G). The silica bands have low $\sum$REEs with an average of 6.14 ppm and the iron bands have higher $\sum$REEs with an average of 28.70 ppm. Both the Zr and P_2O_5 contents are higher in the iron bands than the silica bands (Table 2.2). This may be a result of fine detrital grains of zircon or apatite. However, the non-correlative pattern between Zr vs. $\sum$HREE, and P_2O_5 vs. $\sum$REE (not shown) indicates there is only negligible impact from these grains on the REE budget.

The shale-normalized REY pattern for the iron bands (Fig. 2.7B) demonstrate they are HREE enriched relative to LREE, with an average $(Pr/Yb)_{SN}$ ratio of 0.49. The positive Eu anomalies for the iron bands show a relative narrow range between 2.19-2.82 (average 2.56). The silica bands, in contrast, are more REY fractionated, having an average $(Pr/Yb)_{SN}$ ratio of 0.32 (Table 2.2, Fig. 2.7B). It is noteworthy that bands B and H have Eu anomalies as high as 3.62 and 3.89, respectively. The silica bands exhibits a broader and slightly higher positive Eu anomaly ranging from 2.35-3.86 (average 2.94; Table 2.2, Fig. 2.7B). Even in a chondrite-normalized diagram (inset in Fig. 2.7B) the average iron bands and silica bands show a well-developed Eu anomaly. A positive Y anomaly is seen for all the bands with a combined average $(Y/Ho)_{SN}$ of 1.26 (Table 2.2, Fig. 2.7B). In addition (not shown), any pronounced Ce anomalies have not been developed and most of the bands also show a positive seawater derived La anomaly, which is related to the empty 4f electron shell of La that makes this cation more stable in seawater than neighboring REEs (e.g., De Baar et al., 1985).

2.5.1.3. Layer-by-layer Sm-Nd isotopes

Sm and Nd isotopic data for individual bands are presented in Table 2.3. All the iron bands display relatively similar $^{147}Sm/^{144}Nd$ values between 0.1096-0.1332 (average 0.1238). The $\varepsilon_{Nd}(t)$ for the iron bands show rather consistent radiogenic, positive values of between +1.0 to +2.8 (average of +1.7, Fig. 2.6H) and T_{DM} model ages between ca. 3.12 to 2.94 Ga (average 3.05 Ga). The silica bands show a bimodal $^{147}Sm/^{144}Nd$ distribution, with values for three of the bands (D, F and L) between 0.1146-0.1310, and for four of the bands (B, H, J and M) between 0.1635-0.1693 (Table 2.3). These bands shows a higher spread in their $\varepsilon_{Nd}(t)$ values versus the iron bands where four of the bands have evolved $\varepsilon_{Nd}(t)$ values of -2.2, -1.2, -0.6 and -0.4 (average -1.1) and the other three have $\varepsilon_{Nd}(t)$ values of +1.7, +2.4 and +3.4 (average +2.5). As a result, the calculated T_{DM} model ages vary from ca. 3.92 to 2.90 Ga (Table 2.3).

2.6. Discussion

2.6.1. Geochemical control in CSCG BIF

2.6.1.1. Seawater input: REY and trace metals

An important pathway of REY and other elements into the ocean is through riverine input, after erosion and weathering of nearby continental landmass. By and large, the dissolved REY species of river water have a non-fractionated pattern when normalized to shale (e.g., de Baar et al., 1985; Eldersfield et al., 1990). This flat REY pattern, however, changes when the REY enter the ocean, mostly due to a higher affinity for HREE relative to LREE to form REE-carbonate ion complexes (Cantrell and Byrne, 1987). As such HREE preferentially stay in solution while the LREE are preferentially adsorbed to particle surfaces; the latter are subsequently removed from seawater (e.g., Cantrell and Byrne, 1987; Sholkovitz et al., 1994). In modern oceans, the degree of that fractionation, measured as $(Pr/Yb)_{SN}$, varies between individual ocean basins, and with depth within individual basins (e.g., Andersson et al., 1992). In general, the $(Pr/Yb)_{SN}$ ratio in modern seawater that is not heavily influenced by epiclastic and/or hydrothermal fluids are below

1, with most values ranging between 0.15-0.30 (Zhang and Nozaki, 1996; Bolhar et al., 2004).

For most of the CSCG BIF, the main REY control was seawater and not detrital material. This can be illustrated by the $(Pr/Yb)_{SN}$ versus Ti plot (Fig. 2.8A) where all the $(Pr/Yb)_{SN}$ ratios scatter independently of Ti content, demonstrating that the REYs were in solution prior to BIF deposition, and therefore, were decoupled from any clay-rich aluminosilicates. The high REY fractionation (low $(Pr/Yb)_{SN}$ ratios) within four of the silica bands, furthermore, support experimental studies by Byrne and Kim (1990) who showed that HREE had a strong affinity for silica-rich surfaces in seawater which would result in a high fractionated REY pattern in some chert bands.

The seawater input during Fe precipitation is more enigmatic. The iron bands have Al_2O_3 < 1 wt.%, but have a higher LREE/HREE than the silica bands with $(Pr/Yb)_{SN}$ ratios of between 0.4-0.65. (Figs. 2.7B and 2.8A) This could reflect the soluble LREE being preferentially adsorbed by Fe(III) oxyhydroxide particles in the water column, much like the HREE preferentially sorb to silica.

Based on their abundances in the BIF, the ambient seawater had elevated Y relative to Ho (Figs. 2.7A and 2.7B), suggesting that Ho was more reactive to suspended particles (e.g., Zhang et al., 1994). In size, this Y anomaly $(Y/Ho)_{SN}$, is less pronounced than modern upper seawater (Fig. 2.8B), likely due to a suppression by adjacent sources having chondritic $(Y/Ho)_{SN}$ ratios of ~1. Both submarine hydrothermal systems and continental crust (in Fig. 2.8B illustrated by the Bell Lake basement gneiss) exhibit chondritic $(Y/Ho)_{SN}$ values and minor contribution from this source could have lowered the Y anomaly, and as also shown in Fig. 2.8B, increased the seawater $(Pr/Yb)_{SN}$ ratios.

The trace metals, such as Ni, are found in very low concentrations relative to many other pre-2.7 Ga BIFs (Fig. 2.8C). A reason for this could be that the Ni is locked up in the clay-rich fraction. This is evident in the mixed chemical and clastic rocks from Bell Lake, which have Cr-Ni trends that coincide with the slope of the older Bell Lake basement gneisses, as well as Archaean basalts and komatiites (Fig. 2.8C). Konhauser et al. (2009) showed that the Cr/Ni ratios of Archaean BIF are lower (lower slope in Fig. 2.8D) than the potential lithologies that sourced those elements (e.g., Archaean basalts and komatiites, steeper slope in Fig. 2.8C) implying that Ni likely was mobilized and

supplied in soluble form to the marine environment. Interestingly, the BIF in our study have Cr/Ni ratios similar to those of pre-2.7 Ga BIF (similar slope in Fig. 2.8C), albeit with lower overall abundances. This points to similar processes operating on Cr and Ni from source rock to seawater solution. Whether or not the small amount of Ni was derived through hydrothermal alteration of ultramafic-to-mafic oceanic crust, or from chemical weathering of Ni-bearing minerals (e.g., olivine, pyroxene and Ni-sulphides) on land is unknown. However, we postulate that the overall lower Ni content (Fig. 2.8C) indicates that the continental source region was heavily weathered prior to BIF deposition. In the modern environments, such as the Amazon Basin, the highly weathered Precambrian shield is overlain by lateritic soils that are dominated by kaolinite, gibbsite, quartz and ferric oxyhydroxides that possess low trace metal concentrations (e.g., Konhauser et al., 1994). Consequently, the rivers that drain these terrains are extremely solute-deficient and contain some of the lowest total dissolved solids anywhere on the planet. Furthermore, due to the low trace metal values, the local water of the CSCG basin likely was not in free exchange with the global ocean at the time of BIF deposition. Interestingly, the detrital free BIF sample from Bell Lake has a higher contribution of Cr and Ni, in line with the majority of pre-2.7 Ga BIF (Fig. 2.8C). From a field perspective, the highest proportion of detrital chromite grains and fuchsitic quartzite is also found at that location, potentially indicating continental crust that had a higher mafic component at this location (see section 6.2).

2.6.1.2. Hydrothermal input: the Eu^{2+} enrichment

The only setting where an excess of reduced Eu^{2+} occurs is within fluids associated with high-temperature hydrothermal alteration of submarine mafic crust (e.g., Michard et al., 1983; Bau and Dulski, 1999). The change in valence from Eu^{3+} to the larger divalent Eu^{2+} ion demands fluid temperatures >300°C and extremely reduced conditions, perhaps ten-folds lower than the lowermost estimate for the Archaean atmospheric partial pressure of oxygen of $\sim 10^{-14}$ PAL (Danielson et al., 1992). Therefore, the deep Archaean ocean seems to have been the favorable habitat for mobilizing Eu rather than through subaerial weathering processes. In modern deep-sea metalliferous sediments, the REY pattern approaches that of the seawater with increasing distance from the vent site. The excess of

Eu in these hydrothermal sediments is thus sourced from seawater mixed with high-temperature fluids that were injected at the vent site (Ruhlin and Owen, 1986).

In the CSCG BIF, all samples have the hydrothermal-diagnostic positive Eu anomaly (Fig. 2.7). Within a strongly reduced deep ocean in the Archaean, the residence time of the Eu^{2+} was likely higher and thus could have travelled far distances from the vent source. According to Slack et al. (2007), iron and REE will not be fractionated during transport from spreading ridges or other exhalative centres, and, therefore, a strong positive Eu anomaly indicates that the iron in the BIF precursor sediment was hydrothermally derived. Indeed, the Eu anomaly in the majority of the iron bands seems to be positively correlated with iron content (Fig. 2.8D). However, when including both iron- and silica-bands the magnitude of the Eu anomaly and the iron content is decoupled (Fig. 2.8D). In fact, some of the highest Eu anomalies are found in the silica bands rather than the iron bands. The positive Eu anomalies are best interpreted to indicate that high-T hydrothermal inputs were an important seawater contribution during both silica and iron precipitation.

The CSCG BIF's Eu anomaly is about 1.5 times higher than other contemporaneous BIF, such as the shallow-water 2.94 Ga Pongola BIF in South Africa, or the 2.9 Ga Itilliarsuk BIF in West Greenland, In fact, the size of the Eu anomaly in CSCG BIF is more comparable with the ~3.8 Ga Isua BIF from West Greenland (Fig. 2.8D). Two of the silica bands have even higher Eu anomalies than the Isua BIF. These results demonstrate that the seawater within the rift basin of the CSCG was impacted in high degree by high-T hydrothermal fluids. This also violates the general consensus that the size of the positive Eu anomaly measured in BIFs decreases throughout the Archaean as a consequence of a lower mantle heat flux and correspondingly a lower degree of high-T hydrothermal alteration of the oceanic crust (e.g., Derry and Jacobsen, 1990; Danielson et al., 1992; Huston and Logan, 2004; Kato et al., 2006). Any interpretation of BIF should rather be interpreted from a local depositional setting than from a global scenario.

2.6.2. Mixed chemical and terrigenous sedimentary rock

Rocks that deviate from a clear seawater REY signature may be explained by higher input of aluminosilicates from continental weathering, which would both lead to a higher content of LREE and Al_2O_3, Ti and HFSE. Minor contribution from continental weathering is clearly evident both at Brown Lake and Patterson Lake BIF samples that both show Al_2O_3 content > 1 wt.% (Table 2.2), and an elevated REY pattern with minor LREE enrichment (Fig. 2.7A). At Bell Lake, however, a larger amount of clay material was mixed into the marine chemical sediments. Subsequent metamorphism of this siliciclastic material resulted in the mineral assemblage that includes beds of biotite, hornblende, and garnet (see Figs. 2.4G and 2.4H). That terrigenous fingerprint is readily distinguished geochemically, as the bulk rocks from Bell Lake have elevated Al_2O_3, TiO_2, Zr, trace metals, and ∑REE (Table 2.2), and are LREE enriched relative to the BIF (Figs. 2.7A and 2.8B). In addition, the enrichment of Y, which is associated with seawater, seems to have been suppressed by the detrital material (Fig. 2.8B). Despite the higher content of aluminosilicates, these samples still have a weak HREE enriched signature and the characteristic positive Eu anomaly that are both inherited from the ambient seawater. On a cm scale, in between the individual beds with garnet and hornblende, the rock becomes chemically very pure and it resembles more "true" BIF, with $(Pr/Yb)_{SN}$ of 0.30, a positive $(Y/Ho)_{SN}$ anomaly, very low Al_2O_3 (0.08 wt.%), and very low ∑REE (Table 2.2 and Figs. 2.8A and 2.8B). The fine-scale variation in the sedimentation demonstrates that the aluminosilicates were deposited in the basin during pulses in between BIF precipitation and deposition.

The mixed chemical and fine-grained clastic parentage provides an opportunity to trace the nature of the terrigenous sources that were eroded from exposed crust during BIF deposition The BIF and underlying quartzite were deposited on CSBC granitic to tonalitic gneisses (Fig. 2.1B), providing direct evidence for exposed felsic crust at the time of deposition. Indirect evidence for mafic-to-ultramafic crust comes from thin seams of detrital chromite found within the fuchsitic quartzite (Bleeker et al., 1999a; Figs. 2.1B and 2.3A). These may have had their origin in komatiitic lavas, but unfortunately are no longer exposed within the bedrock exposures of the Slave craton. Particular useful discriminants of source regions in fine-grained sedimentary rocks are the immobile high

field-strength elements (Th, Nb, Hf, Zr, Ti, and V) since they are not fractionated relative to their source by sedimentary processes (e.g., Taylor and McLennan, 1985). The detrital aluminosilicate beds from Bell Lake seem to have been derived from a bimodal mixture of the Bell Lake tonalitic basement and an unknown Archaean mafic-to-ultramafic source (Fig. 2.9). Relative to primitive mantle, the Th, Nb, Hf and Zr concentrations in the detrital sedimentary rock at Bell Lake are below the basement gneiss concentrations, but above average Archaean mafic concentrations (Condie, 1993). This suggests that the tonalitic basement alone cannot explain the composition of the detrital aluminosilicate that is intermixed with the BIF. With respect to the trace metals, the felsic basement likely diluted the seawater for these metals. Any minor contribution from eroded komatiites cannot be excluded in this study, but it seems that if ultramafic rocks delivered a major part of the fine-grained siliciclastics to the basin, then the amount of trace metals like Cr and Ni would have been higher than the results in this study (<50 ppm, Table 2.2, Figs. 2.8C and 2.9).

2.6.3. Layer-by-layer Nd isotopes

2.6.3.1. The water masses and precipitation of silica and iron

The planar-bedded bands of silica and iron reflect either an ocean with a strong heterogeneous water mass, or a homogenous water mass that, at different times, was capable of precipitating both silica and iron. Detailed Sm-Nd isotopes of the individual bands show that the ^{143}Nd/^{144}Nd ratios in the seawater were not well-mixed and varied in response of different water masses having different elemental and isotopic composition of Nd (Table 2.3, Fig. 2.10A). In particular the wide range in $\varepsilon_{Nd}(t)$ values within the silica bands shows that the seawater ^{143}Nd/^{144}Nd was not homogenized by ocean circulation. Assuming the Nd in the Archaean ocean had a similar behavior as in modern ocean, this can be explained by the fact that Nd behaved as a non-conservative element (e.g., Piepgras and Wasserburg, 1987; Eldersfield et al., 1990; Andersson et al., 1992), having a residence time one order of magnitude lower than the turn over time (Andersson et al., 1992, Faure and Mensing, 2005).

In terms of the REY distribution, modern oceans show a clear vertical difference within the water column, where deeper water (>5000 m) is between 5 to 20 times more enriched in dissolved REY than the shallow 500 m of seawater (Zhang and Nosaki, 1996). This suggests that the low REY values of the silica bands (Figs. 2.5D and 2.6G) could represent precipitation from upper seawater, which is more diluted with respect to REY, whereas the iron bands were sourced from deeper water in the basin with higher dissolved REY content.

Both the concentration and isotopic composition of Nd was highly heterogeneous in the water column (Fig. 2.10A). The high bimodality in the $\varepsilon_{Nd}(t)$ values for the silica bands also mean that the isotopic composition of Nd in the silica precipitate was not constant but likely varied as a consequence of the changes in the Sm/Nd ratios in the source region (Figs. 2.10A-2.10B). By contrast, the seawater responsible for precipitating Fe(III) oxyhydroxides had a less variable REY pattern and $\varepsilon_{Nd}(t)$ values (Figs. 2.7B and 2.10B). This reflects either a better mixing of the iron rich water, or that the iron was derived from a more uniform Nd source. Less suspended particles in the deeper parts of oceans, as well as the anoxic conditions, would keep Nd (and the LREE) longer in solution, and hence, increasing their residence time, and ultimately generating water with better mixed and consistent $^{143}Nd/^{144}Nd$ ratios and LREE signatures. This stratification of the ocean with respect to Nd isotope composition has been recorded within the modern Atlantic Ocean as well, which has well-mixed deeper water and more heterogeneous upper water. This reflects a combination of different sources involved and the chemical properties of Nd within the seawater itself (Piepgras and Wasserburg, 1980). The above suggest compositional and isotopic different water masses behind silica and iron deposition where the upper heterogeneous seawater controlled the silica precipitation and deeper water controlled the precipitation of iron. This pattern is be supported by the detailed petrography and geochemistry, which reveals that there is more silica in the iron bands than there is iron in the silica bands (e.g., Figs. 2.5A, 2.6A and 2.6B). This observation implies that during silica precipitation the precipitation of Fe(III) oxyhydroxides were at a minimum, whereas at the peak of Fe(III) oxyhydroxide precipitation relatively more silica was incorporated into the precipitates. A plausible explanation is that the amorphous silica was as background sediment at the site of BIF

deposition (e.g., Morris, 1993), where it was occasionally interrupted by pulses of Fe(II)-rich water (see Fig. 2.11 for a simplified depositional model). A Mesoarchaean stratified ocean could be a possible scenario whereby iron-rich deeper water, separated by a pycnocline, supplied the iron for BIF deposition during either upwelling or by local changes in the position of the pycnocline (e.g., Holland, 1973; Eriksson et al., 1997).

2.6.3.2. Tracing the seawater REY sources

A majority of BIFs reported in the literature have been analyzed as whole-rocks, which inevitably results in mixed seawater isotopic and compositional values. In the case of seawater $^{143}Nd/^{144}Nd$ ratios, whole-rock analyses will thereby treat seawater as being homogenous, leaving out important information about short-term fluctuations in its chemical composition and redox state. For instance, extrapolation to global Archaean ocean composition using existing BIF data has shown that the seawater possessed a narrow range of average +1 to +2 $\varepsilon_{Nd}(t)$ units (e.g., Alexander et al., 2009 and references therein). Thus, submarine hydrothermal input has been argued as the dominant source control on Achaean bulk seawater, whereas modern bulk oceans possess negative $\varepsilon_{Nd}(t)$ values controlled by ancient continental crust (e.g., Piepgras and Wasserburg, 1980). This picture is very generalized as BIF are strongly dependent on the local-to-regional depositional environment (e.g., Haugaard et al., 2013). This is especially true for near-shore BIF such as the CSCG in this study. In this work, the layer-by-layer variations in the initial $^{143}Nd/^{144}Nd$ ratios clearly demonstrate a heterogeneous water column, which, in turn, means that different sources with different Nd isotopic signatures impacted the seawater composition during BIF precipitation (Fig. 2.11).

The consistent positive $\varepsilon_{Nd}(t)$ values of +1.0 to +2.8 for the iron bands suggest that the deeper seawater was largely influenced by depleted mantle sources that had a relatively short crustal residence time. This is also reflected in the T_{DM} model ages that are only slightly older than the BIF deposition age (see Table 2.3 and the Nd isotopic evolution lines in Fig. 2.12). Pre-2.7 Ga BIFs generally display positive ε_{Nd} values of +3 to +4, in agreement with the depleted mantle evolution (Fig. 2.12), and in terms of the break-up of the basement during the deposition of the CSCG, this could have had a large

impact on the REY composition of the deeper parts of the basin. The slightly less positive $\varepsilon_{Nd}(t)$ values in the iron bands relative to depleted mantle values (Fig. 2.12), indicate that the iron rich fluids either interacted with older crust during spreading or, as reported by Piepgras and Wasserburg (1985), that the fluids from the spreading centers were in contact with enriched, continentally-derived sediments at the sea floor before entering the ocean.

The heterogeneous surface water, on the other hand, was controlled by sources with both negative and positive $\varepsilon_{Nd}(t)$ values. Four of the silica bands with negative $\varepsilon_{Nd}(t)$ values imply exposed ancient continent in the source region whereas the three silica bands support dominance from radiogenic sources (positive $\varepsilon_{Nd}(t)$ values). As the iron content in those three bands is amongst the lowest for the silica bands (<8 wt.%), it is unlikely that the positive $\varepsilon_{Nd}(t)$ values can be ascribed to the small amount of Fe(III) oxyhydroxides present. Rather, during precipitation of these silica bands, crustal sources possessing radiogenic $\varepsilon_{Nd}(t)$ values controlled the surface seawater REY budget in the same manner as demonstrated through detailed layer-by-layer studies from the same age Itilliarsuk BIF of West Greenland (Haugaard et al., 2013). There, the silica bands displayed positive $\varepsilon_{Nd}(t)$ values of +0.5 to +4, reminiscent of the associated juvenile TTG basement and supracrustal lithologies.

The CSBC rocks have generally negative $\varepsilon_{Nd}(t)$ values (e.g., Davis and Hegner, 1992; Northrup et al., 1999), but a positive $\varepsilon_{Nd}(t)$ value of +3.4 reported from the ca. 3.15 Ga old Augustus tonalite at Point Lake (Davis and Hegner, 1992) supports the contention that the continental crust had differrent $^{143}Nd/^{144}Nd$ composition at the time of BIF deposition. The occurrence of the stratigraphically underlying fuchsitic quartzite-to-quartz arenite offers a unique opportunity to study the dominant continental crust that was exposed to weathering prior to the BIF deposition at ca. 2.85 Ga. Work by Sircombe et al. (2001) showed that the detrital zircons from the upper part of the Dwyer Lake quartzite had a major U-Pb concordia age population at ~2.96 Ga (29% of the grains). This peak is virtually identical with the average T_{DM} model age of ~2.98 Ga found for the three depleted silica bands, implying that the REY may have been primarily sourced from similarly-aged basement rocks. The negative $\varepsilon_{Nd}(t)$ values in four of the seven silica bands show that a major part of the REY in the upper seawater were controlled by

weathering of older continental crust. The model ages for the four bands are not possible to estimate due to high uncertainties when calculating the model ages, due in part to the lower slope intersection of the Nd evolution line with the depleted mantle curve when $^{147}Sm/^{144}Nd$ ratios > 0.14 (Fig. 2.12; Table 2.3; Miller and O'Nions, 1985). Within the Dwyer Lake quartzite, 26% of the zircons have concordant ages between 3300-3600 Ma, in addition to a very old 3918±10 Ma grain (Sircombe et al., 2001). Thus, the negative $\varepsilon_{Nd}(t)$ values in the silica bands indicate that older continental crust controlled major part of the upper seawater $^{143}Nd/^{144}Nd$. Whether this was through erosion of older continental crust or by recycling of older sedimentary rocks, is unknown. Interestingly, the two highest positive Eu anomalies were found in two of the silica bands exhibiting negative $\varepsilon_{Nd}(t)$ values (Tables 2.2 and 2.3). This is interpreted to indicate that during silica precipitation, the upper seawater REY was dominated by continental crust but had an excess of hydrothermal derived Eu^{2+} as well. This is not surprising since Eu^{2+} is the most mobile of the REY under the presumed highly reduced seawater conditions at that time.

2.6.3.3. Silica and the iron source paradox

Since riverine input carrying detritus and solutes dominated the source of the REY within the upper seawater of the BIF depositional basin, it can be argued that silica was sourced from subaerial weathering of the aforementioned collage of continental crustal components. The source of the iron is more complicated, mostly by the fact that those elements associated with clay particles (e.g., Al_2O_3, TiO_2, K_2O, HFSE and trace metals) are all weakly elevated in the iron bands relative to the silica bands. This indicates that relatively more clay was co-deposited with the Fe(III) oxyhydroxides, and on a first approximation would support the notion that the source of iron was from continental weathering and not submarine hydrothermal derived as we suggested above. Exposed field evidence for a voluminous iron-rich source of presumably mafic-to-ultramafic composition has not yet been found associated with the CSCG. Only indirect evidence through the aforementioned detrital chromite grains within the basal fuchsitic quartzite. The dimensions and nature of this source is uncertain, but importantly, it cannot be excluded that during BIF formation, part of the iron could have been supplied from land

to the marine environment. Certainly, in the absence of atmospheric O_2 at that time, based on S-MIF in shales (Farquhar et al., 2000) and Cr concentrations in BIF (Konhauser et al., 2011), iron would have easily been mobilized from mafic-to-ultramafic rocks and transported to the oceans in reduced form.

With that stated, the uniform REY patterns and Nd isotopic signature of the iron bands is difficult to explain solely by continental weathering since the contemporaneous continents possess crustal components with variable $^{143}Nd/^{144}Nd$ signatures (e.g., as seen in the silica bands). In addition, if an ultramafic continental source dominated the terrigenous input it would be expected to see a higher abundance of trace metals (e.g., Ni) adsorbed to the clay-rich fraction entering the basin (see Fig. 2.9). Instead, we find it reasonable to assume that the incorporation of the smaller amount of clay-rich material in the iron bands is related to adsorption between hydrothermal Fe-colloids that are amphoteric by nature (i.e., can have both negative and positive charges) and the negatively-charged, clay particles within the water column. Enrichment of clay particle surfaces with Fe and associated adsorbed elements is a well-known ocean process (e.g., Hunter and Boyd, 2007 and references therein) and furthermore demonstrates the complex pattern of iron operating within the marine environment.

2.7. Conclusions

The 2.85 Ga Central Slave Cover Group BIF is found associated with basement gneisses and shallow and coastal type shoreline facies, such as quartzite and pebble-to-cobble conglomerate. These observations suggest a near-shore depositional setting for the BIF. In terms of mineralogy, the BIF are composed of quartz and magnetite with locally variable amounts of grunerite, ferro-actinolite and accessory ferro-hornblende. When best preserved, the BIF is reminiscent of a pure marine chemical sedimentary rock illustrated by a shale-normalized HREE-to-LREE enriched pattern with low $(Pr//Yb)_{SN}$, positive La and Y anomalies, and low concentrations of Al_2O_3, Ti, Zr, Nb and Th. Exceptions occur where the input of detrital input of clay has disturbed the seawater REY signal, such as in parts of Bell Lake, which represent a mixture of chemical and clastic sediment, expressed by the metamorphic development of biotite, ferro-hornblende, and garnet. A high, but

variable input of submarine high-T (>350 °C) hydrothermal fluids influenced all the BIF as demonstrated by positive Eu_{SN} anomalies. The large Eu^{2+} in these BIF, relative to other Mesoarchaean BIF, shows that seawater within a rift-dominated basin can produce Eu anomalies that are comparable with older Eoarchaean BIF.

Detailed, layer-by-layer geochemical studies of the BIF reveal that silica bands have lower REY, relative to iron bands. They also exhibit a higher HREE/LREE ratio relative to the iron bands, indicative of being sourced from the upper seawater. In contrast, the iron bands seem to be derived from deeper water where the HREE/LREE ratio is lower. This stratified water column is supported by the Sm-Nd isotopes, which we use to trace the source of the REY. The iron bands show a more uniform $^{144}Nd/^{143}Nd$ signature with positive $\varepsilon_{Nd}(t)$ values characteristic for deeper water controlled by uniform mid-ocean ridge fluid sources. The REY in the silica bands, on the other hand, were dominated by weathering of continental crust having different $^{144}Nd/^{143}Nd$ signatures. One segment of the silica bands has negative $\varepsilon_{Nd}(t)$ values, suggesting it was sourced from >3.5 Ga continental crust, whereas another has positive $\varepsilon_{Nd}(t)$ values sourced from more juvenile crust. Since the amount of silica is higher in the iron bands than the amount of iron in the silica bands, the silica bands likely represent background deposition that was interrupted by short-term pulses of Fe(II)-rich water sourced from deeper in the basin. The evidence of extensive felsic basement gneiss and the occurrence of quartzite, alongside extremely low Ni concentrations and the generally very small amount of REY (e.g., in the silica bands) leads us to speculate that the local continental crust was already heavily weathered prior to deposition of the BIF.

References

Alexander, B. W., Bau, M., Andersson P., Dulski P., 2008. Continentally-derived solutes in shallow Archean seawater: Rare earth element and Nd isotope evidence in iron formation from the 2.9Ga Pongola Supergroup, South Africa. Geochimica et Cosmochimica Acta 72, 378–394.

Alexander B. W., Bau M. and Andersson P., 2009. Neodymium isotopes in Archean seawater and implications for the marine Nd cycle in Earth's early oceans.Earth and Planetary Science Letters 283, 144–155.

Alibert C., McCulloch, M. T. M., 1993. Rare earth element and neodymium isotopic compositions of the banded iron-formations and associated shales from Hamersley, western Australia. Geochimica et Cosmochimica Acta 57, 1–18.

Anders, E., Grevesse, N., 1989. Abundances of the elements: meteoric and solar. Geochimica et Cosmochimica Acta 53, 197–214.

Andersson, P. S., Wasserburg, G. J., Ingri J., 1992. The sources and transport of Sr and Nd isotopes in the Baltic Sea. Earth and Planetary Science Letters 113, 459–472.

Barth, M. G., McDonough, W. F. and Rudnick, R. L. (2000) Tracking the budget of Nb and Ta in the continental crust. Chemical Geology 165, 197-213.

Bau, M., Möller, P., 1993. Rare earth element systematics of the chemically precipitated component in Early Precambrian iron formations and the evolution of the terrestrial atmosphere-hydrosphere-lithosphere system. Geochimica et Cosmochimica Acta 57, 2239–2249.

Bau, M., Dulski, P., 1996. Distribution of yttrium and rare-earth elements in the Penge and Kuruman iron-formations, Transvaal Supergroup, South Africa. Precambrian Research 79, 37–55.

Bau, M., Dulski, P., 1999. Comparing yttrium and rare earths in hydrothermal fluids from the Mid-Atlantic Ridge: implications for Y and REE behaviour during near- vent mixing and for the Y/Ho ratio of Proterozoic seawater. Chemical Geology 155, 77–90.

Bleeker, W., Ketchum, J. W. F., Jackson, V. A., Villeneuve, M. E., 1999a. The Central Slave Basement Complex, Part I: its structural topology and autochthonous cover. Canadian Journal of Earth Sciences 36, 1083-1109.

Bleeker, W., Ketchum, J. W., Davis, W. J., 1999b. The Central Slave Basement Complex, Part II: age and tectonic significance of high-strain zones along the basement-cover contact. Canadian Journal of Earth Sciences 36, 1111–1130.

Bleeker, W., 2002. Archaean tectonics: a review, with illustrations from the Slave craton. In The Early Earth: Physical, Chemical and Biological Development (eds. Fowler C. M. R., Ebinger C. J. and Hawkesworth, C. J.). Geol. Soc. London 199, pp. 151–181.

Bleeker, W., Hall, B., 2007. The Slave Craton: Geological and Metallogenic Evolution. In Mineral Deposits of Canada: A synthesis of major Deposit-types, District Metallogeny, the evolution of geological provinces, and exploration methods (eds. Goodfellow W. D.). Geological Society of Canada Special Publication, p. 849-879.

Bolhar, R., Kamber, B. S., Moorbath, S., Fedo, C. M., Whitehouse, M. J., 2004. Characterisation of early Archaean chemical sediments by trace element signatures. Earth Planetary Science Letters 222, 43–60.

Bolhar, R., Kamber, B., Moorbath, S., Collerson, K., 2005. Chemical characterization of earth's most ancient clastic metasediments from the Isua Greenstone Belt, southern West Greenland. Geochimica et Cosmochimica Acta 69, 1555–1573.

Byrne, R. H., Kim, K.-H., 1990. Rare earth element scavenging in seawater. Geochimica et Cosmochima Acta 54, 2645–2656.

Cantrell, K. J., Byrne J. H., 1987. Rare earth element complexation by carbonate and oxalate ions. Geochimica et Cosmochima Acta 51, 597-605.

Condie, K. C., 1993. Chemical composition and evolution of the upper continental crust: Contrasting results from surface samples and shales. Chemical Geology 104, 1-37.

Cousens, B. L., 2000. Geochemistry of the Archean Kam Group, Yellowknife Greenstone Belt, Slave Province, Canada. Journal of Geology 108, 181-198.

Cousens, B. L., Facey, K., Falck, H., 2002. Geochemistry of the late Archean Banting Group, Yellowknife Greenstone Belt, Slave Province, Canada: simultaneous melting of the upper mantle and juvenile mafic crust. Canadian Journal of Earth Science 39, 1635-1656.

Creaser, R. A., Erdmer, P., Stevens, R. A., Grant, S. L., 1997. Tectonic affinity of Nisutlin and Anvil assemblage strata from the Teslin tectonic zone, northern Canadian Cordillera: Constraints from neodymium isotope and geochemical evidence. Tectonics 16, 107–121.

Cullers, R. L., Chaudhuri, S., Arnold, B., Lee, M., Wolf, C. W., 1975. Rare earth distributions in clay minerals and in the clay-sized fraction of the Lower Permian Havensville and Eskridge shales of Kansas and Oklahoma. Geochimica et Cosmochima Acta 39, 169l-l 703.

Danielson, A., Möller, P., Dulski, P., 1992. The europium anomalies in banded iron formations and the thermal history of the oceanic crust. Chemical Geology 97, 1–12.

Davis, W. J., Hegner, E., 1992. Neodymium isotopic evidence for the tectonic assembly of Late Archean crust in the Slave Province, northwest Canada. Contributions to Mineralogy and Petrology 111, 493–504.

De Baar, H. J. W., Bacon M. P., Brewer, P. G., Bruland K. W., 1985. Rare earth elements in the Pacific and Atlantic Oceans. Geochimica et Cosmochimica Acta 49, 1943–1959.

DePaolo, D. J., 1981. Neodymium isotopes in the Colorado Front Range and crust-mantle evolution in the proterozoic. Nature 291, 193–196.

Derry, L.A., Jacobsen, S.B., 1990. The chemical evolution of Precambrian seawater: evidence from REEs in banded iron formations. Geochimica et Cosmochimica Acta 54, 2965–2977.

Elderfield, H., 1988. The oceanic chemistry of the rare earth elements. Philosophical Transaction of the Royal Society 325, 105-126.

Elderfield, H., Upstill-Goddard, R., Sholkovitz, E. R., 1990. The rare earth elements in rivers, estuaries, and coastal seas and their significance to the composition of ocean waters. Geochimica et Cosmochimica Acta 54, 971–991.

Eriksson, K. A., Krapež, B., Fralick, P. W., 1997. Sedimentological aspects. In Greenstone Belts (eds. De Wit M. J. and Ashwal L .D.). Clarendon Press, Oxford, p. 33-54.

Faure G., Mensing T. M., 2005. Isotopes: Principles and applications. John Wiley and Sons Limited, 897 p.

Frei, R., Polat, A., 2007. Source heterogeneity for the major components of ~3.7 Ga Banded Iron Formations (Isua Greenstone Belt, Western Greenland): tracing the nature of interacting water masses in BIF formation. Earth Planetary Science Letters 253, 266–281.

Fryer, B. J., 1977. Rare earth evidence in iron-formations for changing Precambrian oxidation states. Geochimica et Cosmochimica Acta 41, 361-367.

Hamade, T., Konhauser, K. O., Raiswell, R., Goldsmith, S., Morris, R. C., 2003. Using Ge/Si ratios to decouple iron and silica fluxes in Precambrian banded iron for- mations. Geology 31, 35–38.

Haugaard, R., Frei, R., Stendal, H., Konhauser, K., 2013. Petrology and geochemistry of the ~2.9 Ga Itilliarsuk banded iron formation and associated supracrustal rocks, West Greenland: Source characteristics and depositional environment. Precambrian Research 229, 150–176.

Holland, H. D., 1973. The oceans: A possible source of iron in iron formations. Economic Geology 68, 1169-1172.

Hunter, K. A., Boyd, P. W., 2007. Iron-binding ligands and their role in the ocean biogeochemistry of iron. Environmental Chemistry 4, 221–232.

Huston, D.L., Logan, G.A., 2004. Barite, BIFs and bugs: evidence for the evolution of the Earth's early hydrosphere. Earth and Planetary Science Letters 220, 41–55.

Isachsen, C. E., Bowring, S. A., Padgham, W. A., 1991. U-Pb zircon geochronology of the Yellowknife volcanic belt, NWT, Canada: new constraints on the timing and duration of greenstone belt magmatism. Journal of Geology 99, 55–68.

Isachsen, C. E., Bowring, S. A., 1994. Evolution of the Slave craton. Geology 22, 917–920.

Isachsen, C., Bowring, S., 1997. The Bell Lake group and Anton Complex: a basement-cover sequence beneath the Archean Yellowknife greenstone belt revealed and implicated in greenstone belt formation. Canadian Journal of Earth Science 189, 169–189.

Jacobsen, S. B., Pimentel-Klose, M. R., 1988. A Nd isotope study of the Hamersley and Michipicoten banded iron formations: The source of REE and Fe in Archaean oceans. Earth and Planetary Science Letters 87, 29-44.

Kato Y., Yamaguchi K. and Ohmoto H., 2006. Rare earth elements in Precambrian banded iron formations: Secular changes of Ce and Eu anomalies and evolution of atmospheric oxygen. Geological Society of America Memoir 198, 269-289.

Ketchum, J. W. F., Bleeker W., 2000. New field and U–Pb data from the Central Slave Cover Group near Yellowknife and the Central Slave Basement Complex at Point Lake. In Slave-Northern Cordillera Lithospheric Experiment (SNORCLE) Transect Meeting (compilers Cook F., Erdmer P.). University of Calgary, LITHOPROBE Report No. 72, 27–31 p.

Ketchum, J. W. F., Bleeker, W., Stern, R. A., 2004. Evolution of an Archean basement complex and its autochthonous cover, southern Slave Province, Canada. Precambrian Research 135, 149–176.

Kim, K. H., Byrne, R. H., Lee, J. H., 1991. Gadolinium behaviour in seawater: a molecular basis for gadolinium anomalies. Marine Chemistry 36, 107–120.

Klein C., 1974. Greenalite, stilpnomelane, minnesotaite, crocidolite and carbonates in a very low grade metamorphic precambrian iron-formation. Canadian Mineralogist 12, 1–24.

Klein, C., 2005. Some Precambrian banded iron-formations (BIFs) from around the world: their age, geologic setting, mineralogy, metamorphism, geochemistry, and origins. American Mineralogist 90, 1473–1499.

Konhauser K. O., Fyfe W. S., Kronberg B. I., 1994. Multi-element chemistry of some Amazonian waters and soils. Chemical Geology 111, 155-175.

Konhauser, K. O., Pecoits, E., Lalonde, S. V., Papineau, D., Nisbet, E. G., Barley, M. A., Arndt, N. T., Zahnle, K., Kamber, B. S., 2009. Oceanic nickel depletion and a methanogen famine before the Great Oxidation Event. Nature 458, 750–753.

McLennan S. M., 1989. Rare Earth Elements in sedimentary rocks: Influence of provenance and sedimentary processes. In Geochemistry and mineralogy of Rare Earth Elements (eds. Lipin B. R. and McKay G. A.) Reviews in Mineralogy 21, 169-200.

Michard, A., Albarbde, F., Michard, G., Minster, J. F., Charlou, J. L., 1983. Rare earth elements and uranium in high-temperature solutions from East Pacific Rise hydrothermal vent field (13~N). Nature 303, 795-797.

Miller, R. G., O'Nions, R. K., 1985. Source of Precambrian chemical and clastic sediments. Nature 314, 325–330.

Northrup, C. J., Isachsen, C., Bowring, S. A., 1999. Field relations, U-Pb geochronology, and Sm-Nd isotope geochemistry of the Point Lake greenstone belt and adjacent gneisses, central Slave craton, N.W.T., Canada. Canadian Journal of Earth Sciences 36, 1043-1059.

Ootes, L., Davis, W.J., Bleeker, W., Jackson, V.A., 2009. Two Distinct Ages of Neoarchean Turbidites in the Western Slave Craton: Further Evidence and Implications for a Possible Back-Arc Model. The Journal of Geology 117, 15–36.

Padgham, W., Fyson, W., 1992. The Slave Province: a distinct Archean craton. Canadian Journal of Earth Sciences 29, 2072-2086.

Piepgras, D. J., Wasserburg G. J., 1987. Rare earth element transport in the western North Atlantic inferred from Nd isotopic observations. Geochimica et Cosmochimica Acta 51, 1257-1271.

Ruhlin, D. E., Owen, R. M., 1986. The rare earth clement geochemistry of hydrothcrmal sediments from the East Pacific Rise: Examination of a seawater scavenging mechanism. Geochimica et Cosmochimica Acta 50, 393- 400.

Schmidberger, S. S., Heaman, L. M., Simonetti, A., Creaser, R. A., Whiteford, S., 2007. Lu–Hf, in-situ Sr and Pb isotope and trace element systematics for mantle eclogites from the Diavik diamond mine: evidence for Paleoproterozoic subduction beneath the Slave craton, Canada. Earth Planetary Science Letters 254, 55–68.

Sholkovitz, E. R., Landing, W. M., Lewis, B. L., 1994. Ocean particle chemistry: The fractionation of rare earth elements between suspended particles and seawater. Geochimica et Cosmochimica Acta 58, 1567–1579.

Sircombe, K., Bleeker, W., Stern, R. A., 2001. Detrital zircon geochronology and grain-size analysis of a ~2800 Ma Mesoarchean proto-cratonic cover succession, Slave Province, Canada. Earth and Planetary Science Letters 189, 207–220.

Sun S. S. and McDonough W. F., 1989. Chemical and isotopic systematic of oceanic basalts: implications for mantle composition and processes. In Magmatism in the Ocean Basins (eds. A. D. Saunders and M. J. Norry). Geological Society Special Publications, p. 313–345.

Stubley, M. P., 2005. Slave Craton: interpretive bedrock compilation. Northwest Territories Geoscience Office, NWT-NU Open File 2005-01: Digital files and 2 maps.

Tanaka, T., Togashi, S., Kamioka, H., et al., 2000. JNdi-1: a neodymium isotopic reference in consistency with LaJolla neodymium. Chemical Geology 168, 279–281.

Taylor, S.R., McLennan, S.M., 1985. The Continental Crust: Its Composition and Evolution. Blackwell Scientific, Oxford, 312 p.

Unterschutz, J. L. E., Creaser, R. A., Erdmer, P., Thomson, R. I., Daughtry, K. L., 2002. North American margin origin of Quesnel terrane strata in the southern Canadian Cordillera: Inferences from geochemical and Nd isotopic characteristics of Triassic metasedimentary rocks. Geological Society of America Bulletin 114, 462-475.

Wasserburg G. J., Jacobsen S. B., DePaolo D. J. and McCulloch M. T., 1981. Precise determinations of Sm/Nd ratios, Sm and Nd isotopic abundances in standard solutions. Geochimica et Cosmochima Acta 45, 2311-2323.

Windley, B. F., 1984. The Evolving Continents. John Wiley and Sons Limited, 399 p.

Yamashita, K., Creaser, R. A., Stemler, J. U., Zimaro, T.W. 1999. Geochemical and Nd-Pb isotopic systematics of late Archean granitoids, southwestern Slave Province, Canada: constraints for granitoid origin and crustal isotopic structure. Canadian Journal of Earth Science 36, 1131–1147.

Zhang, J., Nozaki, Y., 1996. Rare earth elements and yttrium in seawater: ICP-MS determinations in the East Caroline, Coral Sea, and South Fiji basins of the western South Pacific Ocean. Geochimica et Cosmochimica Acta 60, 4631–4644.

Table 2.1. Electron micro-probe analysis of amphiboles in the CSCG BIF.

Analysis (wt%)	Grunerite Average (n=21)	std dev	Ferro-actinolite Average (n=21)	std dev
SiO_2	51.44	0.70	51.20	1.20
TiO_2	n.d	-	n.d	-
Al_2O_3	0.50	0.32	2.38	1.03
FeO	33.35	1.11	21.48	0.97
Fe_2O_3	0.00	-	1.07	-
MnO	1.32	0.16	0.39	0.08
MgO	9.61	0.39	9.28	0.71
CaO	1.03	0.44	11.45	0.41
Na_2O	0.05	0.03	0.28	0.11
K_2O	0.05	0.10	0.09	0.05
H_2O+	1.95	-	2.00	-
Total	**99.30**	1.09	**99.62**	0.43

Fe_2O_3 and H_2O content calcualted using the cation normalization scheme by Locock (2014; see also Hawthorne et al., 2012); n.d = not detected.

Formula assignments based on 24 anions (O, OH, F, Cl)

Element	Grunerite Average (n=21)	std dev	Ferro-actinolite Average (n=21)	std dev
Si	7.98	0.04	7.72	0.15
Al	0.02	0.03	0.28	0.15
Ti	0.00	-	0.00	-
Al	0.07	0.04	0.14	0.05
Fe^{3+}	0.00	-	0.12	0.09
Fe^{2+}	2.71	0.08	2.65	0.08
Mg	2.22	0.08	2.09	0.14
Mn^{2+}	0.17	0.02	0.05	0.002
Fe^{2+}	1.62	0.08	0.06	0.05
Ca	0.17	0.07	1.85	0.05
Na	0.02	0.01	0.04	0.015
Na	0.00	-	0.04	0.02
K	0.01	-	0.02	0.01
Total	**14.98**	0.021	**15.06**	0.03

Fe^{3+} obtained by calcualting the $Fe^{3+}/\Sigma Fe$ ratio (average $Fe^{3+}/\Sigma Fe$ for the ferro-actinolite = 0043) using the cation normalization scheme by Locock (2014).

Table 2.2. Selected major and trace elements in the CSCG BIF.

	Location	Dwyer Lake														
	Samples	RHNWT-5a	RHNWT-5b													
Elements	Lithology	Bulk BIF	A (iron)	B (silica)	C (iron)	D (silica)	E (iron)	F (silica)	G (iron)	H (silica)	I (iron)	J (silica)	K (iron)	L (silica)	M (silica)	N (iron)
XRF (wt.%)	D.L. (wt.%)															
SiO_2	0.01	39.83	16.88	80.67	14.46	92.1	14.82	88	29.29	79.59	20.5	96.32	17.52	87.3	90.16	22
Al_2O_3	0.01	1.08	0.18	0.15	0.23	<DL	0.29	0.03	0.4	0.51	0.56	<DL	0.29	0.16	0.03	0.93
Fe_2O_3(tot)	0.01	51.57	78.98	14.45	81.92	4.42	81.72	7.34	63.74	15.44	72.9	3.28	77.54	8.36	8.18	68.91
MnO	0.001	0.237	0.083	0.07	0.071	0.038	0.069	0.044	0.104	0.058	0.12	0.01	0.092	0.06	0.024	0.107
MgO	0.01	3.65	2.75	1.98	2.56	1.23	2.54	1.4	3.21	1.79	3.52	0.28	2.95	1.55	0.83	4.34
CaO	0.01	4.68	3.67	2.87	3.39	1.46	3.38	1.8	4.39	2.53	4.55	0.42	4.04	2.26	0.99	5.06
Na_2O	0.01	0.07	<DL	<DL	<DL	<DL	<DL	<DL	<DL	<DL	<DL	<DL	<DL	<DL	<DL	0.04
K_2O	0.01	0.09	0.01	0.01	0.01	< 0.01	0.04	< 0.01	0.04	0.06	0.05	< 0.01	0.02	0.01	0.01	0.1
TiO_2	0.01	0.06	0.01	0.01	0.01	<DL	0.02	<DL	0.01	0.02	0.02	0.01	0.02	0.01	0.01	0.05
P_2O_5	0.01	0.11	0.17	0.19	0.17	0.02	0.21	0.08	0.36	0.05	0.15	0.02	0.14	0.02	0.01	0.17
LOI		-1	-2.04	0.16	-1.99	0.33	-2.15	0.24	-1.11	0.05	-1.54	0.12	-1.96	0.05	-0.03	-1.33
Total		100.4	100.7	100.6	100.8	99.6	100.9	98.94	100.5	100.1	101	100.5	100.7	99.78	100.2	100.4
ICP-MS (ppm)	D.L. (ppm)															
Al (wt.%)	0.2	0.58	0.12	0.13	0.13	0.03	0.18	0.06	0.32	0.29	0.36	0.03	0.16	0.09	0.05	0.49
Ti	0.09	787	59.4	11.3	64.4	3.94	76.7	5.11	55.2	108	87.1	2.76	92.1	11.5	6.81	263
K	6	337	102	111	133	<DL	211	33	392	339	435	31	159	68	24	907
V	0.05	8.02	6.47	0.24	7.36	<DL	7.59	<DL	9.96	2.35	10.6	<DL	10.5	<DL	<DL	6.41
Cr	0.05	2.65	4.95	2.85	7.15	1.03	5.38	0.89	4.38	3.45	7.30	0.44	5.42	1.05	0.67	5.57
Ni	0.06	0.52	0.21	<DL	3.36	<DL	0.52	<DL	0.75	0.11	0.72	<DL	<DL	<DL	<DL	0.58
Rb	0.04	7.52	1.36	0.52	0.80	0.06	1.21	0.12	1.73	0.67	1.56	0.15	0.96	0.33	0.13	5.87
Sr	0.03	5.08	23.3	18.6	20.7	7.33	25.3	10.2	36.0	15.1	30.8	2.88	18.6	9.33	4.65	31.4
Y	0.02	11.9	8.01	6.95	8.70	1.39	10.5	3.72	14.8	5.54	11.2	0.90	7.91	2.37	1.22	11.4
Zr	0.09	24.9	3.70	0.66	4.96	0.27	5.67	0.41	5.65	13.53	9.40	0.16	6.30	0.62	0.58	27.1
Nb	0.04	1.61	0.31	0.15	0.34	0.04	0.33	0.10	0.58	0.75	0.93	0.07	0.49	0.11	0.08	1.19
Hf	0.05	0.74	0.11	<DL	0.14	<DL	0.13	<DL	0.21	0.66	0.40	<DL	0.19	<DL	<DL	0.86
Ta	0.02	0.33	0.17	<DL	0.20	<DL	0.17	<DL	0.17	0.33	0.51	<DL	0.36	<DL	<DL	0.44
Th	0.01	1.85	0.49	0.12	0.47	<DL	0.60	0.16	0.77	2.16	0.98	<DL	0.53	<DL	<DL	3.06
Mo	0.02	0.99	0.24	0.14	0.18	0.11	0.30	0.10	0.32	0.33	0.26	0.09	0.23	0.07	0.07	0.28
U	0.03	0.57	0.35	<DL	0.38	<DL	0.26	<DL	0.32	0.16	0.27	<DL	0.35	<DL	<DL	0.37
REE La	0.03	2.20	3.90	1.16	4.56	0.64	4.15	1.74	5.60	1.02	5.38	0.22	6.42	1.67	0.23	6.03
Ce	0.03	4.77	7.96	2.61	9.24	1.28	8.65	3.57	11.9	2.35	11.5	0.46	12.5	3.32	0.51	12.7
Pr	0.04	0.57	0.90	0.33	1.03	0.14	0.99	0.41	1.35	0.29	1.31	0.05	1.34	0.36	0.07	1.42
Nd	0.03	2.47	3.61	1.45	4.09	0.55	3.86	1.67	5.41	1.30	5.31	0.23	5.12	1.40	0.28	5.58
Sm	0.04	0.70	0.72	0.40	0.79	0.12	0.79	0.35	1.19	0.35	1.11	0.06	0.93	0.27	0.08	1.14
Eu	0.03	0.23	0.50	0.40	0.53	0.08	0.58	0.20	0.72	0.36	0.73	<DL	0.49	0.17	0.05	0.68
Gd	0.03	1.15	0.97	0.65	1.04	0.16	1.15	0.43	1.65	0.54	1.47	0.10	1.11	0.30	0.12	1.43
Tb	0.03	0.21	0.15	0.11	0.16	<DL	0.18	0.07	0.26	0.10	0.23	0.02	0.16	<DL	<DL	0.21
Dy	0.04	1.45	1.02	0.78	1.04	0.18	1.26	0.43	1.82	0.71	1.61	0.12	1.10	0.30	0.14	1.49
Ho	0.02	0.35	0.24	0.20	0.25	<DL	0.31	0.11	0.44	0.18	0.38	0.03	0.26	0.07	0.04	0.36
Er	0.04	1.10	0.79	0.63	0.83	0.13	1.00	0.35	1.41	0.63	1.28	0.10	0.87	0.23	0.13	1.20
Tm	0.06	0.15	0.11	0.09	0.11	0.02	0.14	<DL	0.20	0.10	0.19	<DL	0.12	<DL	<DL	0.18
Yb	0.05	1.01	0.75	0.62	0.76	0.15	0.89	0.34	1.29	0.67	1.23	0.10	0.85	0.25	0.13	1.21
Lu	0.04	0.16	0.12	0.10	0.12	<DL	0.14	<DL	0.20	0.11	0.19	<DL	0.14	<DL	<DL	0.19
ΣREE		16.52	21.74	9.54	24.54	3.44	24.09	9.67	33.44	8.69	31.93	1.51	31.38	8.34	1.78	33.81
$(Pr/Yb)_{SN}$		0.22	0.47	0.21	0.54	0.37	0.44	0.48	0.41	0.17	0.42	0.21	0.62	0.58	0.21	0.46
$(Eu/Eu^*)_{SN}$		1.19	2.74	3.62	2.70	2.73	2.82	2.35	2.38	3.86	2.62	-	2.19	2.65	2.44	2.45
$(Y/Ho)_{SN}$		1.33	1.27	1.36	1.32	1.15	1.32	1.32	1.28	1.21	1.13	1.15	1.17	1.25	1.31	1.22

Table 2.2. continued.

Elements	RHNWT-5c	Bell Lake RHNWT-14b	RHNWT-14C	RHNWT-14d	Brown Lake RHNWT-BL-1	Patterson Lake RHNWT-34B	Emile River RHNWT-27	Bell Lake RHNWT-15
XRF (wt.%)	Bulk BIF	Mixed chemical/clastic	Bulk BIF	mixed chemical/clastic	Bulk BIF	Bulk BIF	Bulk BIF	Basement gneiss
SiO_2	70.84	77.17	74.35	54.12	51.21	59.22	44.35	-
Al_2O_3	<DL	9.88	0.08	9.84	2.00	1.70	0.75	-
Fe_2O_3(tot)	24.76	6.94	23.23	23.97	43.60	34.14	51.05	-
MnO	0.16	0.58	0.25	0.34	0.13	0.13	0.08	-
MgO	2.27	0.75	1.27	3.54	1.50	2.79	2.30	-
CaO	1.61	1.06	0.38	4.85	1.10	2.41	1.97	-
Na_2O	<DL	1.05	<DL	0.26	0.09	0.13	0.07	-
K_2O	<DL	1.84	0.03	2.33	0.16	0.23	<DL	-
TiO_2	0.01	0.25	0.01	0.55	0.03	0.04	0.02	-
P_2O_5	0.04	0.02	0.03	0.08	0.15	0.07	0.04	-
LOI	0.21	0.67	-0.41	0.88	-0.63	-0.48	-1.21	-
Total	99.92	100.30	99.23	100.80	99.34	100.40	99.43	-
ICP-MS (ppm)								
Al (wt.%)	0.04	4.59	0.81	3.99	1.09	-	-	-
Ti	34	1.51 (wt.%)	39	1.85 (wt.%)	1562	-	-	1731
K	10.9	1366	234	3249	205	-	-	-
V	0.30	43.7	5.9	91.2	13.4	11	6	14.0
Cr	1.58	205	35	130	9.20	<DL	<DL	34.5
Ni	<DL	46.8	29.0	49.8	4.80	<DL	<DL	5.06
Rb	0.20	78.1	2.1	146	12.3	14	<DL	-
Sr	9.59	37.7	1.7	13.1	4.00	8	3	-
Y	2.61	5.31	2.36	11.8	6.90	6	4	6.86
Zr	0.67	101	1	98.6	10.5	8	7	173
Nb	0.07	5.57	0.34	6.79	2.79	<DL	<DL	8.24
Hf	<DL	3.39	<DL	2.99	0.23	0.2	<DL	5.08
Ta	<DL	1.32	0.13	1.78	27.2	2.8	2.2	-
Th	<DL	10.6	0.5	5.76	1.97	1.9	1	38.8
Mo	0.18	2.53	1.05	1.35	2.56	<DL	<DL	-
U	<DL	3.53	0.18	2.75	1.47	0.5	0.2	-
REE La	0.73	9.76	2.68	11.7	5.89	3.5	0.9	-
Ce	1.42	18.7	3.70	26.4	10.8	7	1.7	-
Pr	0.18	1.96	0.26	3.01	1.17	0.82	0.21	16.1
Nd	0.80	6.46	0.66	11.3	4.41	3.4	0.9	-
Sm	0.23	1.05	0.12	2.29	0.90	0.7	0.2	-
Eu	0.19	0.72	<DL	0.79	0.39	0.25	0.12	-
Gd	0.33	1.02	0.18	2.37	1.08	0.8	0.3	-
Tb	<DL	0.15	<DL	0.34	0.16	0.1	<DL	-
Dy	0.33	0.97	0.30	2.19	1.06	0.9	0.4	-
Ho	0.08	0.21	0.08	0.48	0.23	0.2	<DL	0.26
Er	0.25	0.70	0.26	1.46	0.73	0.6	0.3	-
Tm	<DL	0.11	<DL	0.21	0.13	0.09	0.05	-
Yb	0.26	0.78	0.32	1.38	0.73	0.6	0.3	0.48
Lu	<DL	0.12	<DL	0.20	0.11	0.09	0.04	-
ΣREE	4.80	42.71	8.56	64.05	27.82	19.05	5.42	-
(Pr/Yb)$_{SN}$	0.27	0.99	0.31	0.86	0.63	0.54	0.27	13.22
(Eu/Eu*)$_{SN}$	3.18	3.10	-	1.51	1.80	1.52	2.27	-
(Y/Ho)$_{SN}$	1.29	0.96	1.15	0.95	1.16	1.16	-	1.02

Table 2.3. Sm-Nd isotope data (layer-by-layer) in Dwyer Lake BIF

Sample	Sm (ppm)	Nd (ppm)	^{147}Sm/^{144}Nd	^{143}Nd/^{144}Nd	± 2SE[a]	ε_{Nd}(t=0)	ε_{Nd}(t=2853 Ma[b])	T_{DM} (Ga)[c]
A (iron)	0.62	2.98	0.1256	0.511369	±8	-24.7	1.4	3.08
B (silica)	0.33	1.20	0.1665	0.512039	±8	-11.7	-0.6	(3.60)
C (iron)	0.69	3.47	0.1206	0.511273	±5	-26.6	1.4	3.07
D (silica)	0.10	0.44	0.1310	0.511489	±7	-22.4	1.7	3.06
E (iron)	0.69	3.20	0.1295	0.511424	±8	-23.7	1.0	3.12
F (silica)	0.28	1.36	0.1252	0.511418	±7	-23.8	2.5	2.99
G (iron)	1.00	4.55	0.1332	0.511530	±8	-21.6	1.8	3.07
H (silica)	0.28	1.02	0.1677	0.512030	±9	-11.9	-1.2	(3.72)
I (iron)	0.94	4.45	0.1284	0.511452	±8	-23.1	2.0	3.04
J (silica)	0.05	0.18	0.1635	0.511992	±10	-12.6	-0.4	(3.53)
K (iron)	0.81	4.44	0.1096	0.511139	±8	-29.2	2.8	2.94
L (silica)	0.20	1.05	0.1146	0.511268	±10	-26.7	3.5	2.90
M (silica)	0.06	0.23	0.1693	0.512010	±11	-12.2	-2.2	(3.92)
N (iron)	0.90	4.58	0.1195	0.511279	±7	-26.5	1.9	3.03

[a] Uncertainty is quoted as 2 standard errors in the last digits in the ^{143}Nd/^{144}Nd ratio.

[b] 2853 +2/-1 Ma (Sircombe et al., 2001 - the maximum age of the BIF at Dwyer Lake determined by U-Pb zircon dating of a tuffaceous rock deposited on top of the fuchsitic quartzite and underneath the BIF).

[c] Refers to the depleted mantle model age calculated for samples with ^{147}Sm/^{144}Nd < 0.14 using the mantle evolution model of Goldstein (1984). Model ages in brackets calculated for ^{147}Sm/^{144}Nd > 0.14. These ages are less reliable due to insufficient Sm/Nd fractionation relative to depleted mantle values.

Figure 2.1A. The Slave craton showing the sample locations and the dominant lithologies of the craton. These are basement gneisses (CSBC - Central Slave Basement Complex), mafic volcanics (Kam Group), felsic-to-mafic volcanics (Banting Group), volcaniclastic turbidite packages (Duncan Group) and younger intrusive granitoids. The CSCG (Central Slave Cover Group) is sporadically exposed as a thin sheet between the CSBC and the Kam Group volcanics. Map modified by Stubley (2005).
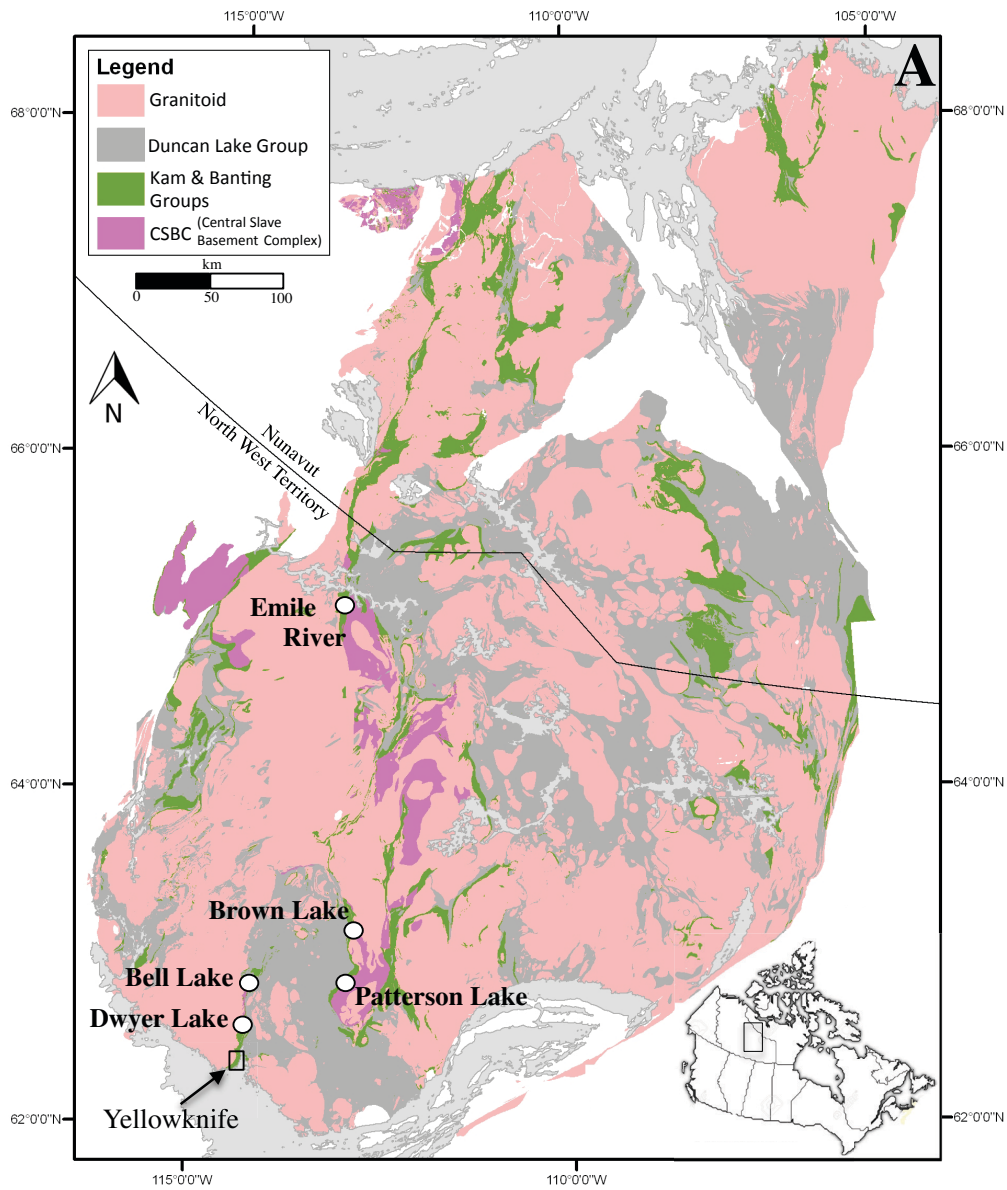
Figure 2.1B. The general stratigraphy of the CSCG. The CSCG were likely formed in a basin related to rifting of the CSBC.
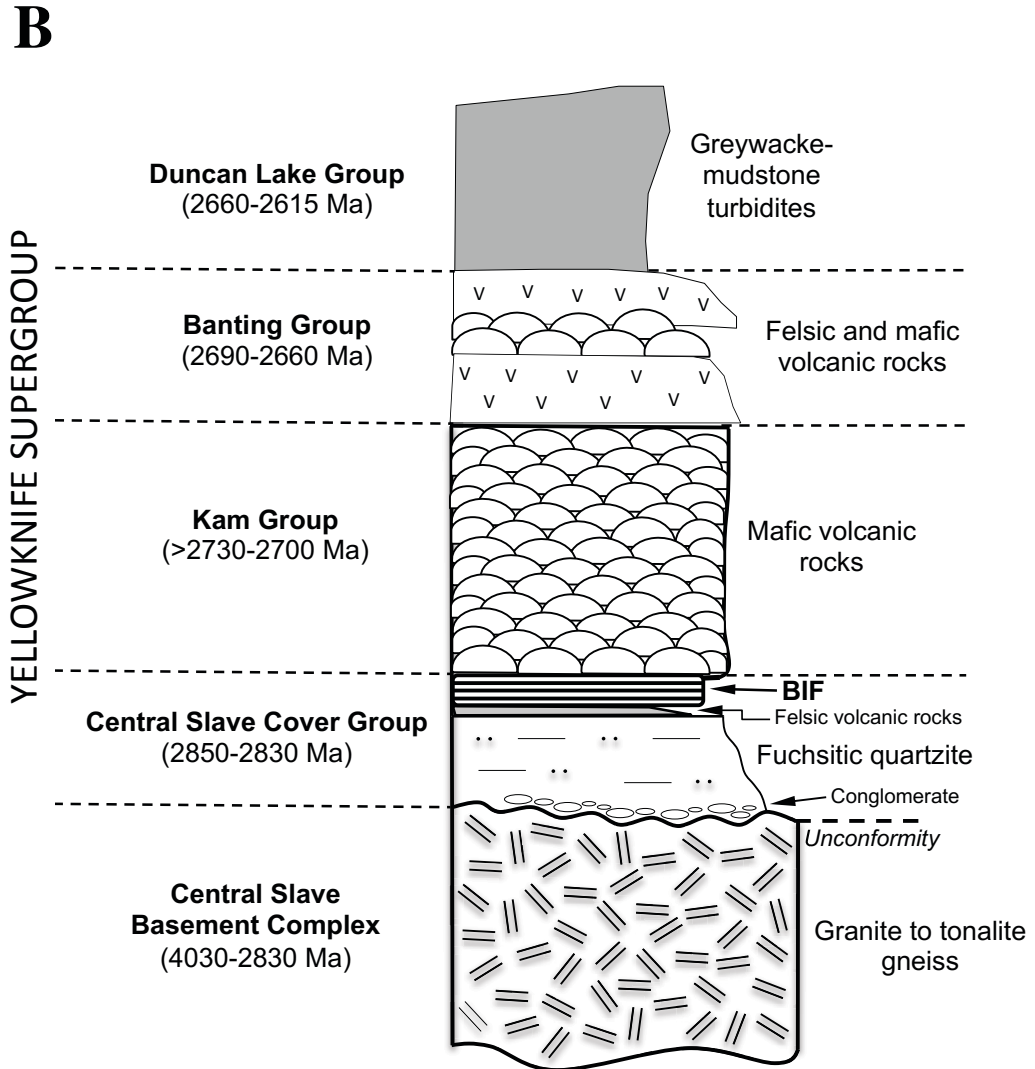
Figure 2.2. The local stratigraphy at the five sample sites with the approximately position of samples collected. Note the difference in relative stratigraphic thickness and of individual rock units. The BIF has the largest thickness at Dwyer Lake and Bell Lake. The pebble-to-cobble basal conglomerate has only been found at Dwyer Lake and Brown Lake. At Patterson Lake, pebble conglomerate is found further up in the stratigraphy in close association with the BIF unit. Note also that the quartzite has a variable content of fuchsite. See text for further explanation.

56
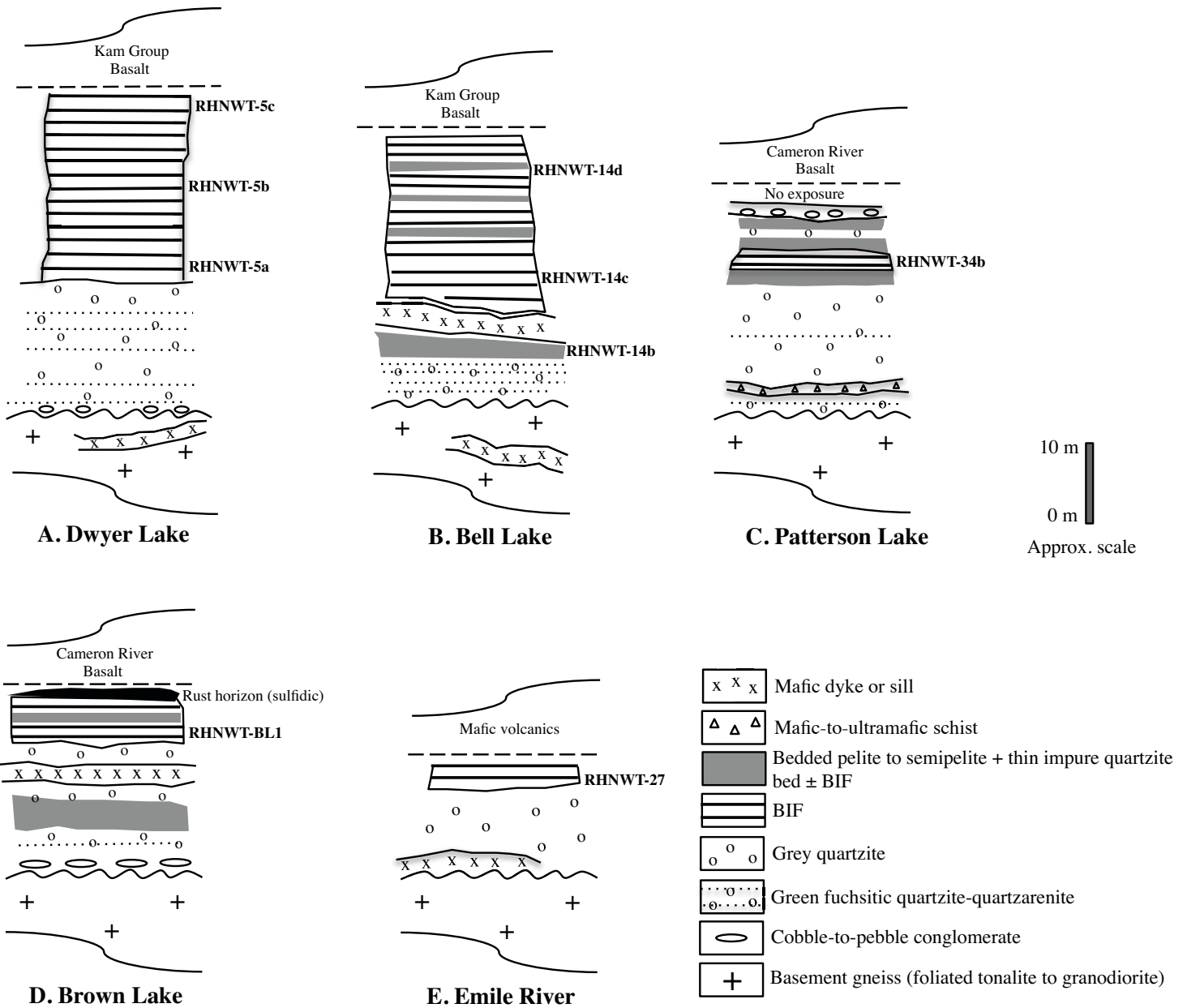
Figure 2.3. Field photos of the CSCG BIF. (A) Bell Lake - showing the bulk of the CSCG with a basal fuchsitic quartzite overlain by BIF. Note that the CSCG stratigraphy has locally been disturbed by later intrusion of mafic dykes/sills. (B), (C) and (D) Dwyer Lake and Emile River - well-laminated mm- to cm-scale quartz and magnetite mesobands. The quartz bands are occasionally greenish due to formation of ferro-actinolite at the quartz-magnetite interface as seen in the inserted photo in (C) and (D). (E) Patterson Lake - well-banded BIF outcrop. Note the recrystallization and tiny micro-folds of the chert bands. (F) Bell Lake - thick BIF sequence with rusty horizons (inset) due to intermix of pelitic material. (G) Patterson Lake - a 25-30 cm thick conglomerate with lenticular shaped pebbles in association with the BIF.
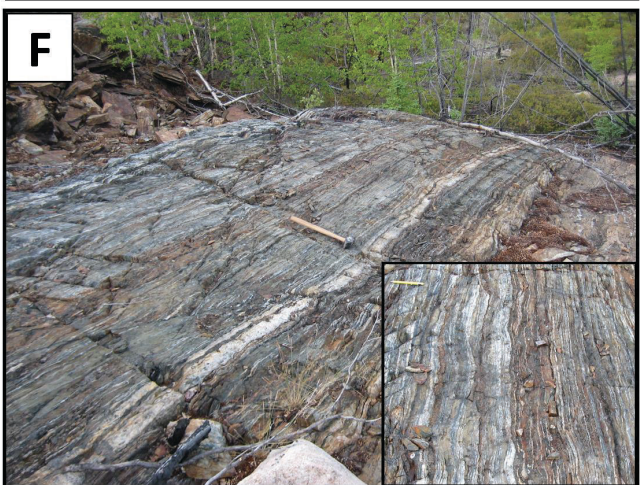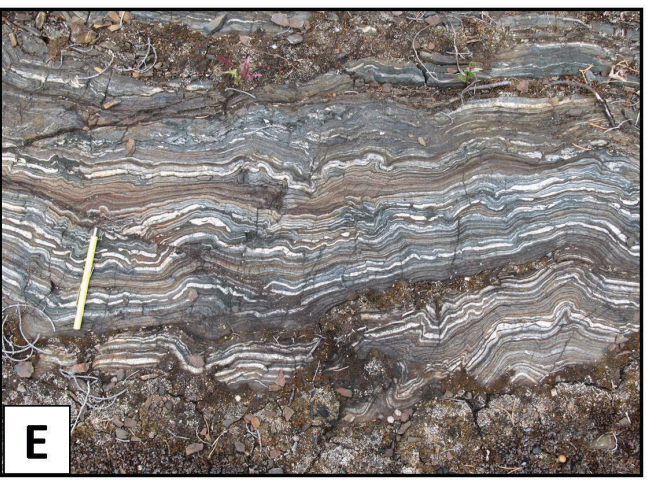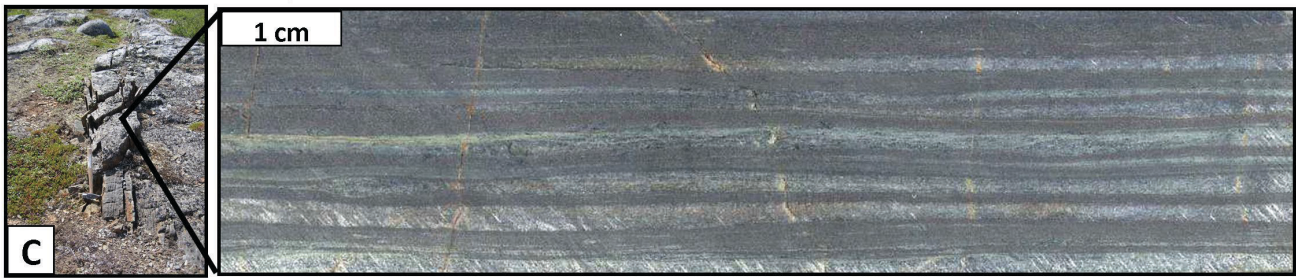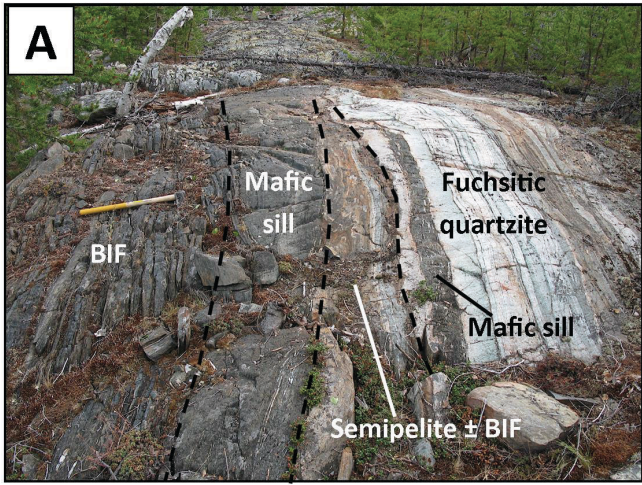
Figure 2.4. Representative hand sample and thins section images of the CSCG BIF. (A) Hand sample from Dwyer Lake with individual marked silica- and iron-bands (A to N) separated in this study. (B) Transmitted light thin section image of (A) showing fine bands of quartz and magnetite with greenish actinolite developed on the quartz-magnetite interface. (C) Transmitted light image from Dwyer Lake with both actinolite and colorless grunerite developed. (D) and (E) Close up of grunerite crystals from (C). (F) Amphibole ternary plot illustrating the two dominant iron-silicates in the detrital free BIF. Probe measurement from (C). (G) and (H) Polarized (G) and transmitted light (H) images of thin beds of hornblende+biotite+garnet from the Bell Lake BIF. (I) Hand sample micro-photo of pebbly sediment with small angular-to-subangular K-feldspar pebbles set in a quartz and biotite matrix. Found adjacent to the BIF and the pebble-conglomerate (see Fig. 2.3G) at Patterson Lake. (J) Polarized thin section image of the K-feldspar pebbles in (I).
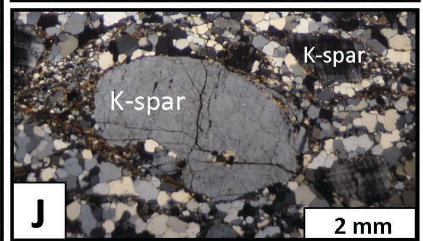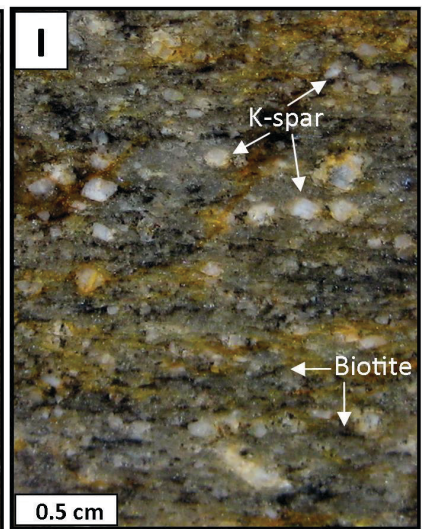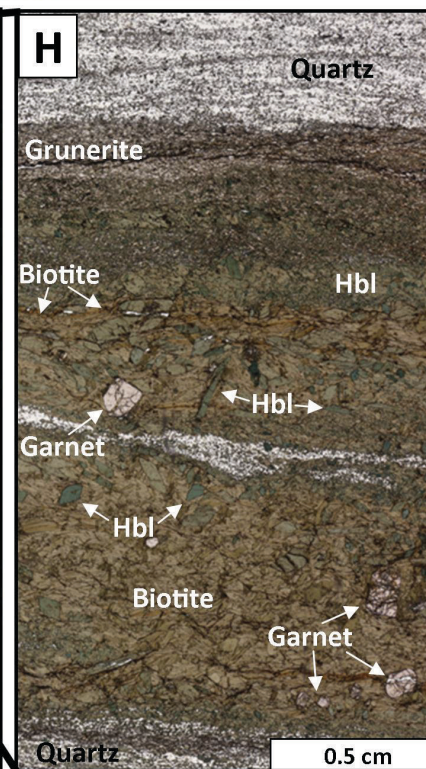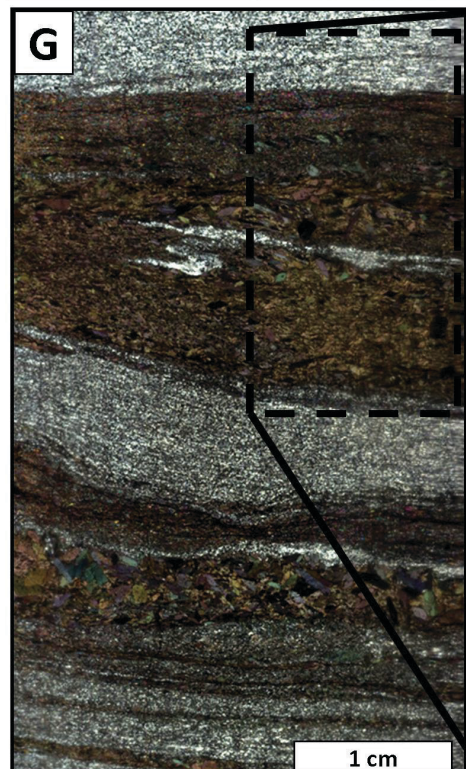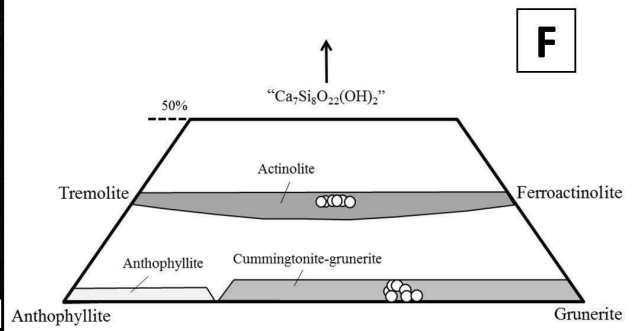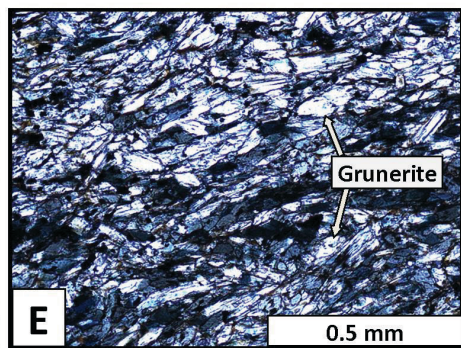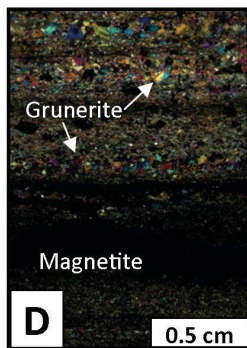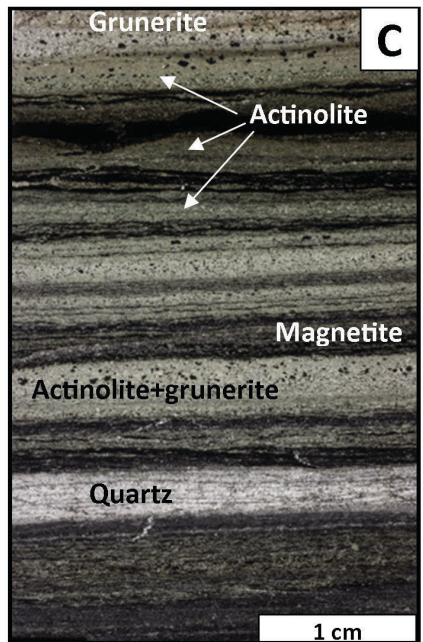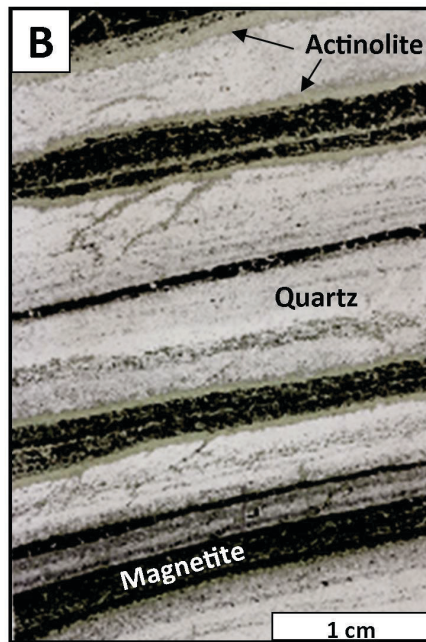
Figure 2.5. Plots displaying the differences between silica bands and iron bands for selected elements in the BIF. See text for further explanation.
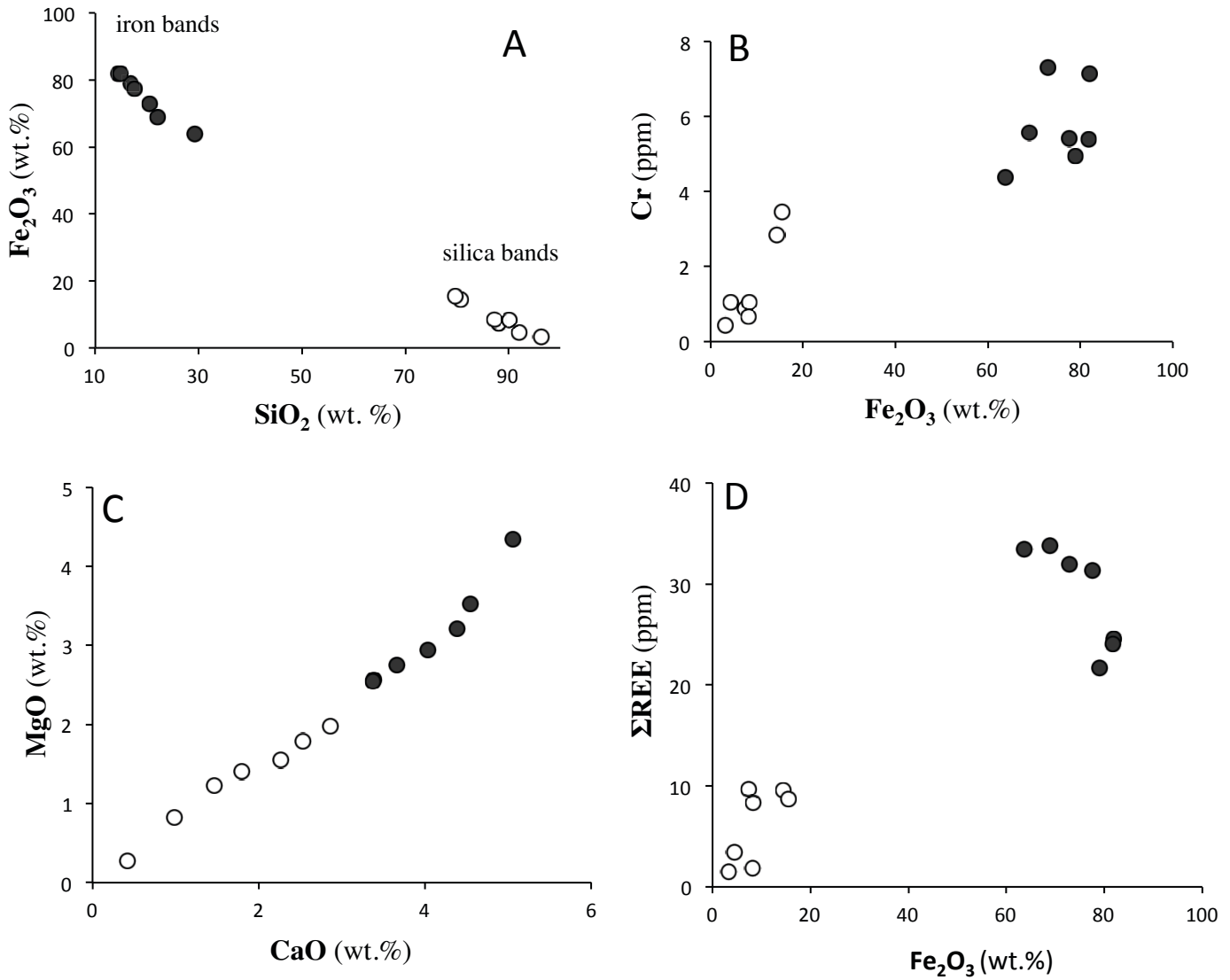
Figure 2.6. (A-G) The variation of selected elements on a layer-by-layer basis from the sample in Fig. 2.4A. Note the general higher concentrations for the iron bands than the silica bands. (H) The detailed $\varepsilon_{Nd}(t)$ values in (H) reveal that the individual silica bands are highly heterogeneous ranging from +3.4 to -2.2, whereas the iron bands are more homogenous ranging from +1 to +2.8 $\varepsilon_{Nd}(t)$ values. Error bars on the $\varepsilon_{Nd}(t)$ values are calculated assuming an error on the Sm^{147}/Nd^{144} ratio of 0.2%.
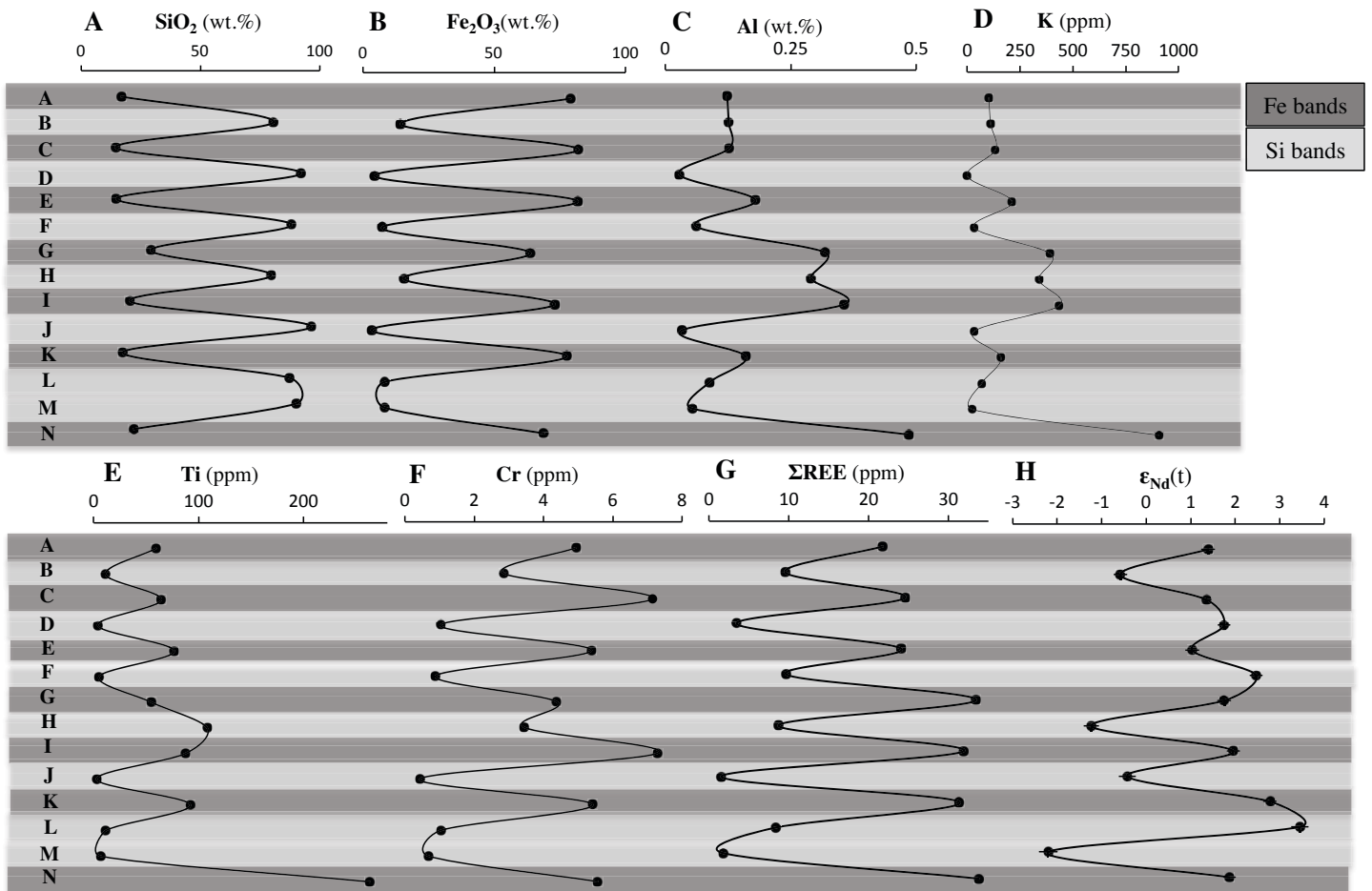
Figure 2.7. (A) The shale normalized REY patterns for the bulk BIF. Note the large HREE-to-LREE enrichment in Dwyer Lake, Emile River and partly Patterson Lake. This enrichment is not seen for the Brown Lake and the two Bell Lake samples, which corresponds to a higher mix of aluminosilicate in the chemical precipitate within these samples. (B) The detailed shale normalized REY pattern for individual bands at Dwyer Lake. A consistent higher abundance of REY and a less fractionated REY pattern is seen for the iron bands while a higher HREE-to-LREE enrichment is noticed for the silica bands. Both the silica- and iron-bands have well developed Y anomalies and a large excess of Eu relative to neighboring REE. The Eu anomaly is also profound within the chondrite normalized REY pattern (inset), which shows the average REY pattern for the silica- and iron bands.
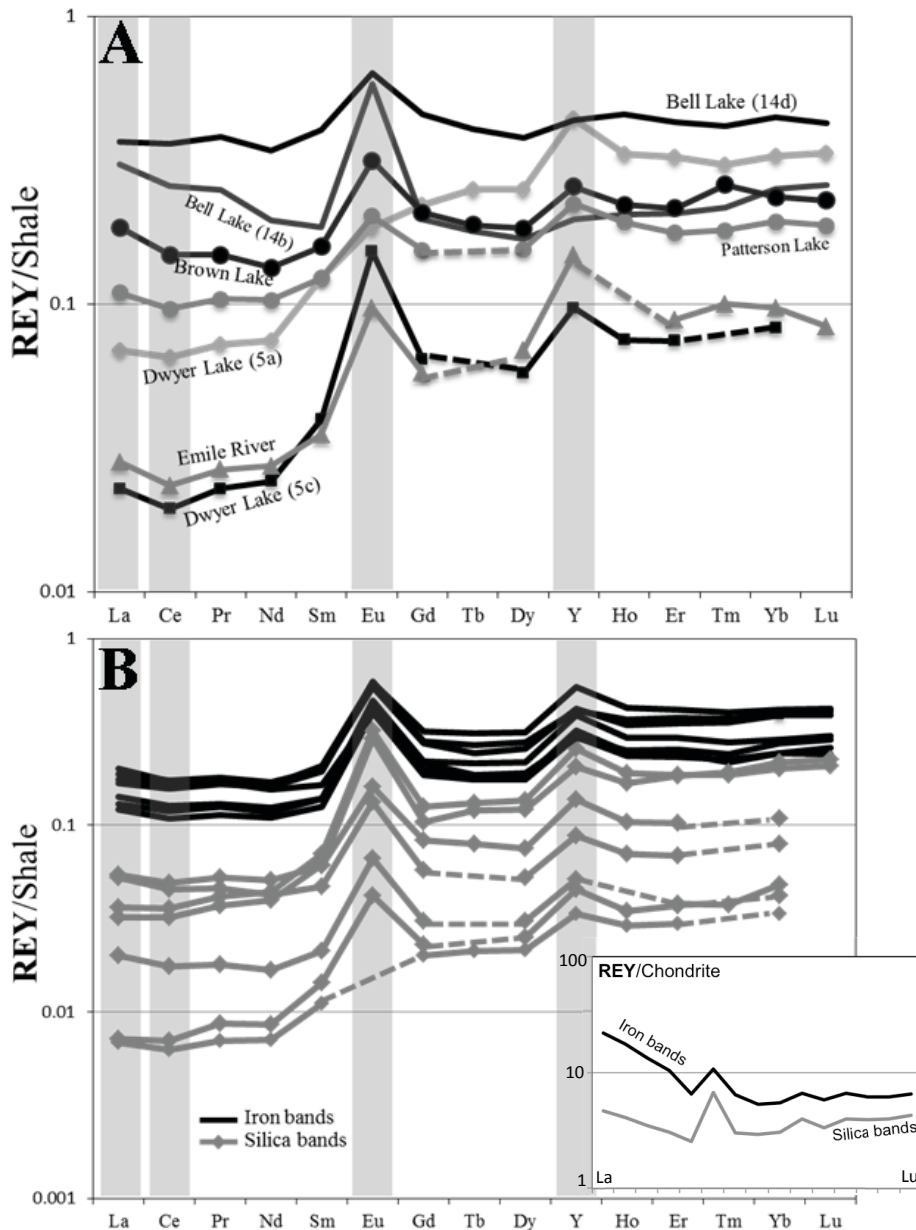
Figure 2.8. (A) The relationship between the seawater generated REY fractionation, represented by the $(Pr/Yb)_{SN}$ ratios, and the detrital component, represented by Ti content. A general large scatter for the BIF samples indicate minimum impact from aluminosilicate on the total REY budget and that a large part of the REY was in solution prior to precipitation of the BIF. (B) A mixing line between potential components to the seawater composition during BIF deposition. All BIF samples have shale normalized seawater $(Pr/Yb)_{SN}$ ration < 1 with one part of the samples having $(Pr/Yb)_{SN}$ ratios analogous to modern upper (<600 m) seawater and the other part relative more LREE enriched either from hydrothermal fluids and/or small input of terrigenous material. Although the BIF samples in this study display shale normalized seawater $(Y/Ho)_{SN}$ ratios > 1, the higher Y anomaly for modern upper seawater could indicate that the Y in the seawater during BIF deposition likely was suppressed by hydrothermal fluids and/or terrigenous material having chondritic $(Y/Ho)_{SN}$ values of ~1. Upper seawater values are from Alibo and Nozaki (1999); High-T hydrothermal fluids from Bau and Dulski (1999). (C) Ni-Cr diagram showing very low concentrations of Cr and Ni in the CSCG BIF. Note that the slope is identical to other pre-2.7 Ga BIF and that it is lower than for potential Cr and Ni igneous source rocks (see text for further explanation). Archaean basalt data from Taylor and McLennan (1985); Komatiite data from Bolhar et al. (2005); Pre-2.7 Ga BIF data from Konhauser et al. (2009). (C) The silica- and iron-bands show similar magnitude of the positive Eu anomaly, whereas the size of the Eu anomaly is comparable to the older Eoarchaean Isua BIF rather than other contemporaneous BIFs. This demonstrates the large influence from high-T hydrothermal fluids to the seawater within the rift-dominated basin. For comparison, all data points normalized after Post-Archaean Australian Shale (PAAS, Taylor and McLennan, 1985). Isua BIF values from Frei and Polat (2007); Pongola BIF values from Alexander et al. (2008); Itilliarsuk BIF values from Haugaard et al. (2013).
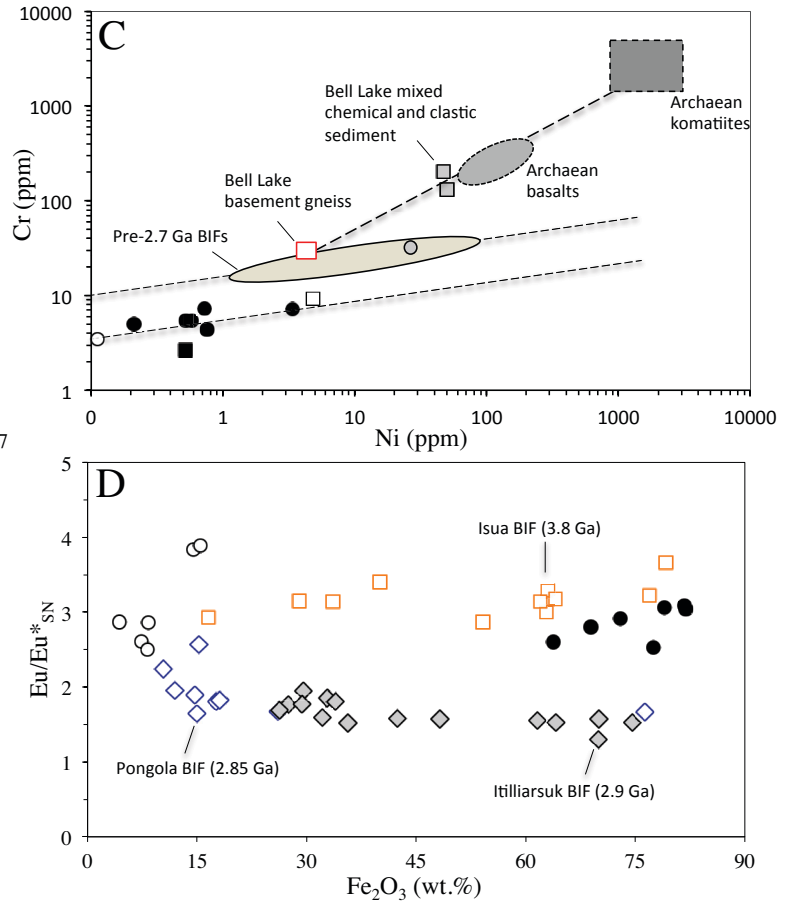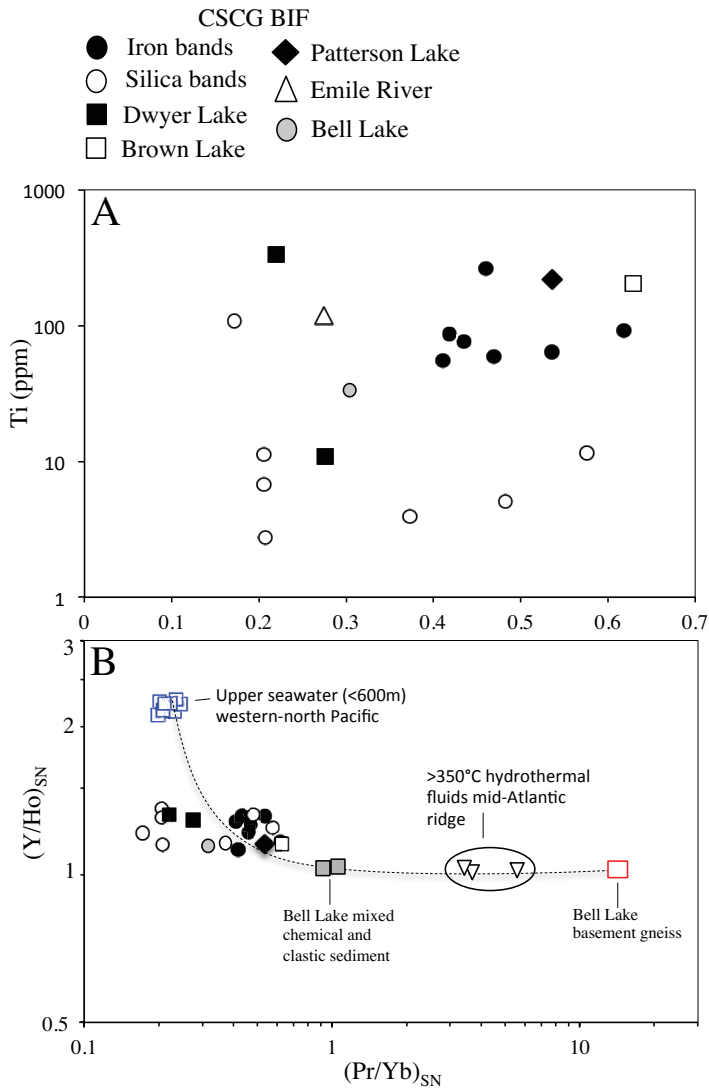
Figure 2.9. Trace element discrimination diagram for the mixed chemical and clastic sediment at Bell Lake. The detrital insoluble components in the mixed Bell Lake rocks cannot be explained by input from an eroded felsic basement alone. A mixture of more mafic-to-ultramafic material is required to explain the pattern. See text for further details. Archaean komatiite- and Archaean mafic-data are from Condie (1993).
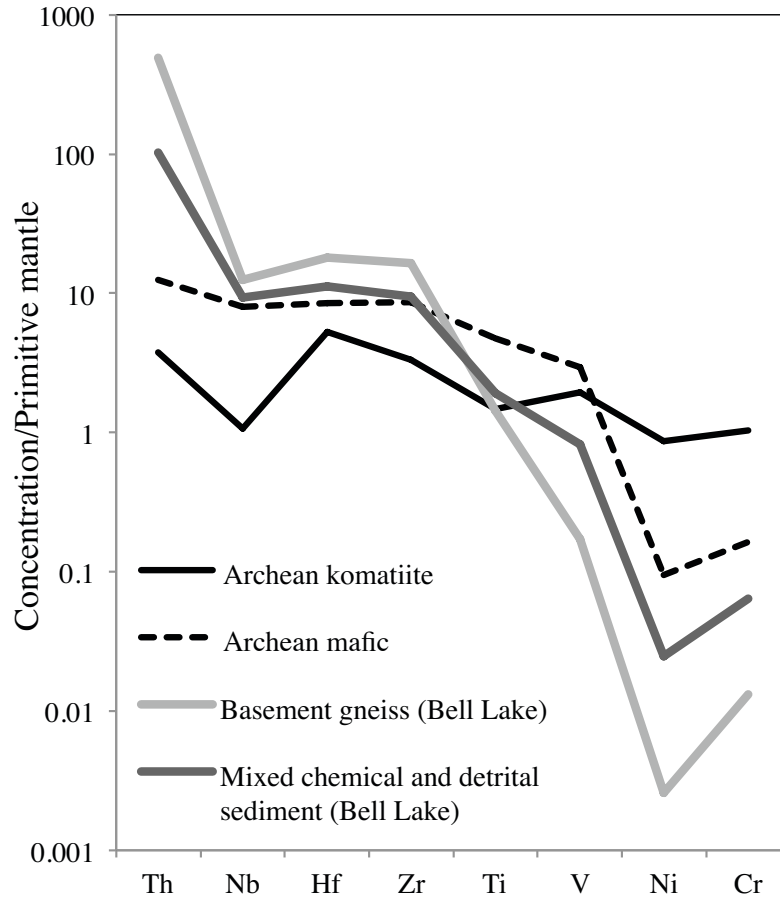
Figure 2.10. (A) The silica bands have lower Nd content and a higher scatter of $\varepsilon_{Nd}(t)$ relative to the iron bands. This reflects a heterogeneous isotopic composition of Nd in the upper seawater. The iron bands are less scattered due to a better mixture of the deeper water possible related to a more uniform $^{143}Nd/^{144}Nd$ source. (B) Both negative and positive $\varepsilon_{Nd}(t)$ values indicate different seawater masses behind silica precipitation whereas only positive $\varepsilon_{Nd}(t)$ values indicate more homogenous seawater mass behind iron precipitation. Error bars on the $\varepsilon_{Nd}(t)$ values are calculated assuming an error on the Sm^{147}/Nd^{144} ratio of 0.2%.
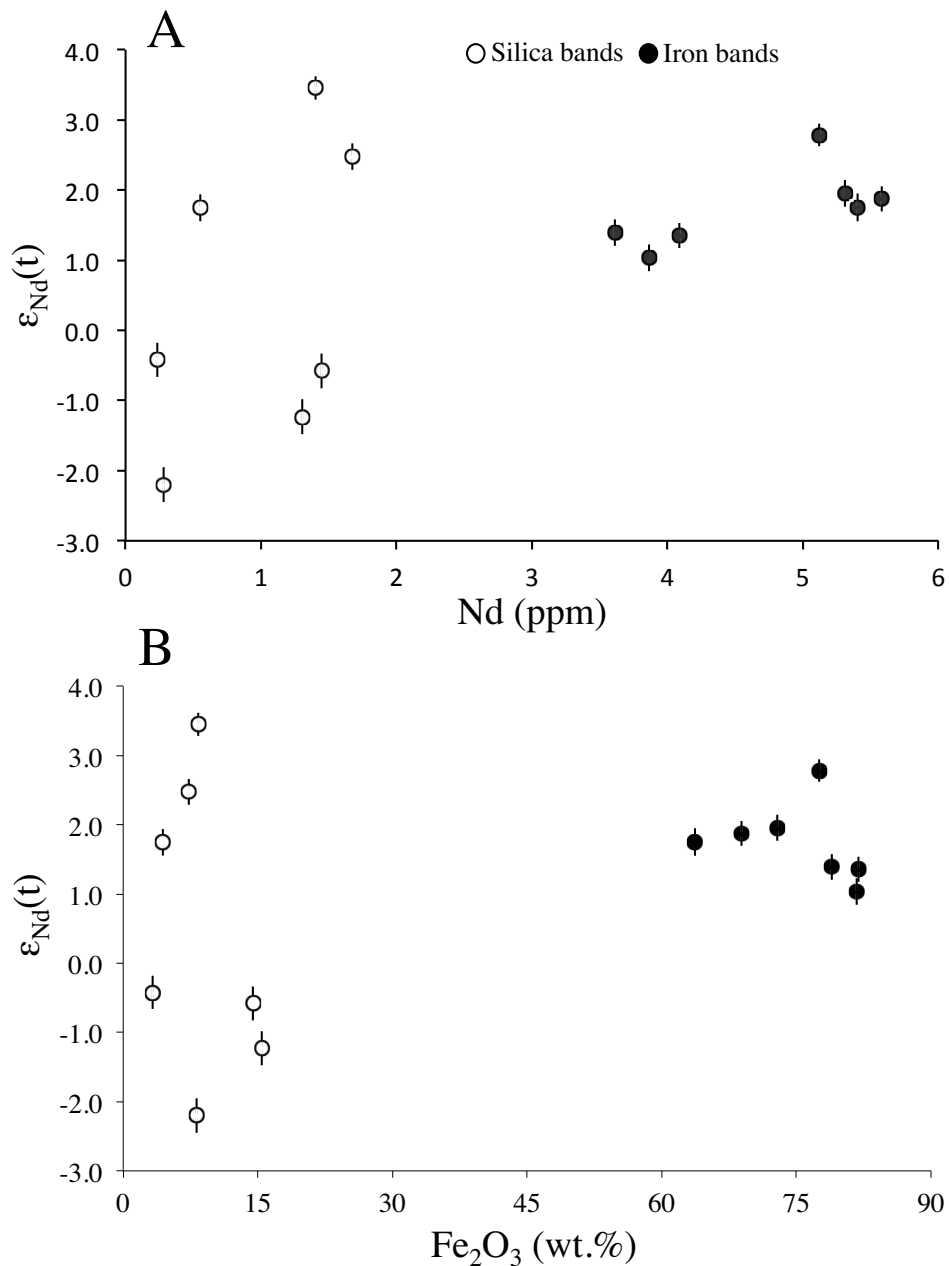
Figure 2.11. Simplified box model showing the deposition of silica and iron bands in the CSCG BIF. A strong heterogeneous upper seawater with respect to ^{143}Nd/^{144}Nd isotopes dominate during silica precipitation while a more well-mixed, uniform ^{143}Nd/^{144}Nd isotopes dominates in the iron rich waters. As for modern seawaters, the REY concentrations are larger and less HREE-to-LREE fractionated for deeper water and more diluted with a higher HREE-to-LREE fractionation in upper seawaters. Noteworthy is that during $Fe(OH)_3$ precipitation, a minor portion of silica gets incorporated into the precipitate. The iron rich waters may have entering the BIF depositional site through repetitive upwelling onto the new-formed rift dominated shelf.
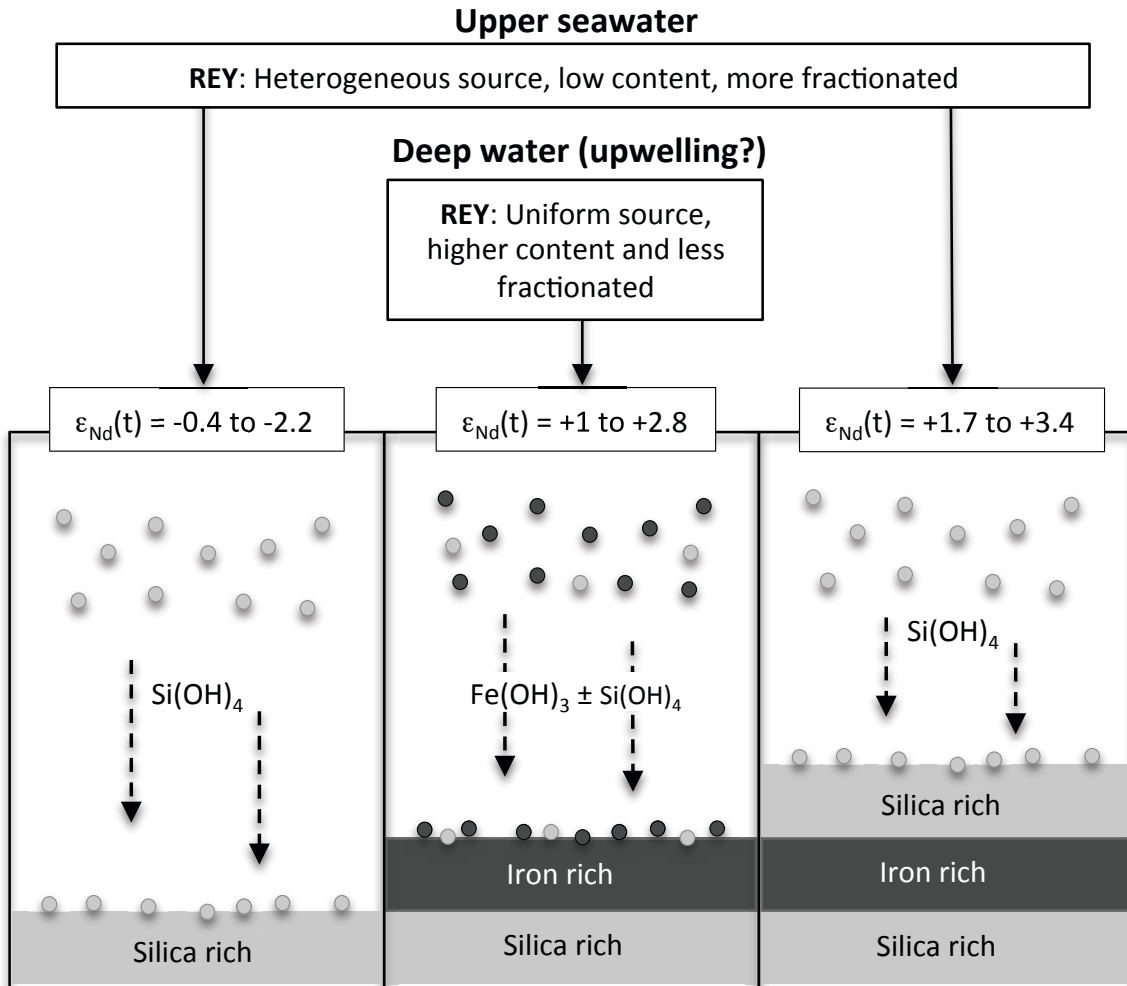
Figure 2.12. The Nd isotopic evolution lines for the BIF reveals positive $\varepsilon_{Nd}(t)$ values and correspondingly relatively juvenile depleted mantle model ages for all the iron bands and parts of the silica bands at the time of BIF deposition (2853 Ma). Four silica bands have incorporated REY from older, enriched continental crust with larger crustal residence time (negative $\varepsilon_{Nd}(t)$ values at the time of BIF deposition). The model ages for the enriched bands are more uncertain due to Sm^{147}/Nd^{144} ratio > 0.14. See text for possible sources of the Nd and REY.
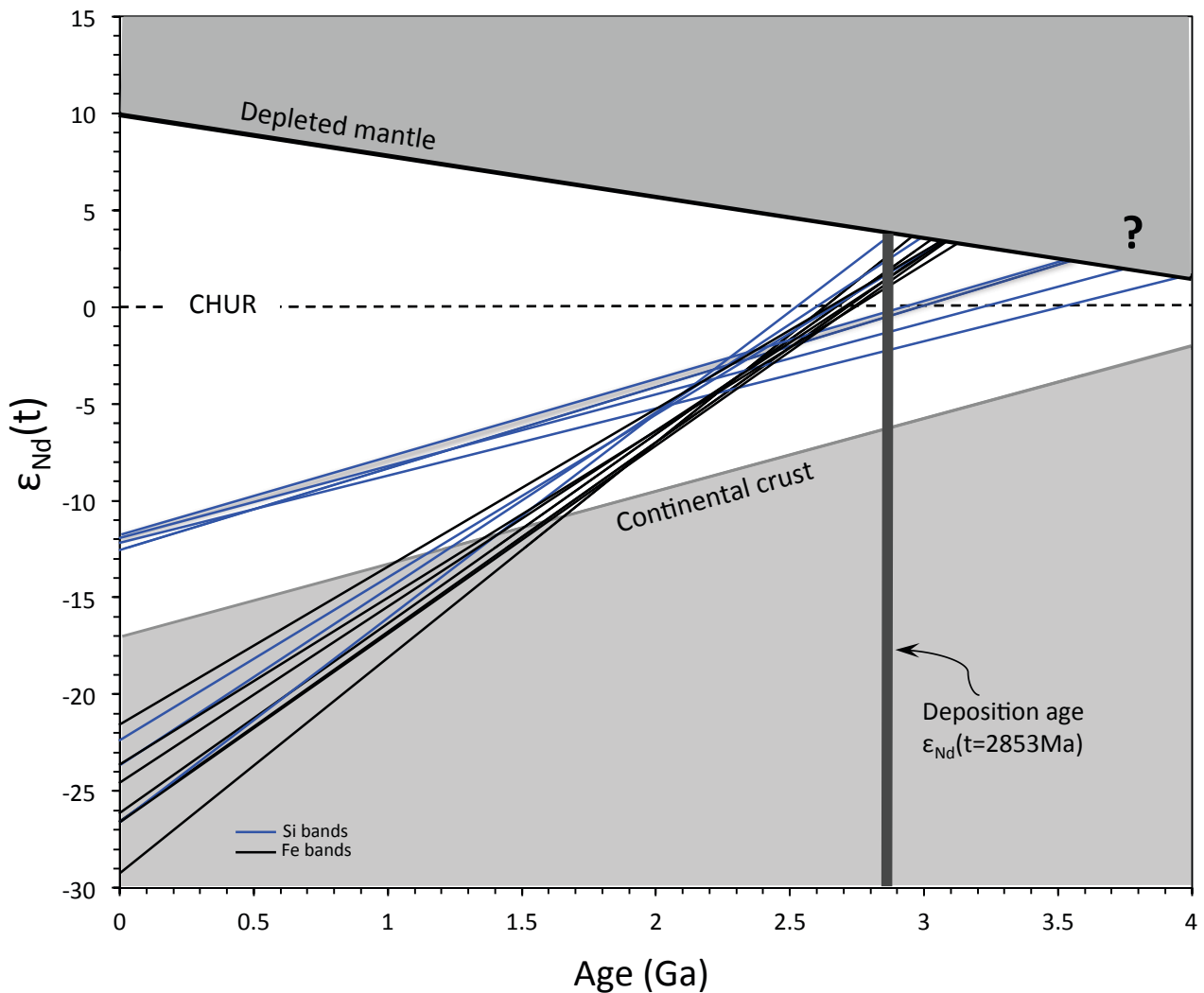
3. Depositional timing of Neoarchaean turbidites of the Slave craton - recommended nomenclature and type localities

3.1. Introduction

The nature of Archaean tectonics is largely surmised from the preserved igneous record, particularly from the geochemistry of basalts, komatiites, and tonalite-trondhjemite-granodiorite (TTG) gneisses/plutons (Kröner and Layer, 1992; Fan and Kerrich, 1997; Arndt et al., 2001; Sharma and Pandit, 2003; Condie, 2004; Bédard et al., 2013), geophysical experiments (e.g., Chen et al., 2009), and mineral inclusions in diamonds from the subcontinental lithosphere (e.g., Shirey and Richardson, 2011). The accumulation of Archaean clastic sedimentary rocks reflects orogenic uplift, erosion, extensional deformation, subsidence and accompanied basin opening; however, due to common notions of post-metamorphic and structural overprinting, they remain under studied. Further to this, Archaean sedimentary rocks lack fossils, and thick siliciclastic accumulations generally lack any kind of unique stratigraphic marker horizon. As such, basin models and tectono-stratigraphic correlations within and between Archaean cratons remain, for the most part, subjective.

Unlike strata in Phanaerozoic orogens, Archaean sedimentary successions lack fossils and as a result U-Pb zircon geochronology in preserved tuff beds, or detrital zircons in clastic sedimentary rocks, has evolved as the key discipline to help establish the timing of deposition and help establish more robust regional correlations (e.g., Davis et al., 1990; Fedo et al., 2003; Ferguson et al., 2005; Kositcin et al., 2008; Ootes et al., 2009; Rasmussen and Fletcher, 2010; Cawood et al., 2012). This is wrought with challenges because the vast majority of Archaean sedimentary rocks represent a mixture of redeposited debris, where synchronous felsic volcanic rocks may not exist (e.g., no ash beds), synchronous volcanic ash can get intermixed with the turbidite flow and diluted, or deposited ash-beds can get reworked by turbidity currents. Second, detrital zircons provide an imperfect record, as maximum deposition ages may not reflect the youngest

single zircon or population of zircons in a sample, which could be millions to 10 of million years older than the actual deposition age. By combining the two approaches, however, some of the challenges with regional correlations and depositional environments can be resolved.

Within the Slave craton, the Yellowknife Supergroup contains some of the largest and best-preserved Archaean turbidite basins in the world (Henderson, 1970, 1972; Padgham and Fyson, 1992; Ferguson et al., 2005). Greywacke-mudstone sedimentary rocks, deposited by turbidity currents in a deep-sea environment are common in Archaean supracrustal successions (e.g., Lowe, 1980; Barrett et al., 1988; Windley, 1995; Haugaard et al., 2013). However, the Slave craton supracrustal stratigraphy consists of approximately 70% of these sedimentary rocks, which is unique amongst Archaean cratons (vs. Superior and Yilgarn for example), providing diverse insights into Archaean tectonic processes (Padgham and Fyson, 1992). The turbidites are often monotonous, but Ootes et al. (2009) have divided them into an older and younger package (I and II). The older includes the well-known Burwash Formation, which is spectacularly preserved in the south-central part of the craton (e.g., Henderson, 1970, 1972; Ferguson et al., 2005) and contains a number of interbedded ash beds that have been dated at ca. 2661 Ma (Bleeker and Villeneuve, 1995; Ferguson, 2002; Ferguson et al., 2005). The younger turbidites are locally distinctive as they contain interstratified banded iron formation (BIF); detrital zircon ages indicate these turbidites have maximum deposition ages younger than ca. 2630 Ma, and were deposited more than 30 million years after the Burwash Formation (Perhsson and Villeneuve, 1999; Bennett et al., 2005; Ootes et al., 2009). That recognition has fundamental importance for: 1) establishing a provenance record for the turbidites; 2) establishing regional correlations across the craton, which are critical in evaluating postulated tectonic evolution models (e.g., Davis et al., 2003; Helmstaedt, 2009), and; 3) temporally constraining the BIF deposition, allowing insight into the nature of early sea water and by analogy atmospheric and biospheric conditions at that time (e.g., Bekker et al., 2010; Haugaard et al., 2013).

To further evaluate the extent and absolute timing of the turbidite depositions, we report a new U-Pb zircon crystallization age for a previously undated ash bed in the type locality of the Burwash Formation and the first U-Pb zircon crystallization age of an ash

bed that is intercalated with the younger BIF-bearing turbidites. Three new U-Pb detrital zircon maximum depositional ages from turbidite sequences across the Slave craton, compliment the ash bed ages and previously determined detrital zircon ages.

Previously, the turbidites in the Slave craton have been assigned to the Duncan Lake Group, with the Burwash Formation as the type locality (Henderson, 1970, 1972). The results of this and previous studies now clearly distinguish the younger BIF-bearing turbidites from the older Duncan Lake Group. As such, we recommend new nomenclature, referring to these younger turbidites as the Slemon Group and recommend the use of a number of formation names and their type localities across the craton.

3.2. Geological setting

The Archaean Slave craton is well known for hosting exposures of the oldest evolved rocks in the world, the Acasta gneiss (e.g., Reimink et al., 2014), ca. 2.7 Ga greenstone belts and orogenic gold (e.g., Bleeker and Hall, 2007; Ootes et al., 2011), and kimberlite-hosted diamond deposits (e.g., Heaman and Pearson, 2010). However, the Slave craton is relatively unique as the supracrustal rock record is dominated by large and extensive Neoarchaean turbidite successions deposited over a minimum area of about 32,000 km^2 (Henderson, 1970, 1972; Ferguson et al., 2005; Bleeker and Hall, 2007; Ootes et al., 2009). The turbidite sequences are part of the Duncan Lake Group of the Yellowknife Supergroup (Fig. 3.1; Henderson 1970) and were deposited on top of or adjacent to older volcanic-dominated supracrustal rocks, namely the ca. 2740-2700 Ma Kam Group and the ca. 2660 Ma Banting Group (e.g., Helmstaedt and Padgham, 1986; Isachsen and Bowring, 1997). The turbidites include the archetypal, up to 5 km thick, Burwash Formation (Henderson, 1970, 1972; Ferguson et al., 2005).

Felsic ash tuff beds are preserved within the Burwash Formation turbidites and have been dated by U-Pb zircon, providing a robust constraint on the time of turbidite deposition at 2661 ± 2 Ma, determined by isotope dilution thermal ionization mass spectrometry (ID-TIMS; Bleeker and Villeneuve, 1995; Ferguson, 2002). While the greywacke-mudstone turbidites are commonly monotonous, they are locally distinctive as they contain interstratified oxide-silicate BIF and were historically considered correlative to the Burwash Formation (e.g., Bostock, 1980, Padgham, 1991; Henderson, 1998;

Jackson, 2001). The advent of U-Pb detrital zircon studies that utilize micro-analytical techniques allowed for statistically robust maximum deposition ages to be determined from turbidites in the central and western parts of the craton. That work showed that some of the turbidites, particularly those with interbedded BIF, were deposited 30 million years after the "BIF-free" Burwash Formation (Pehrsson and Villeneuve, 1999; Bennett et al., 2005; Ootes et al., 2009). The three most precise maximum deposition ages from the young turbidites include a concordant 2629 ± 2 Ma date, determined by U-Pb zircon (ID-TIMS) from a Damoti Lake sample (Pehrsson and Villeneuve, 1999), a concordant 2620 ± 5 Ma date, determined by U-Pb zircon ID-TIMS from a Beechy Lake sample (Villeneuve et al., 2001), and a 2625 ± 6 Ma weighted mean age, determined from multiple analyses on single zircons analyzed using the sensitive high-resolution ion microprobe (SHRIMP) on a sample from Russell Lake (Ootes et al., 2009). Other maximum deposition ages have been determined from a greywacke in the central part of the craton at Point Lake (2615 ± 13 Ma), and from greywackes in the western part of the craton near the Emile River (2637 ± 10 Ma; Ootes et al., 2009), and in the vicinity of Kwejinne Lake (2634 ± 8 Ma, 2636 ± 3, 2637 ± 4 Ma; Bennett et al., 2005, 2012). An age of 2616 ± 3 Ma is reported for turbidites in the High Lake area in the northern Slave craton (Henderson et al., 1994) and a 2612 ± 1 Ma date is reported for a lithic tuff bed within turbidites at Wheeler Lake in the southwestern Slave craton (Isachsen and Bowring, 1994); the supporting data for these latter two reported ages has not been published. Other previously reported, less statistically robust maximum deposition age data are summarized in Ootes et al. (2009).

Both the older and younger turbidites have been locally to extensively intruded by granitic plutons. The Defeat Suite plutons have been dated between ca. 2635 to 2620 Ma and cross-cuts isoclinal folds (F_1) in the Burwash Formation (Davis and Bleeker, 1999). The Defeat Suite crystallization ages approximate the maximum deposition ages recorded in the younger BIF-bearing turbidites (e.g., Davis et al., 2003; Bleeker and Hall, 2007; Ootes et al., 2009). This is a key constraint, indicating that the younger turbidites post-date the F_1 event recorded in the older turbidites. Younger plutonic suites, such as Concession Suite (ca. 2610-2600 Ma) and later granite bloom (ca. 2600 to 2580 Ma), intrude both the older and younger turbidite packages (e.g., van Breemen et al., 1992;

Davis et al., 1994; Davis and Bleeker, 1999; Bennett et al., 2005; Ootes et al., 2005). The granite bloom coincided with regional greenschist- to granulite facies metamorphism (e.g., Davis and Bleeker, 1999; Bethune et al., 1999; Pehrsson et al., 2000; Bennett et al., 2005; Ootes et al., 2005). The depositional setting of the Burwash Formation is thought to be a rifted arc basin (Ferguson et al., 2005) whereas the depositional setting for the younger BIF-bearing turbidites is unclear. Previously proposed depositional models include a passive margin to foreland basin (Pehrsson, 2002), an accretionary wedge setting (Bennett et al., 2005), and a continental back-arc basin adjacent to an active Defeat suite magmatic arc (Ootes et al., 2009).

3.3. Methods

Approximately 1-1.2 kg of rock material was selected for each of the fine-grained turbidite samples. Each sample was cut down to small chips with a rock saw and divided into three batches that subsequently were crushed in a tungsten carbide puck mill. Each batch was crushed with 10-30 sec intervals and for each time sieved with a 70 mesh (210 micron) disposable nylon until all rock debris was sieved. The crushed and sieved rock material was processed on a Wilfrey Table to obtain a heavy mineral concentrate and then, multiple passes (up to 0.4 Amperes) on a Frantz magnetic barrier separator to remove moderately to strongly magnetic grains. The non-magnetic Frantz fraction was then added to a Methylene Iodide heavy liquid with specific gravity of 3.3 g/cm^3 for further density separation.

The recovered zircon grains were handpicked, secured in an epoxy mount, and subsequently polished. Due to minimum material recovered from the tuff bed at Slemon Lake, the crushed fraction was wash panned over multiple steps ending in a head fraction, a second head fraction, and a tail fraction before hand picking. The majority of the zircons were found in the first head fraction with only minor in the second head fraction. No zircon grains were recovered in the tail fraction. Cathodoluminescence (CL) imaging of zircon grains was obtained using a scanning electron microscope (Zeiss EVO LS15 EP-SEM) equipped with a cathodoluminescent and backscattered detectors.

U-Pb isotopic data were obtained at the University of Alberta and were acquired using a Nu Plasma I multi-collector inductively coupled plasma mass spectrometer (ICP-MS)

coupled to a New Wave laser ablation (LA) system with an operating wavelength of 213 nm and energy density of 2-3 J/cm^2. The laser spot diameter was set to 20 μm. Both the full machine parameters and measurement protocols are outlined in Simonetti et al. (2005, 2006). Two zircon standards were analyzed throughout each analytical session; the 1830 Ma LH94-15 zircon (Ashton et al., 1999) was used to correct U/Pb fractionation and an in-house zircon (OG1) with U-Pb TIMS age of 3465.4 ± 0.6 Ma (Stern et al., 2009) was analyzed as a blind standard. The weighted mean ^{207}Pb/^{206}Pb ages of the analyzed OG1 are presented in the supplementary data files (Appendix E). All analytical sessions of the OG1 overlap within analytical uncertainty of the accepted TIMS age of 3465.4 ± 0.6 Ma. However, the exception is for the Courageous Lake greywacke and is dealt with below.

3.4. Sample description and results

All U-Pb zircon data tables are presented in Appendices A-D and the results of the standards are presented in Appendix E.

3.4.1. Ash tuff bed – Slemon Lake turbidites

A 2-3 cm thick, fine- to very fine-grained, felsic-to-intermediate ash tuff bed occurs within the greywacke-mudstone turbidites at Slemon Lake (Figs. 3.2A, 3.2B, 3.2C). The turbidites are BIF-bearing and well-exposed ~0.8 to 1.2 m thick BIF is preserved approximately 1 m below the tuff bed (Fig. 3.2D). The ash bed is traceable for about 15 m along strike and is readily distinguished by having a bleached yellow colour relative to the darker greywacke (Figs. 3.2A and 3.2B). The bed has a relatively sharp base and a more disturbed upper contact along the bedding planes with the underlying and overlying greywacke beds (Fig. 3.2B). The upper contact represents well-developed load structures as a result of soft sediment deformation (white arrows Fig. 3.2B). The tuff shows no sign of reworking and redeposition and it contains randomly distributed fine-grained quartz fragments set in a very fine-grained quartz, biotite, chlorite, and K-feldspar matrix (Fig. 3.2C). A weak foliation is defined by biotite and chlorite.

A sample of the ash bed was collected and separated from surrounding greywacke and mudstone prior to crushing. Zircons are relatively scarce in the ash bed, compared to typical greywacke samples. The individual zircons are ~50 to 80 μm in size and are mostly subhedral with a stubby to weakly prismatic habit (Fig. 3.2E). The colour ranges from colourless to pale pink to brown. They are relatively free of inclusions and have only minor growth zonations, as indicated by electron backscatter imaging (Fig. 3.2E). The zircons were analyzed by LA-MC-ICP-MS and all of the zircon grains analyzed (n=17) are moderatly discordant and a regression line through the data yields an upper intercept age of 2617.2 ± 4.7 Ma and a lower intercept of 6 ± 28 Ma (Fig. 3.3A). A weighted mean $^{207}Pb/^{206}Pb$ age calculation yields an indistinguishable date of 2616.6 ± 3.5 Ma (Fig. 3.3B). When considering only the six most concordant grains in the data set (>92.7% concordant), a best-fit discordia line yields an upper intercept age of 2620.4 ± 5.7 Ma (lower intercept at 0 Ma), and a weighted mean $^{207}Pb/^{206}Pb$ age of 2620.4 ± 5.5 Ma (Figs. 3.3C and 3.3D). We interpret that the ash bed was deposited at 2620 ± 6 Ma, and also record the depositional age of the interleaved turbidites.

3.4.2. Ash tuff bed – Burwash Formation turbidites (Road to Dettah)

On the northeast side of Yellowknife Bay between the Yellowknife Bay and Hay Lake (along the road between the Ingraham Trail and the town of Dettah), outcrops of the Burwash Formation turbidites contain distinctive 2-3 cm thick ash tuff beds in association with the turbidites (Fig. 3.4). At the studied locality (Stop 33 in Bleeker et al., 2007), turbidite beds progressively thin from 1 m thick sand-dominated beds to 5 cm thick mud beds over a lateral, across strike distance of 30 m. The ash beds occur within the thin, mudstone-dominated beds at the north end of the outcrop. The main ash bed is accompanied by ultrafine (~1 mm thin) ash and mud lamina (Figs. 3.4A and 3.4B). The ash bed and enveloping mudstones and thinner ash beds are weakly crenulated by a high-angle second generation foliation (Figs. 3.4A and 3.4B). Oblique-striking glacial striae are also preserved on the outcrop (Fig. 3.4A). The ash bed comprises euhedral quartz grains (~0.2 to 0.3 mm) set in a very fine-grained groundmass of quartz, chlorite, and mica (Fig. 3.4C). The zircons (Fig. 3.4D) are homogeneous and predominantly occur as

elongate slender prisms. Some contain various oxides and other mineral inclusions and few are cracked and fragmented.

The U-Pb ID-TIMS results of three zircon grains from the ash bed (Appendix Am) reveal that the grains are relatively low in U are concordant to slightly reversely discordant, but overlap the Concordia curve within analytical uncertainty (Fig. 3.4E). A best fit line through the data intersects the concordia curve, yielding an upper intercept age of 2652.4 ± 2.9 Ma (Fig. 3.4E).

3.4.3. Greywacke beds – Goose Lake and Courageous Lake turbidites

Greywacke samples from Goose Lake in the east and Courageous Lake in the east-central part of the Slave craton share typical textural and mineralogical features. They are fine- to medium-grained (~0.2-0.5 mm), and contain quartz, biotite, chlorite, K-feldspar, and minor plagioclase. The existence of biotite and chlorite, but no garnet, corresponds to metamorphism in the biotite zone of greenschist facies.

An approximately 0.8 m thick piece of drill core intersection of greywacke (RH18140) from the bottom part of a 100.4 m deep drill hole (#12GSE140) was collected at Goose Lake (Figs. 3.1A and 3.5A). The sample underlies the base of the lowest BIF horizon and is part of a ~4 m thick BIF bearing greywacke-mudstone unit (Fig. 3.5A). This is the lowest stratigraphic unit intersected by drilling and therefore likely represents the oldest interval of the drilled part of Goose Lake turbidites. The detrital zircons from the greywacke are euhedral to subhedral with a rounded to subrounded-to-prismatic habit (Fig. 3.5B). They range between 30-180 μm in size and vary in colour from clear to pale pink to brown and dark brown, with few having a cloudy appearance. Growth (oscillatory) zoning and mineral inclusions are common (Fig. 3.5B). Selected zircons were analyzed by LA-MC-ICP-MS.

The Goose Lake U-Pb detrital zircon results reveal variable zircon populations, representing multiple sources (Fig. 3.5C). The analyzed zircons fall mostly in the age range of ca. 2760 to 2660 Ma, with probability peaks at ca. 2705 Ma and 2670 Ma (Fig. 3.5D), consistent with derivation from the underlying volcanic rocks (van Breemen et al., 1992; Isachsen and Bowring, 1994, 1997; Villeneuve et al., 2001; Sherlock et al., 2012). Five older grains also occur within the sample (3074 ± 15 Ma, 2849 ± 16, 2820 ± 16 Ma,

2814 ± 16 Ma and 2803 ± 15 Ma; Figs. 3.5B and 3.5D). The youngest detrital zircon grain at Goose Lake yields a ^{207}Pb/^{206}Pb age of 2621 ± 18 Ma (1.3% discordance, Figs. 3.5B and 3.5D), which is interpreted as the maximum deposition age of the sample.

A greywacke sample (13AB2206A) was collected from outcrop south of Courageous Lake and east of Matthews Lake (Fig. 3.6A), where the turbidites were deposited on 2671 +5/-4 Ma felsic volcanic rocks and are intruded by 2613 +6/-5 Ma granitic rocks (Moore, 1956; Dillon-Leitch, 1981; Villeneuve et al., 1993). These turbidites lack interbedded BIF. The sample was collected from the coarsest greywacke near the base of the turbidite succession, just above the contact with the underlying rhyolite and basalt (Fig. 3.6A). The zircons recovered are morphologically similar by description to those from the Goose Lake sample, and range from 30 to 120 mm in their longest dimension, with a fraction of the recovered zircons being highly fragmented (Fig. 3.6B). Selected zircons were analyzed by LA-MC-ICP-MS.

The U-Pb detrital zircon results from the Courageous Lake sample reveals variable age populations (although less scattered than for Goose Lake) representing multiple sources (Fig. 3.7A). All of the analyzed grains are <10% discordant, reflecting minimum Pb loss in these sedimentary rocks. The results indicate that 61 out of 69 grains have ages between ca. 2735 and 2660 Ma (Fig. 3.7B). There are three probability peaks within this interval at ca. 2720, 2685, and 2665 Ma (Fig. 3.7B). The youngest grain at Courageous Lake is 2626 ± 14 Ma (9.7% discordance) and the oldest is 2813 ± 13 (5% discordance) (Figs. 3.6B and 3.7B). The weighted average of the four youngest grains yields a ^{207}Pb/^{206}Pb age of 2635 ± 7 Ma (Fig. 3.7C). This age may be on the young side since the measurements on the OG1 standard during this data acquisition yield a weighted average of 3455.5 ± 4.3 Ma, which fall outside the analytical uncertainty of the 3465.4 ± 0.6 Ma (TIMS) age of OG1 (see Appendix E).

3.4.4. Ferruginous bed - Point Lake turbidites

Within the turbidites on the northeast side of Point Lake, 1 to 5 cm thick beds of mafic-to-intermediate clastic sediments are found intercalated with BIF up to 0.5 m thick (Figs. 3.8A and 3.8B). A more thorough petrographic and geochemical study of these beds can be found in Haugaard et al. (in review, chapter 4). The sedimentary beds differ from the

greywackes in that they have about 25-30% modal content of coarse-grained ferro-hornblende throughout. Still, they contain randomly dispersed biotite flakes and fragmented quartz and, occasionally, feldspar laths. These beds are concordant and folded and deformed together with the BIF units (Fig. 3.8A). They contain approximately the same concentration of zircon as the more typical greywackes. The zircons range from ~80 to 150 μm in size (Fig. 3.8C) and from clear and colorless to pale and medium brown in colour. The pale brown zircons often show a cloudy appearance. A major part of the zircons show well-developed oscillatory zonation patterns with an elongated prismatic to stubby habits (Fig. 3.8C). Fragmentation and intense corroded edges of some of the zircons can also be viewed in Fig. 3.8C.

The U-Pb detrital zircon results are plotted in Figs. 3.9A and 3.9B and reveal a zircon population that is generally younger than those in the Goose Lake and Courageous Lake greywacke samples. Most of the zircons have dates that fall into two major age populations that correlate well with the timing of Kam and Banting group volcanism. In addition, there is a younger age peak at ~2610 Ma (Fig. 3.9B). The five youngest (<10% discordant) grains have a weighted mean $^{207}Pb/^{206}Pb$ age of 2608 ± 6 Ma (Figs. 3.9C and 3.9D).

3.5. Discussion

3.5.1. Recommended Nomenclature for Neoarchaean turbidites of the Slave craton

There is now enough age control to clearly separate the older turbidites from the younger BIF-bearing turbidites in the Slave craton. The Burwash Formation turbidites were deposited between ca. 2661 Ma and 2652 Ma, as determined from crystallization ages of ash beds intercalated with the greywacke-mudstone turbidites (Figs. 3.3 and 3.4; Bleeker and Villeneuve, 1995; Ferguson et al., 2005; this study). The F_1 structures identified in the Burwash Formation turbidites are cross-cut by Defeat Suite plutons between 2635 and 2620 Ma (Fig. 10; Davis and Bleeker, 1999). The new 2620 ± 6 Ma ash bed crystallization age in the younger BIF-bearing turbidites (Figs. 3.2 and 3.3) indicate these sedimentary rocks either post-date, or were deposited synchronously with the intrusion of the Defeat Suite plutons; these sedimentary rocks were deposited after uplift and crustal

shortening of the older Burwash Formation turbidites. These two chronologically distinct turbidite sequences, therefore, represent separate depositional environments (Ootes et al., 2009).

We recommend a new nomenclature for these two distinct turbidite sequences and their type localities. In Phanerozoic, or flat lying Precambrian stratigraphy, the nomenclature of a formation or group generally requires a base, top, and type-section. However, such constraints are rarely preserved in Archaean stratigraphy; the voluminous nature of the turbidites in the Slave craton and the multiple generations of structural overprinting generally make such criteria impossible to identify. In addition, without a base or top, a measured section is only a minimal assumption of the overall thickness of a unit. Instead, for the turbidites in the Slave craton, we propose that sample locations that have been dated should be considered the type locality for the turbidites in question, and the formation name assigned should be tied to the dated location and any turbidites traceable from that location. If the location has not been dated it should not be formally considered.

We recognize formations that are correlatable to the Burwash Formation and assign these to the Duncan Lake Group (Henderson, 1972; Helmstaedt and Padgham, 1986). Utilizing new and previously published ash tuff crystallization ages and detrital zircon maximum deposition ages we recommend the young BIF-bearing turbidites be referred to as the Slemon Group and upgrade type localities with recommended formation names (see Fig. 3.10 and Table 3.1 for an overview).

3.5.2. Duncan Lake Group

The Duncan Lake Group terminology first appeared in Henderson (1975) and was used to refer to all of the sedimentary rocks that overlay the Kam Group volcanic rocks at Yellowknife. This included the Burwash Formation and Jackson Lake Formation (Henderson, 1970). Henderson thought these sedimentary rocks were older than the Banting Group volcanic rocks, however, Helmstaedt and Padgham (1986) identified that these sedimentary rocks are in fact younger than, or laterally equivalent to the Banting Group. They also further identified that the Jackson Lake Formation conglomerates and sandstones are much younger and should not be included in the Duncan Lake Group.

Subsequent U-Pb zircon dating has further corroborated this latter interpretation (e.g., Isachsen et al., 1991). Therefore, the Duncan Lake Group and the Burwash Formation specifically refer to the thick accumulation of turbidites east of Yellowknife Bay (e.g., Henderson, 1970, 1975; Ferguson et al., 2005).

3.5.2.1. Burwash Formation

The archetype of the Duncan Lake Group is the renowned Burwash Formation, which has been investigated in detail on the eastern side of Yellowknife Bay (Henderson, 1970, 1972) and from the Hearne Lake area (Ferguson et al., 2005). The Burwash Formation, which is estimated to be about 4.5-5 km in thickness (Henderson, 1970), forms a large synclinorium between Yellowknife and the Sleepy Dragon Complex to the east, and continues south and potentially east of this basement culmination (e.g., Stubley, 2005). The type section is south of Burwash Point in Yellowknife Bay. Each turbidite cycle (greywacke-mudstone) is on average ~0.3-0.4 m thick. In the type area, the rocks have experienced low-grade metamorphism, up to biotite grade; however elsewhere, where proximal to intrusive contacts they have been metamorphosed to higher temperatures, where andalusite, cordierite, and sillimanite is locally present (Henderson, 1970).

Although the date of ca. 2652 Ma from the ash bed in this study (Fig. 7) is younger than the 2661 Ma presented by Bleeker and Villeneuve (1995), it is still comparable. Noteable is that our 2652 Ma age is very close to the detrital zircon age obtained from Mosher Lake (Ootes et al., 2009), and collectively these dates show that the turbidites are likely relatively close to the upper part of Duncan Lake Group (Fig. 3.10 and Table 3.1).

3.5.2.2. Clover Lake Formation

A succession of turbiditic sedimentary rocks that occur just north of Clover Lake in the Hope Bay greenstone belt has been described by Sherlock et al. (2012; Fig. 3.1A). The sedimentary sequence there contains well-bedded greywacke and mudstone facies occasionally with conglomerates of locally derived clasts. The sedimentary succession has been intruded and is interbedded with the Clover Lake felsic volcanic suite, primarily

calc-alkaline flow-banded rhyolites. These rhyolites show distinct wet-sediment interaction texture and suggest emplacement of the volcanics into unlithified wet sediment. A U-Pb TIMS age for one of the rhyolite flows in this section is 2662.7 + 3 .4/ – 2.8 Ma, which is viewed as the minimum age of the turbidites in the Hope Bay greenstone belt (Sherlock et al., 2012).

3.5.2.3. Itchen Lake Formation

The Itchen Formation was named by Bostock (1980) to refer to greywacke-mudstone turbidites in the central part of the Slave craton that do not contain BIF (Bostock, 1980; Henderson, 1998). Bostock (1980) interpreted that the Itchen Formation is younger than the Contwoyto Formation, because the latter is more proximal to the underlying volcanic belts. Ootes et al. (2009) analyzed 58 detrital zircons by the U-Pb SHRIMP method and determined a maximum deposition age of 2658 ± 8 Ma for the Itchen Formation, indicating that the Itchen Formation is likely older than the BIF-bearing Contwoyto Formation. We recommend the Itchen Formation be, from here forward, recognized as the Itchen Lake Formation, and the type locality be the location of the greywacke sampled for detrital zircon analyses (Ootes et al., 2008, 2009). Based on the maximum deposition age, we tentatively retain the Itchen Lake Formation within the Duncan Lake Group, although it should be recognized that the nature of detrital zircon results allows this formation to potentially be younger.

3.5.2.4. Mosher Lake Formation

Greywacke-mudstone turbidites are well preserved at Mosher Lake in the southwestern Slave craton (Ootes and Pierce, 2005; Ootes et al., 2006, 2008, 2009). A total of 58 detrital zircons from a greywacke sample were dated by the U-Pb SHRIMP method and the youngest yielded a maximum deposition age of 2651 ± 6 Ma (Ootes et al., 2006, 2009). These turbidites do not contain interbedded BIF. We recommend referring to these turbidites as the Mosher Lake Formation and the type locality should be considered the location for the detrital zircon sample (Ootes et al., 2006, 2008, 2009). Based on the maximum deposition age, we tentatively assign these turbidites to the Duncan Lake

Group. Although the nature of detrital zircon results allow that these turbidites could be younger (Ootes et al., 2009), structural data presented in Fyson and Jackson (1991) establish that these turbidites contain a deformation fabric that pre-dates fabrics preserved in the Slemon Lake Formation turbidites (below) that occur to the west at Russell and Slemon lakes.

3.5.3. Slemon Group

3.5.3.1. Slemon Lake Formation
The Slemon Lake tuff, with its single-age zircon population, record coeval volcanic input into the chemical and clastic sediment dominated basin at 2620 ± 6 Ma (Figs. 3.2 and 3.3). This date is the best estimate of the depositional age of this tuff bed and constrains the depositional timing of the turbidites and the interbedded BIF. This is the only ash tuff bed discovered and dated in the younger BIF-bearing turbidites in the craton. We recommend referring to these as the Slemon Lake Formation, and this locality should also be considered as the type locality for the young BIF-bearing turbidite sequences in the suggested Slemon Group. The age is similar to or only slightly younger than dates reported for the Defeat Suite plutons (Davis and Bleeker, 1999) and likely the precursor sediment was pyroclastic ash derived from Defeat-related volcanism in the hinterland of the basin.

These BIF-bearing turbidites continue to the east to Russell Lake (Jackson, 2001) where a greywacke produced a U-Pb detrital zircon maximum deposition age of 2625 ± 6 Ma (Ootes et al., 2009). This further demonstrates that these laterally extensive deposits were all formed after uplift and deformation of the turbidite formations in the Duncan Lake Group.

3.5.3.2. Goose Lake Formation (Goose Lake)
The youngest detrital zircon age of 2621 ± 18 Ma (1.3% discordance, Figs. 3.5B and 3.5D) for the Goose Lake greywacke is the only grain of that age that has been recovered from the sample. This date is, however, consistent with another concordant detrital zircon date of 2620 ± 5 Ma (ID-TIMS) reported by Villeneuve et al. (2001) from a greywacke

sample in the Beechy Lake turbidites on the western flank of the Back River volcanic complex. Furthermore, euhedral-to-subhedal zircons from a fine-grained felsic sill that intruded the Beechy Lake turbidites yielded an upper intercept at 2637 +8/-6 Ma placing a minimum age on the deposition of these turbidites (Villeneuve et al., 2001). However this best fit was done on four zircons only and unfortunately none of them were either concordant nor had overlapping error ellipses (Fig. 3.4, Villeneuve et al., 2001). Nevertheless, the U-Pb zircon dates from Beechy Lake together with the 2621 ± 18 Ma age from Goose Lake confirm the belonging of these BIF-turbidites to the suggested Slemon Group and furthermore correlate the eastern turbidite-BIF sequences with the ones from the central and western Slave craton.

We recommend that the BIF-bearing turbidites in the Goose Lake area be referred to as the Goose Lake Formation (Fig. 3.10 and Table 3.1). While the Mesoarchaean Central Slave Cover Group and the Mesoarchaean to Hadean Central Slave Basement Complex rocks are not known to be preserved in the eastern part of the craton (Bleeker et al., 1999), the five zircon grains from Goose Lake dated between 3074 ± 15 Ma and 2803 ± 15 Ma (Fig. 3.5D) indicate that older basement was in the source area of the sediments.

3.5.3.3. Salmita Formation (Courageous-MacKay lakes)

In the central part of the Slave craton, greywacke-mudstone turbidites were deposited stratigraphically on top of the Courageous-MacKay lakes greenstone belt. These turbidites continue well to the east where they may be correlative to the Beechy Lake turbidites that overly the Hackett River greenstone belt (Stubley, 2005; Villeneuve et al., 2001). The large number of detrital zircon age populations for the Courageous Lake sample represent multiple sources with a dominant input of detritus at ca. 2720, 2685, and 2665 Ma (Fig. 3.7B). These ages are consistent with the timing of volcanism in the underlying volcanic belt and volcanic rocks preserved elsewhere in the craton (van Breemen et al., 1992; Isachsen and Bowring, 1997; Sherlock et al., 2012).

The youngest zircon grain identified in the sample is 2626 ±14 Ma, although it is modestly discordant (9.7% discordance, Figs. 3.6B and 3.7B). The weighted average of the four youngest grains yields a $^{207}Pb/^{206}Pb$ age of 2635 ± 7 Ma (Fig. 3.7C). This age may be on the young side since the measurements on the OG1 standard during this data

acquisition yield a weighted average of 3455.5 ± 4.3 Ma, which fall outside the analytical uncertainty of the 3465.4 ± 0.6 Ma (TIMS) age of OG1 (see Appendix E). However, we tentatively assign these turbidites as part of the younger Slemon Group. As many of the local geographic names are generally assigned to other stratigraphic units in the area, we recommend the turbidites at this locality be referred to as the Salmita Formation, in recognition of the past-producing Salmita gold mine that is located just to the southwest of the sampled location.

3.5.3.4. Contwoyto Lake Formation (Point Lake)

These BIF-bearing turbidites are exposed on the northern and eastern side of Point Lake (Henderson, 1998). Bostock (1980) coined the name Contwoyto Formation and pointed out the occurrence of interbedded BIF, which distinguished these turbidites from the higher metamorphic-grade turbidites that were assigned to the Itchen formation further east (see Henderson, 1998). However, Bostock (1980) believed the Contwoyto formation to be older than Itchen formation due to its more proximal nature to volcanic belts. Using detrital zircons, Ootes et al. (2009) suggested the BIF-bearing Contwoyto formation is actually younger than the BIF-absent Itchen formation. We recommend the name Contwoyto Lake Formation for BIF-bearing turbidites in this area, which is defined by the detrital zircon maximum deposition age of 2608 ± 6 Ma (Fig. 3.9D), and the previously reported youngest identified detrital zircon grain at 2615 ± 13 Ma (Ootes et al., 2009; see Fig. 3.10 and Table 3.1). As such, we recommend the name Contowyto Lake Formation for these BIF-bearing turbidites at Point Lake.

The ferruginous clastic sedimentary rock in this study contains a dominant zircon population (ca. 2720-2660 Ma), likely of Banting or Kam Group affinity (Fig. 3.9B). There is a probability trough at ca. 2640-2620 Ma, indicating only minimum input from the Defeat Suite (Fig. 3.9B). The youngest population, at ca. 2610 Ma, indicates a minor proportion of the zircons (n=5) may have been derived from the monzodioritic to granodioritic Concession Suite plutons (Davis et al., 1994, Figs. 3.9B, 3.9C, 3.9D and 3.10). The BIF-bearing turbidites of the Contwoyto Lake Formation either represent the upper part of Slemon Group turbidites, or may be a separate package of even younger turbidites.

3.5.3.5. Damoti Lake Formation

At Damoti Lake, greywacke-mudstone turbidites with interbedded BIF was informally named the Damoti formation by Pehrsson and Villeneuve (1999). They dated 15 detrital zircons by the TIMS method and discovered a single concordant grain at 2629 ± 2 Ma, and interpreted this as the maximum deposition age of the sample. This was the first demonstration of turbidites that were clearly younger than the 2661 Ma Burwash Formation of the Duncan Lake Group. We therefore recommend the BIF-bearing turbidites in the Damoti Lake area to be referred to as the Damoti Lake Formation, with the type locality being the sample location of Pehrsson and Villeneuve (1999).

3.5.3.6. Kwejinne Lake Formation

North of Slemon Lake and along the Snare and Emile rivers in the western Slave craton, greywacke-mudstone turbidites are extensively preserved. At Kwejinne Lake, Bennett et al. (2005) collected a greywacke sample and dated 100 detrital zircons by the LA-ICP-MS method, the youngest of which yielded a maximum deposition age of 2634 ± 8 Ma. These greywackes do not contain interbedded BIF, but they do continue to the east where they are preserved at higher metamorphic grades. There they are preserved as migmatites (metaxite and diatexite) and contain abundant BIF enclaves. Detrital zircon cores, derived from a diatexte with a sedimentary protolith, were dated by Bennett et al. (2012) and the youngest of 68 analyses yielded a maximum deposition age of 2636 ± 3 Ma. Northwest of Kwejinne Lake, along the Emile River at Mattberry Lake, Archaean greywacke-mudstone turbidites underlie Proterozoic quartzite and quartz pebble conglomerate and both were deformed together in the Proterozoic (Fyson and Jackson, 2008; Jackson, 2008; Bennett et al., 2012). Detrital zircons from the Archaean greywacke were dated by the LA-ICP-MS method by Bennett et al. (2012) and the youngest grains of 79 analyses indicate a maximum deposition age of 2637 ± 4 Ma.

All three of the above samples share similar maximum deposition ages and are proximal to Kwejinne Lake, and we therefore recommend they be referred to as the Kwejinne Lake Formation. The type locality should be considered the location at

Kwejinne Lake dated by Bennett et al. (2005). While the maximum deposition ages are younger than the ca. 2661 Ma Burwash Formation of the Duncan Lake Group, the maximum deposition ages are comparable to the oldest Defeat Suite plutons (Davis and Bleeker, 1999). These turbidites locally contain interbedded BIF and occur along strike of the Slemon Lake Formation, and because they are younger than the youngest detrital zircons dated, we assign these to the Slemon Group.

3.5.3.7. Emile River Formation

In the western Slave craton, north of the Damoti Lake Formation, turbidites with interbedded BIF occur within the core of a Central Slave Basement Complex-bounded synclinorium (Ootes et al., 2008). Ootes et al. (2009) dated 66 detrital zircons from a greywacke sample by the SHRIMP method, and determined a maximum deposition age of 2637 ± 10 Ma. We recommend these turbidites be referred to as the Emile River Formation with the type locality being the detrital zircon sample location in Ootes et al. (2008, 2009). As these turbidites contain interbedded BIF and have a maximum deposition age distinctly younger than the 2661 Ma deposition age of Burwash Formation of the Duncan Lake Group, we tentatively recommend these be assigned to the Slemon Group.

3.5.3.8. Wheeler Lake Formation

Isachsen and Bowring (1994) report an age from an ash tuff, interbedded with BIF-bearing turbidites east of Wheeler Lake, of 2612 ± 1 Ma. Ootes et al. (2009) disputed this and interpreted that the dated unit was likely an intrusive sill that was dated in that study as the sample location could not be confirmed in the field and many porphyry sills occur in the area (Ootes and Pierce, 2005). However, since that time it has been confirmed that it was in fact an ash tuff bed that was sampled near Wheeler Lake and dated in that study (W. Fyson personal communication, 2010). Due to the new results from the Contowyto Lake Formation (above), the ca. 2612 Ma deposition age for the BIF-bearing Wheeler Lake turbidites is considered as permissible. We recommend referring to the turbidites in the Wheeler Lake area (Brophy, 1995; Ootes and Pierce, 2005) as the Wheeler Lake

Formation. The type locality for these should be considered as the location dated by Isachsen and Bowring (1994), on the southeast side of Wheeler Lake.

3.5.3.9. James River Formation (High Lake)

In the northern Slave craton, in the vicinity of High Lake, slates and siltstones as well as greywackes overly older volcanic belts (Jackson, 1985; Henderson et al., 1995, 2000). The mudstones and siltstones have long been considered to be younger than the greywackes and Henderson et al. (2000) indicate a deposition age (their unit Asl) of ca. 2616 to 2612 Ma. However, numerous plutons of similar age occur throughout the area and it is not clear from that work if the dated rocks represented felsic dykes or concordant sills, or interbedded felsic volcanic layers (Henderson et al., 2000). In addition, no interbedded BIF have been reported from these sedimentary rocks. Therefore, we cautiously assign these sedimentary rocks to the Slemon Group. Regardless of their age, we recommend they be referred to as the James River Formation. The type locality should be considered the location with reported date from a concordant dacitic porphyry body at 2616 ± 3 Ma (Henderson et al., 1995).

3.5.4. Composite stratigraphy

Depositional ages and field relations among the turbidites in the Slave craton shows that these can be separated into an older (>2640 Ma) Duncan Lake Group and a younger (<2640 Ma) Slemon Group (Fig. 3.10). Since the older turbidites are uplifted, folded and later cut by the ca. 2628 Ma Defeat pluton, we arbitrary put the border between the two groups at 2640 Ma, as illustrated in Fig. 3.10. This age may be slightly older or younger. The backbone of this new stratigraphy is the depositional ages of the ash tuff beds interbedded with the greywacke-mudstone turbidites. The Burwash Formation of the Duncan Lake Group was deposited between ca. 2661 Ma and 2650 Ma whereas the new ca 2620 ± 6 Ma ash bed defines the age of the younger BIF-bearing turbidites of the Slemon Group. This age indicates that these turbidites either post-date, or were deposited synchronously with the intrusion of the ca. 2635-2620 Ma Defeat Suite plutons (Fig.

3.10). The turbidites of the suggested Slemon Group were deposited after uplift and crustal shortening of the older Burwash Formation turbidites. This interpretation is further supported in the detrital zircon record of the Slemon Group BIF-turbidites (see Figs. 3.5D, 3.7B and 3.9B and also Figs. 5 and 8 in Ootes et al., 2009) that shows a general minor input of zircons derived from juvenile (~2620 Ma) sources. Rather, the greywackes of the Slemon Group contain detrital zircons that are similar in age to zircons in the older volcanic belts, indicating further uplift and erosion of those belts, or recycling of the Duncan Lake Group turbidites into the Slemon turbidite basin.

3.5.5. Future considerations

It is evident from the discussion above that the Point Lake, Wheeler Lake and High Lake turbidites (Isachsen and Bowring, 1994; Henderson et al., 1995), may represent an even younger event of turbidite-BIF deposition and therefore we cannot exclude the potential existence of a third package of turbidites within the craton. Collectively, these dates may reflect minor contribution from the younger (2610-2600 Ma) Concession Suite. Unfortunately, however, the data from High Lake and Wheeler Lake is either not published or the date is reported without supporting analytical data. Consequently, the young dates from these locations need to be confirmed. Until these analytical and supporting field data are obtained, we retain all these sequence as the upper part of the Slemon Group.

Finding ash tuff beds within greywacke-mudstone turbidites is challenging as the ash beds are volumetrically minor and commonly only are a few cm thick. However, their importance in constraining the Neoarchaean stratigraphy of the Slave craton, and other Archaean cratons, is crucial for resolving regional stratigraphic relationships. More findings of these beds can produce better-constrained depositional ages of the many turbidite sequences in the craton. For example, the 2620 ± 6 Ma crystallization age of an ash bed presented in this study provides a critical date and horizon in further establishing stratigraphic relationships and evaluating tectonic processes across the Slave craton.

The Burwash Formation of the Duncan Lake Group has been well-studied (Henderson, 1970, 1972; Yamashita and Creaser, 1999; Ferguson et al., 2005), but the petrology of the Slemon Group has not been investigated to the same extent. Thorough

sedimentologically-focussed petrological work comparing the Duncan Lake and Slemon groups is recommended. In addition to the now-identified BIF association with the younger Slemon Group, such study should further reveal any petrological differences between these temporally distinct turbidite sequences. This would not only have profound importance on the crustal composition and tectonic development of the craton but would also help to characterize the depositional basins that accumulated these extensive turbidite deposits during the Neoarchaean.

3.6. Conclusions

The U-Pb LA-ICP-MS zircon results for tuff and sedimentary rock samples investigated in this study refine the depositional ages for Neoarchaean greywacke-dominated packages in the Slave craton. An ash tuff bed within the BIF-bearing turbidites at Slemon Lake yields a U-Pb zircon depositional age of 2620 ± 6 Ma. For the first time, this date constrains the depositional age for the BIF-bearing turbidites in the southwest of the Slave craton. A previously undated ash tuff bed in the Burwash Formation turbidites yields a U-Pb zircon age of 2650 ± 1.5 Ma. This new age is ca. 5 to 14 million years younger than previously reported ash tuff ages from the Burwash Formation, indicating a longer depositional time-frame for the Burwash Formation turbidites than previously considered.

At Goose Lake in the eastern Slave craton, the youngest zircon grain yields an age of 2621 ± 18 Ma (1.3% discordant). These are BIF-bearing turbidites and for the first time the depositional timing of turbidites can be linked from west to east across the craton. At Courageous Lake turbidites yield a maximum deposition age of 2635 ± 7 Ma. At Point Lake, coarse-grained mafic-to-intermediate sediment beds are intercalated with the BIF unit. The detrital zircons obtained from these beds define a maximum depositional age of 2608 ± 6 Ma, supporting that these are either distinctly younger than the ca. 2620 Ma BIF-bearing turbidites, or they are higher in the stratigraphic sequence.

The two new tuff ages, in concert with previously published data, allow the breakout of the younger BIF-bearing turbidite sequence from the Duncan Lake Group. The ca. 2661 to 2650 Ma Burwash Formation remains the archetype of the Duncan Lake Group and we propose the Itchen Lake Formation, Mosher Lake Formation, and Clover

Lake Formation should also be included within this group. The type localities for the formations are the dated sample locations. We propose the demonstrably younger, BIF-bearing turbidites, be referred to as the Slemon Group. The archetypal locality for the Slemon Group is the ash tuff sample site in the proposed Slemon Lake Formation. Using maximum deposition ages that are comparable and younger than the crystallization age of the tuff, we recommend a number of other formation names, their type localities being the sections with dated sample locations. Further petrological work on these two groups is recommended to help resolve depositional environments, and to further help the understanding of Archaean tectonic processes.

References

Arndt, N. T., Bruzak, G., and Reischmann, T., 2001. The oldest continental and oceanic plateaus: Geochemistry of basalts and komatiites of the Pilbara Craton, Australia. Geological Society of America Special Papers 352, 359–387.

Bédard, J. J., Harris, L. B., and Thurston, P. C., 2013. The hunting of the snArc. Precambrian Research 229, 20–48.

Bekker, A., Slack, J. F., Planavsky, N., Krapež, B., Hofmann, A., Konhauser, K. O., Rouxel O. J., 2010. Iron formation: The sedimentary product of a complex interplay among mantle, tectonic, oceanic, and biospheric processes. Economical Geology 105, 467–508.

Bennett, V., Jackson, V. A., Rivers, T., Relf, C., Horan, P., Tubrett, M., 2005. Geology and U–Pb geochronology of the Neoarchean Snare River terrane: tracking evolving tectonic regimes and crustal growth. Canadian Journal of Earth Science 934, 895–934.

Bennett, V., Rivers, T., Jackson, V.A. 2012. A compilation of U-Pb zircon primary crystallization ages from Paleoproterozoic southern Wopmay Orogen, Northwest Territories. Northwest Territories Geoscience Office, NWT Open Report 2012-003, 157 p.

Bethune, K. M., Villeneuve, M. E., Bleeker, W., 1999. Laser ^{40}Ar/^{39}Ar thermochronology of Archean rocks in Yellowknife Domain, southwestern Slave Province: insights into the cooling history of an Archean granite-greenstone terrane. Canadian Journal of Earth Sciences 36, 1189–1206.

Bleeker, W., Villeneuve, M. E., 1995. Structural studies along the Slave portion of the SNORCLE transect. In Cook, F., and Erdmer, P., eds. Slave–Northern Cordillera

Lithospheric Evolution (SNORCLE) Transect and Cordilleran Tectonics Workshop. Lithoprobe Report 44, 8–13.

Bleeker, W., Ketchum, J.W. and Davis, W.J. 1999. The Central Slave Basement Complex, Part II: age and tectonic significance of high-strain zones along the basement-cover contact. Canadian Journal of Earth Sciences, 36: 1111–1130.

Bleeker, W., Hall, B., 2007. The Slave Craton: Geological and Metallogenic Evolution, in Goodfellow, W.D., ed., Mineral Deposits of Canada: A synthesis of major Deposit-types, District Metallogeny, the evolution of geological provinces, and exploration methods. Geological Society of Canada, Mineral deposit division, Special Publication 5, 849-879.

Bleeker, W., LeCheminant, T., Davis, W.J., Buchan, K., Ketchum, J. Sircombe, K., Snyder, D., van Breemen, O., Ootes, L., 2007. Transect across the southwestern Slave craton: from Phanerozoic platform edge to the core of the Yellowknife Supracrustal Domain. Geological Association of Canada, Field Trip Guide Book A1, 232 p.

Bostock, H. H., 1980. Geology of the Itchen Lake area, District of Mackenzie. Geological Survey of Canada Memoir 391, 101 p.

Brophy, J.A., 1995. Additional evidence for syngenetic gold enrichment in amphibolitic banded iron-formation, Slave Province. In Exploration Overview 1995. NWT Geological Mapping Divi- sion, Department of Indian Affairs and Northern Development, pp. 3/6–3/7.

Cawood, P.A., Hawkesworth, C.J., Dhuime, B., 2012. Detrital zircon record and tectonic setting. Geology 40, 875-878.

Chen, C.W., Rondenay, S., Evans, R.L., Snyder, D.B. 2009. Geophysical Detection of relict metasomatism from an Archean (~3.5 Ga) subduction zone. Science, 326, 1089-1091.

Condie, K. C., 2004. Supercontinents and superplume events: distinguishing signals in the geologic record. Physics of the Earth and Planetary Interiors 146, 319–332.

Davies, D. W., Pezzutto, F., Ojakangas, R. W., 1990. The age and provenance of metasedimentary rocks in the Quetico Subprovince, Ontario, from single zircon analyses: implications for Archean sedimentation and tectonics in the Superior Province. Earth and Planetary Science Letters 99: 195–205.

Davis, W. J., Hegner, E., 1992. Neodymium isotopic evidence for the tectonic assembly of Late Archean crust in the Slave Province, northwest Canada. Contributions to Mineralogy and Petrology 111, 493–504.

Davis, W. J., Fryers, B. J., King, J. E., 1994. Geochemistry and evolution of late Archean plutonism and its significance to the tectonic development of the Slave craton. Precambrian Research 67, 207–241

Davis, W. J., Bleeker, W., 1999. Timing of plutonism, deformation, and metamorphism in the Yellowknife Domain, Slave Province, Canada. Canadian Journal of Earth Sciences 36, 1169-1187.

Davis, W., Jones, A., Bleeker, W., Grütter, H., 2003. Lithosphere development in the Slave craton: a linked crustal and mantle perspective. Lithos 71, 575–589.

Dillon-Leitch, H. C. H., 1981. Volcanic stratigraphy, structure and metamorphism in the Courageous-MacKay Lake greenstone belt, Slave Province, Northwest Territories: Unpublished M.Sc. thesis, University of Ottawa, Ottawa, ON, 169 p.

Fan, J., Kerrich, R., 1997. Geochemical characteristics of aluminum depleted and undepleted komatiites and HREE-enriched low-Ti tholeiites, western Abitibi greenstone belt: A heterogeneous mantle plume-convergent margin environment. Geochimica et Cosmochimica Acta 61, 4723–4744.

Fedo, C.M, Sircombe, K.N., Rainbird, R.H. 2003. Detrital zircon analysis of the sedimentary record. Reviews in Mineralogy and Geochemistry 53, 277–303.

Ferguson, M. E., 2002. Sedimentology and tectonic setting of the late Archean Burwash Formation, southern Slave Province. MS dissertation, Dalhousie University, Halifax.

Ferguson, M., Waldron, W. F., Bleeker, W., 2005. The Archean deep-marine environment: turbidite architecture of the Burwash Formation, Slave Province, Northwest Territories. Canadian Journal of Earth Sciences 42, 935-954.

Fyson, W. K., Jackson, V. A., 1991. Reorientation of structures near granitic plutons and orthogonal lineaments, Russell Lake supracrustal domain, southwestern Slave Province. Canadian Journal of Earth Sciences 28, 126-135.

Fyson, W.K., Jackson, V.A., 2008. Images of an unconformity, Mattberry Lake, NWT. Northwest Territories Geological Survey, NWT Open Report 2008-004, 27 p.

Haugaard, R., Frei R., Stendal, H., Konhauser, K., 2013. Petrology and geochemistry of the ~2.9 Ga Itilliarsuk banded iron formation and associated supracrustal rocks, West Greenland: Source characteristics and depositional environment. Precambrian Research 229, 150–176.

Heaman, L.M., Pearson, D. G., 2010. Nature and evolution of the Slave Province subcontinental lithospheric mantle. Canadian Journal of Earth Sciences 47, 369-388.

Helmstaedt, H., 2009. Crust–mantle coupling revisited: The Archean Slave craton, NWT, Canada. In Proceedings of the 9th International Kimberlite Conference. Edited by Stephen Foley, Sonja Aulbach, Gerhard Brey, Herman Grütter, Heidi Höfer, Dorrit Jacob, Volker Lorenz, Thomas Stachel and Alan Woodland. Lithos 112, 1055-1068.

Helmstaedt, H., Padgham, W. A., 1986. A new look at the stratigraphy of the Yellowknife Supergroup at Yellowknife, NWT: implications for the age of gold-bearing shear zones and Archean basin evolution. Canadian Journal of Earth Sciences 23, 454–475.

Henderson, J. B., 1970. Stratigraphy of the Archean Yellowknife Supergroup, Yellowknife Bay–Prosperous Lake Area, District of Mackenzie. Geological Survey of Canada Paper 70-26.

Henderson, J. B., 1972. Sedimentology of Archean turbidites at Yellowknife, Northwest Territories. Canadian Journal of Earth Sciences 9, 882-902.

Henderson, J. B. 1975. Sedimentology of the Archean Yellowknife Supergroup at Yellowknife, District of Mackenzie. Geological Survey of Canada, Bulletin 246, 62 p.

Henderson, J. B. 1998. Geology of the Keskarrah Bay area, District of Mackenzie, Northwest Territories. Geological Survey of Canada Bulletin 527, 122 p.

Henderson, J. R., Kerswill, J. A., Henderson, M. N., Villeneuve, M., Petch, C. A., Dehls, J. F., Okeefe, M. D., 1995. Geology, geochronology, and metallogeny of High Lake greenstone belt, Archean Slave Province, Northwest Territories. Geological Survey of Canada Current Research 1995-C, 97–106.

Henderson, J. R., Henderson, M. N., Kerswill, J. A., Dehls, J. F., 2000. Geology, High Lake greenstone belt, Nunavut. Geological Survey of Canada, Map 1945A, scale 1 : 100; 000.

Isachsen, C. E., Bowring, S. A., 1994. Evolution of the Slave craton. Geology 22, 917–920.

Isachsen, C., Bowring, S., 1997. The Bell Lake group and Anton Complex: a basement-cover sequence beneath the Archean Yellowknife greenstone belt revealed and implicated in greenstone belt formation. Canadian Journal of Earth Science 189, 169–189.

Jackson, V. A., 1985. Geology of the Keskarrah Bay area, parts of NTS areas 86 H/6 and 86 H/7. Northwest Territories Geoscience Office EGS 1985-8:1 map, scale 1:50,000.

Jackson, V. A., 2001. Report on the geology of the northern Russell Lake area (85O=4). Northwest Territories Geoscience Office, EGS 2001–03, 90 p.

Jackson, V.A., 2008. Preliminary geological map of part of the South Wopmay orogen (parts of NTS 86B and 86C; 2007 updates); descriptive notes to accompany 1:100 000 scale map. Northwest Territories Geological Survey, NWT Open Report 2008-007, 53 p. and 1 map, scale 1:100,000.

Kositcin, N., Brown, S. J. A., Barley, M. E., Krapež, B, Cassidy, K. F., Champion, D.C. 2008. SHRIMP U–Pb zircon age constraints on the Late Archean tectonostratigraphic architecture of the Eastern Goldfields Superterrane, Yilgarn Craton. Western Australia. Precambrian Research 161, 5–33.

Kröner, A., Layer, P. W., 1992. Crust Formation and Plate Motion in the Early Archean. Science 256, 1405-1411.

McLennan, S. M., 1984. Petrological characteristics of Archean graywackes. Journal of Sedimentary Petrology 54, 889–898.

Moore, J.C.G. 1956. Courageous-Matthews lakes area, District of Mackenzie, Northwest Territories. Geological Survey of Canada, Memoir 283, 52 pages (4 sheets)

Mortensen., J.K., Henderson, J.B., Jackson, V.A., and Padgham, W.A. 1992. U–Pb geochronology of the Yellowknife Supergroup felsic volcanic rocks in the Russell Lake and Clan Lake areas, southwestern Slave Province, Northwest Territories. In Radiogenic age and isotopic studies: Report 5. Geological Survey of Canada, Paper 91-2, pp. 1–7.

Ootes, L., Buse, S., Davis, W. J., Cousens, B. C., 2005. U-Pb ages from the northern Wecho River area, southwestern Slave Province, Northwest Territories: constraints on late Archean plutonism and metamorphism. Geological Survey of Canada Current Research, 2005-F2, 13 p.

Ootes, L., Pierce, K., 2005. Digital geological atlas of the Wecho River area. Northwest Territories Geoscience Office, NWT Open File 2005-03 map, scale 1 : 100; 000.

Ootes, L., Davis, W. J., Jackson, V. A., 2006. Two turbidite sequences in the Russell Lake–Mosher Lake area: SHRIMP U-Pb detrital zircon evidence and cor- relations in the southwestern Slave craton, North-west Territories. Geological Survey Canada Current Research, 2006- A7, 15 p

Ootes, L. Davis, W. J. Bleeker, W., Jackson, V. A., 2008. Geologic overview of greywacke samples col- lected from the western Slave craton. Northwest Territories Geoscience Office, NWT Open Report 2008-012, p. 14.

Ootes, L., Davis, W.J., Bleeker, W., Jackson, V.A., 2009. Two Distinct Ages of Neoarchean Turbidites in the Western Slave Craton: Further Evidence and Implications for a Possible Back-Arc Model. The Journal of Geology 117, 15–36.

Ootes, L., Morelli, R. M., Creaser, R. A., Lentz, D. R., Falck, H., Davies, W. J., 2011. The timing of Yellowknife gold mineralization: a temporal relationship with crustal anatexis? Economic Geology 106, 713-720.

Padgham, W., Fyson, W., 1992. The Slave Province: a distinct Archean craton. Canadian Journal of Earth Sciences 29, 2072-2086.

Pehrsson, S., Villeneuve, M., 1999. Deposition and imbrication of a 2670–2629 Ma supracrustal sequence in the Indin Lake area, southwestern Slave Province, Canada. Canadian Journal of Earth Sciences 36, 1–21.

Pehrsson, S.J., Chacko, T., Pilkington, M., Villeneuve, M.E., Bethune, K., 2000. Anton terrane revisited: late Archean exhumation of a moderate-pressure granulite terrane in the western Slave Province. Geology 28, 1075–1078.

Rasmussen, B., Fletcher, I. R., 2010. Dating sedimentary rocks using in situ U-Pb geochronology of syneruptive zircon in ash-fall tuffs <1 mm thick. Geology 38, 299–302.

Sharma, R., Pandit, M., 2003. Evolution of early continental crust. Current Science 84, 1–7.

Sherlock, R. L., Shannon, A., Hebel, M., Lindsay, D., Madsen, J., Sandeman, H., Hrabi, B., Mortensen, J. K., Tosdal R. M., Friedman, R., 2012. Volcanic stratigraphy, geochronology, and gold deposits of the Archean hope bay greenstone belt, Nunavut, Canada. Economic Geology 107, 991–1042.

Shirey, S. B., and Richardson, S. H., 2011. Start of the Wilson cycle at 3 Ga shown by diamonds from subcontinental mantle. Science 333, 434-436.

Simonetti, A., Heaman, L. M., Hartlaub, R. P., Creaser, R. A., MacHattie, T. G., Böhm, C., 2005. U–Pb zircon dating by laser ablation–MC–ICP–MS using a new multiple ion counting Faraday collector array. Journal of Analytical Atomic Spectrometry 20, 677–686.

Simonetti, A., Heaman, L. M., Chacko, T., Banerjee, N. R., 2006. In situ petrographic thin section U–Pb dating of zircon, monazite, and titanite using laser ablation–MC–ICP-MS. International Journal of Mass Spectrometry 253, 87–97.

Stern, R. A., Bodorkos, S., Kamo, S. L., Hickman, A. H., Corfu, F., 2009. Measurement of SIMS Instrumental Mass Fractionation of Pb Isotopes During Zircon Dating. Geostandards and Geoanalytical Research 33, 145–168.

Stubley, M. P., 2005. Slave Craton: interpretive bedrock compilation. Northwest Territories Geoscience Office, NWT-NU Open File 2005-01: Digital files and 2 maps.

Van Breemen, O., Davis, W. J., King, J. E., 1992. Temporal distribution of granitoid plutonic rocks in the Archean Slave Province, northwest Canadian Shield. Canadian Journal of Earth Sciences, 29: 2186–2199.

Villeneuve, M. E., 1993. Preliminary geochronological results from the Winter Lake-Lac de Gras Slave Province NATMAP project, Northwest Territories. In: Radiogenic Age and Isotopic Studies: Report 7, Geological Survey of Canada, Paper 93-2, p. 29–38.

Villeneuve, M., Lambert, L., van Breemen, O., and Mortensen, J., 2001. Geochronology of the Back River volcanic complex, Nunavut-Northwest Territories. Geological Survey of Canada Current Research 2001-F2, 8 p.

Yamashita, K., Creaser, R. A., Villeneuve, M. E., 2000. Integrated Nd isotopic evidence and U-Pb detrital zircon systematics of clastic sedimentary rocks from the Slave

Province, Canada: evidence for extensive crustal reworking in the early- to mid-Archean. Earth Planetary Science Letters 174, 283–299.

Table 3.1. A summary of the age constraints on the depositional timing and the recommended nomenclature of the Neoarchaean turbidites in the Slave craton.

Name and location	Latitude, Longitude	Lithology	Deposition Age (Ma)	Methods	Reference	Interpretation	Suggested Formation name	Suggested Group name
Watta Lake - southwest Slave craton	N62°16'53'' W113°6'38''	Tuff	2661 ± 2	TIMS	Bleeker and Villeneuve (1995)	Crystallization age of tuff	Burwash Formation (type locality)	Duncan lake Group
Dettah - southwest Slave craton	N62°29'25'' W114°17'13''	Tuff	2652 ± 1.5		This study	Crystallization age of tuff	Burwash Formation (type locality)	Duncan lake Group
Itchen Lake - east of Point Lake, central Slave craton	N65°25'8" W112°15'7"	Greywacke (turbidite)	2658 ± 8 (DZ, max. deposition age)	SHRIMP (n=60)	Ootes et al. (2009)	Weigted mean age of youngest grain	Itchen lake Formation	Duncan lake Group
Mosher Lake - southwest Slave craton	N63°5'55" W115°25'43"	Greywacke (turbidite)	2651 ± 6 (DZ, max. depositon age)	SHRIMP (n=58)	Ootes et al. (2009)	Weigted mean age of youngest grain	Mosher Lake Formation	Duncan lake Group
Clover Lake - Hope Bay belt, northeast Slave craton	N67°40'07'' W106°27'33''	Rhyolite	2662.7 +3.4/−2.8 (min. deposition age)	TIMS (n=5)	Sherlock et al. (2012)	Crystallization age of rhyolite body intruding wet turbidite sediment	Clover Lake Formation	Duncan lake Group
Slemon Lake - southwestern Slave craton	N63°23'95'' W116° 04' 55''	Tuff	2620 ± 6	LA-ICP-MS (n=17)	This study	Crystallization age of tuff, weighted mean of 6 concordant	Slemon Lake Formation (type locality)	Slemon Group
Goose Lake - east Slave craton	N65° 33' 59'' W112° 32' 48''	Greywacke (turbidite)	2621 ± 18 (DZ, max. depositon age)	LA-ICP-MS (n=61)	This study	Youngest zircon	Goose Lake Formation	Slemon Group
Beechy Lake - east Slave craton	N65°05'27" W108°14'25"	Greywacke (turbidite)	2620 ± 5 (DZ, max. deposition age)	TIMS (n=6)	Villeneuve et al. (2001)	Youngest zircon	Goose Lake Formation	Slemon Group
Courageous Lake - central Slave craton	N64°05'45'' W111°14'30''	Greywacke (turbidite)	2635 ± 7 Ma (DZ, max. depositon age)	LA-ICP-MS (n=69)	This study	Weighted mean age of youngest 4 grains	Salmita Formation	Slemon Group
Point Lake - central Slave craton	N65°15'49'' W112°58'4''	Ferruginous clastic sediment (turbidite)	2608 ± 6 (DZ, max. deposition age)	LA-ICP-MS (n=43)	This study	Weighted mean age of youngest 5 grains	Contwoyto Lake Formation	Slemon Group
Damoti lake - west-southwest Slave craton	N64°9'60'' W115°5'59''	Greywacke (turbidite)	2629 ± 2 (DZ, max. depositon age)	TIMS (n=15)	Pehrsson and Villeneuve (1999)	Youngest concordant grain	Damoti Lake Formation	Slemon Group
Kwejinne Lake area - southeast Slave craton	~N63°46'00'' W115°47'55''	Greywackes (turbidites)	2635 ± 8 2636 ± 3 2638 ± 4 (DZ, max. depositon ages)	LA-ICP-MS (n=100, 79, 68)	Bennett et al. (2005, 2012)	Age defined by regression of selected discordant grains	Kwejinne Lake Formation	Slemon Group
Emile River - west Slave craton (Acasta area)	N65°4'45" W115°5'43"	Greywacke (turbidite)	2637 ± 10 (DZ, max. depositon age)	SHRIMP (n=66)	Ootes et al. (2009)	Weighted mean age of youngest grains	Emile River Formation	Slemon Group
Wheeler Lake - southwest Slave craton	N63°18'29" W114°47'53"	Presumably tuff (analytical data not published)	2612 ± 2	TIMS (n=?)	Isachsen and Bowring (1994)	Age reported without supporting analytical data	Wheeler Lake Formation	Slemon Group
High Lake - north Slave craton	N67°2'00'' W110°54'20''	Porphyritic dacite body between greywacke and mudstone facies	2616 ± 3 Ma	TIMS (n=4)	Henderson et al. (1995)	Age reported without supporting analytical data	James River Formation	Slemon Group

Figure 3.1A. Geological map with location names of the Slave craton showing the distribution of greywacke-mudstone turbidites and older volcanic belts. Note the extent of exposed basement, which is from bedrock mapping and Nd isotopes in ca. 2.63-2.58 Ga granitic rocks. The U-Pb age dating of each location is shown in Table 3.1. Map modified from Bleeker et al. (1999a); Davis and Hegner (1992); Bennett (2006); Buse (2006); Yamashita et al. (1999).

A

Type Location (dated)
△ ash bed
☐ detrital zircon

Dettah
(B-D) Location name
(Formation-Group)

Rock Type

Greywacke-mudstone turbidites

Volcanic belts

East and west extent of gneissic basement

Nunavut
Northwest Territories

Clover Lake
(CL-D)

High Lake
(JR-S)

Goose Lake
(GL-S)

Point Lake
(CL-S)

Itchen Lake
(IL-D)

Beechy Lake
(GL-S)

Emile River
(ER-S)

Mattberry Lake
(KL-M)

Damoti Lake
(DL-S)

Courageous Lake
(S-?)

Kwejinne Lake
(KL-S)

Boundary Creek
(KL-S)

Slemon Lake
(SL-S)

Wheeler Lake
(WL-S)

Russell Lake
(RL-S)

Mosher Lake
(ML-D)

Dettah (B-D)

Watta Lake
(B-D)

N

0   50   100   200
Kilometers

Formation

CL - Contwoyto Lake
DL - Damoti Lake
ER - Emile River
JR - James River
KL - Kwejinne Lake
RL - Russell Lake
SL - Slemon Lake
WL - Wheeler Lake

Group

S - Slemon

B - Burwash
CL - Clover Lake
IL - Itchen Lake
ML - Mosher Lake

D - Duncan Lake

Figure 3.1B. The Neoarchaean stratigraphy of the Slave craton. CSCG = Central Slave Cover Group; BIF = banded iron formation. Modified after Bleeker (2002) and Ootes et al. (2009).
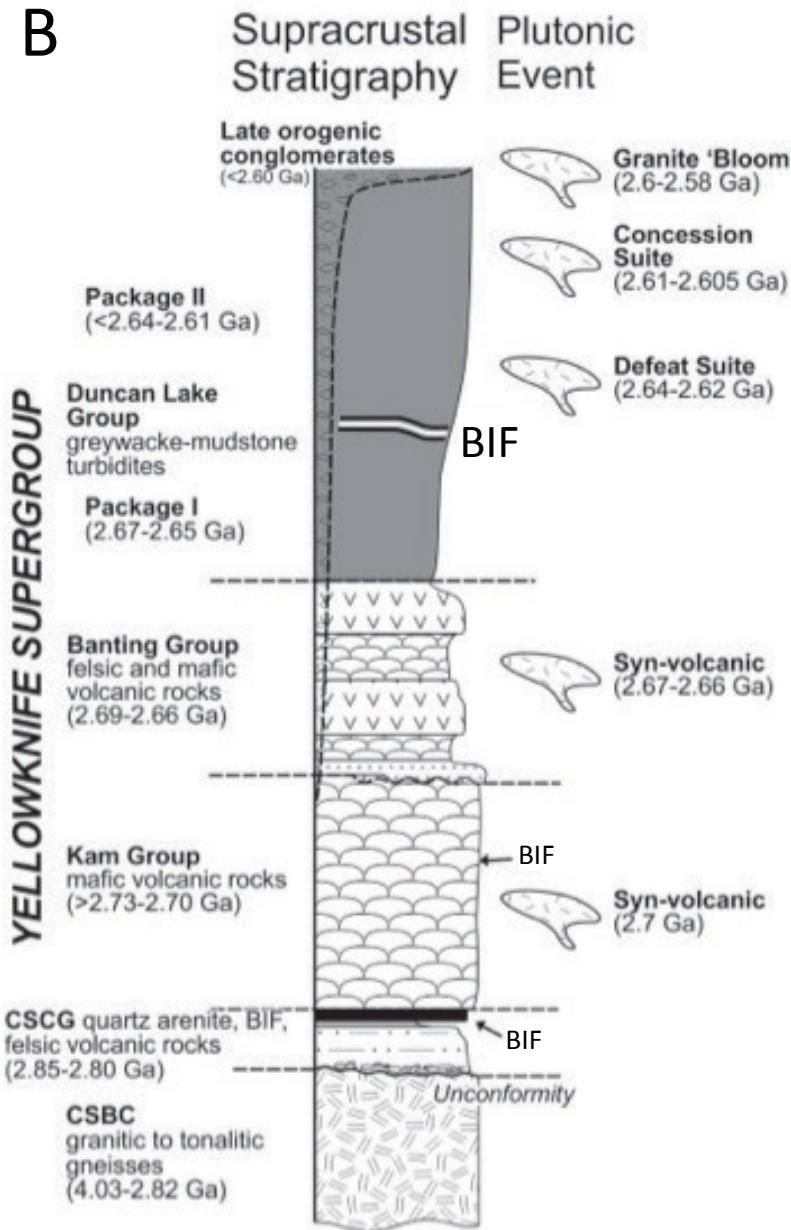
Figure 3.2. The Slemon Lake ash tuff bed. (A, B) photograph of ash tuff bed interbedded in the greywacke. A sharp base and a top with load structures (soft sediment deformation) is marked by white arrows in (B). (C) Crossed polarized micro photo of the tuff showing randomly dispersed fragmented quartz crystals set in a more fine-grained biotite (Bi) + chlorite (Chl) + quartz (Qtz) groundmass. Inset shows a well-crystallized prismatic zircon (Zrn). (D) Outcrop photo of the BIF at Slemon Lake immediately 1 m underneath the tuff bed. (E) Backscatter image of the zircons from the tuff bed at Slemon Lake. The grains are relatively unzoned.

106
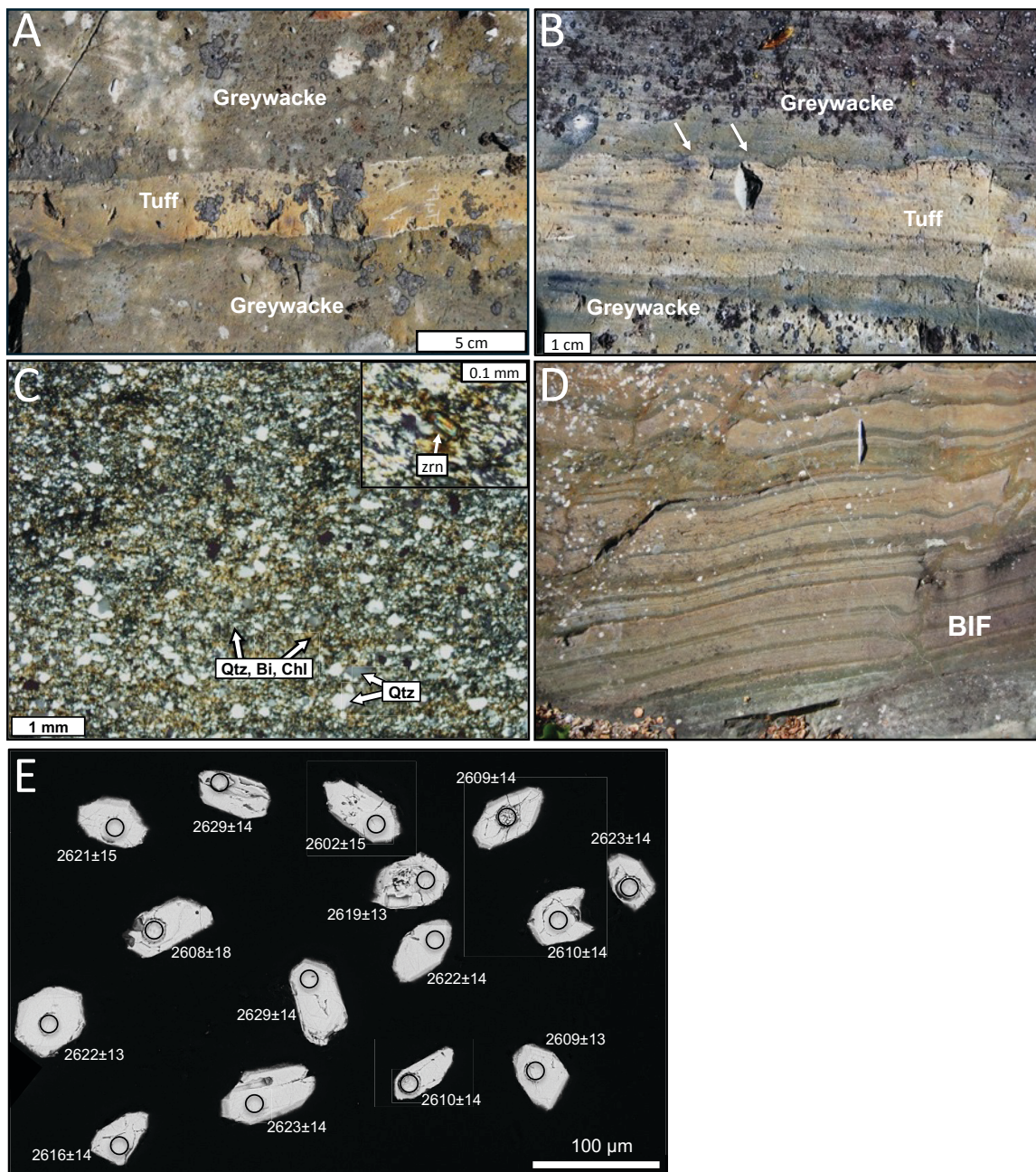
Figure 3.3. LA-MC-ICP-MS U-Pb zircon results for the Slemon Lake ash tuff bed. (A) U-Pb concordia diagram showing a straight line through all the zircons (n=17) plotted. (B) weighted mean $^{207}Pb/^{206}Pb$ age of 2616.6 ± 3.5 Ma of the zircons plotted in (A). (C) U-Pb concordia diagram of the six most concordant grains from the sample. (D) A weighted mean $^{207}Pb/^{206}Pb$ age of 2620.4 ± 5.5 Ma of the six concordant grains.
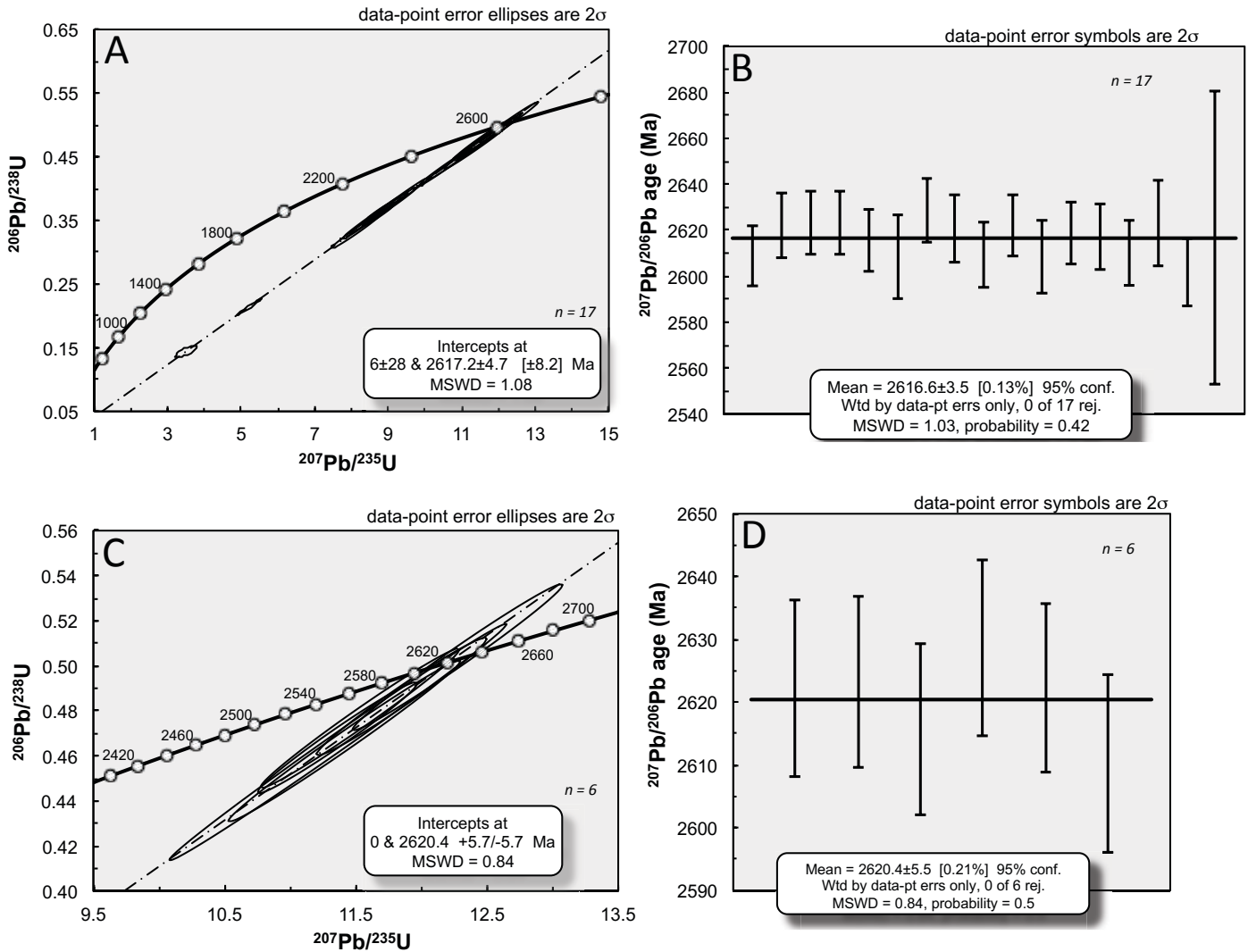
Figure 3.4. The Dettah tuff bed in the Burwash Formation, northeast of Yellowknife Bay (also see Bleeker et al., 2007, p. 163). (A) Outcrop photograph of the tuff bed. (B) Close-up image of the tuff bed in (A). Note the ultra-fine lamina of ash within the mudstone facies. The zircons extracted for this study are from the thickest tuff bed shown. (C) Photomicrograph (crossed polarized light) of the tuff bed showing bimodal distribution of quartz (qtz) grains in a fine-grained chlorite (chl), biotite (bi), and muscovite (mu) groundmass. (D) Microphoto of selected zircon grains from the tuff bed. (E) A U-Pb concordia diagram showing three slightly discordant zircon grains with an upper intercept at ca. 2650.5 Ma.
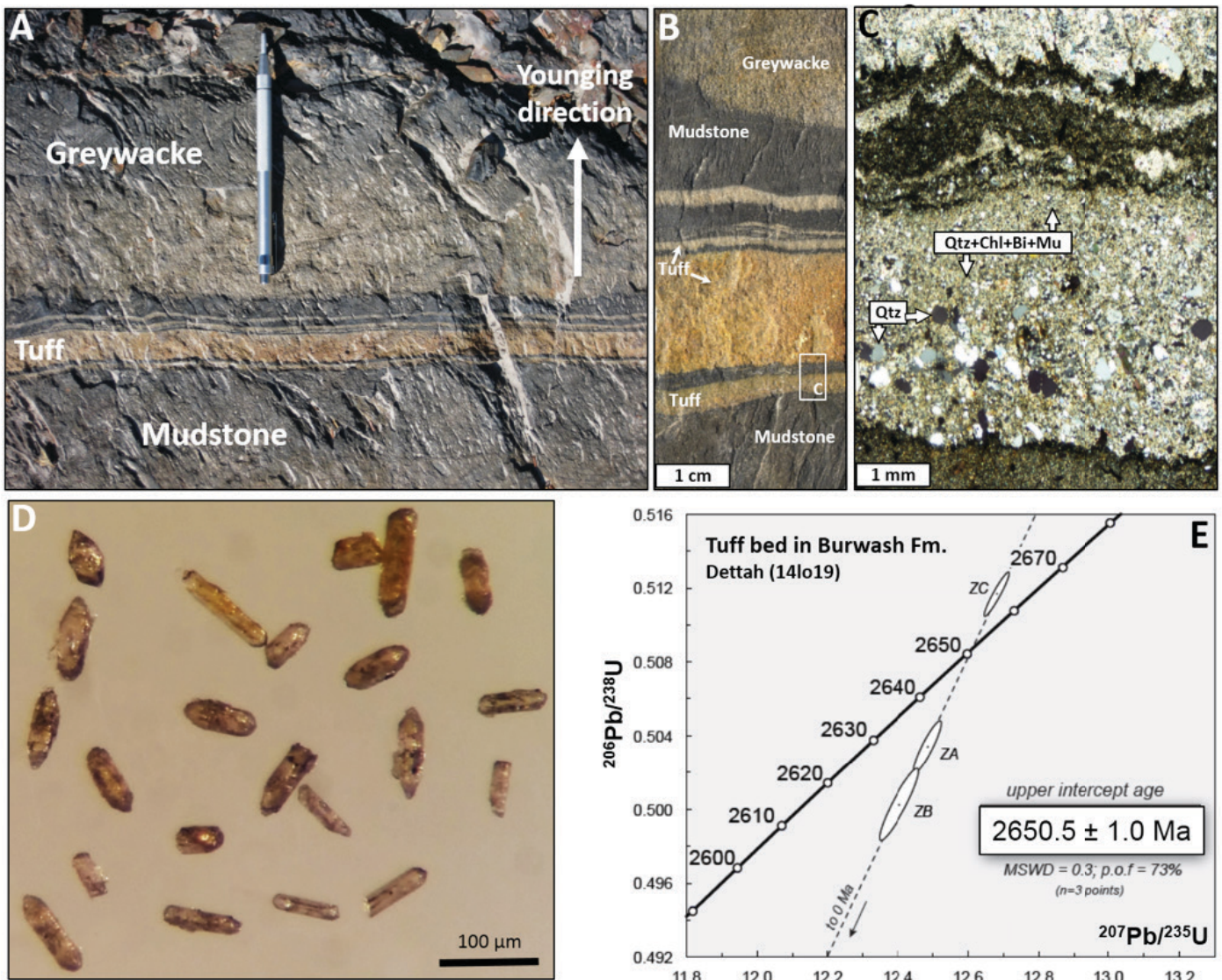
Figure 3.5. The Goose Lake greywacke. (A) Illustration of the Goose Lake core sample showing greywacke-mudstone turbidites associated with BIF. The sample in this study was obtained from the lower part of the lower greywacke. (B) Cathodoluminescence (CL) images of the selected zircon grains. (C) LA-MC-ICP-MS U-Pb detrital zircon results showing U-Pb concordia diagram of all the zircons analyzed. (D) Histogram with probability curve for the detrital zircons (<10% discordance). Note the youngest grain at 2621 ± 18 Ma (1.3% discordance) and the >2800 Ma grains which suggest the existence of older basement lithologies. A large part of the zircons correlate in age with Kam- and Banting-Group detritus.
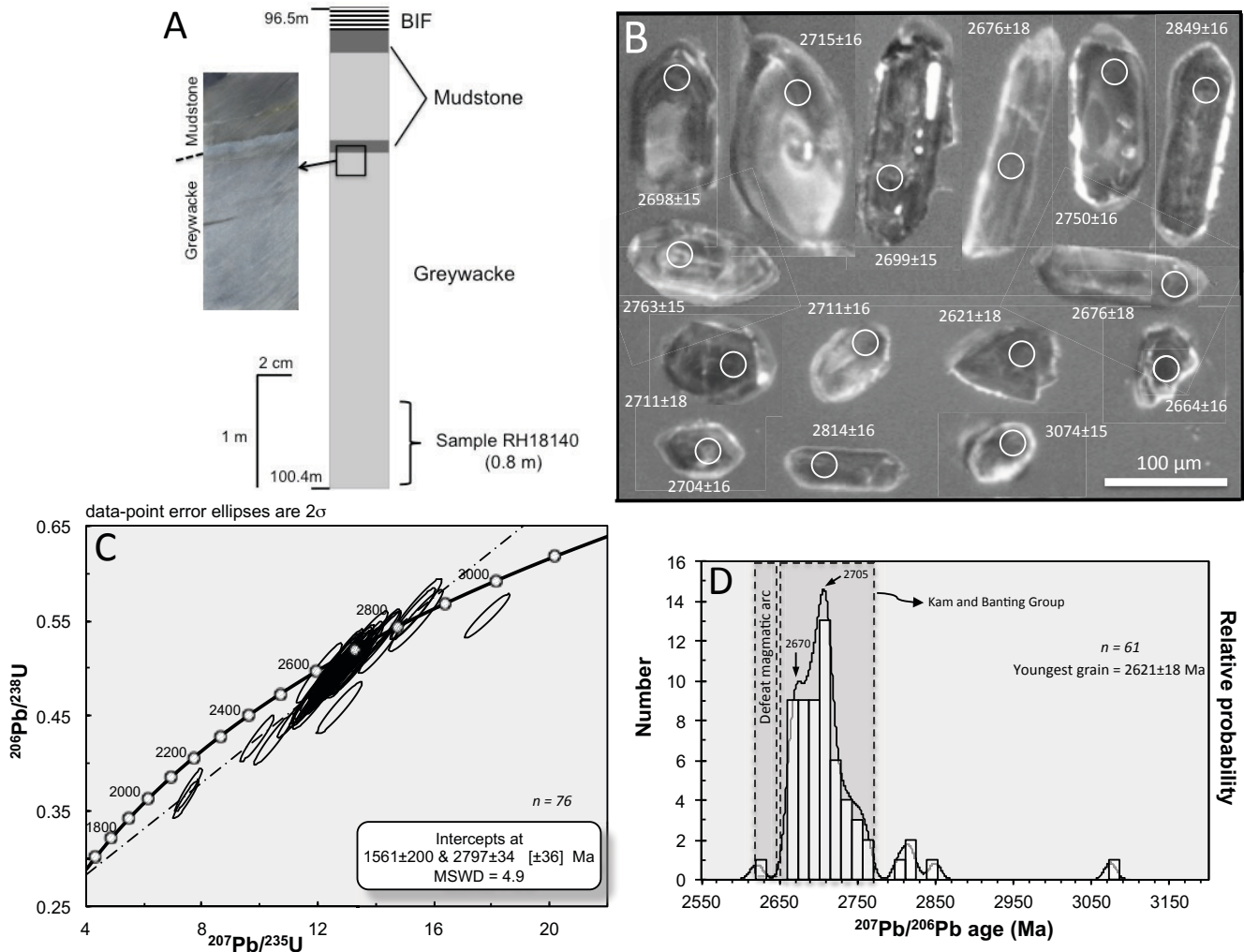
Figure 3.6. The Courageous Lake greywacke. (A) Field photos of the greywacke sample collected from the Courageous Lake turbidites. (B) Cathodoluminescence (CL) images of the selected zircon grains.
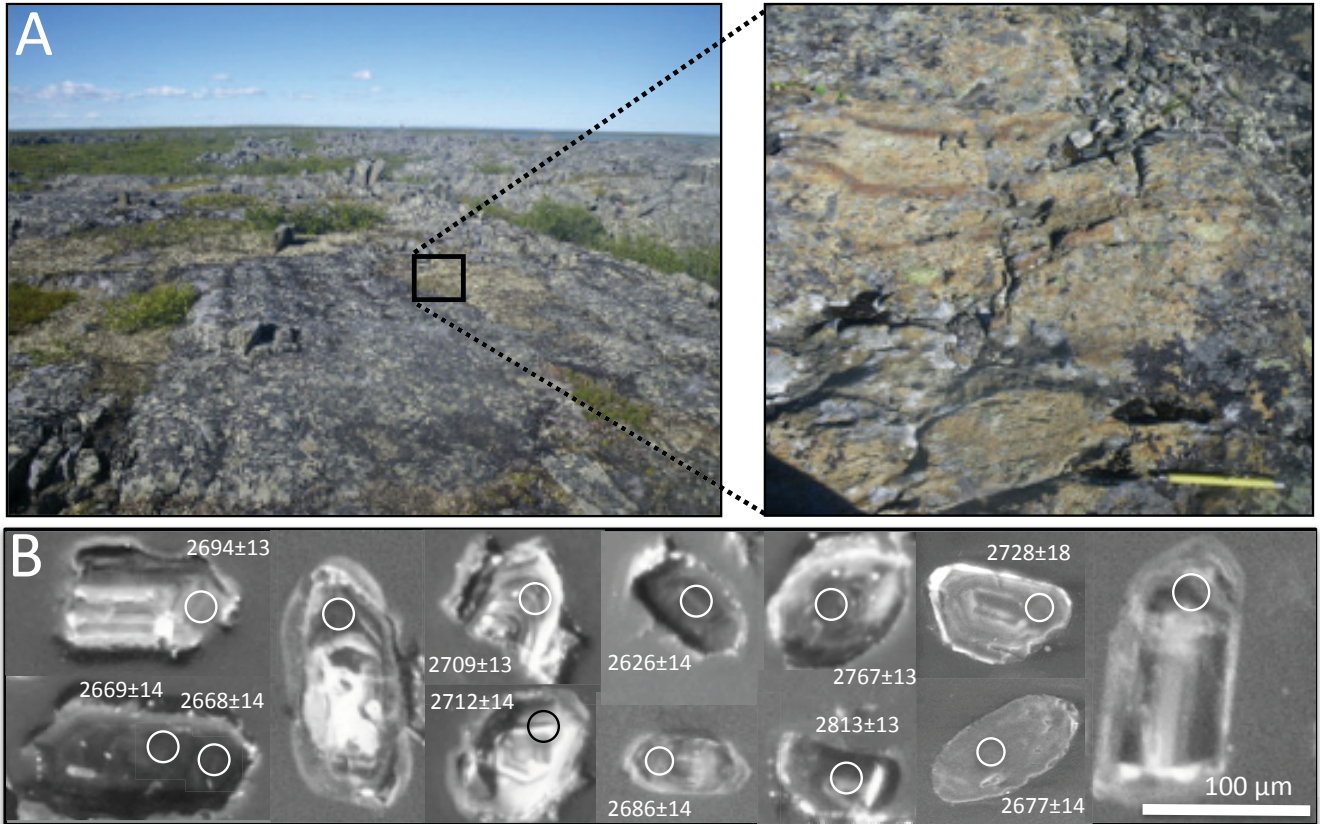
Figure 3.7. The Courageous Lake greywacke showing the LA-MC-ICP-MS U-Pb detrital zircon results. (A) U-Pb concordia diagram showing all the zircons analyzed. (B) Histogram with probability curve for the detrital zircons (<10% discordance). Note the high frequencies of Banting Group detritus. (C) The weighted mean $^{207}Pb/^{206}Pb$ age of the four youngest grains is 2635 ± 6.7 Ma, which we define as the maximum deposition age and likely these zircons are source from the Defeat magmatic arc.
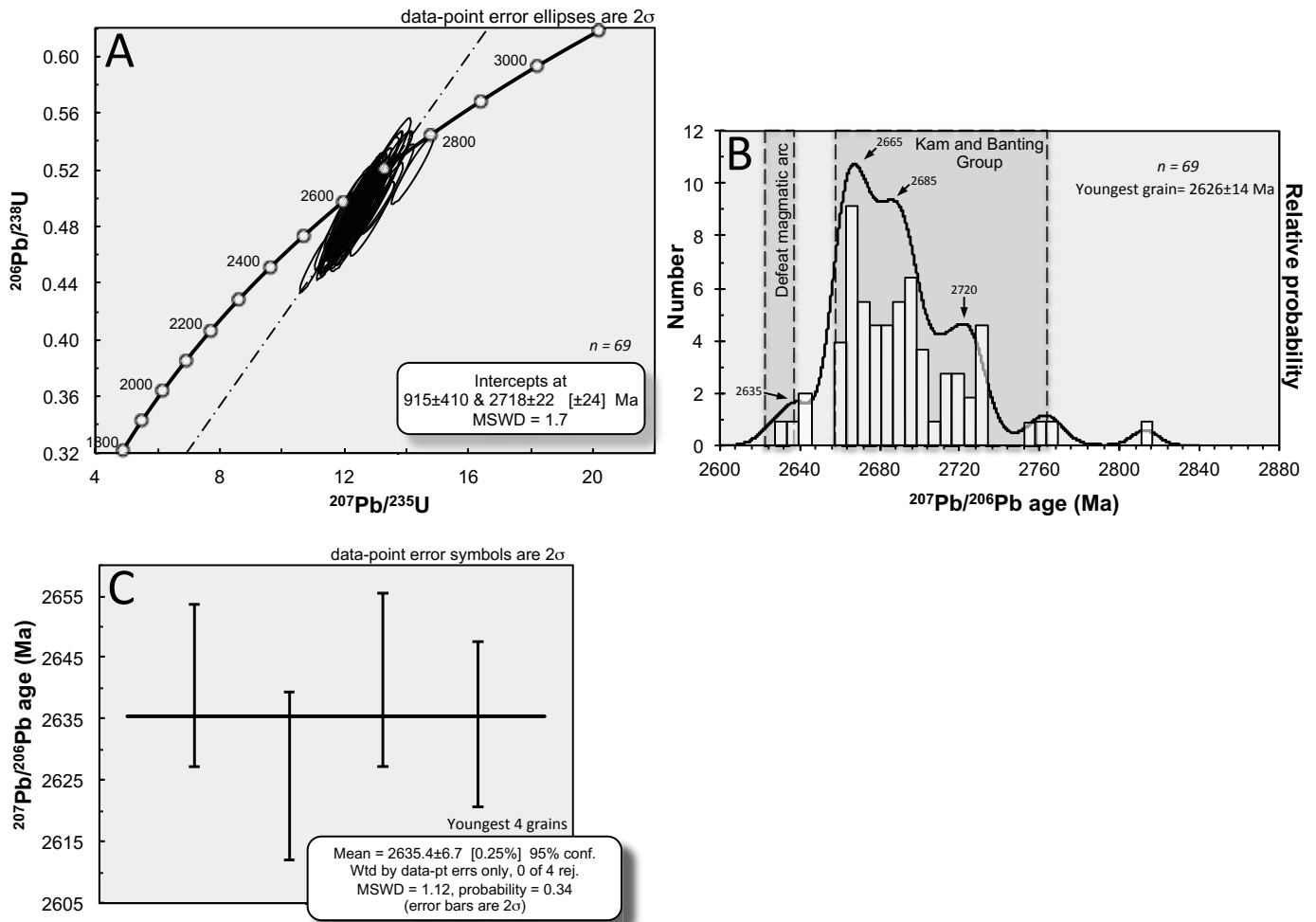
Figure 3.8. The Point Lake ferruginous sediment. (A, B) Field photo of the Point Lake coarse-grained ferruginous sediment beds within the BIF-turbidite sequence. (C) Backscatter image of representative zircons from the ferruginous sediment beds. The grains are well-zoned but occasionally intensive fragmented and corroded.
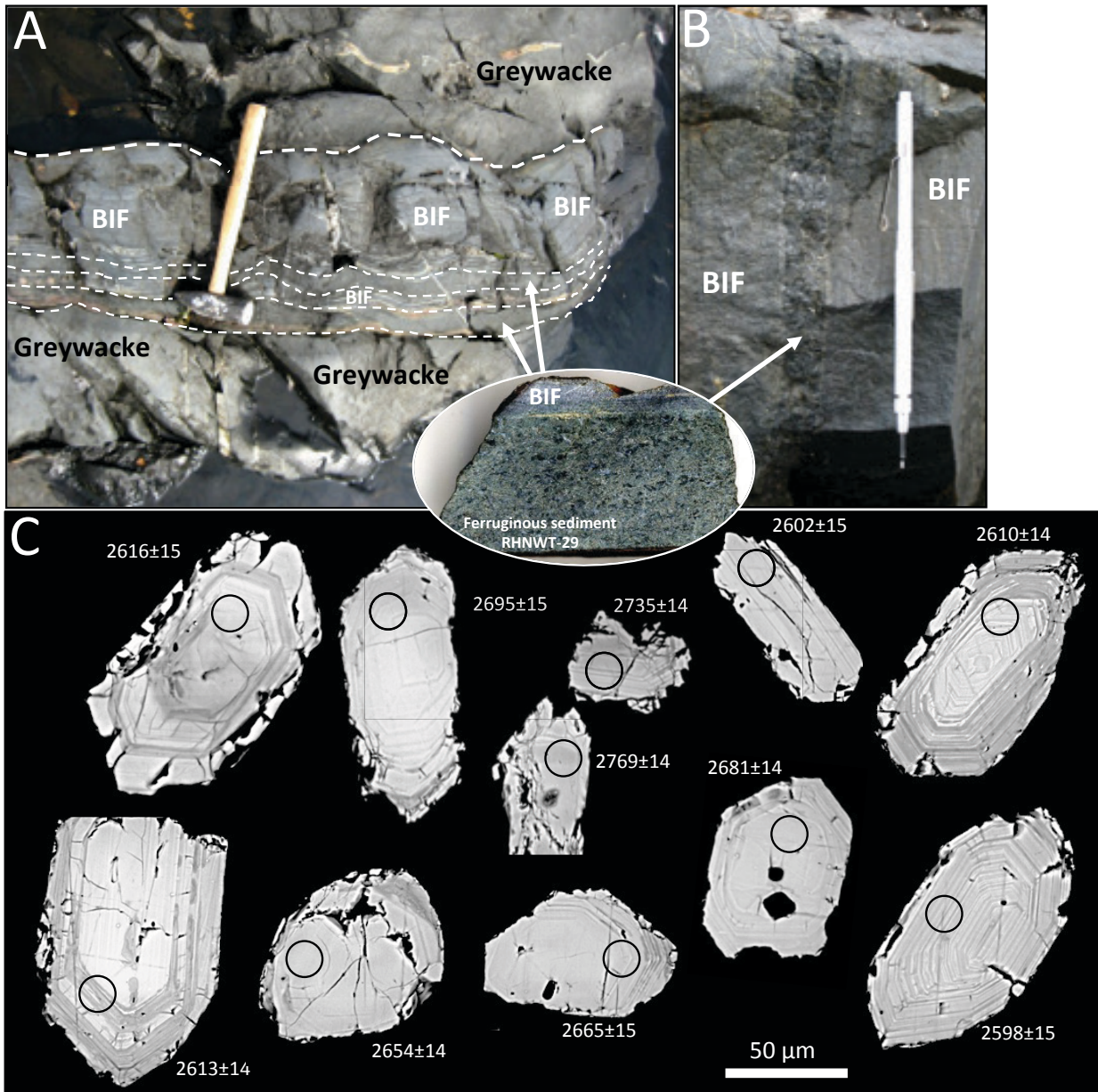
Figure 3.9. LA-MC-ICP-MS U-Pb detrital zircon results from the Point Lake ferruginous sediment. (A) U-Pb concordia diagram showing all the zircons analyzed. (B) Histogram with probability curve for the detrital zircons (<10% discordance). In addition to the high input of Banting Group detritus, note the probability peak at 2608 Ma, which indicate detrital input from the differentiated Concession Suite magmatic rocks. (C) U-Pb concordia diagram of the youngest five grains. (D) The weighted mean $^{207}Pb/^{206}Pb$ age for the five grains are 2607.5 ± 6.4 Ma, which could suggest the existence of an even younger turbidite-BIF sequence in the craton.
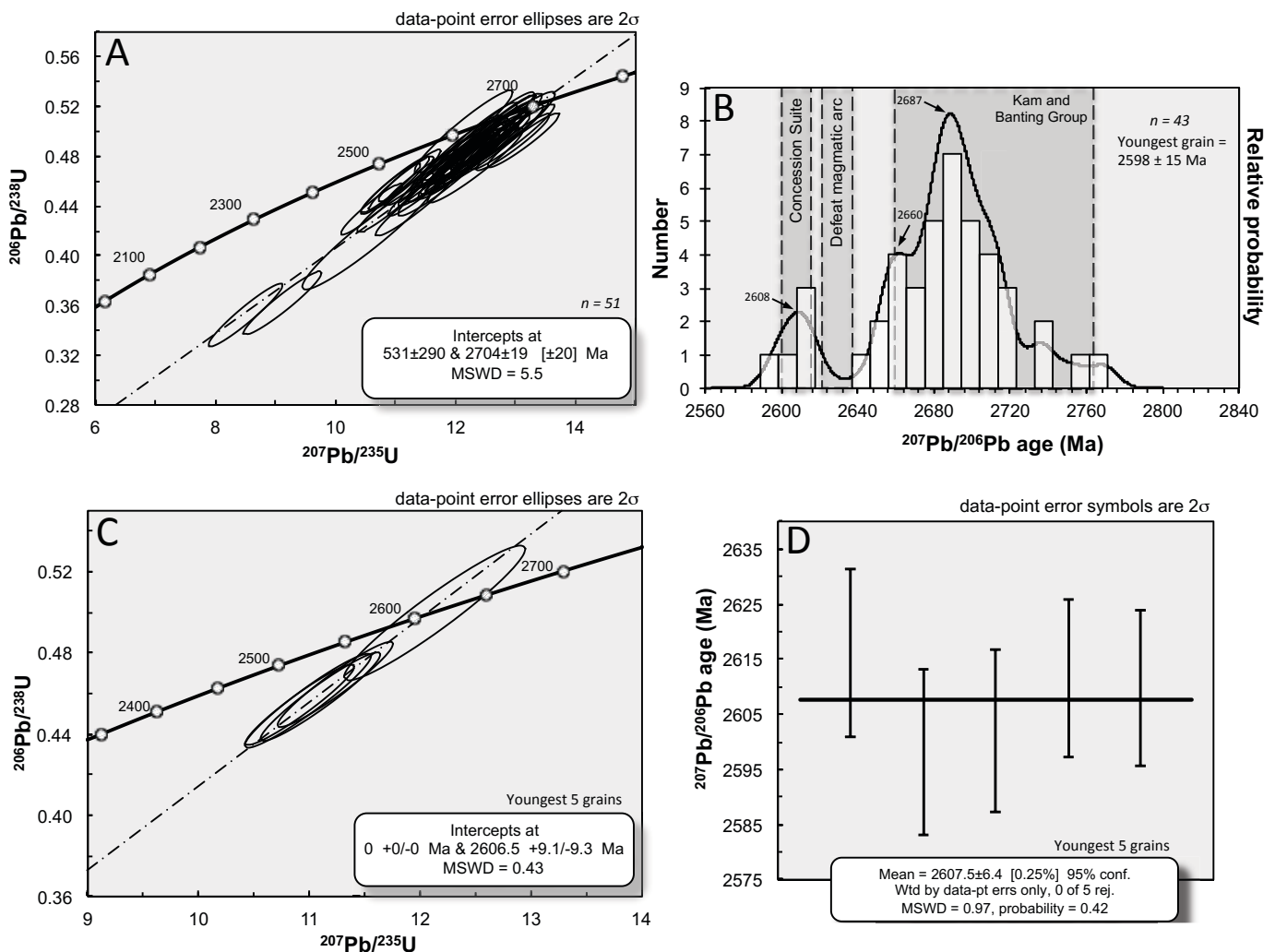
Figure 3.10. Composite U-Pb ages for turbidites in the Slave craton with the recommended Duncan Lake Group (Henderson, 1970, 1972; Helmstaedt and Padgham, 1986; Fergusson, 2002; Fergusson et al., 2005) and the proposed Slemon Group (this study). See text for further explanations.

114
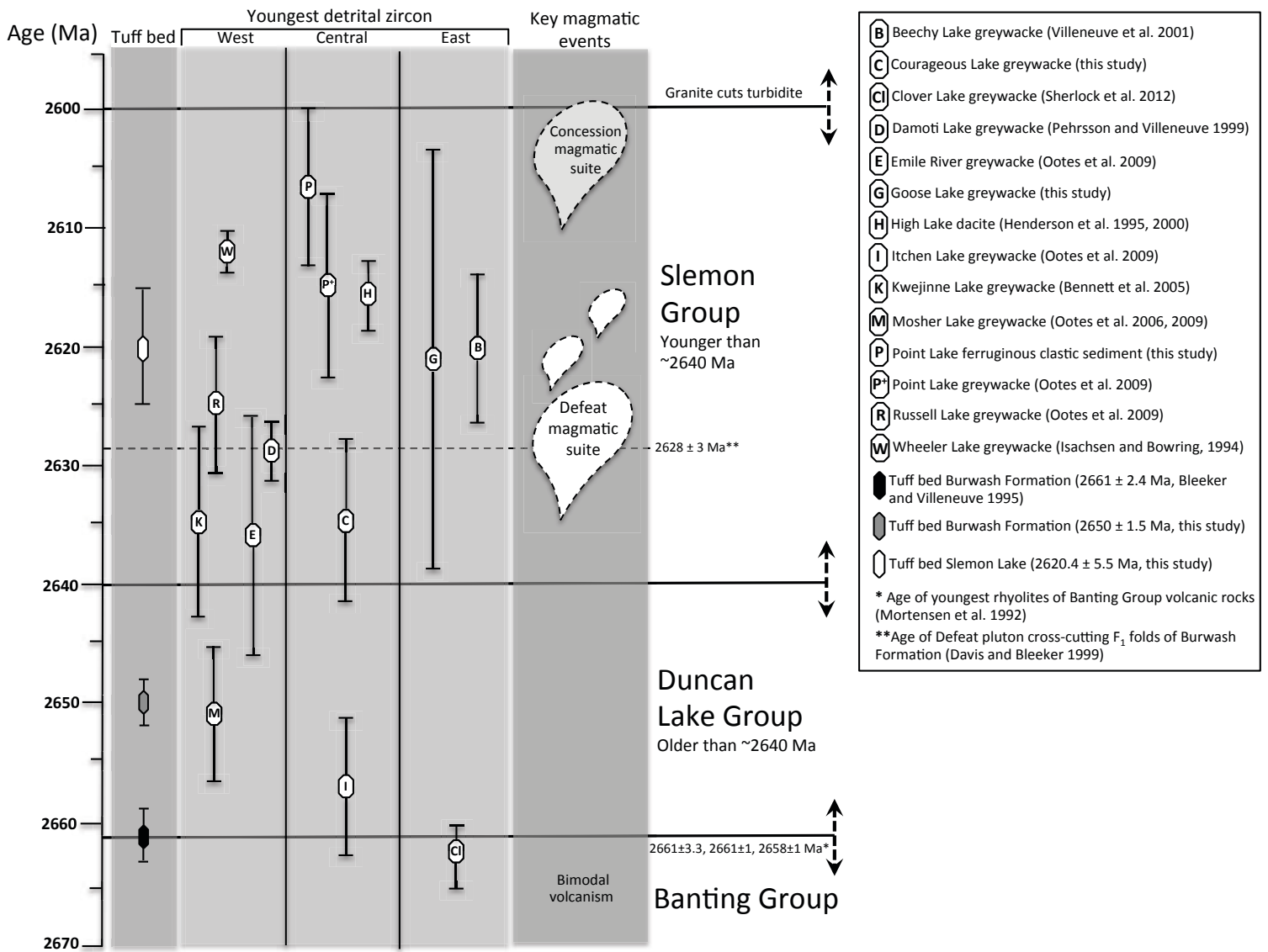
4. Neoarchaean BIF within a 2.62 Ga turbidite-dominated deep water basin, Slave craton, NW Canada

4.1. Introduction

Banded iron formations (BIF) are chemical sedimentary rocks that precipitated from marine waters throughout much of the Archaean and early Palaeoproterozoic. BIF consists of silica (40-60 wt.% SiO_2) and iron (15-50 wt.% Fe_2O_3) that alternate in bands of chert and magnetite or hematite and typically range from small-scale laminated microbands (<1 cm), through mesobands (≥1 cm), and up to meter-scale macrobands (Trendall and Blockley, 2004). Post-depositional processes, such as diagenesis and later metamorphism, modified the primary mineralogy and make any interpretation of the precursor sediment challenging. Minerals such as quartz, hematite, magnetite, stilpnomelane, grunerite, actinolite, hornblende, calcite and dolomite-ankerite are all of diagenetic and metamorphic origin. Proposed primary minerals and compounds are amorphous silica, ferric hydroxide, siderite and in some cases, greenalite (Klein, 2005). The amount of continentally derived detritus in BIF is sparse as they have generally low Al_2O_3 (< 1 wt.%) and other insoluble elements (i.e., Ti, Zr, Nb, Th, and Hf). Compared to modern seawater, the shale-normalized rare earth element + yttrium (REY) pattern in most BIFs show enrichment in the heavy-REE relative to the mid-REE and light-REE (HREE>MREE>LREE), signifying the seawater origin of BIF (e.g., Byrne and Kim, 1990; Bolhar et al. 2004). The iron in BIF was likely sourced from submarine hydrothermal venting, where the ferrous iron (Fe^{2+}) could have been transported great distances under the strongly anoxic conditions of the oceans during the Archaean (Holland, 1973). A proxy for this process is evident in an enrichment of reduced Eu^{2+} measured as a shale-normalized positive Eu anomaly in the BIF (Bau and Möller, 1993). The dissolved iron was oxidized to Fe^{3+} in the photic zone by either abiological or biological oxidation and subsequently settled to the sea floor as a ferric oxyhydroxide,

such as ferrihydrite, $Fe(OH)_3$ (e.g., Bekker et al., 2010, 2014). Dissolved silica, on the other hand, was sourced from either continental weathering (Hamade et al., 2003) or hydrothermal alteration (Steinhöfel et al., 2010). The silica likely acted as a background sedimentation occasionally interrupted by pulses of iron upwelling (e.g., Frei and Polat, 2007; Haugaard et al., 2013).

Since the deposition of BIF is restricted to the Precambrian, the puzzle of solving their origin and depositional environment are more likely to be understood by the interpretation of the interbedded volcanic and sedimentary rocks, both of which have modern analogues (e.g., Drever, 1974; Pickard et al., 2004). Archaean turbidites, as their modern counterparts, are dominated by massive to graded greywacke-mudstone sequences. They contain a mixture of epiclastic and volcaniclastic debris activated and shed from steep subaqueous slopes. The depositional relationship between the turbidites and BIF is enigmatic since the origin and rate of deposition for these two facies are highly different. BIF is believed to represents slow precipitation and settling of iron hydroxides and amorphous silica $(Si(OH)_4)$ from deep (>200 m) marine waters. For instance, well-studied depositional rates for Superior-type BIF are on the average of 30 m (compacted)/1 million year (Pickard, 2002). Turbidites, on the other hand, represent dynamic and rapid sedimentation that can be measured within hours or days (e.g., Selley, 1988).

The turbidite-hosted BIF in the Slave craton, NW Canada, are hosted within one of the largest and best-preserved Archaean sedimentary basins in the world (Padgham and Fyson 1992). The timing of BIF deposition in this sedimentary sequence is now well-constrained to ca. 2620 Ma, from U-Pb zircon dating of an interbedded ash tuff bed (Haugaard et al. in review). These Neoarchaean BIF are relatively rare in the rock record and therefore characterizing these BIF are another key tool for characterizing the palaeoenvironmental conditions during the late Archaean.

In this study, we present new petrologic and geochemical insight into the deposition of these Neoarchaean BIF. We interpret the seawater geochemical signature and relate this to the ambient palaeoenvironment and the role of the dominant sources controlling the seawater composition. Since BIF should be understood in its depositional context rather than as an isolated rock type, we also describe the interbedded turbidite

deposits since, unlike BIF, the origin and nature of the latter can be studied using modern analogues.

4.2. The BIF-bearing turbidites of the Slave craton

Approximately 70% of the Slave craton supracrustal rocks are composed of greywacke-mudstone turbidites (Padgham and Fyson, 1992). This Archaean turbidite basin(s) is one of the largest and best preserved in the world, with deposition of up to 10 km of greywacke-mudstone cycles across an area of at least 32,000 km^2 (Ferguson et al., 2005; Bleeker and Hall, 2007; Ootes et al., 2009). The homogenous succession often lacks marker horizons, such as tuffaceous beds or discernable biostratigraphic units, making any subdivision of these turbidites difficult. However, Ootes et al (2009) demonstrated that the turbidite basin in the central-western part of the craton could be subdivided into at least two temporally different "packages". An older, turbidite succession, that was deposited at ca. 2661 Ma (Fig. 4.1; Bleeker and Villeneuve, 1995; Fergusson et al. 2005), and a younger succession deposited at ca. 2620 Ma (Pehrsson and Villeneuve, 1999; Bennett et al., 2005; Ootes et al., 2009; Haugaard et al., in review). These younger turbidites are locally distinctive as they contain interstratified BIF. Three depositional settings are proposed for the BIF-bearing turbidites from passive margin and foreland basin (Pehrsson, 2002), to accretionary wedge setting (Bennett et al., 2005), to a continental back-arc basin Ootes et al., 2009). The latter model is supported by the fact that the timing of BIF and turbidite deposition coincides with the Defeat Suite plutons, interepreted as the root of a continental arc (Davis et al., 2003; Bleeker and Hall, 2007; Ootes et al., 2009).

4.2.1. Post-depositional history

The Slave craton has experienced a complex history of magmatism and polyphase deformation and metamorphism during the accretion of the craton (Davis and Bleeker 1999; Bleeker and Hall 2007; Helmstaedt 2009). The turbidite-BIF sequences were intruded by plutonic rocks of various generations (e.g., van Breemen et al., 1992; Davis et al., 1994; Davis and Bleeker, 1999; Bennett et al., 2005; Ootes et al., 2005). Associated

with the intrusions are regional thermal metamorphic overprints that range from low greenschist up to granulite facies (e.g., Bennett et al. 2005). The latter has resulted in the development of various porphyroblasts such as cordierite, garnet and sillimanite, which are locally developed in the mudstone pelites. The turbidites underwent up to three generations or more of deformation and has resulted in a structurally complex overprinting (Fyson and Jackson, 1992; Bennett et al., 2005),

The turbidite- BIF sequences are also important host rocks for epigenetic gold (Padgham, 1991). Quartz and carbonate veining and a high-degree of hydrothermal alteration from sulfur-rich fluids has resulted in the formation of gold-bearing iron sulfides (pyrrhotite, pyrite and arsenopyrite) within tightly folded BIF horizons. These horizons provided favorable chemical and structural traps for gold-bearing sulfur fluids. The structural timing of this mineralization event is likely of syn- to late-metamorphic origin (Bleeker and Hall, 2007).

4.3. Field observations

4.3.1. Slemon Lake

The Slemon Lake area in the southwest Slave craton is underlain by extensive greywacke-mudstone turbidites with locally interbedded BIF (Fig. 4.1; Jackson, 2001). The BIF-bearing outcrops at Slemon Lake are characterized by tightly folded and faulted sequences of interleaved BIF and greywacke-mudstone sequences (Figs. 4.2A and 4.2B). Each finely laminated, up to 0.5 m thick BIF unit is commonly underlain and capped by greywacke (Fig. 4.2A).

The BIF have two scales of banding, microbanding (mm-scale) and mesobanding (cm-scale), the latter shows magnetite mesobands with internal mm-scale of chert microbands (hand sample in Fig. 4.2C). The freshest outcrops have variable oxide (magnetite) content. Those with highest oxide content (Fig. 4.2A) show alternating bands of very fine-grained greenish chert and magnetite (Fig. 4.2C), whereas the outcrops with less magnetite contain more silicates represented by bands of fine-to-medium grained greenish amphiboles and chert (Figs. 4.2D and 4.2E). The most weathered BIF outcrops show pervasive red hematite alteration as a result of secondary oxidation of magnetite

(Fig. 4.2B). Adjacent to the BIF, within the greywackes are up to 30 cm thick calc-silicate beds interbedded with semi-pelitic mudstone beds. The greywacke units commonly show a fining upward gradation, which in places terminate with deposition of mudstone facies. In relation to this gradation, climbing ripple lamination can be found in the fine-grained top part of the turbidite (Fig. 4.2F). The turbidite-BIF sequences at Slemon Lake are also directly associated with synchronous volcanism, which is evident through an interbedded thin (2-5 cm) and yellowish-bleached tuffaceous bed (Fig. 4.2G). This ash tuff bed has been dated by U-Pb zircon, yielding a crystallization age of $2620 \pm$ 6 Ma (Haugaard et al., in review). That ash bed is intercalated with more fine-grained greywacke and a well exposed ~0.8-1.2 m thick BIF unit, which occurs immediately underneath the ash bed (Fig. 4.2D). The bed has a relatively sharp base and a more disturbed upper contact with the underlying and overlying greywacke beds (Fig. 4.2B). The upper contact represents well-developed load structures as a result of soft sediment deformation (Fig. 4.2G).

4.3.2. Point Lake

The east side of Point Lake in the central Slave craton, is underlain by extensive greywacke-mudstone turbidites with locally interbedded BIF (Fig. 4.1; Bostock 1980; Henderson, 1998). The BIF-bearing turbidites at Point Lake are characterized by alternating oxide BIF and turbidites, of which the latter are mainly composed of sandy greywacke with only minor mudstone (Figs. 4.3A and 4.3B). Each BIF unit ranges between 0.2-0.5 m in thickness (Figs. 4.3A and 4.3B). Where preserved, each BIF unit has a sharp and straight lower contact to the underlying greywacke, whereas the BIF terminates with a wavy, erosional upper contact with the overlying greywacke (Fig. 4.3B). A large proportion of the individual BIF units have well-developed microbands (≤1 mm) of chert and magnetite which illustrate the fine-scale nature of the BIF (Fig. 4.3C). Individually greywacke units vary from small cm-scale beds to larger beds that are 1-1.5 m in thickness (Figs. 4.3A and 4.3B). The greywackes also range from being vertically unstructured to having weakly defined fining-upward bedding. During burial of the sediment package, the water-saturated sediment in the greywacke increased the fluid

pressure resulting in a sediment expulsion/discharge that penetrated the bordering BIF unit as a sedimentary dyke (Fig. 4.3D). Locally concordant and interstratified with the BIF horizons are thin (2-8 cm) mafic ferruginous beds containing coarse-grained black-to-dark green hornblende (Figs. 4.3E).

4.3.3. Damoti Lake

The Damoti Lake area in the western Slave is underlain by extensive greywacke-mudstone turbidites with locally interbedded BIF (Fig. 4.1). The area around Damoti Lake is geological complex with a multiphase deformational history. Within the central part of the turbidite-BIF supracrustal belt the metamorphic facies range from lower greenschist to amphibolite grade, although the studied BIF was metamorphosed at greenschist facies. The BIF exhibits variation in both the physical appearance and the mineral composition. The best-preserved BIF outcrops (Fig. 4.4A) are found stratigraphically within the central part of the belt outside the intense zones of hydrothermal sulfide alteration. Here, small pockets of grunerite-bearing BIF varies from having well-defined bands that range from <1 mm to a few cm in thickness (Fig. 4.4B) to more homogenous and massive BIF with a mixture of magnetite, chert, and radiating amphiboles.

Within the laminated to bedded BIF, early diagenetic chert nodules show evidence of differential compaction as indicated by the curved microbands above and below them (see Fig. 4.4C). Graded greywacke and mudstone occurs stratigraphically below and above the BIF units. Similar to Point Lake, the BIF is associated with dark-greenish and dark- to silver-grey ferruginous sediment beds ranging from almost pure coarse-grained amphibole to more fine-grained beds containing amphibole with randomly distributed biotite porphyroblasts (1-2 mm in size) and minor graphite which gives the rock a metallic luster (Fig. 4.4D). Stratigraphically, these ferruginous sediment beds occur immediately above the BIF unit as a basal occurrence to the greywacke-mudstone turbidites (see also Waychison, 2010). From drill-core studies, the greywacke beds have been reported to locally contain both detrital magnetite grains and rip-up clasts from the BIF itself (Waychison, 2010). The ferruginous sediment locally shows a graded texture

over an outcrop scale of only 20-50 cm. Here the crystal size ranges from very coarse-grained (~1-1.5 cm) to more fine-grained (1-2 mm) crystals (Fig. 4.4D).

4.3.4. Goose Lake

The Goose Lake area in the eastern Slave is underlain by extensive greywacke-mudstone turbidites with locally interbedded BIF (Fig. 4.1; Frith, 1987). Where exposed, the BIF at Goose Lake is characterized by centimeter-scale mesobands of chert alternating with magnetite having intergrown radiating amphiboles (Fig. 4.4E). As such, in outcrop, the Goose Lake BIF is similar to the BIF at Damoti Lake (Fig. 4.4A). Drill core-samples obtained from the least sulfide-altered zones show individually BIF units (chert+magnetite+amphibole bands) that vary in thickness from 10 cm to 50 cm. The magnetite bands ranges from millimeter scale up to 2 cm in thickness (Fig. 4.4F). The thickness of the alternating chert bands range from millimeter scale up to 5 cm in thickness (Fig. 4.4F). Typically, at the magnetite-chert interface, dark-to-pale green to colorless radiating amphiboles (actinolite+grunerite) are developed (Fig. 4.4F). Brown stilpnomelane is locally found in association with the pale green amphiboles (Fig. 4.4F).

The associated greywackes contain fine-to-medium grained quartz-rich sand and have stratigraphical thickness ranging from 25 cm to 3 m. Parts of the greywackes show a weakly graded (fining upward) bedding, whereas other parts are vertically unstructured and massive (Fig. 4.5). The greywackes often grade into 10-20 cm thin clay- and silt-rich mudstone beds that form sharp bounded couplets (Fig. 4.5). However, as seen in Fig. 4.5, exceptions do occur where the greywacke deposition is found interstratified with BIF units only. Locally, the mudstone is weakly magnetic, containing graphite and visible chlorite.

4.4. Samples and Analytical techniques

BIF samples suitable for separation of individual chert- and magnetite-bands were obtained at Slemon Lake and from the Goose Lake drill cores. These are designated with the letter A (Si) and B (Fe) in Table 4.3. Due to the microbanded nature of the Point Lake BIF and the difficulties in separating bands from Damoti Lake, only the bulk BIF

geochemical results from these two locations are presented here. The separation of individual bands was done with a 10 cm diameter diamond disc. The crushed BIF and associated rock samples were analyzed by fusion-XRF and trace elements were analyzed by fusion-ICPMS at the Activation Laboratories, Ancaster, ON. Repeate analysis of internal standards always yielded accuracy better than ±10%, and often better than ±5%. Precision on the duplicate samples is within ±5%, relative.

Backscatter electron images, elemental distribution X-ray maps, EDS (energy dispersive spectrometry) and WDS (wavelength dispersive spectrometry) analyses were obtained with a JEOL Microprobe 8900 at the University of Alberta, Edmonton, AB. The machine parameters were set to a current of 30 nA and the probe beam diameter was 2 microns. Counting time was 30 sec on peak, and 15 sec on each background. Recalculations of amphibole analyses were done using the scheme of Locock (2014). For greenalite, all Fe is assumed to occur as FeO, which is in agreement with other studies (e.g., Gole, 1980a, 1980b; Klein and Gole, 1981). Stilpnomelane, on the other hand, is more complex and can accommodate various oxidation states of Fe (see Eggleton and Chappell, 1978 and references therein). As such, stilpnomelane often contains various amount of Fe^{3+}, either originating from the unaltered mineral growth or introduced later during weathering and alteration. On the basis of the reported literature (see Klein, 1974 and references therein), we assume an average $Fe^{3+}/\Sigma Fe$ of 0.1 in stilpnomelane as the best approximation.

4.5. Petrographic and mineralogical results

4.5.1. The BIF

The size of quartz- and magnetite-grains are typically <0.1 mm, with a small fraction of the magnetite being recrystallized into larger ≤0.5 mm grains. The microcrystalline quartz creates a tight mosaic and the magnetite bands are compact with sharply defined boundaries to the silica-rich bands. Major parts of the magnetite bands are opaque but minor parts of the bands have interlayered microcrystalline quartz microbands.

Together with the typical chert and iron oxide component, the BIF samples all contain variable amount of silicates. Electron microprobe analysis reveals that the

majority of the silicates are in the form of grunerite and ferro-actinolite, with minor greenalite and stilpnomelane (see Tables 4.1, 4.2 and compositional diagrams in Fig. 4.6). At Slemon Lake, very fine-grained actinolite and lesser chlorite is interspersed within many of the chert bands. This gives the bands a greenish tint in hand sample and in outcrop (Fig. 4.2C). The actinolite and chlorite constitute up ~15-30% of the modal mineralogy in the chert bands. The most well-developed amphiboles are found in the Damoti and Goose Lake BIF, where up to 1 cm radiating grunerite crystals are shown to grow perpendicular to the original bedding planes of the BIF. In detail, at Goose Lake, the amphibole bands at the interface between bands of chert and magnetite represent a metamorphic product between the two latter minerals; this textural relationship demonstrates their metamorphic origin (Figs. 4.7A, 4.7B and 4.7C). The grunerite typically grows on, and outwards, from the magnetite bands, whereas actinolite occurs further into the chert bands where magnetite becomes less abundant. The actinolite ranges from stubby to radiating and to perfect diamond-shaped crystals (Fig. 4.7D). At Goose Lake, both greenalite and stilpnomelane are developed in association with grunerite and actinolite (Figs. 4.7E and 4.7F). The greenalite has a stubby crystal habit and ranges in size from ~50 to ≤150 µm whereas the bladed and needle like stilpnomelane are up to 100 µm in length and 10 µm across (Fig. 4.7F). Stilpnomelane commonly occur within greenalite crystals or on the edges of actinolite (Figs. 4.7E and 4.7F). In addition to the grunerite and actinolite, a network of fine-grained subhedral ferro-hornblende exists within magnetite microbands at both Point Lake and Goose Lake.

4.5.2. The interbedded tuff and ferruginous sediment

4.5.2.1. Tuff

The 5 cm thick ash tuff bed at Slemon Lake, dated at 2620 ± 6 Ma (Haugaard et al., in review), contains randomly distributed fine-grained (≤100 µm) quartz fragments set in a very fine-grained (≤20 µm) quartz, biotite, chlorite, and feldspar groundmass (Figs. 4.7G and 4.7H). In certain areas, the biotite and chlorite show a weak crenulated foliation. The grains are distributed homogenously with no particular grading. A thorough review of the beds zircon and geochronology can be found in Haugaard et al. (in review).

4.5.2.2. Ferruginous sediment

In contrast to the monotonous greywacke-mudstone turbidites, the ferruginous sediment beds vary significantly in their texture and mineralogy but collectively they all contain iron-rich phases such as chlorite, Fe-amphiboles and biotite, with lesser amount of quartz that was characteristic of the greywacke sediment. At Point Lake, these beds contain coarse-grained, euhedral ferro-hornblende (Fig. 4.8A). The hornblende, which makes up approximately 25-35% of the rock by volume, are found randomly interspersed with medium-grained quartz rock fragments and alkali-feldspar all set in a very fine-grained biotite groundmass (Fig. 4.8A). For the composition of the ferro-hornblende see Table 4.1 and Fig. 4.6C. Both hornblende and biotite groundmass have multiple inclusions of radiogenic zircons. The stubby-to-prismatic hornblende is clearly of metamorphic origin as they engulf fragmented quartz crystals (Fig. 4.8A). They also likely grew after the main deformation as they are randomly distributed. The ferruginous sediment at Damoti Lake lacks quartz and quartz fragments. Instead the sediment contains randomly distributed biotite porphyroblasts (up to 2-3 mm in size) and fine-grained (≤1 mm) angular to subangular plagioclase grains all set in a massive chlorite groundmass (Figs. 4.8B and 4.8C). Disseminated throughout are large (2-3 mm) altered grunerite crystals with overgrowths of ferro-hornblende (Fig. 4.8D).

Although some of the plagioclase grains are zoned with a Ca-rich core and Na-rich rim, the overall plagioclase composition is $\sim Ab_{87}An_{13}$, corresponding to oligoclase. The plagioclase grains are accompanied by another plagioclase, namely slawsonite (Sr-plagioclase). These grains form aggregates and mosaic networks with poorly developed crystal shapes (Fig. 4.8C). In addition to the slawsonite, other Sr-rich phases found are Sr-bearing epidote and Sr-bearing clinozoisite. In parts of the groundmass and as inclusion trails in amphiboles is found ultra fine-grained graphite (Fig. 4.8E). Other accessory phases in this sediment include allanite, apatite, bastnasite, monazite, quartz, zircon and smectite.

4.6. Geochemical results

4.6.1. BIF

4.6.1.1. Major and trace elements

For the bulk BIF samples, the SiO_2 concentration is ~45-67 wt.% and the Fe_2O_3) concentration ~30-52 wt.% (Table 4.3). For the individual silica-bands, the SiO_2 concentration ranges from ~70 wt.% at Slemon Lake and up to as high as 94 wt.% at Goose lake. For the iron bands, the minimum Fe_2O_3 concentration is found at Slemon Lake with ~63 wt.% and the highest is ~75 wt.% at Goose Lake. The average SiO_2 concentration in the iron bands is ~25.5 wt.% whereas the average Fe_2O_3 concentration in the silica bands is only 10.5 wt.%.

When comparing the Al_2O_3 (and TiO_2) concentration between the four localities the highest average abundance is found at Slemon Lake, with a steady decrease from Damoti to Point and then Goose lakes (Fig. 4.9A, note TiO_2 is not shown). For Goose Lake, the Al_2O_3 content is generally higher (1.58 wt.%) for the iron bands and lowest (0.19 wt.%) for the silica bands. This pattern is reversed at Slemon Lake where the silica band contains ~5.4 wt.% Al_2O_3 and the iron band only ~2.2 wt.% (Table 4.3).

The high-field-strength elements (HFSE; Zr, Th, Sc and Hf) are all at relatively low concentrations (e.g., average of ~6 ppm Zr and ~0.4 ppm Th, Table 4.3) with the exception of Slemon Lake which has average of ~18 ppm Zr and ~1.4 ppm Th. In general, Al_2O_3 is well-correlated with other these immobile elements, as illustrated by the Al_2O_3 vs. Th plot in Fig. 4.9B. A higher scatter exists between Al_2O_3 and ∑REE (Fig. 4.9C).

The transition metals (e.g., Ni, Cr, V, Sc) are generally positively correlated, as shown for example by Sc vs. Ni (Fig. 4.9). For the majority of the samples, the Cr content varies between 15-45 ppm but are below detection for the silica bands at Goose Lake (Table 2). A strong covariation also exists when comparing transition metals with highly immobile elements such as Th (see Sc vs. Th in Fig. 4.9E).

The siderophile element germanium (Ge) has been used as an important tracer for the different iron and silica sources involved in BIF deposition (e.g., Hamade et al.,

2003). In Fig. 4.9F, Ge shows an inverse relationship with SiO_2 (r^2=0.68) and a positive correlation with Fe_2O_3 (r^2=0.65).

4.6.1.2. Rare earth elements and yttrium (REY)

The shale-normalized rare earth elements and yttrium (REY_{NASC}) patterns (normalized after McLennan, 1989) for the four BIF locations are characterized by HREE enrichment relative to both MREE (Sm/Yb_{NASC} = 0.33-0.99) and LREE (Pr/Yb_{NASC} = 0.26-0.89) whereas the LREE/MREE shows a higher variability (Pr/Sm_{NASC} = 0.68-1.44) (Figs. 4.10A-D). In all the samples, a well-defined Eu ($Eu/Eu*_{NASC}$ = 1.24-3.4, average 1.92) and Y anomalies are developed (Fig. 4.10A-D and Table 2). Noteworthy, and as also reported by Alexander et al. (2009), is that higher Eu anomalies, and therefore a higher Eu enrichment, is generally occurs with the lowest total REY abundances (e.g., Figs. 4.10C and 4.10D). The excess of Y relative to Ho can be quantified through their concentration ratios, which shows an average Y/Ho ratio of 36 (Table 4.3).

Among the four locations, the REY_{NASC} pattern for Slemon Lake is highly elevated relative to the other locations studied (Fig. 4.10A) with $\sum$REE between 35-43 ppm (Table 2 and Fig. 4.10A). At Goose Lake (Fig. 4.10D), the iron bands contain the highest amount of REE ($\sum$REE = 28-32 ppm) and the REY patterns have comparable shape of MREE and HREE as Slemon Lake, whereas the LREE abundances are more depleted (Fig. 4.10D). Importantly, the REY_{NASC} patterns of the iron bands at Goose Lake are elevated, the silica bands are the contrary with $\sum$REE ranging from as low as 1.4 ppm up to 8.2 ppm (Fig. 4.10D, Table 4.3). The LREE patterns are general concave-up (Figs. 4.10A-D) and show distinct positive La anomalies (the combination of Pr/Pr* ~ 1 and Ce/Ce* < 1; Fig. 4.11; Bau and Dulski 1996). In addition to the La anomaly, four samples (two iron bands, one silica band and the bulk BIF) from Goose Lake, one sample from Damoti Lake and one from Point Lake exhibit a clear negative Ce anomaly (Pr/Pr* > 1.05, Fig. 4.11).

4.6.2. Tuff and turbidites

4.6.2.1. Tuff

The up to 5 cm thick ash tuff bed at Slemon Lake (Table 4.4), dated at 2620 ± 6 Ma (Haugaard et al., in review), contains high Al^2O^3 (23-24 wt.%) and relative high (3 wt.%)

loss on ignition (LOI), which includes the presence of volatile materials such as water and CO_2. Utilizing the relatively immobile elemental ratios the tuff is classified as a rhyodacite-dacite (Fig. 4.12A) and plots in the field of volcanic arc and syn-collision granites in Fig. 4.12B. The chondrite-normalized REE pattern of the tuff (Fig. 4.12C) shows that the tuff bed has a fractionated REE pattern (La_{chon}/Lu_{chon}~7). The tuff also has a weak, but distinctly positive Eu anomaly (Eu/Eu* = 1.16; Fig. 4.12C). The tuff is further characterized by primitive mantle-normalized positive anomalies of Th, Zr, Eu, and Y (Fig. 4.12D). Negative anomalies of Nb, P and Ti are also evident (Fig. 4.12D).

4.6.2.2. Turbidites - greywacke, mudstone and ferruginous sediment

The three greywacke samples analyzed in this study (Table 4.4) are characterized by low SiO_2 concentration but high Al_2O_3, Fe_2O_3 and MgO concentrations (Table 2) relative to more mature sandstones. The chemically immaturity of the greywacke is further indicated by the Al_2O_3/Na_2O ratio of ~4.8 which is lower than ~10 for average sandstones (e.g., Henderson, 1975). The Na_2O/K_2O ratio for all the turbidites (greywacke, mustone and ferruginos sediment) is ≤ 1 with the highest ratio in the greywackes.

The two mudstone samples have less SiO_2 and more TiO_2, Fe_2O_3, MgO, trace metals and LOI than the sandy greywackes (Table 4.4). The ferruginous sediments have less SiO_2 but a higher Fe_2O_3 than the mudstones. Noticeable is that all the presented sediment have close to similar Al_2O_3/TiO_2 ratios of ~25 (Table 4.4). Together with field observations, the often high LOI in the mudstone and ferruginous sediment is reminiscent of high organic (graphite) content. This has also been supported by X-ray diffraction analysis by Waychison (2010) who showed that the ferruginous sediment at Damoti Lake contains up to 13.5 wt.% graphite.

4.7. Discussion

4.7.1. Greenalite and stilpnomelane - a retrograde or prograde mineral assemblage?

In prograde metamorphism, greenalite generally forms during late diagenesis and very low-grade metamorphism (<300 °C, Gole, 1980a), where it typically occurs with stilpnomelane, minnesotaite and siderite (Klein, 2005). Stilpnomelane on the other hand, has been reported being stable with grunerite from sub-greenschist- to greenschist-facies

conditions (up to ~450°C). As a prograde mineral, greenalite is typically microcrystalline (an order of magnitude smaller than co-existing minerals), and it forms either cement or very fine-grained granules or needles and seldom recrystallizes into larger grains. Texturally, the greenalite in this study often form larger patches and has diffuse grain boundaries filling in small spaces within existing well-crystallized actinolite and grunerite crystals (Fig. 4.7E). It is, therefore, unlikely that greenalite is part of the original prograde mineral assemblage. Supportive of this interpretation is the mineralogy of the associated greywackes at Goose Lake that stabilized within the biotite zone. Similar with respect to stilpnomelane, the smaller sheaves that cross-cut both greenalite, actinolite and grunerite are of secondary origin. Furthermore, the very fine-grained stilpnomelane needles developed on the edge of large grains of actinolite and sprays into neighboring greenalite are good indicators of the later stage stilpnomelane growth.

The gold mineralization in the area of Goose Lake is linked to felsic dykes carrying sulfur- and chlorine-rich fluids related to the Neoarchaean "granite bloom" that was a main factor in stabilizing the Slave craton. The bulk rock geochemistry (Table 4.3) reveals higher sulfur content in the Goose Lake samples, which demonstrates some degree of sulfide mineralization in the area, while up to 1 wt.% chlorine (Cl) found solely in the greenalite and stilpnomelane (Table 4.2) further points to the secondary origin of these hydrous phyllosilicates during Cl-rich fluid interaction. Accordingly, we suggest that the greenalite and stilpnomelane are products of retrograde metamorphism, similar to that been reported elsewhere for the 2.7-2.6 Ga BIF from the Yilgarn craton, Western Australia (Gole, 1980b). There, unlike the more interspersed grains in our study, the greenalite and stilpnomelane mostly occur in veins and veinlets cross-cutting the original bedding planes (Gole, 1980b). Although sampling of the highest altered core sections was avoided, the retrograde mineralization could therefore potentially impact the geochemical REY signal obtained in the Goose Lake BIF.

4.7.2. The impact of secondary fluids on the REY

One of the advantages of using REY in interpreting metamorphic rocks is their relative high resistance towards secondary alteration. In this regard, previous work by Bau and Dulski (1992) and Bau (1993) concluded that any REY mobilization during post-

depositional processes, such as diagenesis and metamorphism, would thus lead to a homogenization of the REYs between individual silica and iron bands. Notably, for the Goose Lake samples, differences in REY abundances are evident in both the silica and iron bands, supporting the notion that the REY patterns of the BIF are still preserved and can be used in interpreting the ambient seawater. Furthermore, a high rock-to-water ratio in the BIF sediment during metamorphism can potentially result in LREE depletion and generate negative Eu anomalies. The latter is due to the higher fluid mobility of the larger Eu^{2+} ion whereas the former is due to a smaller difference in ionic size between Fe^{2+} and the HREE relative to the LREE. This means that the HREE will preferentially get incorporated into the lattice of metamorphic magnetite. Thus, a metamorphic fluid percolating through BIF will gain higher LREE/HREE ratio than the source rock BIF (Bau, 1993). Neither of those features are apparent in the BIF samples. In support of the LREE/HREE ratios, the poorer co-variation between Al_2O_3 and the $\sum REE$ (see Fig. 4.9C) relative to the perfect correlations between the immobile elements, such as Al_2O_3, Th and Sc, further implies that the REY were in their existing rations while still in seawater prior to BIF precipitation, rather than the impact of post-depositional fluid alteration.

4.7.3. The Neoarchaean seawater composition

4.7.3.1. La, Ce and the REY fractionation

In order to facilitate comparison between different chemical sediments around the world BIF-REY is commonly normalized to one either the PAAS (post-Archaean Australian shale; Taylor and McLennan, 1985) or the NASC (North American Shale Composite; McLennan, 1989); the latter is used in this study.

The Neoarchaean BIFs contain positive La anomalies as seen in Fig. 4.11. This shows that La in seawater is more stable in solution relative to neighboring REEs. This is a consequence of the absence of electrons in the inner 4f shell (e.g., De Baar et al., 1985). The positive La anomaly, therefore suggests that La has been stabilized and weakly fractionated relative to the other LREE in the seawater column prior to precipitation. The six BIF samples also have negative Ce anomalies (see Fig. 4.11) which tends to indicate that a strong oxidant (e.g., O_2) was present in seawater that could oxidize Ce^{3+} to Ce^{4+},

thus leaving the local water column deficient in Ce because Ce^{4+} preferentially binds to Fe and Mn oxyhydroxides (e.g., Sholkovitz et al., 1994).

The NASC-normalized REY patterns display Pr/Yb ratios < 1, which is best, interpreted as being of seawater origin (Fig. 4.13). The evolution of the post-Archaean upper crust (as a whole) has largely been reconstructed through the chemistry of shales because their overall composition largely represents the erosion of the upper continental crust (e.g., Taylor and McLennan, 1987, 2009). When addressing the REY pattern, normalization to local shale, however, may be more relevant as it is more contextually related to the depositional environment of the BIF. The contemporaneous local crust during the deposition of the BIF can be considered as the Damoti and Goose lakes shales (DGS; When normalizing the BIF samples after DGS, the REY fractionation (Pr/Yb_{DGS}) is constantly lower (higher HREE-to-LREE) compared to the NASC normalized Pr/Yb_{NASC} (Fig. 4.13) suggesting that the ambient seawater clearly fractionated the REY prior to BIF precipitation. The fractionation likely originates from the fact that the HREE tends to stay longer in solution than the LREE, which will preferentially be adsorbed to particle surfaces (e.g., clay, organic matter) and thus becomes removed from solution (e.g., Cantrell and Byrne, 1987; Sholkovitz et al., 1994). A relatively high input of fine-grained detrital material is recorded particularly for the Slemon Lake samples making them immediately less suitable for detecting the seawater REY chemistry. However, on closer inspection, despite the up to 5.4 wt.% Al_2O_3 and the largest ∑REE of all BIF samples in this study, the Slemon Lake silica bands still have a lower $Pr/Yb_{NASC/DGS}$ ratio than both the iron bands and the bulk BIF (Fig. 4.13B). This, along with its positive La and Y anomalies, demonstrate the high influence of seawater on the REY budget and the likelihood that the REY patterns were not due to detrital input.

4.7.3.2. Seawater Y/Ho and hydrothermal Eu/Sm

In the BIF, two of the most pronounced REY signatures are superchondritic Y/Ho (>28) and the excess of Eu (relative to neighboring REEs, both resultings in positive normalized anomalies in (Fig. 4.10). Modern seawater is known to hold Y longer in solution (due to lower particle reactivity) than Ho, thereby increasing the Y/Ho ratio (Bau and Dulski, 1999; Bolhar et al., 2004). The excess of Eu (as reduced Eu^{2+}) originates

from high-T (>350 ºC) hydrothermal fluids that circulate through submarine mafic crust along mid-ocean ridges (Danielson et al., 1992). The relative contribution from hydrothermal fluids to seawater composition can therefore be viewed through the elemental ratio of Eu/Sm (e.g., Alexander et al., 2008). Using modern reservoirs and the associated sediment from the craton, the Eu/Sm-Y/Ho ratios (Fig. 4.14) show that the BIF can be viewed as a mixture of continental weathering (represented by the interbedded clastic sediment), hydrothermal injected fluids and the seawater itself (Fig. 4.14). The influence from the sediment has likely suppressed the superchondritic Y/Ho as seen for the three BIF samples, which plot in or nearby the field of the interbedded sediment. Relative to NASC, and to a lesser degree the DGS, all BIF samples are skewed towards higher Eu/Sm ratios. From a regional craton perspective, it is noteworthy that the older Mesoarchaean Slave craton BIF has a larger hydrothermal input (larger Eu/Sm) than the Neoarchaean BIF of the craton, whereas the latter has overall higher seawater Y/Ho ratios (Fig. 4.14).

4.7.3.3. Hydrothermal versus continental weathering: Decoupling of iron and silica?
The source of iron and silica for Precambrian BIF has been a long-standing debate (e.g., Holland, 1973; Simonson, 1985; Dymek and Klein, 1988; Alibert and McCulloch, 1993). It is now generally accepted that Fe^{2+} was sourced from mid-ocean hydrothermal activity and injected into anoxic bottom waters (e.g., Holland, 1973; Jacobsen and Pimental-Klose, 1988; Klein and Beukes, 1989; Polat and Frei, 2005; Frei and Polat, 2007). The Fe^{2+} was occasionally upwelled to the continental shelf, oxidized to Fe^{3+} by biological mechanisms (e.g., Pecoits et al., 2015), and subsequently precipitated as ferric oxyhydroxide, such as ferrihydrite. The provenance of silica, on the other hand, remains enigmatic since its origin has been linked to both primary hydrothermal processes (Steinhöfel et al., 2010), weathering of the surrounding landmasses (Hamade et al., 2003; Haugaard et al., in review) or incorporation via secondary fluids during post-depositional alteration (i.e. diagenesis; Rasmussen et al., 2015). Nevertheless, the work by Hamade et al. (2003) and Frei and Polat (2007), reveal that the siderophile element germanium (Ge), in conjunction with the silica content in BIF, can be used to characterize two interacting water masses during BIF precipitation. In many low-temperature processes the Ge/Si

ratio do not fractionate as Ge and Si have similar atomic radii and bond lengths (see Hamade et al., 2003 and references therein).

The Ge/Si molar ratio of present day mid-ocean hydrothermal fluids is between $\sim$8-14*10^{-5} mole/mole (Mortlock et al., 1993), whereas the average continental crustal value is $\sim$0.13*10^{-5} (Froelich et al., 1992). The Ge/Si of river waters, and hence the surface seawater, is very low ($\sim$0.06*10^{-5}) because Ge uptake by land plants strongly fractionates the crustal Ge/Si ratio (Derry et al., 2005). However, on a plant-free Neoarchaean Earth it is reasonable to assume that ambient upper seawater was close to the crustal Ge/Si value at the time. The silica and iron are geochemically linked to Ge with a positive co-variation to iron and an inverse relation to silica (Fig. 4.9F). The BIF samples in this study reveal a exponential distribution of Si versus Ge/Si (Fig. 4.15A) reflecting mixing between hydrothermally controlled bottom water and continentally controlled surface water. Germanium concentrations are relatively high in hydrothermal fluids but will be scavenged by ferric oxyhydroxides during precipitation, relative to Si. Therefore the Ge/Si will be higher than crustal values for bottom water and in the ferric iron precipitate. The low Ge/Si ratios in BIF with high Si content therefore likely represent the Ge/Si in upper ambient seawater. Similar mixing pattern between seafloor vented hydrothermal fluids and upper seawater, have also been demonstrated to exist within the 3.8 Ga Isua BIF (Frei and Polat, 2007) and the Palaeoproterozoic Dales Gorge BIF, Hamerley Group, Western Australia (Hamade et al., 2003) and is shown in Fig. 4.15B. The Neoarchaean BIF samples from the Slave craton plot within the same Ge/Si range as the Hamersley BI, with the exception of three iron bands from Goose Lake. These have a higher Ge/Si signature reminiscent of a higher hydrothermal fluid input (Fig. 4.15B). The Ge/Si ratio in the Isua BIF is even higher, likely reflecting a larger Ge input due to the more vigorous submarine hydrothermal venting at that time (Fig. 4.15B; Frei and Polat, 2007).

The greywacke samples in this study show very low Ge/Si, closer to upper continental crustal values, whereas the mudstones, which naturally have less silica, are more elevated in the Ge/Si (Fig. 4.15A). As the mudstones represent slow settling of pelagic clay- and silt-particles from iron-rich seawater, they may have inherited a hydrothermal Ge/Si component relative to the interbedded sandy greywackes. Therefore,

the Neoarchaean crustal Ge/Si value is better represented by the greywackes, which have values comparable to the modern (~0.13*10^{-5}, Fig. 4.15A). The extreme high SiO$_2$ content for some of the silica bands from Goose Lake (Fig. 4.15A) also have the same Ge/Si ratio as the greywackes, demonstrating the usefulness of the Ge/Si system to infer the silica and iron source characteristics and the interaction of different water masses in the seawater.

4.7.4. The nature of the interbedded rocks

4.7.4.1. Active volcanism during BIF deposition

The presence of a tuffaceous ash bed within the deep-water turbidite-BIF sequence suggests that the depositional basin was linked to adjacent volcanism. The detrital zircon record of the turbidite-BIF sequence supports this, as the, youngest zircons found in the associated greywackes have ages corresponding to the ca. 2635-2620 Ma Defeat Suite plutons (Ootes et al. 2009). These plutons are preserved in a northeast-southwest belt across the southern part of the craton (e.g., Davis et. al., 2003; Ootes et al., 2009). It is, therefore, likely that the tuff bed at Slemon Lake, dated at ca. 2620 Ma (Haugaard et al., in review) was derived from late stage volcanism related to this magmatic event.

Determining the source of a single ash tuff bed deposited in the Archaean marine environment is not without complications. Weathering, adsorption and leaching of elements during ash deposition through the water column may alter primary chemical attributes (e.g., Censi et al., 2007; Haugaard et al., 2016). For example, the 23-24 wt.% Al$_2$O$_3$ content of the tuff (Table 4.4) is likely a weathering phenomenon in the sense that other more mobile major elements were selectively leached away. The same with the high volatile content (3 wt. % LOI) suggests that the bed was altered to some degree. As such, classifying the rock type with the major elements is considered suspect. Utilizing HFSE ratios, the tuff appears chemically similar to the Defeat Suite granodiorite plutons (Fig. 4.12A). The Defeat Suite are I-type plutons, and have elevated chondrite-normalized LREE, Th and pronounced negative Nb, P and Ti anomalies analogous to modern magmatism along active continental margins such as the Andes (Figs. 4.12B, 4.12C and 4.12D; Ootes et al. 2009). The tuff from Slemon Lake displays the same

normalized pattern, suggesting that the depositional basin for the BIF-turbidites was within a larger, convergent margin (arc?)-type tectonic setting (Figs. 4.12B, 4.12C and 4.12D).

The REE and trace elements in Slemon Lake tuff bed are less fractionated than the Defeat Suite plutons and the older (ca. 2663Ma) Banting Group rhyolites (Fig. 4.12C). This pattern could reflect that (1) the tuffs parental magma was of more intermediate character than the Defeat and Banting rocks, or (2) the fine-grained ash particles reacted with the ambient seawater during settling, thereby inheriting a portion of the seawater HREE by ion adsorption to reactive particle surfaces. Also the weakly elevated Eu anomaly (Fig. 4.12C) could potentially be inherited from the ambient hydrothermal enriched seawater rather than being a direct proxy of the magma source. These seawater-influenced processes on the REE budget have similarly been demonstrated to occur for tuffaceous beds within the Hamersley BIF, Western Australia (Haugaard et al., 2016). In favor of hypothesis (1) above is the very low SiO_2 content (54 wt.%) and an elevated concentrations of trace metals (e.g., Cr, Ni and V) in the tuff bed relative to both the Defeat and Banting rocks.

4.7.4.2. The BIF-turbidite association

The presence of large volume of greywacke-turbidites with chemical sediment (BIF) is intriguing because the two deposits represent two significantly different styles of marine sedimentation. The BIF is characterized by a slow rainout of ferric oxyhydroxides and amorphous silica from low-energy seawater (below storm-wave base). The siliciclastic rocks represent dynamic and high-energy avalanche-like flow processes with depositional rates measured within days or even hours (e.g., Selley, 1988).

A slow background precipitation of the precursor components to BIF was periodically interrupted by influxes of clastic sediments sourced from distal-to-proximal unstable submarine fans. These pulses of sediment occasionally eroded the top portion of the underlying BIF unit leaving both erosional scour marks on the BIF surface (Fig. 4.3B) and intraformational rip-up mud clasts demonstrating the dynamic character of the sandy parts of the turbidites (see also Henderson, 1975).

We interpret the thickest turbidites to have been deposited proximal to the source channel at the submarine fan below the continental slope or ramp. The thinner and finer-grained sequences then represent channel-distal deposition delivered by sediment lobes prograding further out into more quiet and deeper water. As such, the BIF-turbidite deposition was restricted to deeper waters associated with the basin plain. A possible analogue to the BIF-turbidites is in the late-Archaean Beardmore-Geraldton metasedimentary belt in the Superior craton. There, a large proportion of the sedimentary rocks contain oxide-facies BIF that are interbedded with the same style turbidites as in this study (Barrett and Fralick, 1985; 1989). A model for that BIF-turbidite succession is a submarine interchannel setting (Barrett and Fralick 1989). In interchannel areas, between feeder channels and fan development, BIF could have precipitated alongside repeated episodes of clastic input from channel spill-over during the progradation of turbidite currents (Barrett and Fralick 1989). Although more sedimentologic work needs to be carried out on these interbedded deposits, it is evident that not all of the sandy greywackes are fining upwards (e.g., at Goose Lake). Instead, some display vertical unstructured sedimentology with a homogenous grain size distribution (Fig. 4.5).

If the BIF-turbidites were deposited within a back-arc basin, as suggested by Ootes et al. (2009) and supported by this study, it is likely that the tectonically active arc-terrain would supply a fast and large accumulation of sediments to the outer shelf through various distributary mouth bars. Subsequently, movement of this sediment could be triggered as gravity flows and slumps prograding down the continental slope, causing unsorted mass-flow deposits rather than true turbiditic deposits (e.g., Barrett and Fralick, 1989; Haugaard et al., 2013).

The nature of the more mafic ferruginous sediment is not as straight forward as the greywacke-mudstone turbidites. Field observations suggest that the ferruginous sediment at Damoti Lake contains both detrital magnetite grains and rip-up clasts of the underlying BIF (Waychison, 2010). They also demonstrate soft-sediment deformation of the BIF, suggesting that this lithofacies was formed by flow processes similar to the greywacke turbidites. At Point Lake, the sediment contains same style of angular detrital quartz grains (Fig. 4.8A) and multi-sourced zircon crystals (see Haugaard et al., in review for a fully detrital zircon overview of this bed) as the greywackes. As such, they represent

the contaminated base of the turbidite that is intermixed with the underlying BIF. This would furthermore explain their high iron content (Table 4.4) and why these sediment beds only are found immediately adjacent to the BIF beds. A redeposition of submarine silt and mud by turbiditic currents seems plausible. Supportive of this hypothesis is the variation of grain size within the ferruginous sediment (Fig. 4.4D) which could be related to depositional grading.

4.7.4.3. Sediment sources

The provenance of detrital zircon in the ca. 2620 Ma turbidites indicates that most of the detrital input from older volcanic rocks (ca. 2700 to 2660 Ma), with only a minor input of younger contemporaneous zircons (Ootes et al. 2009; Haugard et al. in review). The dominant source for the greywackes is therefore the older supracrustal rocks of the Slave craton (see Fig. 4.1b). Studies of the older (~2661 Ma) Burwash turbidites by Jenner et al. (1981), and later confirmed by Yamashita and Creaser (1999), show that those greywacke turbidites can best be explained by a mixture of 55% felsic volcanic rocks, 25% granite and 20% mafic-intermediate volcanic rocks similar in proportion as what is exposed in the Yellowknife area. The geochemistry of the younger greywackes in this study shows that these also have contributions from both felsic and mafic sources. The higher SiO_2, elevated Na_2O/K_2O ratio (although still ≤1) and lower content of Fe_2O_3 and MgO (relative to the corresponding mudstone and ferruginous sediment) collectively imply that the greywackes contain more quartz and feldspar than fine argillaceous material of chlorite and mica. However, when comparing these to the older Burwash Formation, the latter have a reverse ratio of Na_2O/K_2O, with sodium content between 1.5 to 2 times its potassium content (Henderson, 1975; Yamashita and Creaser, 1999). A Na_2O/K_2O ratio >1 relates to a higher albite content of the feldspars in these turbidites whereas the low Na_2O/K_2O in the turbidites in our study reflect a higher K-feldspar component in the source terrain or a higher recycling of the sediment.

The compositional heterogenic ferruginous sediment has a higher content of mafic minerals alongside lower SiO_2 and greater Fe_2O_3 and MgO content. It is important to point out that the high iron content may not be entirely due to the composition of the source material, but potentially a result of either interaction of the fine-grained detritus

with the deep iron-rich seawater prior to deposition or the assimilation of iron through the submarine erosion of the underlying BIF sediment as reported above. At Point Lake, a large input of angular quartz, together with many zircon inclusions in the biotite, points towards a significant contribution from greywacke sediment at this location. In contrast, the angular detrital grains at Damoti Lake are dominated by plagioclase (Fig. 4.8B) that may have been derived by input from more intermediate-to-mafic provenance.

To discriminate between different provenances of sediment, measurements of Th, La and Sc have previously proved useful as Th and La are incompatible and Sc compatible during magmatic differentiation (e.g., Taylor and McLennan, 1985). Scandium is highly compatible in clinopyroxene and, therefore, a good indicator of any mafic sources. Using those elements (Fig. 4.16A), the turbidite sediment, together with the Burwash turbidites, plot as intermediate between mafic sources (best represented by the Kam and Banting group basalts) and felsic sources (Banting Group rhyolite and Defeat Suite granodiorite plutons). In fact, the sediment are more mafic (lower Th/Sc and La/Sc) than the average upper crust of the Archaean. This is particularly the case for some of the mudstones and ferruginous sediments (Fig. 4.16A).

The evidence of ultra-fine graphite in the fine-grained portions of the ferruginous sediment and the mudstone facies is particularly pronounced at Damoti Lake, and locally at Goose Lake. Graphite, a reduced carbon form, has been reported from various chemical and pelitic rocks within Archaean sedimentary rocks (e.g., Beukes, 1973; Kamber et al., 2005; Haugaard et al., 2013) and has been linked to the first origin of photosynthetic microorganisms in the water column (e.g., Mojzsis et al., 1996; Rosing, 1999). As such, it may originally have been marine pelagic phytoplankton that was co-deposited with the fine-grained clay and silt material. Although the graphite only seems to be restricted to the mudstone and the fine-grained components of the ferruginous sediment, the interpretation of graphite being biologic in origin is far from straightforward because graphite can be produced abiologically during metamorphism by thermal decomposition of carbonate minerals such as siderite (e.g., Zuilen et al., 2003). It is evident, however, that within the ferruginous sediment the graphite only occurs as tiny inclusion trails within the larger randomly distributed biotite and amphibole porphyroblasts (Fig. 4.8E), demonstrating graphite formation before the main growth of

the porphyroblasts. Thus, whether the source of the organic matter is primary or secondary is unknown. If the ferruginous sediment assimilated the carbon after deposition, it may have been hydraulically emplaced during compaction, deformation and shearing of the sediment package as suggested by Waychison (2010).

4.8. Detrital control in BIF deposition

Along with the hydrothermal and seawater signatures in the BIF, the high amount of clastic input to the basin impacted the chemical sedimentation, and as such, the overall chemistry of the BIF. For example, during precipitation of the Slemon Lake BIF, fine-grained detritus was co-deposited, leading to a higher content of Al_2O_3, TiO_2, Zr, Th, Nb, and even to some degree, the REY in the BIF.

The detrital impact on BIF precipitation can be assessed by the concentrations of Al_2O_3 and TiO_2. It is generally believed that Al and Ti do not fractionate during weathering and transport within the sedimentary environment (e.g., Sugitani et al., 2006). Thus, the Al_2O_3/TiO_2 ratio in the detrital material deposited in the BIF basin would reflect the average Al_2O_3/TiO_2 ratio of the source detrital material. The BIF samples display a relative constant intermediate Al_2O_3/TiO_2 ratio of 25 (the best fit in Fig. 4.16B). This correlates well with the interbedded turbidite sediment, including the many Burwash turbidites reported by Yamashita and Creaser (1999) and, not surprisingly, it shows a dominant control on the detritus in the BIF from these lithologies. Although they share the same Al_2O_3/TiO_2 ratios, the lower content of both Al_2O_3 and TiO_2 in the turbidites from this study, relative to the Burwash turbidites (Fig. 4.16B), probably reflects modal differences in the proportion of fine sand, silt and clay. Due to a higher mafic input, the mudstones from Damoti Lake have elevated concentrations of TiO_2 approaching some of the Kam Group basaltic lithologies (Fig. 4.16B). The positive relationship between Th and Sc (Fig. 4.9E) also shows that the detritus in the BIF was delivered from already well-mixed sources, perhaps from activation of submarine sediment lobes on the paleo-continental outer slope.

The trace metals Ni and Cr in the BIF are largely controlled by the fine-grained mudstone and ferruginous sediment facies, not by the greywacke sediment (Fig. 4.16C). The Cr-Ni trends for many BIF have shown to be non-representative of the source that

provided the detritus because, unlike Cr, Ni is more likely to go in solution and as a result gets concentrated in the seawater and subsequently the BIF deposit (Konhauser et al., 2009). This will significantly lower the overall Cr/Ni ratio relative to the sources that provided those metals. In this study, the Cr/Ni ratio of ~1.6 is significantly lower than the ratio of the greywacke sediment of ~2.4 (Fig. 4.16C). However, the BIF Cr/Ni ratio seems to have been controlled by the finer-grained mudstone and ferruginous sediment and not the ambient seawater. This control from clastic sources is not surprising since the BIF basin was significantly impacted by turbiditic sedimentation and this demonstrates that the impact of detrital sediment in BIF deposition can obscure the subtle signal of the seawater chemistry.

4.9. Conclusions

The Neoarchaean (~2620 Ma) BIF of the Slave craton is found deposited within one of the most extensive and well-preserved turbidite basins in the world. The BIF contains micro- and meso-bands of chert and magnetite, along with well-crystallized amphiboles (grunerite and ferro-actinolite) and minor retrograde greenalite and stilpnomelane. The BIF is intercalated with greywacke-mudstone turbidites, ferruginous sediment and dacitic tuff.

On a layer-by-layer basis, there is relatively more silica in the iron bands than iron in the silica bands, a pattern that likely resulted from a continuous rainout of silica that was interrupted by pulses of iron rich deep water. The Ge/Si ratio supports a decoupling of silica and iron during BIF deposition, with weathering of local landmasses supplying the silica in the surface waters, while hydrothermal fluids with higher Ge/Si ratio supplied the deeper iron-rich waters.

A high input of clastic sediment contaminated the chemical precipitates on various scales. The BIF has similar Al_2O_3/TiO_2 and Cr/Ni ratios as the turbidite sediment, illustrating the strong control from the latter on the element budget in the BIF. Despite this, the BIF still records some important seawater features such as a NASC (North American Shale Composite)-normalized fractionated REY pattern with Pr/Yb<<1, and a positive La and Y anomaly (average Y/Ho=36). When normalizing to local shale, an even higher REY fractionation and La anomaly occur emphasizing the seawater influence on

the BIF deposition. The hydrothermal contribution to the ambient seawater is recorded as a pronounced Eu anomaly (average of 1.92) whereas parts of the BIF samples exhibit a negative Ce anomaly indicating that the presence of an oxygen agent large enough to fractionate Ce^{3+} (as Ce^{4+}) from neighboring REE.

The trace elements from the tuff bed at Slemon Lake reveals that the BIF was deposited in a basin influenced by volcanism from an active arc, presumably linked to the ca. 2635-2620 Ma Defeat magmatic suite. We propose that the most likely depositional scenario for the BIF is on the basin plain proximal to a steep continental slope. Here, turbidite currents and debris flows moved through submarine feeder channels, episodically interrupted the chemical rainout of ferric oxyhydroxides and amorphous silica.

References

Alexander, B.W., Bau, M., Andersson, P., 2009. Neodymium isotopes in Archean sea-water and implications for the marine Nd cycle in Earth's early oceans. Earth and Planetary Science Letters 283, 144–155.

Alexander, B.W., Bau, M., Andersson, P., Dulski, P., 2008. Continentally-derived solutes in shallow Archean seawater: rare earth element and Nd isotope evi- dence in iron formation from the 2.9Ga Pongola Supergroup, South Africa. Geochimica et Cosmochimica Acta 72, 378–394.

Alibert C., McCulloch M. T., 1993. Rare earth element and neodymium composition of the banded iron formations and associated shales from Hamersley, Western Australia, Geochimica et Cosmochimica Acta 57, 187-204.

Anders, E., Grevesse, N., 1989. Abundances of the elements: meteoric and solar. Geochimica et Cosmochimica Acta 53, 197–214.

Barrett, T. J., Fralick, P. W., 1985. Sediment redeposition in Archean Iron Formation: Examples from the Beardmore-Geraldton Belt, Ontario. Journal of Sedimentary Petrology 55, 205–212.

Barrett, T. J. and Fralick, P. W., 1989. Turbidites and iron formations, Beardmore-Geraldton, Ontario: application of a combined ramp/fan model to Archaean clastic and chemical sedimentation. Sedimentology 36, 221–234.

Bau, M., 1991. Rare earth element mobility during hydrothermal and metamorphic fluid–rock interaction and the significance of the oxidation state of europium. Chemical Geology 93, 219–230.

Bau, M., 1993. Effects of syn- and post-depositional processes on the rare-earth element distribution in Precambrian iron-forma- tions. European Journal of Mineralogy 5, 257–267.

Bau, M., 1999. Scavenging of dissolved yttrium and rare earths by precipitating iron oxyhydroxide: experimental evidence for Ce- oxidation, Y–Ho fractionation, and lanthanide tetrad effect. Geochimica et Cosmochima Acta 63, 67–77.

Bau, M., Dulski, P., 1992. Small-scale variations of the rare- earth element distribution in Precambrian iron formations. European Journal of Mineralogy 4, 1429–1433.

Bau, M., Möller, P., 1993. Rare earth element systematics of the chemically precipitated component in Early Precambrian iron formations and the evolution of the terrestrial atmosphere–hydrosphere–lithosphere system. Geochimica et Cosmochima Acta 57, 2239–2249.

Bekker, A., Slack, J. F., Planavsky, N., Krapež, B., Hofmann, A., Konhauser, K. O. and Rouxel, O. J., 2010. Iron formation: The sedimentary product of a complex interplay among mantle, tectonic, oceanic, and biospheric processes. Economic Geology 105, 467–508.

Bennett, V., Jackson, V. A., Rivers, T., Relf, C., Horan, P., Tubrett, M., 2005. Geology and U – Pb geochronology of the Neoarchean Snare River terrane : tracking evolving tectonic regimes and crustal growth. Canadian Journal of Earth Science 934, 895–934.

Bleeker, W., 2002. Archaean tectonics: a review, with illustrations from the Slave craton. In: Fowler, C.M.R., Ebinger, C.J., Hawkesworth, C.J. (Eds.), The Early Earth: Physical, Chemical and Biological Development, vol. 199. The Geological Society, London, 151–181 p.

Bleeker, W., Hall, B., 2007. The Slave Craton: Geological and Matallogenic Evolution, in Goodfellow, W.D., ed., Mineral Deposits of Canada: A synthesis of major Deposit-types, District Metallogeny, the evolution of geological provinces, and exploration methods. Geological Society of Canada, Mineral deposit division, Special Publication 5, 849-879.

Bleeker, W., Ketchum, J.W.F., Jackson, V.A., Villeneuve, M.E., 1999a. The Central Slave Basement Complex, Part I: its structural topology and autochthonous cover. Canadian Journal of Earth Science 36, 1083-1109.

Bolhar, R., Kamber, B.S., Moorbath, S., Fedo, C.M., Whitehouse, M.J., 2004. Characterisation of early Archaean chemical sediments by trace element signatures. Earth Planetary Scince Letters 222, 43–60.

Byrne, R. H. and Kim, K.-H., 1990. Rare earth element scavenging in seawater. Geochimica et Cosmochima Acta 54, 2645–2656.

Cantrell, K. J. and Byrne J. H., 1987. Rare earth element complex- ation by carbonate and oxalate ions. Geochimica et Cosmochima Acta 51, 597-605.

Censi P., Saiano F., Mazzola S. and Ferla P., 2007. Alteration effects of volcanic ash in seawater : Anomalous Y/Ho ratios in coastal waters of the Central Mediterranean sea. Geochimica et Cosmochima Acta 71, 5405–5422.

Davis, W. J., Hegner, E., 1992. Neodymium isotopic evidence for the tectonic assembly of Late Archean crust in the Slave Province, northwest Canada. Contributions to Mineralogy and Petrology 111, 493–504.

Davis, W., Jones, A., Bleeker, W., & Grütter, H., 2003. Lithosphere development in the Slave craton: a linked crustal and mantle perspective. Lithos 71, 575–589.

De Baar, H. J. W., Bacon M. P., Brewer, P. G., Bruland K. W., 1985. Rare earth elements in the Pacific and Atlantic Oceans. Geochimica et Cosmochimica Acta 49, 1943–1959.

Derry, L. A., Kurtz, A. C., Ziegler, K., Chadwick, O. A., 2005. Biological control of terrestrial silica cycling and export fluxes to water-sheds. Nature 433, 728–731.

Drever, J. I., 1974. Geochemical model for the origin of Precambrian Banded Iron Formations. Geological Society of American Bulletin 85, 1099–1106.

Dymek, R. F., Klein, C., 1988. Chemistry, petrology and origin of banded iron-formation lithologies from the 3800 Ma Isua supracrustal belt, west Greenland. Precambrian Research 39, 247-302.

Eggleton, R., Chappell, B., 1978. The crystal structure of stilpnomelane Part III Chemistry and physical properties. Mineralogical Magazine 4, 361-368.

Ferguson, M., Waldron, W.F., Bleeker, W. (2005). The Archean deep-marine environment: turbidite architecture of the Burwash Formation, Slave Province, Northwest Territories. Canadian Journal of Earth Sciences 42, 935-954.

Frei, R., Polat, A., 2007. Source heterogeneity for the major components of ~3.7 Ga Banded Iron Formations (Isua Greenstone Belt, Western Greenland): tracing the nature of interacting water masses in BIF formation. Earth Planetary Science Letters 253, 266–281.

Frith, R. A, 1987. Precambrian geology of the Hackett River area, District of Mackenzie, NWT. Geological Survey of Canada, Memoir 417, 61 p.

Froelich, P. N., Blanc, V., Mortlock, R. A., Chillrud, S. N., Dunstan, W., Udomkit, A., and Peng, T.- H., 1992, River fluxes of dissolved silica to the ocean were higher during glacials: Ge/Si in diatoms, rivers, and oceans: Paleoceanography 7, 739–767.

Gole, M.J., 1980b. Low temperature retrograde minerals in metamorphosed Archean banded iron formations, western Australia. Canadian Mineralogy 18, 205–214.

Gole, M.J. 1980a. Mineralogy and petrology of very low metamorphic grade Archaean banded iron-formations, Weld Range, Western Australia. American Mineralogist 66, 8-25.

Gross, G., 1980. A classification of iron formations based on depositional environments. Canadian Mineralogy 18, 215–222.

Gross, G., 1983. Tectonic systems and the deposition of iron-formation. Precambrian Res. 20, 171–187.

Hamade, T., Konhauser, K.O., Raiswell, R., Goldsmith, S., Morris, R.C., 2003. Using Ge/Si ratios to decouple iron and silica fluxes in Precambrian banded iron for- mations. Geology 31, 35–38.

Haugaard, R., Frei, R., Stendal, H., Konhauser, K., 2013. Petrology and geochemistry of the ~2.9 Ga Itilliarsuk banded iron formation and associated supracrustal rocks, rocks, West Greenland: source characteristics and depositional environment. Precambrian Research 229, 150–176.

Holland, H. D., 1973. The oceans: A possible source of iron in iron formations. Economic Geology 68, 1169-1172.

Henderson, J. B., 1970. Stratigraphy of the Archean Yellowknife Supergroup, Yellowknife Bay–Prosperous Lake Area, District of Mackenzie. Geological Survey of Canada Paper 70-26.

Henderson, J. B., 1975. Stratigraphy of the Archean Yellowknife Supergroup at Yellowknife, District of Mackenzie. Geological Survey of Canada Bulletin 246, 62 p.

Holland, H.D., 1973. The oceans: a possible source of iron in iron formations. Economic Geology 68, 1169–1172.

Jacobsen, S. B., Pimental-Klose, M. R., 1988. A Nd isotope study of the Hamersley and Michipicoten banded iron formations: The source of REE and Fe in Archaean oceans. Earth and Planetary Science Letters 87, 29-44.

Jenner, G. A., Fryer, B. J., McLennan, S. M., 1981. Geochemistry of the Archean Yellowknife Supergroup. Geochimica et Cosmochimica Acta 45, 1111–1129

Kato, Y., Yamaguchi, K., Ohmoto, H., 2006. Rare earth elements in Precambrian banded iron formations: Secular changes of Ce and Eu anomalies and evolution of atmospheric oxygen. Geological Society of America Memoirs 198, 269-289.

Klein, C., 1974. Greenalite, stilpnomelane, minnesotaite, crocidolite and carbonates in a very low grade metamorphic precambrian iron-formation. Canadian Mineralogist 12, 1–24.

Klein, C., 2005. Some Precambrian banded iron-formations (BIFs) from around the world: their age, geologic setting, mineralogy, metamorphism, geochemistry, and origins. American Mineralogist 90, 1473–1499.

Klein, C., Beukes, N. J., 1989. Geochemistry and sedimentology of a facies transition from limestone to iron-formation deposion in the Early Proterozoic Transvaal Supergroup, South Africa. Economic Geology 84, 1733-1774.

Konhauser, K.O., Pecoits, E., Lalonde, S.V., Papineau, D., Nisbet, E.G., Barley, M.B., Arndt, N.T., Zahnle, K., Kamber, B.S., 2009. Oceanic nickel depletion and a methanogen famine before the Great Oxidation Event. Nature 458, 750–754.

Locock, A. J. 2014. An Excel spreadsheet to classify chemical analyses of amphiboles following the IMA 2012 recommendations. Computers & Geosciences 62, 1-11.

Ootes, L., Davis, W.J., Bleeker, W., Jackson, V.A., 2009. Two Distinct Ages of Neoarchean Turbidites in the Western Slave Craton: Further Evidence and Implications for a Possible Back-Arc Model. The Journal of Geology 117, 15–36.

Padgham, W., 1992. Mineral deposits in the Archean Slave Structural Province; lithological and tectonic setting. Precambrian Research 58, 1–24.

Padgham, W., Fyson, W., 1992. The Slave Province: a distinct Archean craton. Canadian Journal of Earth science 29, 2072-2086.

Pecoits, E., Smith, M.L., Catling, D.C., Philippot, P., Kappler, A., and Konhauser, K.O., 2015. Atmospheric hydrogen peroxide and Eoarchean iron formations. Geobiology, 13:1-14.

Pehrsson, S., Villeneuve, M., 1999. Deposition and imbrication of a 2670–2629 Ma supracrustal sequence in the Indin Lake area, southwestern Slave Province, Canada. Canadian Journal of Earth Science 36, 1–21.

Pickard, A.L., Barley, M.E., Krapeˇ z, B., 2004. Deep-marine depositional setting of banded iron formation: sedimentological evidence from interbedded clastic sedimentary sequence in the rocks in the early Palaeoproterozoic Dales Gorge Member of Western Australia. Sedimentary Geology 170, 37–62.

Piper, D.J.W., and Normark, W.R. 2001. Sandy fans: from Amazon to Hueneme and beyond. AAPG Bulletin 85, 1407–1438.

Polat, A., Frei, R., 2005. The origin of early Archean banded iron formations and of continental crust, Isua, southern West Greenland. Precambrian Research 138, 151–175.

Mortlock, R. A., Froelich, P. N., 1987. Continental weathering of germanium; Ge/Si in the global river discharge, Geochimica et Cosmochimica Acta 51, 2075–2082.

Selley, R.C., 1988. Applied Sedimentology. Academic Press, 446 p.

Sholkovitz E. R., Landing W. M., and Lewis B. L. (1994) Ocean particle chemistry: The fractionation of rare earth elements be- tween suspended particles and seawater. Geochimica et Cosmochima Acta 58, 1567-1579.

Simonson, B. M., 1985, Sedimentological constraints on the origins of Precambiran iron-formations. Geological Society of America Bulletin 96, 244-252.

Steinhofel, G., von Blackenburg, F., Horn, I., Konhauser, K.O., Beukes, N., Gutzmer, J., 2010. Deciphering formation processes of banded iron formations from the Transvaal and the Hamersley Sequence by combined Si and Fe isotope analysis using UV femtosecond laser ablation. Geochimica et Cosmochima Acta 74, 2677–2696.

Sugitani, K., Yamashita, F., Nagaoka, T., Yamamoto, K., Minami, M., Mimura, K., Suzuki, K., 2006. Geochemistry and sedimentary petrology of Archean clastic sedimentary rocks at Mt. Goldsworthy, Pilbara Craton, Western Australia: evi- dence for the early evolution of continental crust and hydrothermal alteration. Precambrian Research 147, 124–147.

Taylor, S.R., McLennan, S.M., 1985. The Continental Crust: Its Composition and Evo-lution. Blackwell Scientific, Oxford, 312 p.

Taylor, S.R., McLennan, S.M., 2009. Planetary Crusts: Their Composition, Origin and Evolution. Cambridge University Press, New York, 378 p.

Trendall, A.F., Blockley, J.G., 2004. Precambrian iron-formation. In: Eriksson, P.G., Altermann, W., Nelson, D.R., Mueller, W.U., Catuneanu, O. (Eds.), The Precam- brian

Earth: Tempos and Events. Developments in Precambrian Geology, 12. Elsevier, Amsterdam, pp. 403–421.

Viana, A.R., Faugeres, J.-C., Stow, D.A.V., 1998. Bottom-current-controlled sand deposits - a review of modern shallow- to deep-water environments. Sedimentary Geology 115, 53-80.

Windley, B.F. (1984). The Evolving Continents. John Wiley and Sons Limited, 399 pp.

Yamashita K. and Creaser R. A. (1999) Geochemical and Nd isotopic constraints for the origin of late Archean turbidites from the Yellowknife area, Northwest Territories, Canada. Geochimica et Cosmochima Acta 63, 2579–2598.

Yamashita, K., Creaser, R. A., Stemler, J. U., Zimaro, T.W. 1999. Geochemical and Nd-Pb isotopic systematics of late Archean granitoids, southwestern Slave Province, Canada: constraints for granitoid origin and crustal isotopic structure. Canadian Journal of Earth Science 36, 1131–1147.

Table 4.1. Mineral data of the various amphiboles in the BIF and the interbedded ferruginous sediment.

Analysis (wt%)	BIF Grunerite	-	-	- Ferro-actinolite	-	-	BIF/Ferruginous sediment Ferro-hornblende		
	Min	Max	Ave	Min	Max	Ave	Min	Max	Ave
SiO_2	49.49	50.08	49.87	47.92	50.92	49.54	40.09	46.01	42.07
TiO_2	0.00	0.01	0.00	0.00	0.06	0.02	0.01	0.33	0.14
Al_2O_3	0.10	0.52	0.25	1.28	3.96	2.39	5.61	16.45	12.71
Cr_2O_3	0.00	0.02	0.01	0.00	0.02	0.01	0.00	0.10	0.02
MnO	0.16	0.23	0.20	0.05	0.08	0.07	0.04	0.19	0.12
FeO	43.32	45.27	44.14	27.36	31.45	28.87	20.08	28.91	23.31
Fe_2O_3	0.00	0.30	0.04	0.93	3.52	2.11	1.78	5.21	3.58
MgO	3.10	4.18	3.52	3.67	5.16	4.45	1.65	5.87	3.81
CaO	0.49	1.30	0.76	10.60	11.51	11.26	11.10	11.56	11.33
SrO	0.00	0.03	0.00	0.00	0.08	0.05	0.00	0.05	0.01
Na_2O	0.00	0.09	0.05	0.20	0.50	0.32	0.71	1.68	1.33
K_2O	0.00	0.04	0.01	0.05	0.21	0.12	0.32	0.77	0.44
H_2O+	1.85	1.86	1.85	1.91	1.93	1.92	1.88	1.97	1.94
Cl	0.0000	0.0170	0.0035	0.0000	0.0120	0.0052	0.0000	0.0280	0.0037
Total	99.94	101.15	100.72	100.94	101.39	101.15	99.86	101.58	100.81

Formula assignments - based on 24 (OH, F, Cl, O)

	Min	Max	Ave	Min	Max	Ave	Min	Max	Ave
Si	7.93	8.04	8.00	7.41	7.81	7.64	6.17	7.19	6.46
Al	0.01	0.07	0.04	0.19	0.59	0.36	0.81	1.84	1.54
Ti	0.00	0.00	0.00	0.00	0.01	0.00	0.00	0.04	0.02
Al	0.02	0.05	0.03	0.04	0.13	0.08	0.22	1.14	0.75
Cr	0.00	0.00	0.00	0.00	0.00	0.00	0.00	0.01	0.00
Fe^{3+}	0.01	0.03	0.02	0.11	0.41	0.24	0.20	0.62	0.42
Fe^{2+}	3.96	4.24	4.12	3.48	3.89	3.65	2.49	3.72	2.95
Mg	0.74	0.99	0.84	0.85	1.18	1.02	0.39	1.32	0.87
Mn^{2+}	0.02	0.03	0.03	0.01	0.01	0.01	0.01	0.03	0.02
Fe^{2+}	1.74	1.85	1.80	0.04	0.19	0.08	0.03	0.10	0.05
Ca	0.08	0.22	0.13	1.76	1.89	1.86	1.81	1.92	1.86
Sr	0.00	0.00	0.00	0.00	0.01	0.00	0.00	0.01	0.00
Na	0.00	0.03	0.01	0.03	0.07	0.05	0.04	0.10	0.07
Na	0.00	0.01	0.01	0.03	0.08	0.05	0.14	0.43	0.33
K	0.00	0.01	0.00	0.01	0.04	0.02	0.06	0.15	0.09
OH	2.00	2.00	2.00	2.00	2.00	2.00	1.99	2.00	2.00
Cl	0.0010	0.0050	0.0026	0.0010	0.0030	0.0025	0.0010	0.0070	0.0019

Table 4.2. Mineral data of greenalite and stilpnomelane from the Goose Lake BIF.

	Greenalite[*]			Stilpnomelane[#]		
	Min	Max	Ave	Min	Max	Ave
SiO_2	34.55	35.58	35.23	41.35	45.04	44.08
TiO_2	0.00	0.02	0.01	0.00	0.02	0.00
Al_2O_3	0.14	1.97	0.71	4.62	6.49	6.05
FeO	49.57	52.85	51.93	31.85	35.80	32.91
Fe_2O_3	-	-	-	3.93	4.42	4.06
Cr_2O_3	0.00	0.04	0.01	0.00	0.04	0.01
MnO	0.11	0.20	0.16	0.04	0.08	0.06
MgO	0.89	1.23	1.07	1.59	2.05	1.74
CaO	0.01	0.12	0.05	0.04	0.37	0.11
Na_2O	0.01	0.07	0.03	0.36	1.61	0.94
K_2O	0.00	0.18	0.03	2.01	4.10	2.79
Cl	0.48	1.05	0.77	0.03	0.17	0.08
H_2O calc	9.72	11.24	10.04	7.28	8.54	7.77
O=F,Cl	-0.24	-0.11	-0.17	-0.04	-0.01	-0.02
Total	97.83	100.95	99.88	98.52	101.87	100.18
	Formula assignments based on 14 oxygen equivalent (10 oxygen and 8 OH,F,Cl)			Formula assignments based on 15 octahedral and tetrahedral cations and 27 (O,OH,F,Cl)		
	Min	Max	Ave	Min	Max	Ave
Si	4.11	4.30	4.21	7.52	7.94	7.83
Al	0.00	0.00	0.00	0.99	1.24	1.11
Al	0.02	0.28	0.10	0.00	0.28	0.16
Ti	0.00	0.00	0.00	0.00	0.00	0.00
Fe^{2+}	5.09	5.29	5.20	4.70	5.44	4.89
Fe^{3+}	-	-	-	0.52	0.60	0.54
Mn	0.01	0.02	0.02	0.01	0.01	0.01
Mg	0.16	0.22	0.19	0.43	0.54	0.46
Ca	0.00	0.02	0.01	0.01	0.07	0.02
Na	0.00	0.02	0.01	0.12	0.55	0.32
K	0.00	0.03	0.00	0.46	0.95	0.63
O	10.00	10.00	10.00	19.85	21.35	20.92
OH	7.78	7.90	7.84	5.63	7.12	6.05
Cl	0.10	0.22	0.16	0.01	0.05	0.03
H_2O	-	-	-	1.50	1.64	1.58

[*]Final weight percent values with H_2O calculated from OH content. Total Fe as Fe2+ only.

[#]Final weight percent values with H_2O calculated from OH content. Oxidation state of Fe assumed to be $Fe^{3+}/(Fe^{2+}+Fe^{3+}) = 0.1$.

Table 4.3. Selected major and trace elements from the Neoarchean BIF.

Sample	D.L.	Slemon Lake 8A (bulk)	8B (Si)	8C (Fe)	Damoti Lake 22A (bulk)	22C (bulk)	Point Lake 29B (bulk)	29C-1 (bulk)	29D-1 (bulk)	Goose Lake 12140-A (Si)	12140-B (Fe)	10142-A (Si)	10142-B (Fe)	10B14 2-A (Si)	10B142-B (Fe)	24164 (bulk)
Element (wt.%)	D.L.															
SiO_2	0.01	45.13	68.7	33	66.7	53.6	53.1	49.15	46.8	92.86	25.77	80.02	20.3	93.68	22.68	45.38
Al_2O_3	0.01	2.96	5.39	2.21	1.39	1.58	1.11	1.49	1.07	0.08	2.15	0.41	1.62	0.08	0.98	1.19
$Fe_2O_3(t)$	0.01	48.36	15.8	63.4	29.8	43.7	41.6	47.93	51.8	4.12	64.31	17.15	74.62	4.76	72.75	50.99
TiO_2	0.001	0.124	0.19	0.1	0.06	0.08	0.04	0.042	0.05	0.004	0.096	0.008	0.072	0.005	0.052	0.049
MgO	0.01	1.51	2.83	1.03	1.16	1.28	0.4	0.78	0.56	0.22	1.92	1.25	1.33	0.35	0.88	2.07
CaO	0.01	0.9	1.86	0.24	0.16	0.28	3.02	1.73	1.09	1.36	5.68	1.08	1.93	0.3	2.49	2.4
Na_2O	0.01	< D.L.	< D.L.	< D.L.	0.03	0.08	0.12	0.13	0.07	0.01	0.21	0.05	0.15	0.01	0.1	0.11
K_2O	0.01	0.98	1.89	0.81	0.54	0.55	0.04	0.08	0.05	0.01	0.22	0.04	0.18	0.01	0.07	0.06
MnO	0.001	0.036	0.06	0.03	0.02	0.03	0.05	0.043	0.04	0.015	0.088	0.025	0.04	0.011	0.061	0.041
P_2O_5	0.01	0.4	0.14	0.2	0.02	0.05	0.15	0.15	0.08	0.12	0.17	< D.L.	0.16	< D.L.	0.57	0.15
LOI		0.37	3.31	-0.8	-0.37	-0.8	0.56	-1.08	-1.6	1.1	-1.69	-0.46	-1.21	0.01	-1.75	-2
Total		100.8	100	100	99.5	101	100	100.4	100	99.9	98.91	99.55	99.2	99.21	98.91	100.4
Zr (ppm)	1	17	25	13	6	8	6	7	7	1	13	1	10	2	7	7
Nb	0.2	2.2	1.7	1.5	1.8	1.6	2	1.5	1.2	2.4	1.3	2.8	1	1.7	0.8	1.1
Th	0.05	1.25	2.1	0.95	0.51	0.57	0.46	0.42	0.54	0.06	1.09	0.06	0.77	0.1	0.48	0.52
Hf	0.1	0.5	0.7	0.3	0.2	0.2	0.2	0.2	0.2	< 0.1	0.4	< 0.1	0.2	< 0.1	0.2	0.2
Rb	1	47	88	40	64	61	1	3	< D.L.	< D.L.	6	< D.L.	8	< D.L.	2	2
Sc	0.01	3.94	5.62	3	2.31	2.47	1.48	1.62	1.61	0.42	3.53	0.24	2.69	0.84	1.8	2.13
Cr	0.5	31.5	45	27.6	15.8	17.3	19.6	19.7	25.5	< 0.5	24.9	< 0.5	19.1	< 0.5	16.1	19.5
Ni	1	25	30	19	11	11	11	14	10	2	17	3	12	4	10	11
V	5	33	19	39	18	22	15	20	13	< D.L.	30	< D.L.	22	5	17	15
Ta	0.01	1.77	0.15	0.09	4.27	4.07	4.89	3.21	2.43	7.48	1.11	8.1	0.92	5.25	0.81	1.73
Ge	0.5	5	2.8	5.7	3.7	4.3	2.1	2.5	2.5	1.4	7.4	1	6.8	2.2	8.8	7
U	0.01	0.46	0.57	0.42	0.13	0.22	0.13	0.18	0.16	0.03	0.25	0.02	0.21	0.05	0.18	0.12
Mo	2	< D.L.	< D.L.	< D.L.	< D.L.	< D.L.	< D.L.	< D.L.	< D.L.	< D.L.	< D.L.	< D.L.	< D.L.	< D.L.	< D.L.	< D.L.
S (%)	0.001	0.067	0.11	0.01	0.01	0.01	0	0.007	0.03	0.017	0.01	0.008	1.03	0.171	0.651	0.091
La	0.05	8.42	10.1	10	3.13	1.69	3.35	4.73	3.03	1.93	5.38	0.37	5.74	0.97	5.76	2.79
Ce	0.05	13.9	16.9	14.4	5.02	3.13	5.01	8.19	4.68	2.91	9.96	0.52	11.1	1.48	10.8	5.45
Pr	0.01	1.46	1.77	1.44	0.49	0.41	0.54	0.87	0.41	0.31	1.19	0.06	1.33	0.17	1.25	0.67
Nd	0.05	5.59	6.78	5.23	1.63	1.61	2.06	3.11	1.26	1.48	4.8	0.26	5.32	0.65	5.2	2.62
Sm	0.01	1.01	1.25	0.87	0.35	0.32	0.38	0.49	0.22	0.33	1.04	0.03	1.23	0.15	1.16	0.67
Eu	0.005	0.328	0.52	0.26	0.19	0.12	0.29	0.202	0.11	0.229	0.534	0.025	0.376	0.064	0.415	0.279
Gd	0.01	0.99	1.21	0.71	0.46	0.33	0.43	0.62	0.25	0.28	1.16	0.04	1.56	0.17	1.61	0.79
Tb	0.01	0.18	0.22	0.12	0.07	0.06	0.07	0.1	0.05	0.04	0.2	< 0.01	0.26	0.04	0.28	0.11
Dy	0.01	1.19	1.47	0.79	0.51	0.36	0.41	0.61	0.34	0.27	1.24	0.04	1.72	0.27	1.87	0.81
Y	2	10	11	5	4	3	3	4	3	4	9	4	12	<D.L.	15	7
Ho	0.01	0.28	0.33	0.18	0.11	0.09	0.09	0.14	0.08	0.06	0.27	< D.L.	0.4	0.06	0.42	0.19
Er	0.01	0.91	1.06	0.58	0.32	0.29	0.27	0.45	0.25	0.2	0.86	0.03	1.25	0.2	1.32	0.63
Tm	0.005	0.141	0.18	0.09	0.05	0.05	0.04	0.072	0.05	0.03	0.139	0.006	0.203	0.037	0.191	0.102
Yb	0.01	0.97	1.34	0.63	0.34	0.38	0.26	0.52	0.29	0.18	0.97	< D.L.	1.32	0.25	1.18	0.62
Lu	0.002	0.163	0.23	0.1	0.06	0.06	0.04	0.08	0.04	0.027	0.158	0.007	0.208	0.035	0.187	0.102
ΣREE		35.5	43.4	35.4	12.7	8.9	13.2	20.2	11.1	8.3	27.9	1.4	32.0	4.5	31.6	15.8
$(Pr/Yb)_{NASC}$		0.59	0.52	0.90	0.57	0.42	0.81	0.66	0.55	0.68	0.48	-	0.40	0.27	0.42	0.42
$(La/La^*)_{NASC}$		1.22	1.21	1.36	1.12	0.91	1.31	1.04	1.19	2.15	1.04	1.65	0.98	0.91	1.20	1.13
$(Eu/Eu^*)_{NASC}$		1.40	1.80	1.40	2.24	1.59	3.26	1.69	2.00	3.40	2.15	-	1.24	1.85	1.56	1.37
Y/Ho		35.7	33.3	27.8	36.4	33.3	33.3	28.6	37.5	66.7	33.3	-	30.0	-	35.7	36.8

Table 4.4. Selected major and trace elements of the turbidite sediments associated with the BIF.

Lithology		Tuff bed	Greywacke	-	-	Mudstone	-	Ferruginous sediment	-	-	-
Location		Slemon Lake	-	Point Lake	Goose Lake	Damoti Lake	Goose Lake	Damoti Lake	-	-	Point Lake
Sample		RH-chisel	RHNWT-9A	RHNWT-29A	RH18140	RHNWT-20	RH36155	RHNWT-21	RHNWT-23A	RHNWT-23B	RHNWT-29C-2
Element (wt.%)	D.L.										
SiO_2	0.01	54.08	67.25	65.99	72.19	50.82	59.44	51.81	45.6	49.46	48.9
Al_2O_3	0.01	23.44	12.78	13.18	13.42	12.65	14.12	7.19	13.89	13.1	11.8
$Fe_2O_3(t)$	0.01	6.64	9	9.21	3.69	23.86	14.37	33.79	25.93	24.82	23.44
TiO_2	0.001	0.49	0.51	0.52	0.42	0.67	0.59	0.39	0.60	0.67	0.52
MgO	0.01	2.8	2.21	2.5	1.47	4.82	2.86	2.99	4.88	5.09	4.73
CaO	0.01	0.84	1.31	1.55	1.63	0.11	0.75	2.63	1.52	0.62	5.66
Na_2O	0.01	3.54	3.04	2.5	2.69	< 0.01	0.26	0.34	0.65	0.07	0.59
K_2O	0.01	5.17	2.91	3.21	3.2	0.03	4.15	1.24	2.53	0.92	2.61
MnO	0.001	0.029	0.026	0.033	0.042	0.068	0.04	0.054	0.067	0.072	0.1
P_2O_5	0.01	0.15	0.1	0.1	0.07	0.09	0.07	0.07	0.05	0.1	0.15
LOI		2.96	0.92	0.89	0.91	5.81	3.66	0.27	4.15	5.4	1.22
Total	0.01	100.1	100.1	99.68	99.78	98.92	100.3	100.8	99.87	100.3	99.71
Zr (ppm)	1	202	136	103	105	78	99	60	149	96	113
Nb	0.2	10.7	5	3.4	5.50	5.4	5	3	8	6	4.4
Th	0.05	21.8	11	5.97	7.02	7.05	9.9	3.7	13.3	6.6	5.44
Hf	0.1	6.3	3.1	2.6	2.98	2.2	2.4	1.4	3.8	2.2	2.9
U	0.01	6.83	3.4	1.95	2.15	2.28	2.6	0.9	3.3	2.2	1.46
Ta	0.01	2.32	1.8	1.71	0.65	0.96	1.3	1.2	1.2	0.9	1.11
Sr	2	319	833	377	299.00	9	191	95	2494	422	31
Rb	1	154	114	113	134.00	3	185	103	208	77	110
Y	1	19	11	12	9.21	7	11	8	18	11	5
Sc	0.01	9.5	11	11.9	-	16.3	17	13	18	18	11.6
Cr	0.5	44.3	120	148	105	141	120	80	120	120	129
Ni	1	46	50	63	43.1	74	70	50	70	60	53
V	5	70	85	89	66.5	121	124	86	121	138	88
Ge	0.5	2	2	1.1	-	2	3	4	5	4	2.7
S (%)	0.001	0.005			0.004	-	0.005				0.01
La	0.05	16.9	25	21.4	22.1	21	23.5	13.1	34.4	20.2	18.4
Ce	0.05	37.1	50.4	46.2	50.7	41.4	45.2	28.4	72.1	40.8	37.8
Pr	0.01	4.37	5.63	5.27	5.80	4.49	5.16	3.61	8.83	4.87	4.4
Nd	0.05	17.3	20.6	19.6	21.5	16.6	19	15	32.4	17.6	17.6
Sm	0.01	3.81	3.5	3.67	3.69	3.3	3.3	2.9	5.7	3.1	3.22
Eu	0.005	1.48	0.76	1	1.11	1.26	1	1.1	1.83	1.31	1.13
Gd	0.01	3.24	2.7	2.85	2.91	2.83	2.6	2.3	4	2.4	2.63
Tb	0.01	0.49	0.4	0.42	0.33	0.44	0.4	0.3	0.6	0.4	0.37
Dy	0.01	2.88	2.2	2.28	1.83	2.71	2.2	1.7	3.6	2.1	1.95
Ho	0.01	0.56	0.4	0.41	0.35	0.54	0.5	0.3	0.7	0.4	0.38
Er	0.01	1.61	1.3	1.19	1.02	1.55	1.4	1	2.1	1.2	1.05
Tm	0.005	0.24	0.20	0.17	0.14	0.23	0.20	0.15	0.30	0.19	0.15
Yb	0.01	1.51	1.40	1.16	0.92	1.52	1.40	1.10	2.00	1.30	1.01
Lu	0.002	0.24	0.21	0.17	0.13	0.22	0.21	0.17	0.30	0.18	0.17

Figure 4.1. (A) The main geology of the Slave craton with the four sample sites. Note, the Slemon Lake contains tuff beds with a crystallization age of ca. 2620 Ma (Haugaard et al., in review), which defines the age of the Slave craton Neoarchaean BIF-turbidites. The crystallization age of ca. 2661 Ma (Bleeker and Villeneuvre, 1995) defines the age of the older Burwash Formation turbidites. (B) The supracrustal stratigraphy in the Slave craton with the major plutonic events illustrated. The Neoarchaean BIF in this study is hosted within the Package II greywacke-mudstone turbidites. Map and stratigraphy modified after Bleeker (2002) and Ootes et al. (2009).
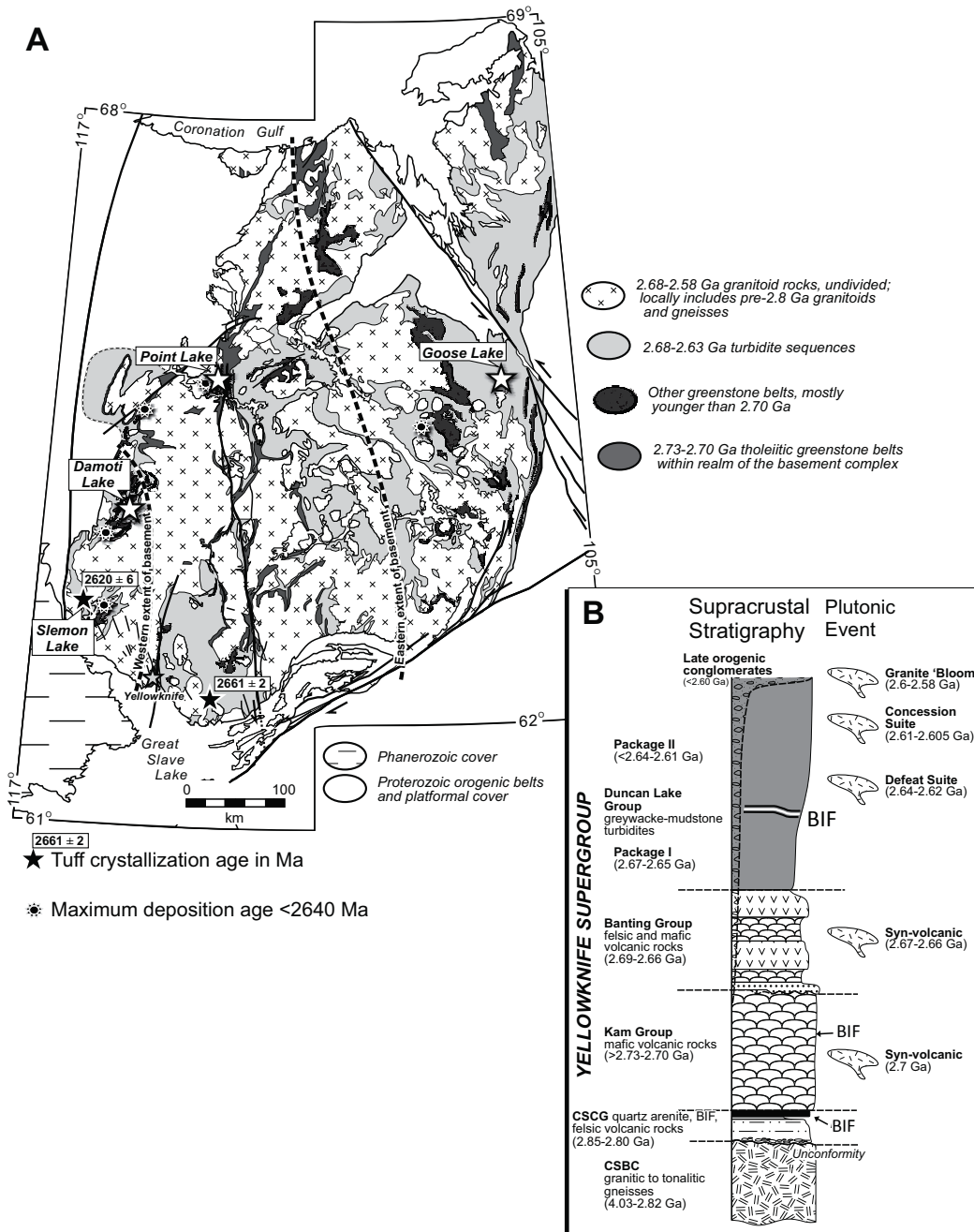
Figure 4.2. Slemon Lake BIF. (A) Faulted magnetite-rich BIF bordered by two sandy greywacke deposits. (B) Hematite weathered BIF with tight folds. (C) Close up photo of a fresh hand-cut sample showing alternating bands of magnetite and silica. Note the microbands of chert within mesobands of magnetite (white arrows). The greenish color in the silica bands is due to fine-grained silicates. The sample numbers represent the silica and iron bands separated for geochemical analysis (see Table 4.3). (D, E) Silicate-BIF with lesser amount of magnetite relative to (A). The greenish color is due to the existence of actinolite. (F) Fine-scale climbing ripple lamination in the top part of the greywacke unit. (G) Tuff ash bed found hosted within fine-grained greywacke/silty mudstone unit immediately above the BIF deposit in (D).

Figure 4.3. Point Lake BIF. (A, B) BIF interbedded with sandy greywacke. The BIF within the greywackes has a flat and sharp lower contact and where preserved, a wavy and erosional upper contact (white arrows in B). (C) Fine-scale microbands of the oxide-BIF. (D) Sedimentary dyke generated when the sediment was still wet during burial and compaction. (E) Ferruginos sediment consists of dark coarse-grained hornblende found concordant with the BIF. The petrography and geochemistry of the bed is studied in this paper (sample RHNWT-29C-2).
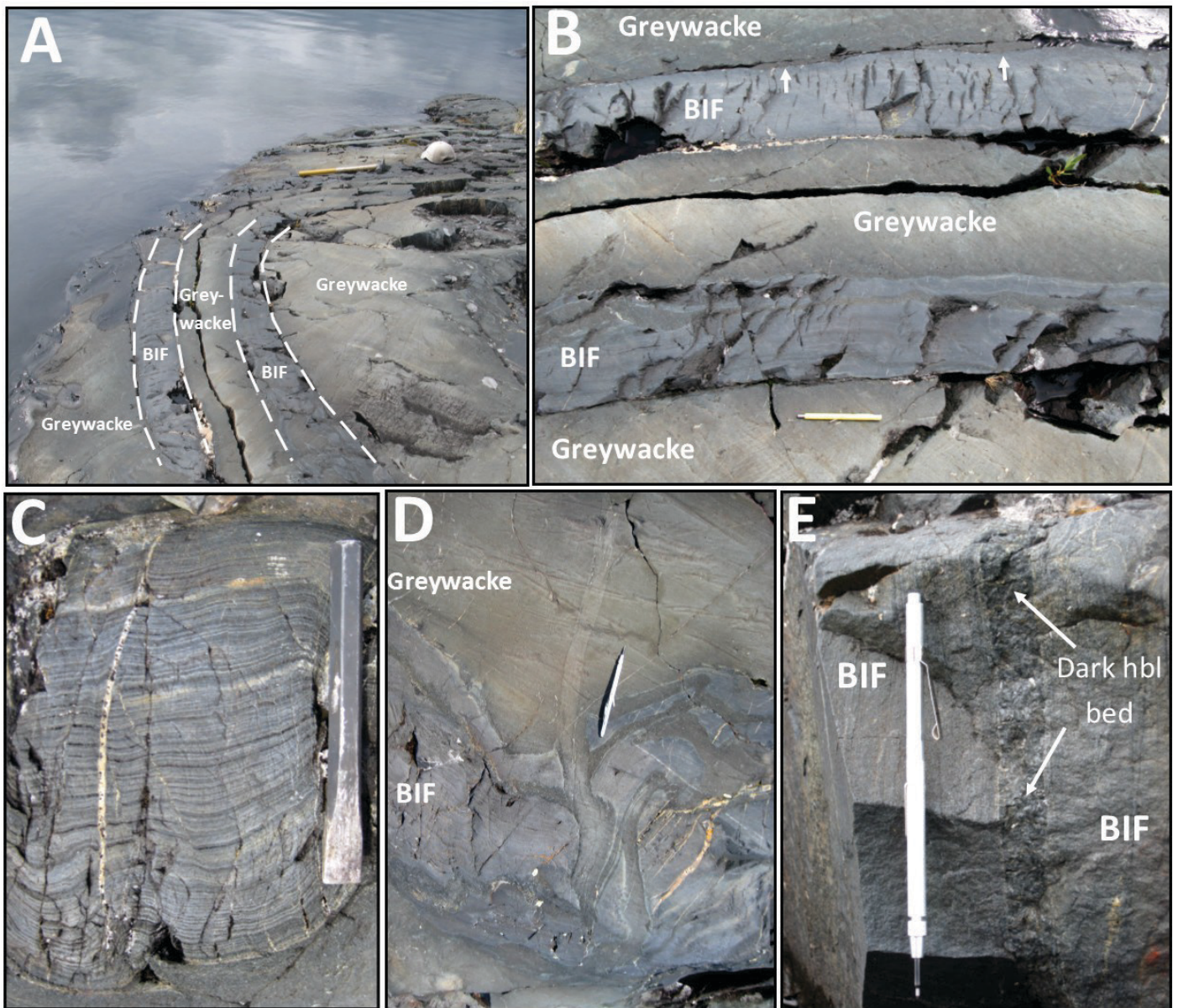
Figure 4.4. Damoti and Goose Lake BIF. (A) The BIF outcrop at Damoti Lake showing alternating chert and magnetite mesobands. (B, C). Close up photos showing magnetite micobands within chert mesobands. The mesobands contain radiating grunerite crystals (upper part of C). The chert nodule in (C) was likely generated by differential compaction during late stage diagenesis. (D) Hornblende-rich ferruginous sediment showing fining upward grain size distribution. The upper finer-grained greyish beds contain biotite porphyroblasts, plagioclase and graphite. (E) Goose Lake BIF showing a similar style of mesobands as at Damoti Lake. (F) Pristine core samples from Goose Lake with amphibole growth on the magnetite chert interface. Note the thick chert bands relative to the magnetite bands. The sample numbers represent the silica and iron bands separated for geochemical analysis (see Table 4.3). Ch=chert, mag=magnetite, gru=grunerite, act=actinolite, stp=stilpnomelane.
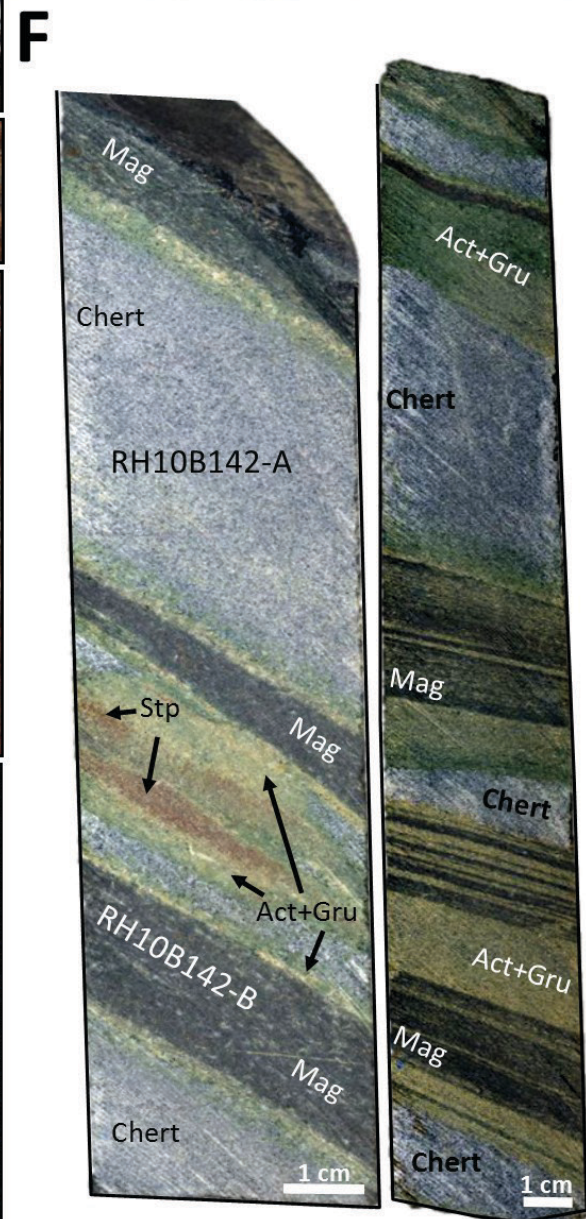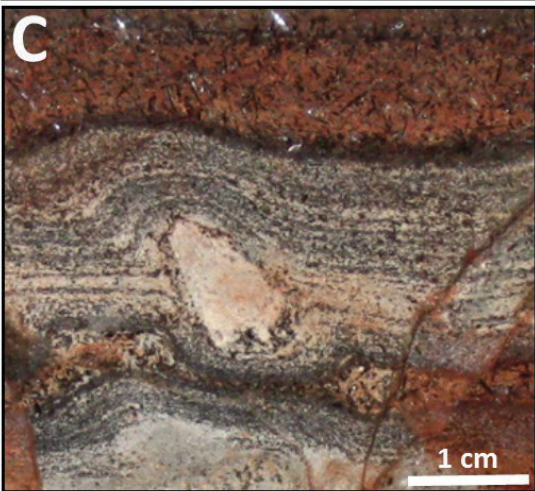
Figure 4.5. Examples of the lithostratigraphy of two core sections from Goose Lake BIF that illustrate the BIF and the associated greywacke-mudstone turbidites. Not all of the greywackes are sorted but instead are ungraded with uniform grain size distribution. BIF do not appear between all greywacke-mudstone sequences and not all greywacke units terminate with mudstone facies either. This is presumably due to lack of preservation. See text for further details.
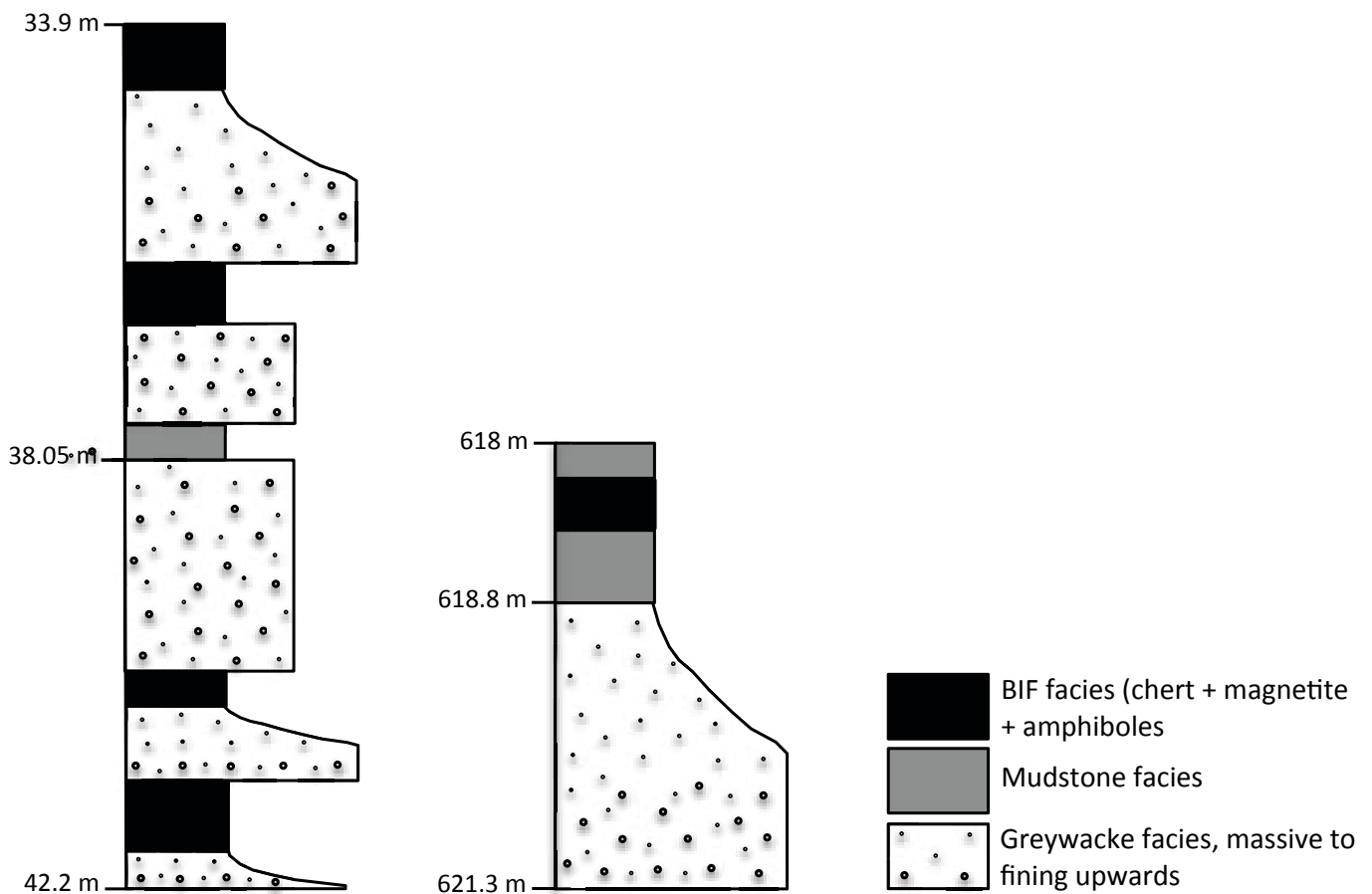
Figure 4.6. Compositional diagrams illustrating the mineral chemistry of the BIF. (A) Ternary diagram showing the two main amphiboles (grunerite and ferro-actionlite) in the BIF. Ferro-hornblende, which has significantly more alumina, is mostly restricted to the associated clastic ferruginous sediment. (B) The compositional relationship between the greenalite measurements from Goose Lake BIF and related phases of chamosite, clinochlore and serpentine. (C) Ternary diagram showing the retrograde greenalite and stilpnomelane from the Goose Lake BIF.
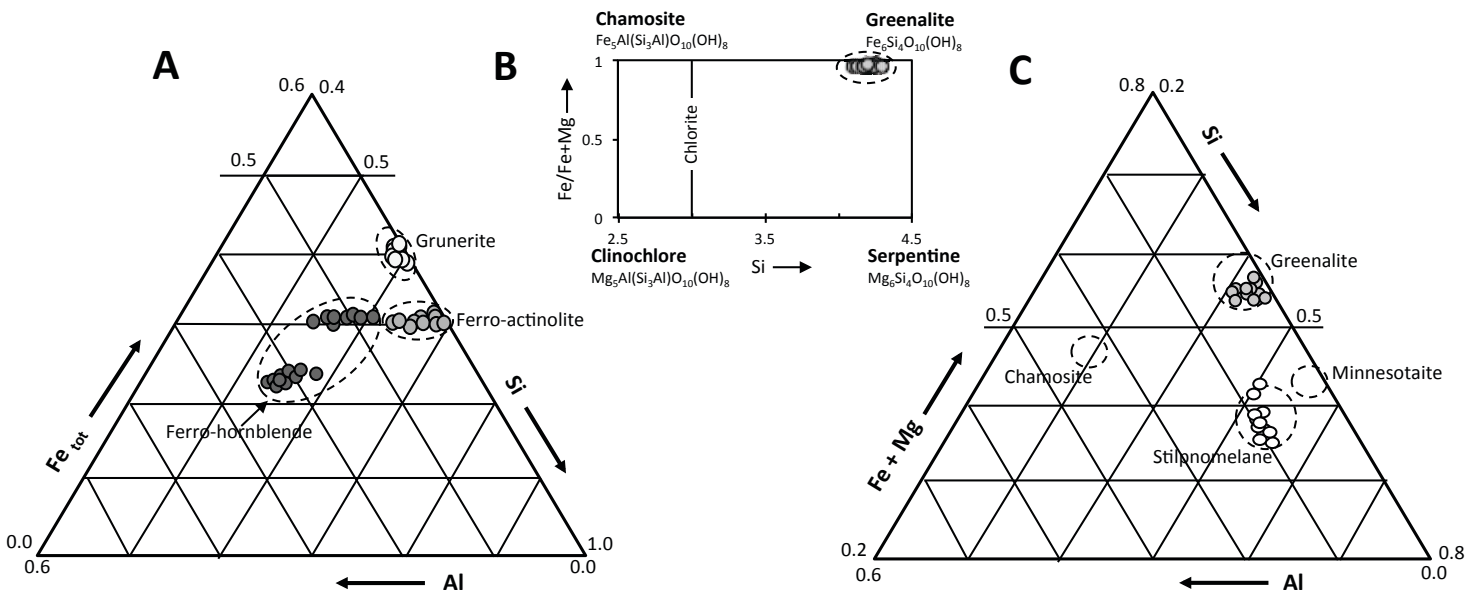
Figure 4.7. (A, B) Photo-micrographs of the Damoti Lake BIF showing large grunerite crystals cross-cutting the original bedding planes (in crossed polarized light = XPL). (C) Goose Lake BIF showing a mixture of chert, grunerite and ferro-actinolite (XPL). (D) Electron microprobe backscatter image of (C) showing euhedral, diamond-shaped ferro-actinolite and radiating grunerite. (E) Goose Lake BIF showing ferro-actinolite with small bladed brown stilpnomelane on the edges and with large anhedral patches of greenalite (plane polarized light = PPL). (F) Goose Lake BIF with electron microprobe backscatter image of grunerite and ferro-actinolite with greenalite and thin bladed stilpnomelane crystals. The stilpnomelane grows mostly within, or associated with, greenalite grains. (G) The tuff ash bed at Slemon Lake (RH-chisel) showing randomly distributed quartz fragments set in a very fine-grained groundmass of quartz, biotite and chlorite (XPL). (H) PPL image showing the large amount of greenish chlorite.

163
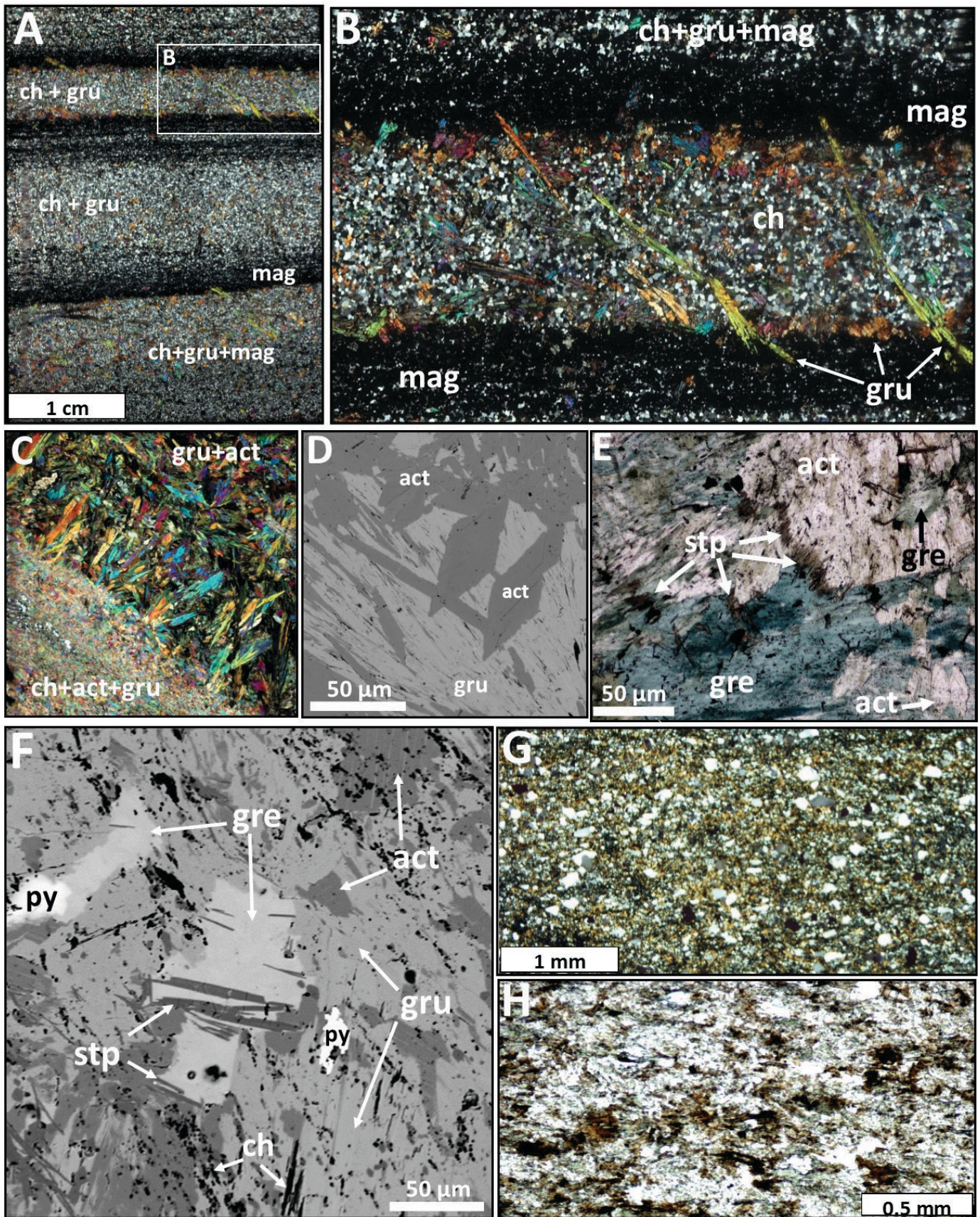
Figure 4.8. (A) Hand sample, large thin section and photo micrograph images (in PPL) of the BIF-interbedded ferruginous sediment at Point Lake (see also field photo in Fig. 3E). The bed contains large ferro-hornblende porphyroblasts and quartz fragments that are randomly distributed in a biotite groundmass. Note the ferruginous sediment bed and the BIF are repetitive within the scale of the hand sample. (B) Photo-micrograph (in PPL) of the ferruginous sediment at Damoti Lake. The sediment is texturally heterogeneous with variable grain sizes, in particularly for the biotite porphyroblasts. Many of the plagioclase grains range from angular to sub-spherical. The lower half of the image has a darker appearance due to the abundance of ultra-fine grained graphite in the groundmass. (C) Detailed electron microprobe backscatter image showing the relationship between angular plagioclase and the hydrothermal altered Sr-plagioclase (slawsonite). The plagioclase was likely altered by fluids related to magmatic activity in the area. (D) Ferro-hornblende exists both as full-crystals and as rims on existing grunerite (in XPL). (E) Ferruginous sediment with grunerite porphyroblasts set in a crenulated chlorite and graphite groundmass (in PPL). The ultrafine graphite also appears as inclusion trails within grunerite crystals. Qtz=quartz, bi=biotite, hbl=hornblende, pl=plagioclase, chl=chlorite, - slw=slawsonite, zrn=zircon, gru=grunerite, gr=graphite.
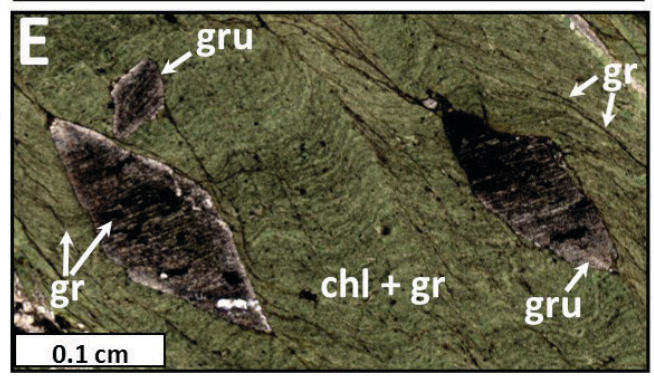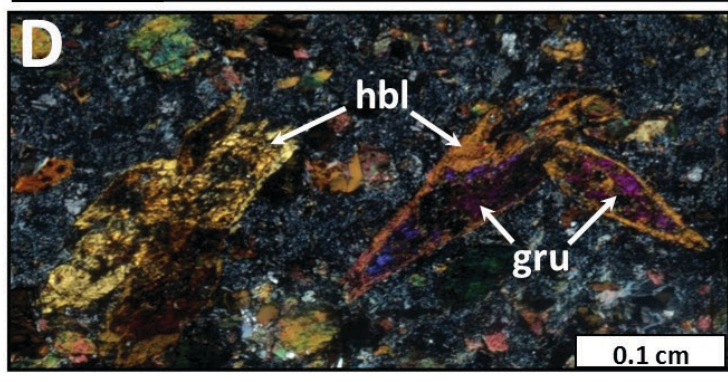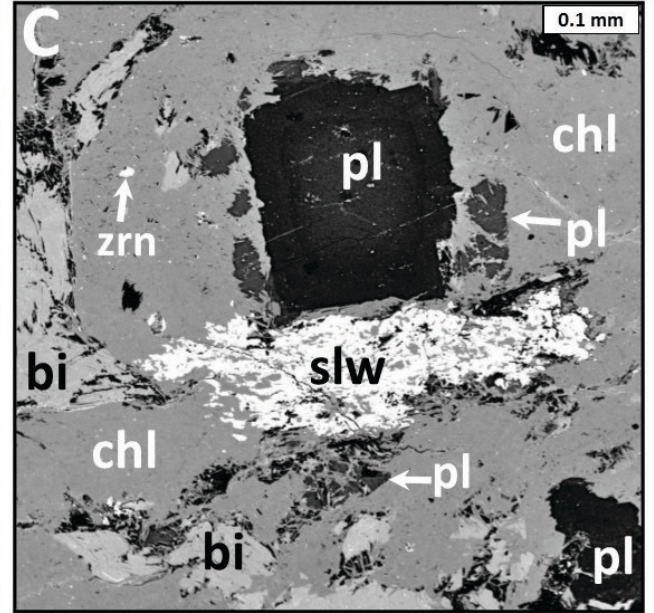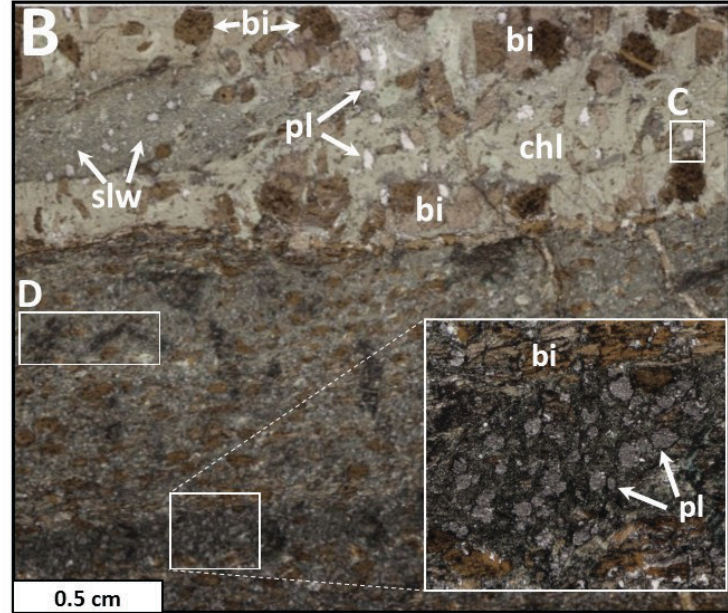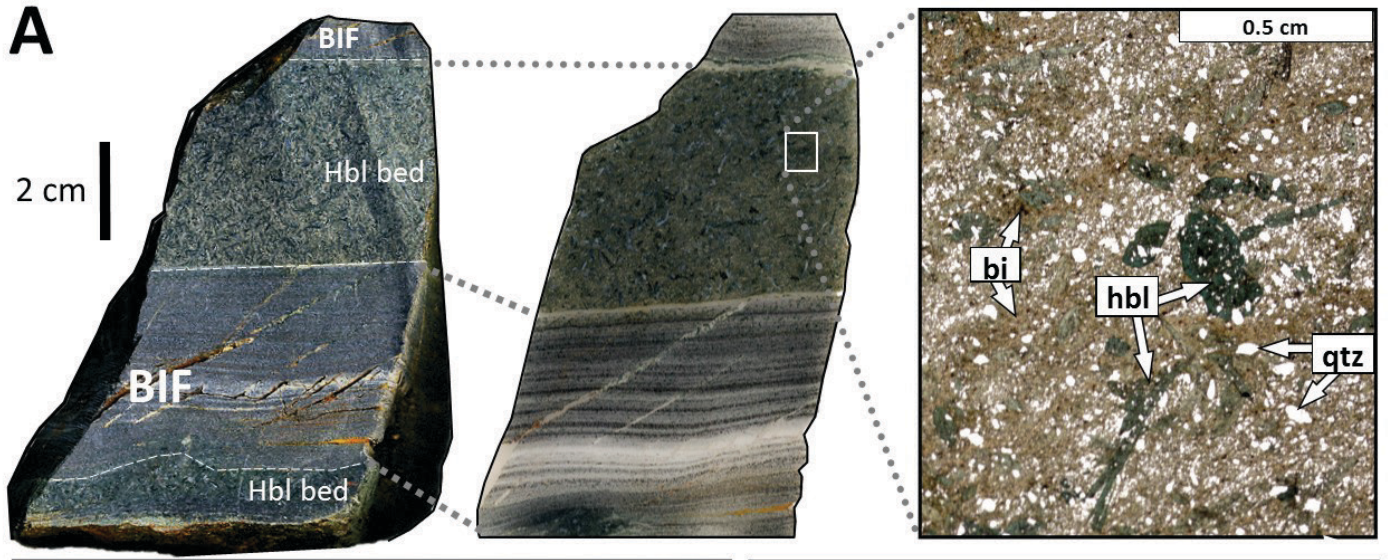
Figure 4.9. Diagrams showing important relationships between selective elements in the BIF. (A) Of the four locations, the Slemon Lake BIF contains the largest amount of detrital material as recognized by its Al_2O_3 content. Only Goose Lake BIF has an Al_2O_3 content ≤ 1 wt.%. (B) The Al_2O_3 vs. Th showing a well-constrained positive correlation. (C) The Al_2O_3 vs. $\sum$REE showing a scattered relationship with only a weak linear correlation..(D, E) Both Th and Ni display a positive co-variation when plotted against Sc. (F) An inverse, negatively correlated relationship exists between SiO_2 and Ge, with the opposite relationship for Fe_2O_3 vs. Ge (inset).
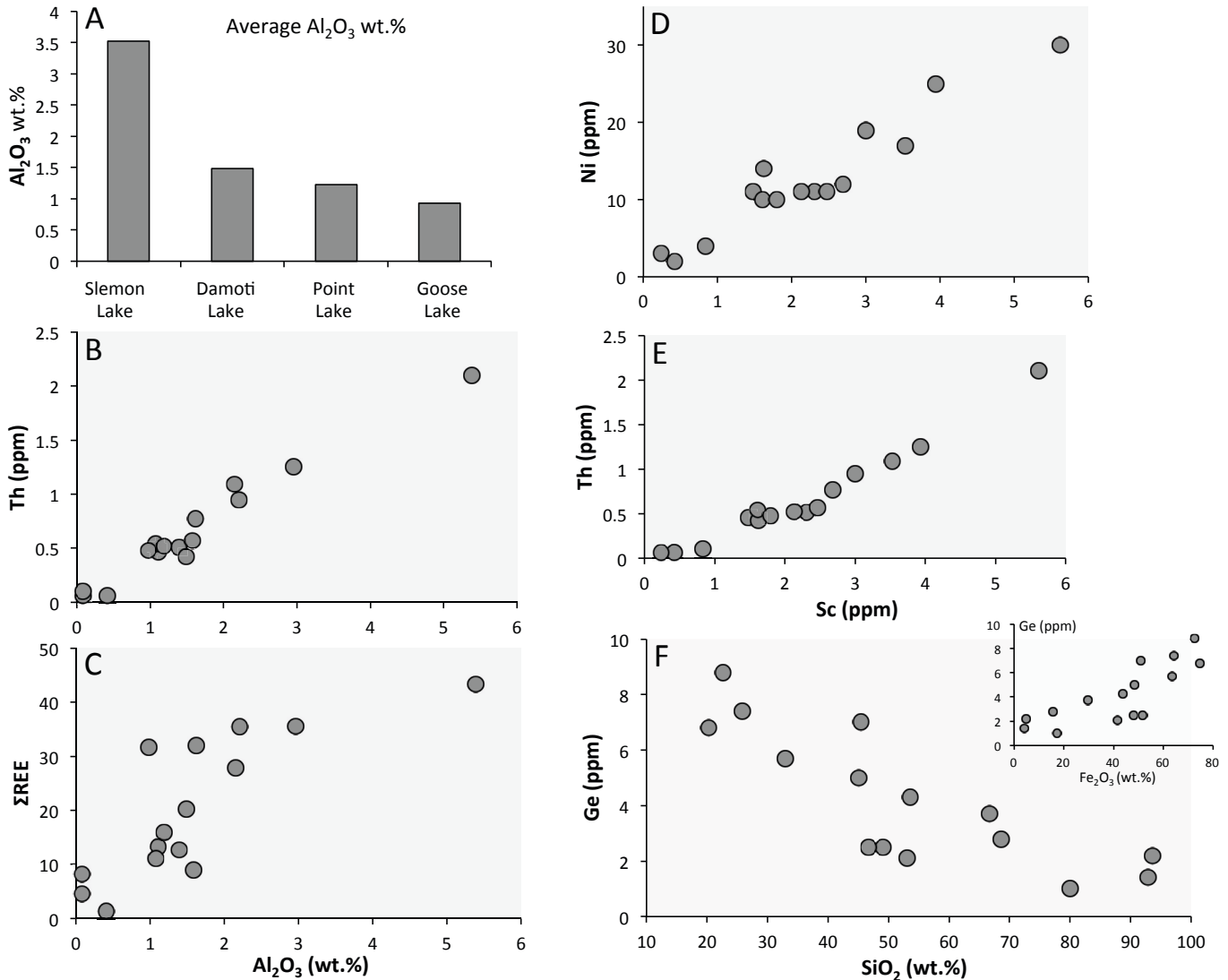
Figure 4.10. The shale-normalized (NASC) REY systematics of the BIF at the four locations. In general, all samples have positive La-, Eu and Y-anomalies. (A) Slemon Lake. Three samples (1 bulk, 1 silica band, 1 iron band) all show an elevated REY pattern with relatively high LREE signatures. Note the higher REY content in the silica band relative to the iron band and the high La anomaly in the iron band. (B) Damoti Lake and (C) Point Lake. Relative to Slemon Lake, these locations are recognized by a higher HREE-to-LREE enrichment and by their lower REY content. (D) In contrast to Slemon Lake, the iron bands at Goose Lake contain the highest amount of REY relative to the silica bands. Note the REY abundance in the iron bands are comparable to Slemon Lake. Dashed connection lines = below detection limit. NASC normalization values from McLennan (1989).
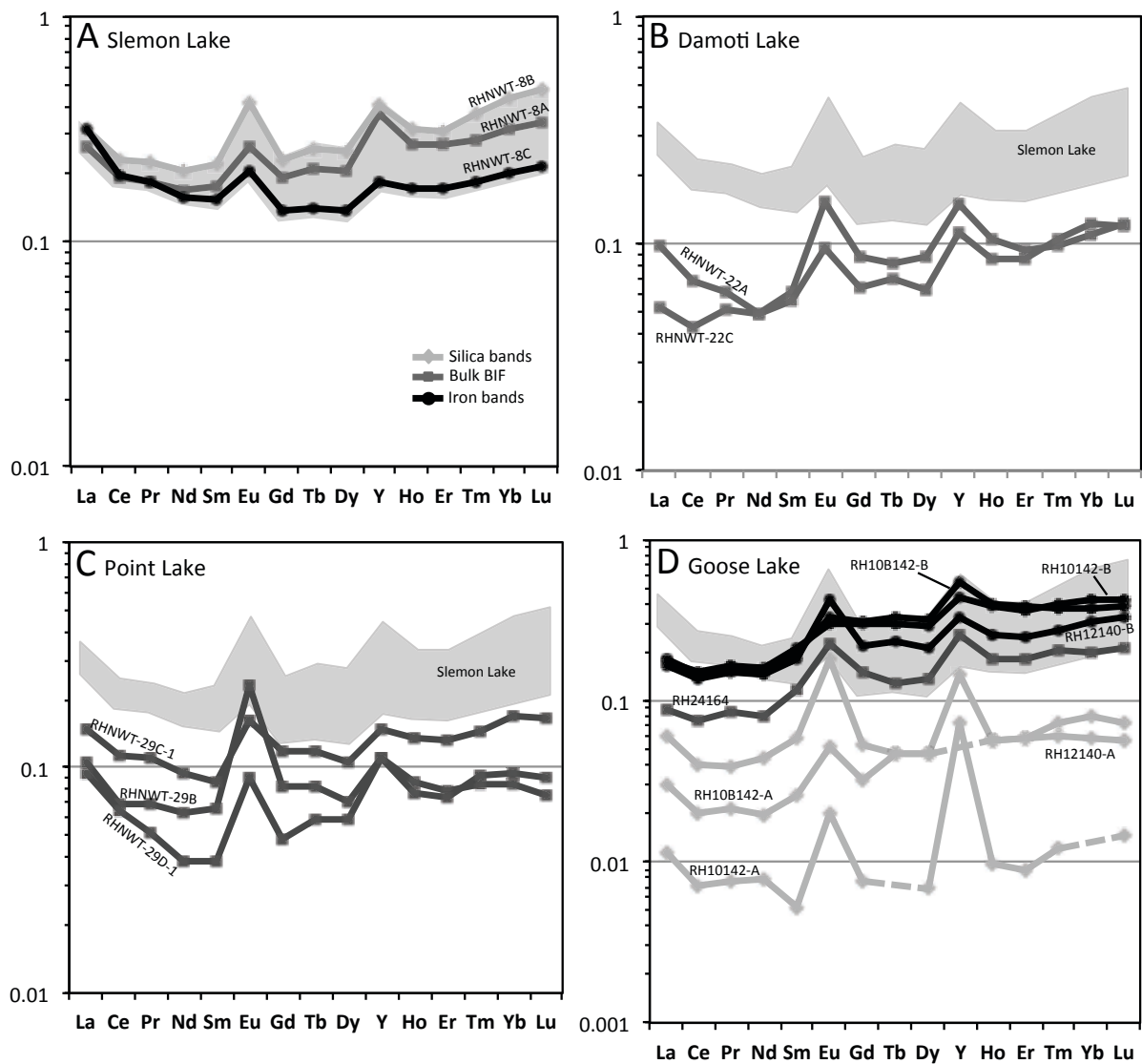
Figure 4.11. The shale-normalized (NASC) depletion/enrichment of La and Ce in the BIF. The largest part of the samples plot in the field of positive La anomaly with no Ce anomaly (diagram modified from Bau and Dulski, 1996). Six of the BIF samples plot within the field of negative cerium anomalies $((Pr/Pr^*)_{NASC}>1.05)$.
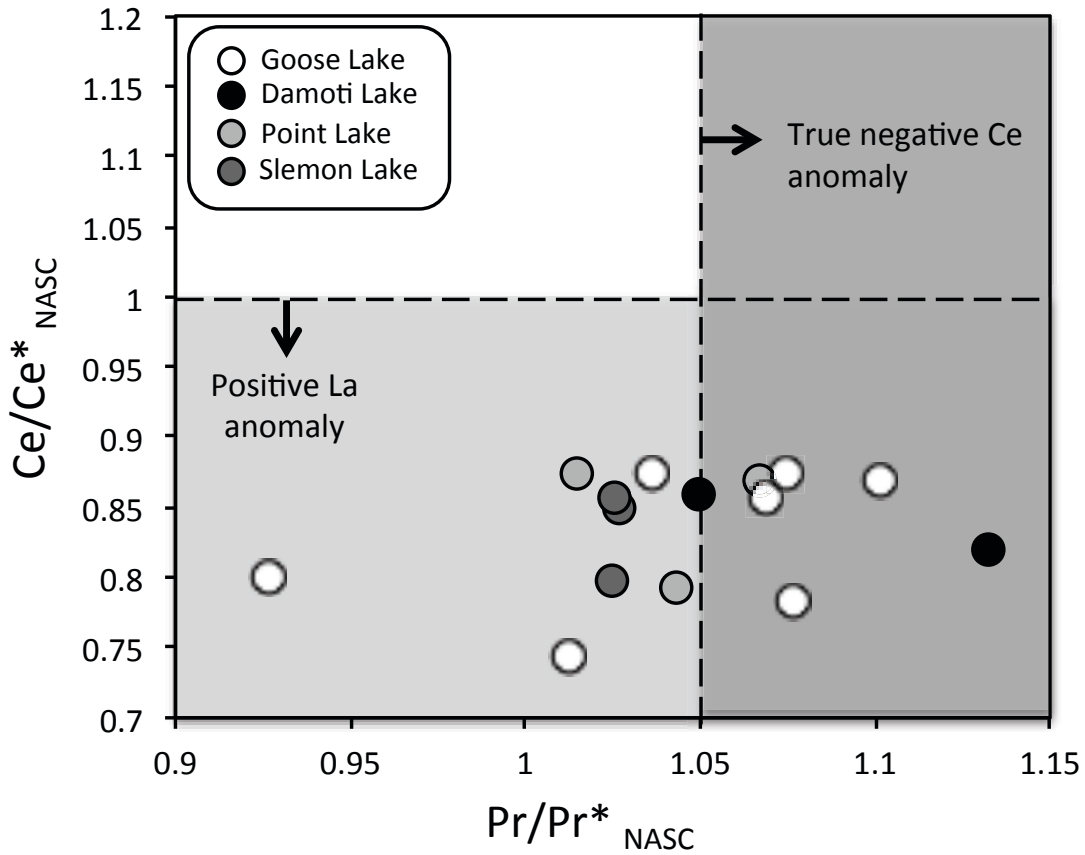
Figure 4.12. (A) Classification diagram (Winchester and Floyd, 1977) of the tuff bed at Slemon Lake using Nb/Y-Zr/Ti ratios. The tuff bed are classified as a rhyodacite-dacite and plot alongside the coeval Defeat magmatic arc rocks from Meintzer (1987) and Yamashita et al. (1999). (B) Tectonic discrimination diagram from Pearce et al. (1984) with the Slemon Lake tuff bed plotted alongside the Defeat granitoid rocks. A volcanic arc is the preferable setting for the deposited ash in the BIF-turbidite basin. Defeat magmatic arc suite from Meintzer (1987) and Yamashita et al. (1999). (C) The chondrite normalized REE pattern of the tuff bed at Slemon Lake, which relative to both the Defeat magmatic arc suites and Banting Group rhyolite, is HREE enriched and shows a weakly developed Eu anomaly (normalization values after Anders and Grevasse, 1989). (D) Trace element diagram of the tuff bed at Slemon Lake displaying enrichment in HREE, Th, Y and Zr. Negative anomalies are found for Nb, P and Ti (normalization values after Sun and McDonough, 1989).
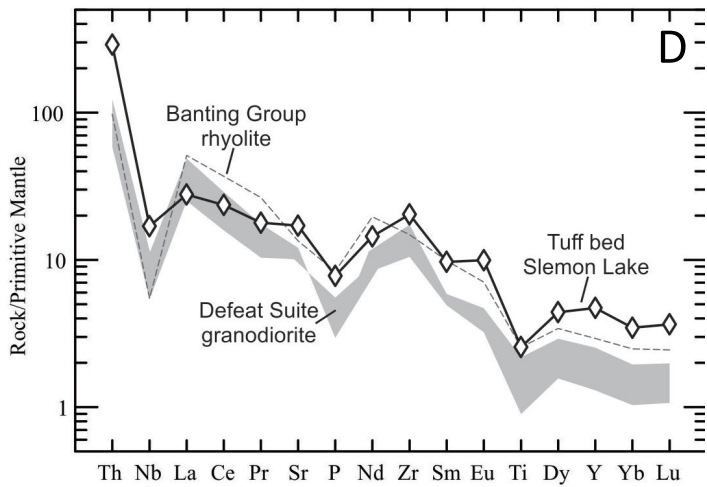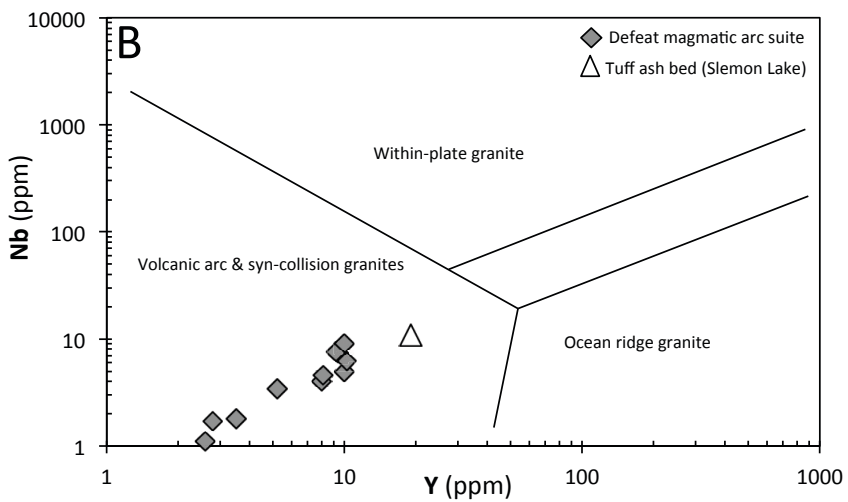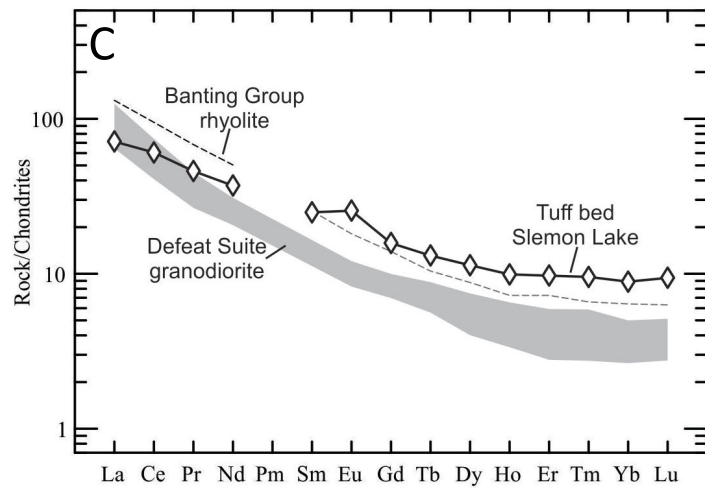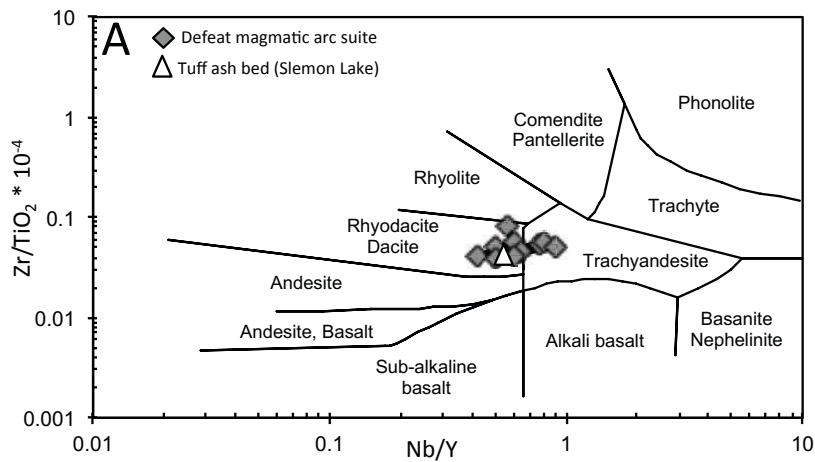
Figure 4.13. The enrichment of HREE relative to LREE when normalizing after both NASC and local shale (DGS). Note the Pr/Yb is always below 1 but the fractionation is more pronounced when normalizing after DGS. See text for further explanations.
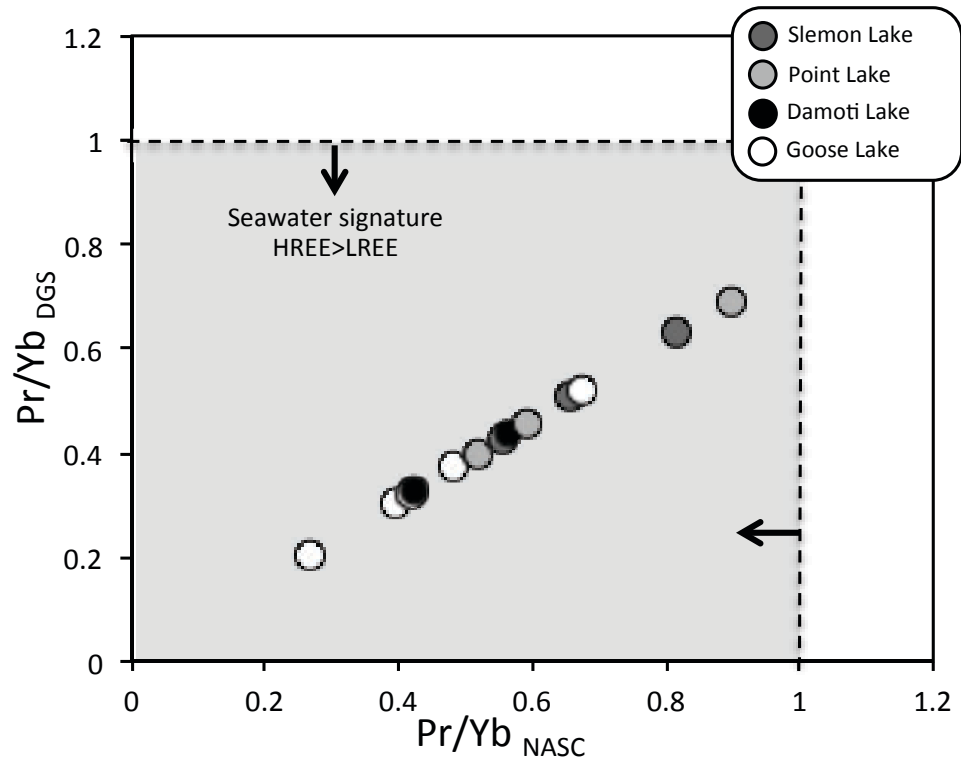
Figure 4.14. Eu/Sm-Y/Ho elemental ratios showing the dominant sources in the BIF. Relative to modern seawater, the BIF can be characterized as a mixture between seawater (elevated Y/Ho), hydrothermal fluids (elevated Eu/Sm) and small detrital pelagic input controlled by the composition of the turbidite sediment. Note, the seawater input is higher and the hydrothermal input lower than for the Slave craton Mesoarchaean BIF. Modern hydrothermal fluids by Bau and Dulski (1999); modern seawater data by Alibo and Nozaki (1999); Slave craton 2.85 Ga BIF from Haugaard et al. (in review).
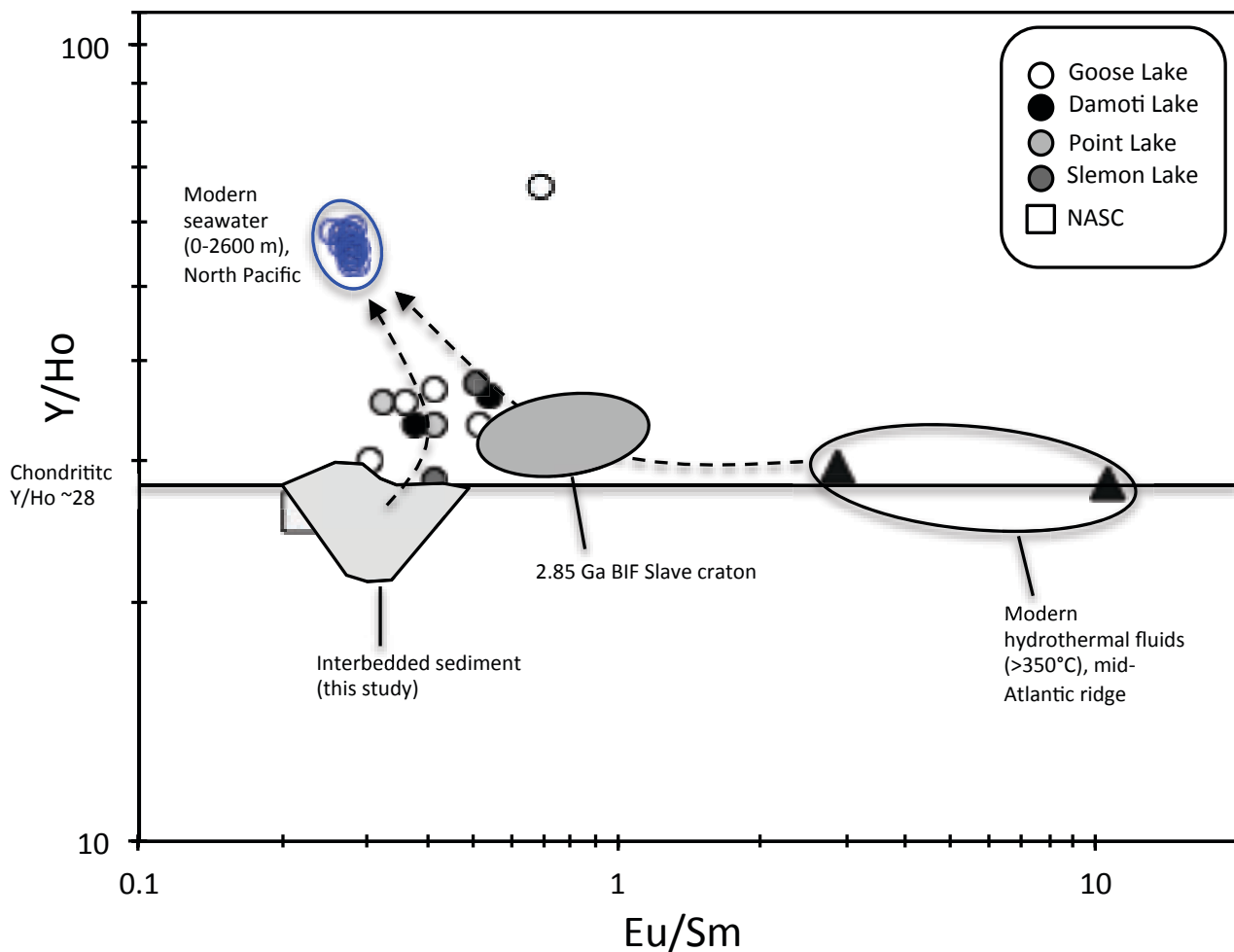
Figure 4.15. The Ge/Si ratios in BIF. (A) A perfectly developed mixing-hyperbola characterizes the BIF sediment and illustrates the mixing between hydrothermally-controlled bottom water and continentally-controlled surface water. The Ge/Si ratio is high for the iron precipitate, whereas the Ge/Si values are low in the silica rich BIF. (B) Same plot as (A) but with the Hamerley Group BIF (Hamade et al., 2003) and Isua BIF (Frei and Polat, 2007) added for comparison. A similar pattern is evident amongst the three BIFs. The elevated Isua BIF is due to higher hydrothermal input into the bottom waters.
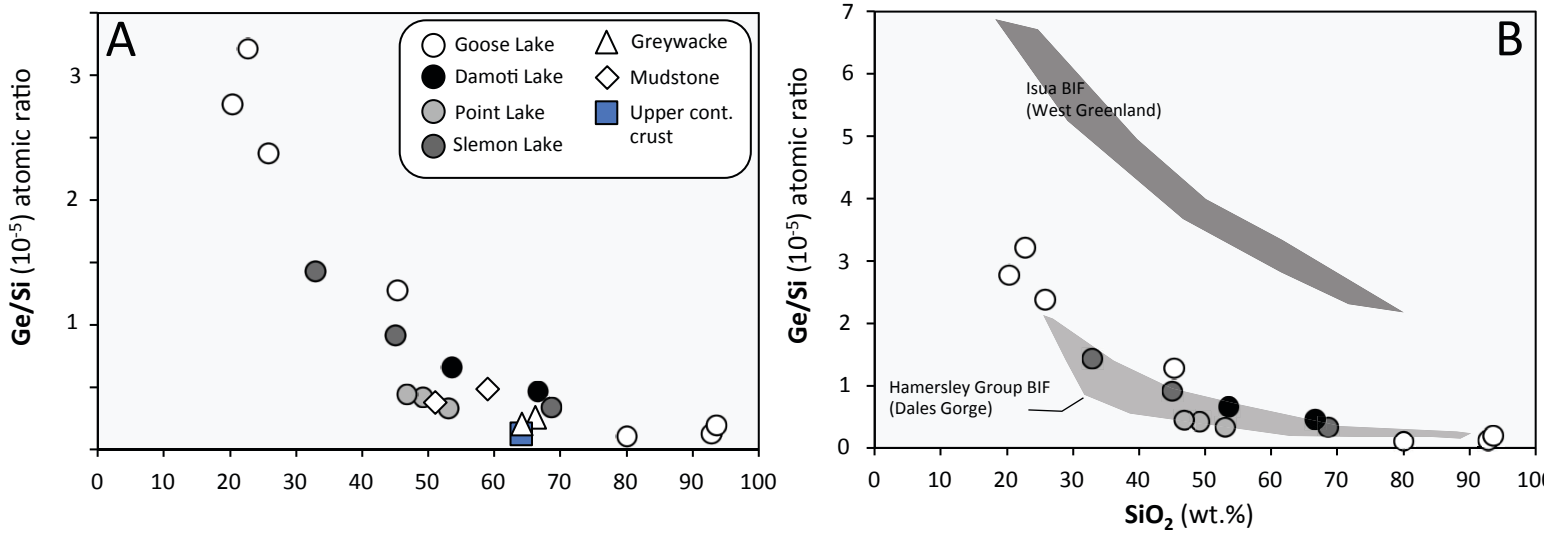
Figure 4.16. (A) Th/Sc-La/Sc diagram used to discriminate the influences from local mafic and felsic sources on the sediment budget. The turbiditic sediment resembles that of the Burwash greywacke sediment with an erosive mixture of Kam Group basalt and Banting/Defeat granodiorite detritus. Note that the sediment generally has higher Sc than the average Archaean upper crust. (B) The average Al_2O_3/TiO_2 ratio of the BIF (~25) is controlled by detritus sourced from the interbedded greywacke and mudstone sediment. The exception is the one mudstone and one ferruginous sediment from Damoti Lake which both have lower Al_2O_3/TiO_2 ratios due to higher TiO_2 content contributed from mafic sources. The BIF Al_2O_3/TiO_2 ratio also lines up perfectly with the Burwash sediment suggesting that a major part of the sediment in the BIF basin was sourced from already existing sediment, such as the Burwach turbidites. (C) The control of the trace metals in the BIF is directly related to the fine-grained mudstone and ferruginous sediment. With a Cr/Ni ratio of ~1.6 it is unlikely that Ni was preferentially concentrated in the seawater prior to BIF precipitation. The higher Cr/Ni ratio for the greywackes is unrelated to those found in the BIF (note the one ferruginous sediment from Point Lake has a high input of greywacke sediment explaining why it correlates well with the other greywackes). Kamp Group basalt and Burwash sediment from Yamashita and Creaser (1999); Defeat magmatic arc suite from Meintzer (1987) and Yamashita et al. (1999). Archaean upper crust from Taylor and McLennan (2009).
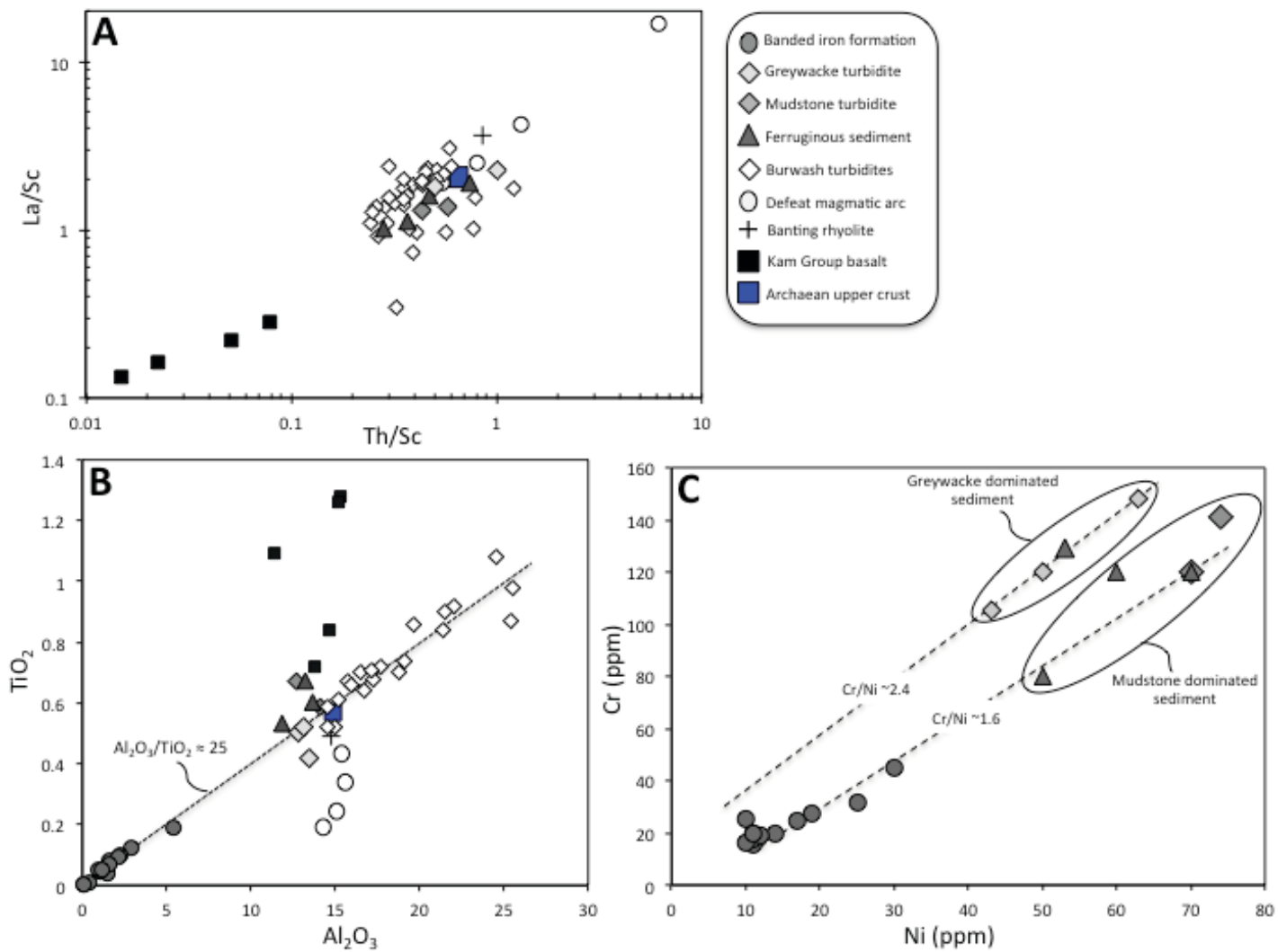
5. Conclusions

The Slave craton hosts two BIFs that were deposited in very different depositional environments. The 2.85 Ga Mesoarchaean BIF originated on a newly formed shelf during a continental rifting event. It is found associated with basement gneisses and shallow-water shelf facies, such as pebble-to-cobble conglomerates, fuchsitic quartzites and quartzarenites. These shallow-water facies sedimentary rocks were deposited during the first stages of rifting as evidenced by the erosional unconformity on the basement-cover contact. Further rifting caused subsidence and drowning of the basement, and the consequent deposition of deeper water facies such as semi-pelites and BIF (e.g., Ketchum et al., 2004; Bleeker and Hall, 2007). In contrast, the ~2.62 Ga BIF (new age constraint, see Chapter 4) was likely deposited in a continental arc basin(s) as evidenced by the spatial and temporal relation to the ca. 2.63-2.61 Ga Defeat magmatic arc (e.g., Ootes et al., 2009). BIF deposition was frequently interrupted by large volume of deep-water greywacke-mudstone turbidites.

The studies within this PhD thesis contribute novel petrographic and geochemical insights into the BIFs of the Slave Craton. Specifically, this work shows that the solutes in the seawater from which these BIFs precipitated from, as reflected by their geochemical signatures, was strongly influenced by continental crust and submarine hydrothermal fluids within their local-to-regional depositional basin environment. On a layer-by-layer approach, this work further demonstrates that short-term trends in the chemistry can be related to the changes in the composition and structure of the ambient seawater. For the first time, a depositional age of the Neoarchaean BIF-turbidite sequence is obtained. This result, together with U-Pb detrital zircon dates of other turbidite units across the craton, enables the construction of a new framework within which the Neoarchaean BIF-turbidites should be interpreted.

5.1. A seawater origin of the Slave craton BIF

The majority of all BIF samples (bulk BIF + individual bands) collected from the Slave Craton for this thesis show a seawater origin. They exhibit seawater derived shale-normalized rare earth elements + yttrium (REY) patterns that are enriched in HREE relative to LREE (HREE>LREE), and with positive La and Y anomalies. Generally, the iron bands have higher total REE and a more uniform and less fractionated REY pattern than the silica bands.

5.1.1. Oxidation of cerium (Ce) in 2.62 Ga seawater

A general difference between the older 2.85 Ga BIF and the younger 2.62 Ga BIF is the evidence of negative Ce anomalies in parts of the younger BIF samples. This likely indicates the presence of a strong oxidizing agent (e.g., O_2) in the ambient water column, which could oxidize Ce^{3+} to Ce^{4+} and reduces the solubility of Ce relative to neighboring REE. The Ce^{4+} may have been preferential removed onto various particles, such as Mn–Fe oxyhydroxides, organic matter and clay (e.g., German, 1991; Byrne and Sholkovitz, 1996).

5.1.2. Continental and hydrothermal sources to local and regional seawater

Beside the seawater-like REY patterns, two source components can be distinguished within the geochemical signature of these BIFs: a continental input and a hydrothermal fluid input. In the former, a higher input of detritus resulted in greater input of LREE and the less fractionated REY pattern. The input of continentally derived detritus during BIF deposition is also reflected by a mixture of chemical and terrigenous sediment having up to 10 wt.% Al_2O_3. In addition, a detailed layer-by-layer Sm-Nd isotope study obtained in the purest chemical precipitates of the 2.85 Ga BIF reveals the sources of its REYs. The silica bands show a variable $^{143}Nd/^{144}Nd$ signature with both positive and negative $\varepsilon_{Nd}(t)$ values reflecting the existence of radiogenic and unradiogenic continental landmasses in the source water during silica formation. In contrast, the iron bands have consistently positive radiogenic $\varepsilon_{Nd}(t)$ values with relatively uniform $^{143}Nd/^{144}Nd$ that reflect a deep-

marine hydrothermal source of the dissolved REY during the precipitation of the primary ferric iron minerals.

Surprisingly, the REY in the upper water column and the overall seawater Ni content as reflected in the ca. 2.85 Ga BIF is low relative to other pre-2.7 Ga BIF (e.g., Konhauser et al., 2009). Since the basement gneisses may contain a metamorphosed weathering profile (see section 5.4), it can be speculated if the contemporaneous crust was a highly weathered surface at the time of BIF deposition, unable to contribute a significant dissolved load to the near-shore marine environment.

In the ca. 2.62 BIF, evidence for continental versus hydrothermal sources comes from Ge/Si ratios within individual iron and silica bands. This BIF reveals a exponential distribution of Si versus Ge/Si, illustrating the mixing of hydrothermally controlled water (high Ge/Si ratio) and continentally controlled water (low Ge/Si ratio) masses within the depositional basin. The hydrothermal contribution to this seawater is thus reflected in both BIF deposits. However, during active rifting of the basement during deposition of the ca. 2.85 Ga BIF, excess of Eu^{2+} input to the basin resulted in shale-normalized positive Eu anomalies larger than both the ca. 2.62 Ga BIF and contemporaneous BIFs from other settings.

5.2. A stratification of the seawater and the interaction of water masses

The high-resolution (layer-by-layer) petrographic and geochemical investigation of these BIF deposits allow a highly detailed view of the nature of the local ambient seawater. The results of this thesis imply that the interaction of compositionally and isotopically different water masses were the main control behind silica and iron deposition.

Both BIFs have more silica (up to 20 wt.% SiO_2) in their iron bands, and comparatively less iron (down to 4 wt.% Fe_2O_3) in the silica bands, implying that dissolved Fe^{2+} came into the water column in pulses (possibly convective upwelling), while silica likely represented background seawater deposition. Furthermore, the abundances of the dissolved REY are lower in the silica bands than in the iron bands, demonstrating the dilution of REY in the shallow water mass, and the enrichment of REY

in the deep water mass. This vertical REY distribution is also evident in modern seawater (e.g., Zhang and Nosaki, 1996).

In the 2.85 Ga BIF, the heterogeneous $\varepsilon_{Nd}(t)$ values in the silica bands implies that the ^{143}Nd/^{144}Nd in the upper seawater was not homogenized by ocean circulation, but was likely controlled by sourcing from crustal components with different Sm-Nd signatures. The iron bands, on the other hand, were deposited from water sourced from deeper parts of the basin. This water was controlled by hydrothermal fluids, and was well-mixed having more consistent ^{143}Nd/^{144}Nd isotopic composition and a more homogenous REY content. This stratification of the ocean with respect to Nd isotopes, with a well-mixed deeper water and more heterogeneous upper water, has also been recorded within modern ocean basins (e.g., Piepgras and Wasserburg, 1980; Andersson et al., 1992).

Within the 2.62 Ga BIF, the above scenario is geochemically supported by the Ge/Si distribution, which illustrates mixing between hydrothermally controlled bottom water and continentally controlled surface water. Ge concentrations are relatively high in hydrothermal fluids (and therefore the bottom water), and Ge will preferentially be scavenged during upwelling by ferric-oxyhydroxides. In contrast, low Ge/Si ratios in upper seawater were captured during background silica precipitation within the water column.

5.3. A new Group in the Slave craton - depositional timing of the young turbidite-BIF sequences

The depositional timing of the BIF within the greywacke-mudstone turbidites has so far only been determined by the minimum ages of detrital zircons within these sedimentary rocks. They have, therefore, traditionally been grouped into the Duncan Lake Group, which also contains the renowned Burwash turbidites.

During the thesis fieldwork, a previously unrecognized felsic-to-intermediate ash tuff bed was discovered interlayered with the turbidite-BIF sequence at Slemon Lake in the southwest part of the craton. This tuff yielded a single zircon age population with a U-Pb zircon crystallization age of 2620 ± 6 Ma, as determined by LA-ICP-MS analysis. This tuff crystallization age defines the depositional timing of these BIF-bearing

turbidites. Based on this new tuff ash age, combined with constructed detrital zircon ages from greywacke deposits collected across the Slave Craton, and together with previously published U-Pb zircon ages, a new stratigraphic framework for the turbidite-BIF sequences of the Slave craton is proposed: the older turbidites remain part of the Duncan Lake Group whereas the younger turbidite-BIF sequences are grouped under the new name Slemon Group. As a consequence, where robust age-dates exist, we also upgrade the various location names to formations and include type localities for each.

5.4. Preliminary and future work

5.4.1. The source of detrital chromite in fuchsitic quartzite

Until recently, only the felsic contribution to the fuchsitic quartzites of the Central Slave Cover Group (CSCG), in the form of detrital zircons, had been studied (Sircombe et al., 2001). However, the ultramafic contribution to these fuchsitic quartzites, in the form of detrital chromites, has received little attention. This is surprising given that no significant exposures of ultramafic (komatiites) have been found in the Slave craton (e.g., Isachsen and Bowring, 1997; Bleeker et al., 1999), and these grains may, therefore, be the only remnants left of ultramafic komatiitic rocks that were exposed during the formation of the CSCG. Important compositional information on the source rocks of these chromite grains can significantly contribute to our understanding of basement-CSCG formation. Ongoing preliminary work (petrography, bulk rock geochemistry, mineral separation, electron microprobe analysis, PGE and Re-Os systematics) was conducted, and some results can be found in Appendix E. Mineral separation of chromite grains was done and subsequently analyzed by electron microprobe to gain a better insight into the composition and nature of these grains. As seen in the plots in Appendix E, they show typical elemental behavior of amphibolite metamorphosed chromite grains. Analysis of the discrimination plots and the chondrite-normalized PGE patterns suggest they were likely sourced from a komatiitic, Al-depleted, source (e.g., Barnes and Roeder, 2001; Puchtel et al., 2014). However, further work needs to be conducted on these chromite PGE patterns in order to confirm these interpretations. Furthermore, the Re-Os systematic obtained on these chromite grains (see Table E1 in Appendix E) needs more work

because obtaining meaningful model ages for the Dwyer Lake and Bell Lake detrital chromite grains has been problematic due to isotope reequilibrium during metamorphism.

5.4.2. A metamorphosed weathering profile

Some of the best evidence for an in-situ unconformity on the Central Slave Basement Complex (CSBC) and the CSCS interface is the possible existence of a relict weathering profile on the tonalitic bedrock (Bleeker et al., 1999; Ketchum et al., 2004). Since one of the main contributions to seawater composition is continental weathering, the preservation of continental landmass that once was exposed to the Mesoarchaean atmosphere is extremely useful.

At Dwyer Lake and Brown Lake, within a short zone just below the CSBC-CSCG contact, metamorphic andalusite and sillimanite has been reported to occur in a possible metamorphosed weathering horizon (Bleeker et al., 1999; J.W.F. Ketchum, personal field notes). This field observation could indicate a pre-metamorphic removal of alkali metals, Mg and perhaps Fe, leaving alumina upgraded in the top part of the weathered bedrock. Therefore, fieldwork and sample collection by saw-cutting the basement rocks underlying the CSCG was carried out at Dwyer Lake and Brown Lake. Petrography, geochemistry and electron microprobe analysis were furthermore undertaken (see selected microprobe images in Appendix F).

Questions that arise from the preliminary work are: does the metamorphosed weathering profile at Dwyer Lake and Brown Lake represent a relict paleosol? Various criteria must be met to classify a weathering profile as a definite ancient soil, including textural, mineralogical and chemical changes that are in line with soil forming processes, and which are different from the fresh and homogenous parent rock (Rye and Holland, 1998). Following these criteria, one of the oldest recognized paleosol was developed on top of the 2.76 Ga old Mt. Roe basalts, Western Australia. This palaeosol shows that iron had been mobilized and removed from those profiles corresponding to a PO_2 level of ≤ 0.002 atm (Rye and Holland, 1998).

Electron microprobe data in this preliminary study reveal that the targeted basement profile has many Al- and Ti-rich phases that so far have not been found in the "fresh" basement gneiss located distally to the contact. For instance, agglomerations of

tiny sillimanite needles were found in multiple muscovite grains. The sillimanite was accompanied by fine-grained margarite, a high-Al mica. Disseminated Al-spinel was also found in these profiles, and, titanium-oxide minerals (either rutile or anatese) were found to be in higher abundances.

Secondly, if the profile can be characterized as a palaeosol, then what was the degree of weathering and which elements were mobilized and leached to the oceans, and conversely, which were not? What does this tell us about the Mesoarchaean atmosphere? Given that soils are normally in direct chemical exchange with atmospheric gasses, such as CO_2 and O_2, semi-quantitative first-order approximations can be made on the degree of oxidation within the soil and atmosphere at the time of formation (e.g., Holland and Beukes, 1990). Also, since continental weathering is a major source for seawater composition, is it possible to link the weathering processes on land to the abundances of solutes measured in BIF? The work on the older BIF shows that the upper seawater was likely very dilute with respect to REY and trace metals something that could indicate a deeply weathered landmass. This would also explain why we do not find any significant volume of preserved komatiites in the Slave craton today.

5.4.3. The Slemon Group

Finding ash tuff beds within greywacke-mudstone turbidites is challenging. However, and as shown in this thesis, they are critical in constraining the stratigraphic framework of these lithologically monotonous sedimentary rocks. More findings of these beds can produce better-constrained deposition ages of the many turbidite sequences in the craton. For example, the ca. 2.62 Ga crystallization age of the ash bed presented in this study provides a critical date and horizon in further establishing stratigraphic relationships and evaluating tectonic processes.

The petrology of the Burwash Formation of the Duncan Lake Group has been well-studied (e.g., Henderson 1970, 1972; Yamashita and Creaser 1999; Ferguson et al., 2005), but the petrology of the Slemon Group has not been investigated to the same degree. Thorough petrography and provenance studies comparing the Duncan Lake Group and Slemon Group is strongly recommended since it will provide a more detailed picture on the depositional basins that accumulated these extensive turbidite deposits and

it will also shed light on the crustal composition and tectonic development of the Slave craton.

References

Andersson, P. S., Wasserburg, G. J., Ingri J., 1992. The sources and transport of Sr and Nd isotopes in the Baltic Sea. Earth and Planetary Science Letters 113, 459–472.

Barnes, S., Roeder P., 2001. The range of spinel compositions in terrestrial mafic and ultramafic rocks. Journal of Petrology 42, 2279–2302.

Bleeker W., Hall B., 2007. The Slave Craton: Geological and Metallogenic Evolution, in Goodfellow, W.D., ed., Mineral Deposits of Canada: A synthesis of major Deposit-types, District Metallogeny, the evolution of geological provinces, and exploration methods. Geological Society of Canada, Mineral deposit division, Special Publication 5, 849-879.

Bleeker, W., Ketchum, J. W. F., Jackson, V. A., Villeneuve, M. E., 1999. The Central Slave Basement Complex, Part I: its structural topology and autochthonous cover. Canadian Journal of Earth Science 36, 1083-1109

Byrne, R., Sholkovitz, E., 1996. Marine chemistry and geochemistry of the lanthanides. In: Gschneider Jr., K.A., Eyring, L. (Eds.), Handbook on the Physics and Chemistry of the Rare Earths, 23. Elsevier, Amsterdam, pp. 497–593.

Ferguson, M., Waldron, W. F., Bleeker, W., 2005. The Archean deep-marine environment: turbidite architecture of the Burwash Formation, Slave Province, Northwest Territories. Canadian Journal of Earth Sciences 42, 935-954.

German, C. R., Holliday, B. P., Elderfield, H., 1991. Redox cycling of rare earth elements in the suboxic zone of the Black Sea. Geochimica et Cosmochimica Acta 55, 3553–3558.

Henderson, J. B., 1970. Stratigraphy of the Archean Yellowknife Supergroup, Yellowknife Bay–Prosperous Lake Area, District of Mackenzie. Geological Survey of Canada Paper 70-26.

Henderson, J. B., 1972. Sedimentology of Archean turbidites at Yellowknife, Northwest Territories. Canadian Journal of Earth Sciences 9, 882-902.

Holland H., Beukes N., 1990. A paleoweathering profile from Griqualand West, South Africa: evidence for a dramatic rise in atmospheric oxygen between 2.2 and 1.9 BYBP. American Journal of Science 290-A, 1-34.

Isachsen, C., Bowring, S., 1997. The Bell Lake group and Anton Complex: a basement - cover sequence beneath the Archean Yellowknife greenstone belt revealed and implicated in greenstone belt formation. Canadian Journal Earth Science 189, 169–189.

Ketchum, J. W. F., Bleeker, W., Stern, R. A., 2004. Evolution of an Archean basement complex and its autochthonous cover, southern Slave Province, Canada. Precambrian Research 135, 149–176.

Konhauser, K. O., Pecoits, E., Lalonde, S. V., Papineau, D., Nisbet, E. G., Barley, M. A., Arndt, N. T., Zahnle, K., Kamber, B. S., 2009. Oceanic nickel depletion and a methanogen famine before the Great Oxidation Event. Nature 458, 750–753.

Piepgras, D. J., Wasserburg G. J., 1987. Rare earth element transport in the western North Atlantic inferred from Nd isotopic observations. Geochimica et Cosmochimica Acta 51, 1257-1271.

Puchtel, I. S., Walker, R. J., Touboul, M., Nisbet, E. G. and Byerly, G. R., 2014. Insights into early Earth from the Pt-Re-Os isotope and highly siderophile element abundance systematics of Barberton komatiites. Geochimica et Cosmochimica Acta 125, 394–413.

Rye, R., Holland, H., 1998. Paleosols and the evolution of atmospheric oxygen: A critical review. American Society of London Special Publications 95, 11–25.

Sholkovitz, E. R., Landing, W. M., Lewis B. L. (1994) Ocean particle chemistry: The fractionation of rare earth elements between suspended particles and seawater. Geochimica et Cosmochimica Acta 58, 1567–1579.

Sircombe, K., Bleeker, W., Stern, R. A., 2001. Detrital zircon geochronology and grain-size analysis of a ~2800 Ma Mesoarchean proto-cratonic cover succession, Slave Province, Canada. Earth and Planetary Science Letters 189, 207–220.

Yamashita, K., Creaser, R. A., 1999. Geochemical and Nd isotopic constraints for the origin of late Archean turbidites from the Yellowknife area, Northwest Territories, Canada. Geochimica et Cosmochimica Acta 63, 2579–2598.

Zhang, J., Nozaki, Y., 1996. Rare earth elements and yttrium in seawater: ICP-MS determinations in the East Caroline, Coral Sea, and South Fiji basins of the western South Pacific Ocean. Geochimica et Cosmochimica Acta 60, 4631–4644.

References

Alexander, B. W., Bau, M., Andersson, P. and Dulski, P., 2008. Continentally-derived solutes in shallow Archean seawater: Rare earth element and Nd isotope evidence in iron formation from the 2.9Ga Pongola Supergroup, South Africa. Geochimica et Cosmochimica Acta 72, 378–394.

Alexander, B.W., Bau, M., Andersson, P., 2009. Neodymium isotopes in Archean seawater and implications for the marine Nd cycle in Earth's early oceans. Earth and Planetary Science Letters 283, 144–155.

Alibert C., McCulloch M. T., 1993. Rare earth element and neodymium composition of the banded iron formations and associated shales from Hamersley, Western Australia, Geochimica et Cosmochimica Acta 57, 187-204.

Anbar, A. D., Duan, Y., Lyons, T. W., Arnold, G. L., Kendall, B., Creaser, R. A., Kaufman, A. J., Gordon, G. W., Scott, C., Garvin, J., Buick, R., 2007. A whiff of oxygen before the Great Oxidation Event? Science 317, 1903–1906.

Anders, E., Grevesse, N., 1989. Abundances of the elements: meteoric and solar. Geochimica et Cosmochimica Acta 53, 197–214.

Andersson, P. S., Wasserburg, G. J., Ingri, J., 1992. The sources and transport of Sr and Nd isotopes in the Baltic Sea. Earth and Planetary Science Letters 113, 459–472.

Arndt, N. T., Bruzak, G., Reischmann, T., 2001. The oldest continental and oceanic plateaus: Geochemistry of basalts and komatiites of the Pilbara Craton, Australia. Geological Society of America Special Papers 352, 359–387.

Barley, M., Pickard, A., Sylvester, P., 1997. Emplacement of a large igneous province as a possible cause of banded iron formation 2.45 billion years ago. Nature 385, 1–4.

Barley, M., Bekker, A., Krapež, B., 2005. Late Archean to Early Paleoproterozoic global tectonics, environmental change and the rise of atmospheric oxygen. Earth and Planetary Science Letters 238, 156–171.

Barnes, S., Roeder P., 2001. The range of spinel compositions in terrestrial mafic and ultramafic rocks. Journal of Petrology 42, 2279–2302.

Barrett, T. J., Fralick, P. W., 1985. Sediment redeposition in Archean Iron Formation: Examples from the Beardmore-Geraldton Belt, Ontario. Journal of Sedimentary Petrology 55, 205–212.

Barrett, T. J. and Fralick, P. W., 1989. Turbidites and iron formations, Beardmore-Geraldton, Ontario: application of a combined ramp/fan model to Archaean clastic and chemical sedimentation. Sedimentology 36, 221–234.

Barth, M. G., McDonough, W. F., Rudnick, R. L., 2000. Tracking the budget of Nb and Ta in the continental crust. Chemical Geology 165, 197-213.

Bau, M., 1991. Rare earth element mobility during hydrothermal and metamorphic fluid–rock interaction and the significance of the oxidation state of europium. Chemical Geology 93, 219–230.

Bau, M., 1993. Effects of syn- and post-depositional processes on the rare-earth element distribution in Precambrian iron-forma- tions. European Journal of Mineralogy 5, 257–267.

Bau, M., 1999. Scavenging of dissolved yttrium and rare earths by precipitating iron oxyhydroxide: experimental evidence for Ce- oxidation, Y–Ho fractionation, and lanthanide tetrad effect. Geochimica et Cosmochima Acta 63, 67–77.

Bau, M., Dulski, P., 1992. Small-scale variations of the rare- earth element distribution in Precambrian iron formations. European Journal of Mineralogy 4, 1429–1433.

Bau, M., Dulski, P., 1996. Distribution of yttrium and rare-earth elements in the Penge and Kuruman iron formations, Transvaal Supergroup, South Africa. Precambrian Research 79, 37–55.

Bau, M., Dulski, P., 1999. Comparing yttrium and rare earths in hydrothermal fluids from the Mid-Atlantic Ridge: implications for Y and REE behaviour during near- vent mixing and for the Y/Ho ratio of Proterozoic seawater. Chem. Geol. 155, 77–90.

Bau, M., Möller, P., 1993. Rare earth element systematics of the chemically precipitated component in Early Precambrian iron formations and the evolution of the terrestrial atmosphere–hydrosphere–lithosphere system. Geochimica et Cosmochima Acta 57, 2239–2249.

Bédard, J.J., Harris, L.B., and Thurston, P.C. 2013. The hunting of the snArc. Precambrian Research 229, 20–48.

Bekker, A., Holland, H. D., Wang, P. -L., Rumble III, D., Stein, H. J., Hannah, J. L., Coetzee, L. L., Beukes, N. J., 2004. Dating the rise of atmospheric oxygen. Nature 427, 117–120.

Bekker, A., Slack, J. F., Planavsky, N., Krapež, B., Hofmann, A., Konhauser, K. O. and Rouxel, O. J., 2010. Iron formation: The sedimentary product of a complex interplay among mantle, tectonic, oceanic, and biospheric processes. Economic Geology 105, 467–508.

Bekker, A., Holland, H. D., 2012. Oxygen overshoot and recovery during the early Paleoproterozoic. Earth and Planetary Science Letters 317-318, 295-304.

Bennett, V., Jackson, V. A., Rivers, T., Relf, C., Horan, P., Tubrett, M., 2005. Geology and U–Pb geochronology of the Neoarchean Snare River terrane: tracking evolving tectonic regimes and crustal growth. Canadian Journal of Earth Science 934, 895–934.

Bennett, V., Rivers, T., Jackson, V.A. 2012. A compilation of U-Pb zircon primary crystallization ages from Paleoproterozoic southern Wopmay Orogen, Northwest Territories. Northwest Territories Geoscience Office, NWT Open Report 2012-003, 157 p.

Bethune, K. M., Villeneuve, M. E., Bleeker, W., 1999. Laser ^{40}Ar/^{39}Ar thermochronology of Archean rocks in Yellowknife Domain, southwestern Slave Province: insights into the cooling history of an Archean granite-greenstone terrane. Canadian Journal of Earth Sciences 36, 1189–1206.

Beukes, N., 1973. Precambrian iron-formations of southern Africa. Economical Geology 68, 960–1004.

Bleeker, W., 2002. Archaean tectonics: a review, with illustrations from the Slave craton. In: Fowler, C. M. R., Ebinger, C. J., Hawkesworth, C. J. (Eds.), The Early Earth: Physical, Chemical and Biological Development. The Geological Society of London 199, 151–181.

Bleeker, W., Villeneuve, M. E., 1995. Structural studies along the Slave portion of the SNORCLE transect. In Cook, F., and Erdmer, P., eds. Slave–Northern Cordillera Lithospheric Evolution (SNORCLE) Transect and Cordilleran Tectonics Workshop. Lithoprobe Report 44, 8–13.

Bleeker, W., Ketchum J. W. F., Jackson, V. A., Villeneuve, M. E., 1999a. The Central Slave Basement Complex, Part I: its structural topology and autochthonous cover. Canadian Journal of Earth Sciences 36, 1083-1109.

Bleeker, W., Ketchum, J. W., Davis, W. J., 1999b. The Central Slave Basement Complex, Part II: age and tectonic significance of high-strain zones along the basement-cover contact. Canadian Journal of Earth Sciences 36, 1111–1130.

Bleeker, W., Hall, B., 2007. The Slave Craton: Geological and Metallogenic Evolution, in Goodfellow, W.D., ed., Mineral Deposits of Canada: A synthesis of major Deposit-types, District Metallogeny, the evolution of geological provinces, and exploration methods. Geological Society of Canada, Mineral deposit division, Special Publication 5, 849-879.

Bleeker, W., LeCheminant, T., Davis, W.J., Buchan, K., Ketchum, J. Sircombe, K., Snyder, D., van Breemen, O., Ootes, L., 2007. Transect across the southwestern Slave craton: from Phanerozoic platform edge to the core of the Yellowknife Supracrustal Domain. Geological Association of Canada, Field Trip Guide Book A1, 232 p.

Bolhar, R., Kamber, B.S., Moorbath, S., Fedo, C.M., Whitehouse, M.J., 2004. Characterisation of early Archaean chemical sediments by trace element signatures. Earth and Planetary Science Letters 222, 43–60.

Bolhar, R., Kamber, B., Moorbath, S., Collerson, K., 2005. Chemical characterization of earth's most ancient clastic metasediments from the Isua Greenstone Belt, southern West Greenland. Geochimica et Cosmochimica Acta 69, 1555–1573.

Bostock, H. H., 1980. Geology of the Itchen Lake area, District of Mackenzie. Geological Survey of Canada Memoir 391, 101 p.

Brophy, J.A., 1995. Additional evidence for syngenetic gold enrichment in amphibolitic banded iron-formation, Slave Province. In Exploration Overview 1995. NWT Geological Mapping Divi- sion, Department of Indian Affairs and Northern Development, pp. 3/6–3/7.

Byrne, R. H., Kim, K.-H., 1990. Rare earth element scavenging in seawater. Geochimica et Cosmochima Acta 54, 2645–2656.

Byrne, R., Sholkovitz, E., 1996. Marine chemistry and geochemistry of the lanthanides. In: Gschneider Jr., K.A., Eyring, L. (Eds.), Handbook on the Physics and Chemistry of the Rare Earths, 23. Elsevier, Amsterdam, p. 497–593.

Canfield, D.E., 2005. The early history of atmospheric oxygen: homage to Robert M. Garrels. Annual Review. Earth and Planetary Science 33, 1–36

Cantrell, K. J., Byrne J. H., 1987. Rare earth element complexation by carbonate and oxalate ions. Geochimica et Cosmochima Acta 51, 597-605.

Cawood, P.A., Hawkesworth, C.J., Dhuime, B., 2012. Detrital zircon record and tectonic setting. Geology 40, 875-878.

Censi P., Saiano F., Mazzola S., Ferla P., 2007. Alteration effects of volcanic ash in seawater : Anomalous Y/Ho ratios in coastal waters of the Central Mediterranean sea. Geochimica et Cosmochima Acta 71, 5405–5422.

Chen, C.W., Rondenay, S., Evans, R.L., Snyder, D.B. 2009. Geophysical Detection of relict metasomatism from an Archean (~3.5 Ga) subduction zone. Science, 326, 1089-1091.

Condie, K. C., 1993. Chemical composition and evolution of the upper continental crust: Contrasting results from surface samples and shales. Chemical Geology 104, 1-37.
Condie, K. C., 2004. Supercontinents and superplume events: distinguishing signals in the geologic record. Physics of the Earth and Planetary Interiors 146, 319–332.

Cousens, B. L., 2000. Geochemistry of the Archean Kam Group, Yellowknife Greenstone Belt, Slave Province, Canada. Journal of Geology 108, 181-198.

Cousens, B. L., Facey, K., Falck, H., 2002. Geochemistry of the late Archean Banting Group, Yellowknife Greenstone Belt, Slave Province, Canada: simultaneous melting of the upper mantle and juvenile mafic crust. Canadian Journal of Earth Science 39, 1635-1656.

Creaser, R. A., Erdmer, P., Stevens, R. A., Grant, S. L., 1997. Tectonic affinity of Nisutlin and Anvil assemblage strata from the Teslin tectonic zone, northern Canadian Cordillera: Constraints from neodymium isotope and geochemical evidence. Tectonics 16, 107–121.

Cullers, R. L., Chaudhuri, S., Arnold, B., Lee, M., Wolf, C. W., 1975. Rare earth distributions in clay minerals and in the clay-sized fraction of the Lower Permian Havensville and Eskridge shales of Kansas and Oklahoma. Geochimica et Cosmochima Acta 39, 169l-l 703.

Danielson, A., Möller, P., Dulski, P., 1992. The europium anomalies in banded iron formations and the thermal history of the oceanic crust. Chemical Geology 97, 1–12.

Davies, D. W., Pezzutto, F., Ojakangas, R. W., 1990. The age and provenance of metasedimentary rocks in the Quetico Subprovince, Ontario, from single zircon analyses: implications for Archean sedimentation and tectonics in the Superior Province. Earth and Planetary Science Letters 99: 195–205.

Davis, W. J., Hegner, E., 1992. Neodymium isotopic evidence for the tectonic assembly of Late Archean crust in the Slave Province, northwest Canada. Contributions to Mineralogy and Petrology 111, 493–504.

Davis, W. J., Fryers, B. J., King, J. E., 1994. Geochemistry and evolution of late Archean plutonism and its significance to the tectonic development of the Slave craton. Precambrian Research 67, 207–241

Davis, W.J., and Bleeker, W. 1999. Timing of plutonism, deformation, and metamorphism in the Yellowknife Domain, Slave Province, Canada. Canadian Journal of Earth Sciences, 36:1169-1187.

Davis, W., Jones, A., Bleeker, W., Grütter, H., 2003. Lithosphere development in the Slave craton: a linked crustal and mantle perspective. Lithos 71, 575–589.

De Baar, H. J. W., Bacon M. P., Brewer, P. G., Bruland K. W., 1985. Rare earth elements in the Pacific and Atlantic Oceans. Geochimica et Cosmochimica Acta 49, 1943–1959.

DePaolo, D. J., 1981. Neodymium isotopes in the Colorado Front Range and crust-mantle evolution in the proterozoic. Nature 291, 193–196.

Derry, L.A., Jacobsen, S.B., 1990. The chemical evolution of Precambrian seawater: evidence from REEs in banded iron formations. Geochimica et Cosmochimica Acta 54, 2965–2977.

Derry, L. A., Kurtz, A. C., Ziegler, K., Chadwick, O. A., 2005. Biological control of terrestrial silica cycling and export fluxes to water-sheds. Nature 433, 728–731.

Dillon-Leitch, H. C. H., 1981. Volcanic stratigraphy, structure and metamorphism in the Courageous-MacKay Lake greenstone belt, Slave Province, Northwest Territories: Unpublished M.Sc. thesis, University of Ottawa, Ottawa, ON, 169 p.

Drever, J. I., 1974. Geochemical model for the origin of Precambrian Banded Iron Formations. Geological Society of American Bulletin 85, 1099–1106.

Dymek, R. F., Klein, C., 1988. Chemistry, petrology and origin of banded iron-formation lithologies from the 3800 Ma Isua supracrustal belt, west Greenland. Precambrian Research 39, 247-302.

Eggleton, R., Chappell, B., 1978. The crystal structure of stilpnomelane Part III Chemistry and physical properties. Mineralogical Magazine 4, 361-368.

Eigenbrode, J. L., Freeman, K. H., 2006. Late Archean rise of aerobic microbial ecosystems. Proceedings of the National Academy of Sciences 103, 15759–15764.

Elderfield, H., 1988. The oceanic chemistry of the rare earth elements. Philosophical Transaction of the Royal Society 325, 105-126.

Elderfield, H., 1988. The oceanic chemistry of the rare earth elements. Philosophical Transaction of the Royal Society 325, 105-126.

Elderfield, H., Upstill-Goddard, R., Sholkovitz, E. R., 1990. The rare earth elements in rivers, estuaries, and coastal seas and their significance to the composition of ocean waters. Geochimica et Cosmochimica Acta 54, 971–991.

Eriksson, K.A., 1995. Crustal growth, surface processes, and atmospheric evolution on the early Earth. Geological Society of London Special Publications 95, 11-25.

Eriksson, K. A., Krapež, B., Fralick, P. W., 1997. Sedimentological aspects. In Greenstone Belts (eds. De Wit M. J. and Ashwal L .D.). Clarendon Press, Oxford, p. 33-54.

Eriksson, P. G., Martins-Neto, M. A., Nelson, D. R., Aspler, L. B., Chiaranzelli, J. R., Catuneanu, O., Sakar, S., Altermann, W., Rautenbach, C. J., 2001. An introduction to Precambrian basins: their characteristics and genesis. Sedimentary Geology 141-142, 1–35.

Eriksson, P. G., Altermann, W., 2004. Evolution of the Hydrosphere and Atmosphere. In: Eriksson P.G. et al. (eds.). The Precambrian Earth: Tempos and Events. Elsevier, Amsterdam. p. 359-513.

Fan, J., Kerrich, R., 1997. Geochemical characteristics of aluminum depleted and undepleted komatiites and HREE-enriched low-Ti tholeiites, western Abitibi greenstone belt: A heterogeneous mantle plume-convergent margin environment. Geochimica et Cosmochimica Acta 61, 4723–4744.

Faure G., Mensing T. M., 2005. Isotopes: Principles and applications. John Wiley and Sons Limited, 897 p.

Fedo, C.M, Sircombe, K.N., Rainbird, R.H. 2003. Detrital zircon analysis of the sedimentary record. Reviews in Mineralogy and Geochemistry 53, 277–303.

Ferguson, M. E., 2002. Sedimentology and tectonic setting of the late Archean Burwash Formation, southern Slave Province. MS dissertation, Dalhousie University, Halifax.

Ferguson, M., Waldron, W. F., Bleeker, W., 2005. The Archean deep-marine environment: turbidite architecture of the Burwash Formation, Slave Province, Northwest Territories. Canadian Journal of Earth Sciences 42, 935-954.

Frei, R., Polat, A., 2007. Source heterogeneity for the major components of ~3.7 Ga Banded Iron Formations (Isua Greenstone Belt, Western Greenland): tracing the nature of interacting water masses in BIF formation. Earth Planetary Science Letters 253, 266–281.

Frei, R., Dahl, P. S., Duke, E. F., Frei, K. M., Hansen, T. R., Frandsson, M. M., Jensen, L. A., 2008. Trace element and isotopic characterization of Neoarchaean and Paleo-proterozoic iron formations in the Black Hills (South Dakota, USA): assessment of chemical change during 2.9–1.9Ga deposition bracketing the 2.4–2.2Ga first rise of atmospheric oxygen. Precambrian Research 162, 441–474.

Frei, R., Gaucher, C., Poulton, S.W., Canfield, D.E., 2009. Fluctuations in Precam- brian atmospheric oxygenation recorded by chromium isotopes. Nature 461, 250–253

Frith, R. A, 1987. Precambrian geology of the Hackett River area, District of Mackenzie, NWT. Geological Survey of Canada, Memoir 417, 61 p.

Froelich, P. N., Blanc, V., Mortlock, R. A., Chillrud, S. N., Dunstan, W., Udomkit, A., and Peng, T.- H., 1992, River fluxes of dissolved silica to the ocean were higher during glacials: Ge/Si in diatoms, rivers, and oceans. Paleoceanography 7, 739–767.

Fryer, B. J., 1977. Rare earth evidence in iron-formations for changing Precambrian oxidation states. Geochimica et Cosmochimica Acta 41, 361-367.

Fyson, W. K., Jackson, V. A., 1991. Reorientation of structures near granitic plutons and orthogonal lineaments, Russell Lake supracrustal domain, southwestern Slave Province. Canadian Journal of Earth Sciences 28, 126-135.

Fyson, W.K., Jackson, V.A., 2008. Images of an unconformity, Mattberry Lake, NWT. Northwest Territories Geological Survey, NWT Open Report 2008-004, 27 p.

German, C. R., Holliday, B. P., Elderfield, H., 1991. Redox cycling of rare earth elements in the suboxic zone of the Black Sea. Geochimica et Cosmochimica Acta 55, 3553–3558.

Goldstein S. J., Jacobsen S. B., 1987. The Nd and Sr isotopic systematics of river-water dissolved material - Implications for the sources of Nd and Sr in seawater. Chemical Geology 66, 245–272.

Gole, M.J. 1980a. Mineralogy and petrology of very low metamorphic grade Archaean banded iron-formations, Weld Range, Western Australia. American Mineralogist 66, 8-25.

Gole, M.J., 1980b. Low temperature retrograde minerals in metamorphosed Archean banded iron formations, western Australia. Canadian Mineralogy 18, 205–214.

Gole, M.J., Klein, C., 1981a. Banded Iron-Formation through much of Precambrian time. Journal of Geology 89, 169–183.

Gole, M.J., Klein, C., 1981b. High-grade metamorphic Archean banded iron-formations, West- ern Australia: Assemblages with coexisting pyroxenes ± fayalite. American Mineralogist 66, 87–99.

Gross, G., 1980. A classifiacation of iron formations based on depositional environments. Canadian Mineralogist 18, 215-222.

Gross G., 1983. Tectonic systems and the deposition of iron-formation. Precambrian Research 20, 171-187.

Hamade, T., Konhauser, K. O., Raiswell, R., Goldsmith, S., Morris, R. C., 2003. Using Ge/Si ratios to decouple iron and silica fluxes in Precambrian banded iron for- mations. Geology 31, 35–38.

Haugaard, R., Frei R., Stendal, H., Konhauser, K., 2013. Petrology and geochemistry of the ~2.9 Ga Itilliarsuk banded iron formation and associated supracrustal rocks, West Greenland: Source characteristics and depositional environment. Precambrian Research 229, 150–176.

Haugaard R., Pecoits E., Lalonde S., Rouxel O. and Konhauser K., 2016. The Joffre Banded Iron Formation, Hamersley Group, Western Australia: Assessing the Palaeoenvironment through detailed Petrology and Chemostratigraphy. Precambrian Research 273, 12–37.

Heaman, L.M., Pearson, D. G., 2010. Nature and evolution of the Slave Province subcontinental lithospheric mantle. Canadian Journal of Earth Sciences 47, 369-388.

Helmstaedt, H., 2009. Crust–mantle coupling revisited: The Archean Slave craton, NWT, Canada. In Proceedings of the 9th International Kimberlite Conference. Edited by Stephen Foley, Sonja Aulbach, Gerhard Brey, Herman Grütter, Heidi Höfer, Dorrit Jacob, Volker Lorenz, Thomas Stachel and Alan Woodland. Lithos 112, 1055-1068.

Helmstaedt, H., Padgham, W. A., 1986. A new look at the stratigraphy of the Yellowknife Supergroup at Yellowknife, NWT: implications for the age of gold-bearing shear zones and Archean basin evolution. Canadian Journal of Earth Sciences 23, 454–475.

Henderson, J. B., 1970. Stratigraphy of the Archean Yellowknife Supergroup, Yellowknife Bay–Prosperous Lake Area, District of Mackenzie. Geological Survey of Canada Paper 70-26.

Henderson, J. B., 1972. Sedimentology of Archean turbidites at Yellowknife, Northwest Territories. Canadian Journal of Earth Sciences 9, 882-902.

Henderson, J. B. 1975. Sedimentology of the Archean Yellowknife Supergroup at Yellowknife, District of Mackenzie. Geological Survey of Canada, Bulletin 246, 62 p.

Henderson, J. B. 1998. Geology of the Keskarrah Bay area, District of Mackenzie, Northwest Territories. Geological Survey of Canada Bulletin 527, 122 p.

Henderson, J. R., Kerswill, J. A., Henderson, M. N., Villeneuve, M., Petch, C. A., Dehls, J. F., Okeefe, M. D., 1995. Geology, geochronology, and metallogeny of High Lake greenstone belt, Archean Slave Province, Northwest Territories. Geological Survey of Canada Current Research 1995-C, 97–106.

Henderson, J. R., Henderson, M. N., Kerswill, J. A., Dehls, J. F., 2000. Geology, High Lake greenstone belt, Nunavut. Geological Survey of Canada, Map 1945A, scale 1 : 100; 000.

Holland, H. D., 1973. The oceans: A possible source of iron in iron formations. Economic Geology 68, 1169-1172.

Holland, H. D., 1999. When did the Earth's atmosphere become oxic? A reply. Geochemical News 100, 20–22.

Holland, H. D., 2002. Volcanic gases, black smokers, and the Great Oxidation Event. Geochimica et Cosmochimica Acta 66, 1-16.

Holland H., Beukes N., 1990. A paleoweathering profile from Griqualand West, South Africa: evidence for a dramatic rise in atmospheric oxygen between 2.2 and 1.9 BYBP. American Journal of Science 290-A, 1-34.

Hunter, K. A., Boyd, P. W., 2007. Iron-binding ligands and their role in the ocean biogeochemistry of iron. Environmental Chemistry 4, 221–232.

Huston, D.L., Logan, G.A., 2004. Barite, BIFs and bugs: evidence for the evolution of the Earth's early hydrosphere. Earth and Planetary Science Letters 220, 41–55.

Isachsen, C. E., Bowring, S. A., Padgham, W. A., 1991. U-Pb zircon geochronology of the Yellowknife volcanic belt, NWT, Canada: new constraints on the timing and duration of greenstone belt magmatism. Journal of Geology 99, 55–68.

Isachsen, C. E., Bowring, S. A., 1994. Evolution of the Slave craton. Geology 22, 917–920.

Isachsen, C., Bowring, S., 1997. The Bell Lake group and Anton Complex: a basement-cover sequence beneath the Archean Yellowknife greenstone belt revealed and implicated in greenstone belt formation. Canadian Journal of Earth Science 189, 169–189.

Isley, A. E., 1995. Hydrothermal plumes and the delivery of iron to banded iron formation. Journal of Geology 103, 169–185.

Isley, A. E., Abbott D., 1999. Plume-related mafic volcanism and the deposition of banded iron formation. Journal of Geophysical Research 104, 15461-15477.

Jackson, V. A., 1985. Geology of the Keskarrah Bay area, parts of NTS areas 86 H/6 and 86 H/7. Northwest Territories Geoscience Office EGS 1985-8:1 map, scale 1:50,000.

Jackson, V. A., 2001. Report on the geology of the northern Russell Lake area (85O=4). Northwest Territories Geoscience Office, EGS 2001–03, 90 p.

Jackson, V.A., 2008. Preliminary geological map of part of the South Wopmay orogen (parts of NTS 86B and 86C; 2007 updates); descriptive notes to accompany 1:100 000 scale map. Northwest Territories Geological Survey, NWT Open Report 2008-007, 53 p. and 1 map, scale 1:100,000.

Jacobsen, S. B., Pimentel-Klose, M. R., 1988. A Nd isotope study of the Hamersley and Michipicoten banded iron formations: The source of REE and Fe in Archaean oceans. Earth and Planetary Science Letters 87, 29-44.

James, H. L., 1954. Sedimentary facies of iron-formation. Economic Geology 49, 235–291.

Jenner, G. A., Fryer, B. J., McLennan, S. M., 1981. Geochemistry of the Archean Yellowknife Supergroup. Geochimica et Cosmochimica Acta 45, 1111–1129.

Kato Y., Ohta I. and Tsunematsu T., 1998. Rare earth element variations in mid-Archean banded iron formations: Implications for the chemistry of ocean and continent and plate tectonics. Geochimica et Cosmochimica Acta 62, 1–23.

Kato Y., Yamaguchi K. and Ohmoto H., 2006. Rare earth elements in Precambrian banded iron formations: Secular changes of Ce and Eu anomalies and evolution of atmospheric oxygen. Geological Society of America Memoir 198, 269-289.

Ketchum, J. W. F., Bleeker W., 2000. New field and U–Pb data from the Central Slave Cover Group near Yellowknife and the Central Slave Basement Complex at Point Lake. In Slave-Northern Cordillera Lithospheric Experiment (SNORCLE) Transect Meeting (compilers Cook F., Erdmer P.). University of Calgary, LITHOPROBE Report No. 72, 27–31 p.

Ketchum, J. W. F., Bleeker, W., Stern, R. A., 2004. Evolution of an Archean basement complex and its autochthonous cover, southern Slave Province, Canada. Precambrian Research 135, 149–176.

Kim, K. H., Byrne, R. H., Lee, J. H., 1991. Gadolinium behaviour in seawater: a molecular basis for gadolinium anomalies. Marine Chemistry 36, 107–120.

Klein, C., 1973, Changes in mineral assemblages with metamorphism of some banded Precambrian iron-formations. Economic Geology 68, 1075-1088.

Klein C., 1974. Greenalite, stilpnomelane, minnesotaite, crocidolite and carbonates in a very low grade metamorphic precambrian iron-formation. Canadian Mineralogist 12, 1–24.

Klein, C., 2005. Some Precambrian banded iron-formations (BIFs) from around the world: their age, geologic setting, mineralogy, metamorphism, geochemistry, and origins. American Mineralogist 90, 1473–1499.

Klein, C., Gole, M., 1981. Mineralogy and petrology of parts of the Marra Mamba Iron Formation, Hamersley Basin, Western Australia. American Mineralogist 66, 1–19.

Klein, C., Beukes, N. J., 1989. Geochemistry and sedimentology of a facies transition from limestone to iron-formation deposion in the Early Proterozoic Transvaal Supergroup, South Africa. Economic Geology 84, 1733-1774.

Konhauser K. O., Fyfe W. S., Kronberg B. I., 1994. Multi-element chemistry of some Amazonian waters and soils. Chemical Geology 111, 155-175.

Konhauser, K. O., Pecoits, E., Lalonde, S. V., Papineau, D., Nisbet, E. G., Barley, M. A., Arndt, N. T., Zahnle, K., Kamber, B. S., 2009. Oceanic nickel depletion and a methanogen famine before the Great Oxidation Event. Nature 458, 750–753.

Konhauser, K. O., Lalonde, S. V, Planavsky, N. J., Pecoits, E., Lyons, T. W., Mojzsis, S. J., Rouxel, O. J., Barley, M. E., Rosiere, C., Fralick, P. W., Kump, L. R., Bekker, A., 2011. Aerobic bacterial pyrite oxidation and acid rock drainage during the Great Oxidation Event. Nature 478, 369–373.

Kositcin, N., Brown, S. J. A., Barley, M. E., Krapež, B, Cassidy, K. F., Champion, D.C. 2008. SHRIMP U–Pb zircon age constraints on the Late Archean tectonostratigraphic architecture of the Eastern Goldfields Superterrane, Yilgarn Craton. Western Australia. Precambrian Research 161, 5–33.

Kröner, A., Layer, P. W., 1992. Crust Formation and Plate Motion in the Early Archean. Science 256, 1405-1411.

Locock, A. J., 2014. An Excel spreadsheet to classify chemical analyses of amphiboles following the IMA 2012 recommendations. Computers & Geosciences 62, 1-11.

Lowe, D.R., 1980. Archean sedimentation. Annual Reviews of Earth and Planetary Sciences 8, 145-167.

Lowe, D. R., Tice, M. M., 2007. Tectonic controls on atmospheric, climatic, and biological evolution 3.5–2.4 Ga. Precambrian Research 158, 177–197.

McLennan, S. M., 1984. Petrological characteristics of Archean graywackes. Journal of Sedimentary Petrology 54, 889–898.

McLennan S. M., 1989. Rare Earth Elements in sedimentary rocks: Influence of provenance and sedimentary processes. In Geochemistry and mineralogy of Rare Earth Elements (eds. Lipin B. R. and McKay G. A.) Reviews in Mineralogy 21, 169-200.

Michard, A., Albarbde, F., Michard, G., Minster, J. F., Charlou, J. L., 1983. Rare earth elements and uranium in high-temperature solutions from East Pacific Rise hydrothermal vent field (13~N). Nature 303, 795-797.

Miller, R. G., O'Nions, R. K., 1985. Source of Precambrian chemical and clastic sediments. Nature 314, 325–330.

Moore, J. C. G., 1956. Courageous-Matthews lakes area, District of Mackenzie, Northwest Territories. Geological Survey of Canada, Memoir 283, 52 p. (4 sheets).

Mortensen., J. K., Henderson, J. B., Jackson, V. A., Padgham, W. A. 1992. U–Pb geochronology of the Yellowknife Supergroup felsic volcanic rocks in the Russell Lake and Clan Lake areas, southwestern Slave Province, Northwest Territories. In Radiogenic age and isotopic studies: Report 5. Geological Survey of Canada, Paper 91-2, p. 1–7.

Mortlock, R. A., Froelich, P. N., 1987. Continental weathering of germanium; Ge/Si in the global river discharge, Geochimica et Cosmochimica Acta 51, 2075–2082.

Nisbet, E. G., Cheadle, M. J., Arndt, N. T., Bickle, M. J., 1993. Constraining the potential temperature of the Archean mantle — a review of the evidence from komatiites. Lithos 30, 291–307.

Northrup, C. J., Isachsen, C., Bowring, S. A., 1999. Field relations, U-Pb geochronology, and Sm-Nd isotope geochemistry of the Point Lake greenstone belt and adjacent gneisses, central Slave craton, N.W.T., Canada. Canadian Journal of Earth Sciences 36, 1043-1059.

Ootes, L., Buse, S., Davis, W. J., Cousens, B. C., 2005. U-Pb ages from the northern Wecho River area, southwestern Slave Province, Northwest Territories: constraints on late Archean plutonism and metamorphism. Geological Survey of Canada Current Research, 2005-F2, 13 p.

Ootes, L., Pierce, K., 2005. Digital geological atlas of the Wecho River area. Northwest Territories Geoscience Office, NWT Open File 2005-03 map, scale 1 : 100; 000.

Ootes, L., Davis, W. J., Jackson, V. A., 2006. Two turbidite sequences in the Russell Lake–Mosher Lake area: SHRIMP U-Pb detrital zircon evidence and cor- relations in the southwestern Slave craton, North-west Territories. Geological Survey Canada Current Research, 2006- A7, 15 p

Ootes, L., Davis, W. J., Bleeker, W., Jackson, V. A., 2008. Geologic overview of greywacke samples col- lected from the western Slave craton. Northwest Territories Geoscience Office, NWT Open Report 2008-012, p. 14.

Ootes, L., Davis, W.J., Bleeker, W., Jackson, V.A., 2009. Two Distinct Ages of Neoarchean Turbidites in the Western Slave Craton: Further Evidence and Implications for a Possible Back-Arc Model. The Journal of Geology 117, 15–36.

Ootes, L., Morelli, R. M., Creaser, R. A., Lentz, D. R., Falck, H., Davies, W. J., 2011. The timing of Yellowknife gold mineralization: a temporal relationship with crustal anatexis? Economic Geology 106, 713-720.

Padgham, W., 1992. Mineral deposits in the Archean Slave Structural Province; lithological and tectonic setting. Precambrian Research 58, 1–24.

Padgham, W., Fyson, W., 1992. The Slave Province: a distinct Archean craton. Canadian Journal of Earth Sciences 29, 2072-2086.

Pecoits, E., Smith, M. L., Catling, D. C., Philippot, P., Kappler, A., Konhauser, K. O., 2015. Atmospheric hydrogen peroxide and Eoarchean iron formations. Geobiology, 13:1-14.

Pehrsson, S., Villeneuve, M., 1999. Deposition and imbrication of a 2670–2629 Ma supracrustal sequence in the Indin Lake area, southwestern Slave Province, Canada. Canadian Journal of Earth Sciences 36, 1–21.

Pehrsson, S.J., Chacko, T., Pilkington, M., Villeneuve, M.E., Bethune, K., 2000. Anton terrane revisited: late Archean exhumation of a moderate-pressure granulite terrane in the western Slave Province. Geology 28, 1075–1078.

Pickard, A.L., Barley, M.E., Krapež, B., 2004. Deep-marine depositional setting of banded iron formation: sedimentological evidence from interbedded clastic sedimentary sequence in the rocks in the early Palaeoproterozoic Dales Gorge Member of Western Australia. Sedimentary Geology 170, 37–62.

Piepgras, D. J., Wasserburg G. J., 1987. Rare earth element transport in the western North Atlantic inferred from Nd isotopic observations. Geochimica et Cosmochimica Acta 51, 1257-1271.

Piper, D. J. W., Normark, W. R., 2001. Sandy fans: from Amazon to Hueneme and beyond. AAPG Bulletin 85, 1407–1438.

Polat, A., Frei, R., 2005. The origin of early Archean banded iron formations and of continental crust, Isua, southern West Greenland. Precambrian Research 138, 151–175.

Puchtel, I. S., Walker, R. J., Touboul, M., Nisbet, E. G., Byerly, G. R., 2014. Insights into early Earth from the Pt-Re-Os isotope and highly siderophile element abundance systematics of Barberton komatiites. Geochimica et Cosmochimica Acta 125, 394–413.

Rasmussen, B., Fletcher, I. R., 2010. Dating sedimentary rocks using in situ U-Pb geochronology of syneruptive zircon in ash-fall tuffs <1 mm thick. Geology 38, 299–302.

Rasmussen, B., Meier, D., Krapež, B., Muhling, J., 2013. Iron silicate microgranules as precursor sediments to 2.5-billion-year-old banded iron formations. Geology 41, 435–438.

Rasmussen, B., Krapež, B., Meier, D.B., 2014. Replacement origin for hematite in 2.5 Ga banded iron formation: evidence for postdepositional oxidation of iron- bearing minerals. Geological Society of America Bulletin 126 (3–4), 438–446.

Rasmussen, B., Krapež, B., Muhling, J.R., 2015. Seafloor silicification and hardground development during deposition of 2.5 Ga banded iron formations. Geology 43, 235–238.

Robbins,L. J., Lalonde, S. V., Saito, M. A., Planavsky, N. J., Mloszewska, M. A., Pecoits, E., Scott, C., Dupont, C. L., Kappler, A., Konhauser, K. O., 2013. Authigenic iron oxide proxies for marine zinc over geological time and implications for eukaryotic metallome evolution. Geobiology 11, 295-306.

Ruhlin, D. E., Owen, R. M., 1986. The rare earth clement geochemistry of hydrothcrmal sediments from the East Pacific Rise: Examination of a seawater scavenging mechanism. Geochimica et Cosmochimica Acta 50, 393- 400.

Rye, R., Holland, H., 1998. Paleosols and the evolution of atmospheric oxygen: A critical

review. American Society of London Special Publications 95, 11–25.

Schmidberger, S. S., Heaman, L. M., Simonetti, A., Creaser, R. A., Whiteford, S., 2007. Lu–Hf, in-situ Sr and Pb isotope and trace element systematics for mantle eclogites from the Diavik diamond mine: evidence for Paleoproterozoic subduction beneath the Slave craton, Canada. Earth Planetary Science Letters 254, 55–68.

Selley, R.C., 1988. Applied Sedimentology. Academic Press, 446 p.

Sharma, R., Pandit, M., 2003. Evolution of early continental crust. Current Science 84, 1–7.

Sherlock, R. L., Shannon, A., Hebel, M., Lindsay, D., Madsen, J., Sandeman, H., Hrabi, B., Mortensen, J. K., Tosdal R. M., Friedman, R., 2012. Volcanic stratigraphy, geochronology, and gold deposits of the Archean hope bay greenstone belt, Nunavut, Canada. Economic Geology 107, 991–1042.

Shirey, S. B., and Richardson, S. H., 2011. Start of the Wilson cycle at 3 Ga shown by diamonds from subcontinental mantle. Science 333, 434-436.

Sholkovitz, E. R., Landing, W. M., Lewis, B. L., 1994. Ocean particle chemistry: The fractionation of rare earth elements between suspended particles and seawater. Geochimica et Cosmochimica Acta 58, 1567–1579.

Simonetti, A., Heaman, L. M., Hartlaub, R. P., Creaser, R. A., MacHattie, T. G., Böhm, C., 2005. U–Pb zircon dating by laser ablation–MC–ICP–MS using a new multiple ion counting Faraday collector array. Journal of Analytical Atomic Spectrometry 20, 677–686.

Simonetti, A., Heaman, L. M., Chacko, T., Banerjee, N. R., 2006. In situ petrographic thin section U–Pb dating of zircon, monazite, and titanite using laser ablation–MC–ICP-MS. International Journal of Mass Spectrometry 253, 87–97.

Simonson, B. M., 1985, Sedimentological constraints on the origins of Precambiran iron-formations. Geological Society of America Bulletin 96, 244-252.

Sircombe, K., Bleeker, W., Stern, R. A., 2001. Detrital zircon geochronology and grain-size analysis of a ~2800 Ma Mesoarchean proto-cratonic cover succession, Slave Province, Canada. Earth and Planetary Science Letters 189, 207–220.

Steinhofel, G., von Blackenburg, F., Horn, I., Konhauser, K.O., Beukes, N., Gutzmer, J., 2010. Deciphering formation processes of banded iron formations from the Transvaal and the Hamersley Sequence by combined Si and Fe isotope analysis using UV femtosecond laser ablation. Geochimica et Cosmochima Acta 74, 2677–2696.

Stern, R. A., Bodorkos, S., Kamo, S. L., Hickman, A. H., Corfu, F., 2009. Measurement of SIMS Instrumental Mass Fractionation of Pb Isotopes During Zircon Dating. Geostandards and Geoanalytical Research 33, 145–168.

Stubley, M. P., 2005. Slave Craton: interpretive bedrock compilation. Northwest Territories Geoscience Office, NWT-NU Open File 2005-01: Digital files and 2 maps.

Sugitani, K., Yamashita, F., Nagaoka, T., Yamamoto, K., Minami, M., Mimura, K., Suzuki, K., 2006. Geochemistry and sedimentary petrology of Archean clastic sedimentary rocks at Mt. Goldsworthy, Pilbara Craton, Western Australia: evidence for the early evolution of continental crust and hydrothermal alteration. Precambrian Research 147, 124-147.

Sun S. S. and McDonough W. F., 1989. Chemical and isotopic systematic of oceanic basalts: implications for mantle composition and processes. In Magmatism in the Ocean

Basins (eds. A. D. Saunders and M. J. Norry). Geological Society Special Publications, p. 313–345.

Tanaka, T., Togashi, S., Kamioka, H., et al., 2000. JNdi-1: a neodymium isotopic reference in consistency with LaJolla neodymium. Chemical Geology 168, 279–281.

Taylor S. R., McLennan S. M., Armstrong R. L., Tarney, J., 1981. The Composition and Evolution of the Continental Crust: Rare Earth Element Evidence from Sedimentary Rocks. Philosphia Transaction of the Royal Society 301, 381–399.

Taylor, S.R., McLennan, S.M., 1985. The Continental Crust: Its Composition and Evolution. Blackwell Scientific, Oxford, 312 p.

Taylor, S.R., McLennan, S.M., 2009. Planetary Crusts: Their Composition, Origin and Evolution. Cambridge University Press, New York, 378 p.

Trendall, A. F., 1968. Three Great Basins of Precambrian banded iron formation deposition: a systematic comparison. Geological Society of American Bulletin 79, 1527–1544.

Trendall, A. F., Blockley, J. G., 1970. The Iron-Formations of the Precambrian Hamersley Group, Western Australia. Geological Survey Western Australia Bulletin 119.

Trendall, A. F., Blockley, J. G., 2004. Precambrian iron-formation. In: Eriksson, P.G., Altermann, W., Nelson, D.R., Mueller, W.U., Catuneanu, O. (Eds.), The Precam- brian Earth: Tempos and Events. Developments in Precambrian Geology, 12. Elsevier, Amsterdam, pp. 403–421.

Unterschutz, J. L. E., Creaser, R. A., Erdmer, P., Thomson, R. I., Daughtry, K. L., 2002. North American margin origin of Quesnel terrane strata in the southern Canadian Cordillera: Inferences from geochemical and Nd isotopic characteristics of Triassic metasedimentary rocks. Geological Society of America Bulletin 114, 462-475.

Van Breemen, O., Davis, W. J., King, J. E., 1992. Temporal distribution of granitoid plutonic rocks in the Archean Slave Province, northwest Canadian Shield. Canadian Journal of Earth Sciences, 29: 2186–2199.

Viana, A. R., Faugeres, J.-C., Stow, D. A. V., 1998. Bottom-current-controlled sand deposits - a review of modern shallow- to deep-water environments. Sedimentary Geology 115, 53-80.

Villeneuve, M. E., 1993. Preliminary geochronological results from the Winter Lake-Lac de Gras Slave Province NATMAP project, Northwest Territories. In: Radiogenic Age and Isotopic Studies: Report 7, Geological Survey of Canada, Paper 93-2, p. 29–38.

Villeneuve, M., Lambert, L., van Breemen, O., and Mortensen, J., 2001. Geochronology of the Back River volcanic complex, Nunavut-Northwest Territories. Geological Survey of Canada Current Research 2001-F2, 8 p.

Wasserburg G. J., Jacobsen S. B., DePaolo D. J. and McCulloch M. T., 1981. Precise determinations of Sm/Nd ratios, Sm and Nd isotopic abundances in standard solutions. Geochimica et Cosmochima Acta 45, 2311-2323.

Webb, A. D., Dickens, G. R., Oliver, N. H. S., 2003. From banded iron-formation to iron ore: geochemical and mineralogical constraints from across the Hamersley Province, Western Australia. Chemical Geology 197, 215–251.

Windley, B. F., 1984. The Evolving Continents. John Wiley and Sons Limited, 399 p.

Yamashita, K., Creaser, R. A., 1999. Geochemical and Nd isotopic constraints for the origin of late Archean turbidites from the Yellowknife area, Northwest Territories, Canada. Geochimica et Cosmochimica Acta 63, 2579–2598.

Yamashita, K., Creaser, R. A., Stemler, J. U., Zimaro, T.W. 1999. Geochemical and Nd-Pb isotopic systematics of late Archean granitoids, southwestern Slave Province, Canada:

constraints for granitoid origin and crustal isotopic structure. Canadian Journal of Earth Science 36, 1131–1147.

Yamashita, K., Creaser, R. A., Villeneuve, M. E., 2000. Integrated Nd isotopic evidence and U-Pb detrital zircon systematics of clastic sedimentary rocks from the Slave Province, Canada: evidence for extensive crustal reworking in the early- to mid-Archean. Earth Planetary Science Letters 174, 283–299.

Zhang, J., Nozaki, Y., 1996. Rare earth elements and yttrium in seawater: ICP-MS determinations in the East Caroline, Coral Sea, and South Fiji basins of the western South Pacific Ocean. Geochimica et Cosmochimica Acta 60, 4631–4644.

Appendix A

Table A1. Zircon U-Pb data of the tuff ash bed at Slemon Lake

Slemon Lake tuff

Grain #	^{207}Pb/^{206}Pb	2 σ (Ma)	^{207}Pb/^{235}U	2 σ (Ma)	^{206}Pb/^{238}U	2 σ (Ma)	^{207}Pb/^{206}Pb	2 σ (Ma)	^{207}Pb/^{235}U	2 σ (Ma)	^{206}Pb/^{238}U	2 σ (Ma)	% discord.
			Ratios						**Ages (Ma)**				
RHch-1	0.17528	0.00140	8.73326	0.63773	0.36136	0.02623	2609	13	2311	64	1989	123	27.6
RHch-2	0.17670	0.00150	11.84994	0.52771	0.48638	0.02126	2622	14	2593	41	2555	92	3.1
RHch-3	0.17681	0.00145	11.36382	1.04939	0.46615	0.04288	2623	14	2553	83	2467	186	7.2
RHch-4	0.17681	0.00145	8.75007	0.37299	0.35892	0.01501	2623	14	2312	38	1977	71	28.5
RHch-5	0.17601	0.00145	11.35981	0.49951	0.46810	0.02022	2616	14	2553	40	2475	88	6.5
RHch-6	0.17523	0.00191	8.53698	0.67006	0.35333	0.02746	2608	18	2290	69	1950	130	29.2
RHch-7	0.17740	0.00151	11.41266	0.72230	0.46659	0.02926	2629	14	2557	57	2469	127	7.3
RHch-8	0.17653	0.00155	5.22008	0.27425	0.21446	0.01111	2621	15	1856	44	1253	59	57.2
RHch-9	0.17534	0.00149	9.37857	0.63648	0.38792	0.02612	2609	14	2376	60	2113	120	22.3
RHch-10	0.17671	0.00143	12.27582	0.65421	0.50382	0.02654	2622	13	2626	49	2630	113	-0.4
RHch-11	0.17523	0.00168	9.02231	0.43049	0.37342	0.01745	2608	16	2340	43	2045	81	25.1
RHch-12	0.17635	0.00143	10.53811	0.61411	0.43341	0.02501	2619	13	2483	53	2321	112	13.5
RHch-13	0.17619	0.00153	9.11028	0.55413	0.37502	0.02258	2617	14	2349	54	2053	105	25.1
RHch-14	0.17544	0.00150	11.53202	0.61856	0.47672	0.02524	2610	14	2567	49	2513	109	4.5
RHch-15	0.17682	0.00201	8.13116	0.55962	0.33352	0.02264	2623	19	2246	60	1855	109	33.6
RHch-16	0.17453	0.00155	8.72956	0.34611	0.36276	0.01402	2602	15	2310	35	1995	66	27.0
RHch-17	0.17614	0.00691	3.50343	0.23860	0.14426	0.00803	2617	64	1528	52	869	45	71.2

Table A2. Zircon U-Pb TIMS data of the Dettah tuff bed

Fraction	Description	Weight (mg)	U (ppm)	Pb^T (pg)	Pb$_C$ (pg)	Th/U	^{206}Pb/ ^{204}Pb	^{206}Pb/ ^{238}U	± 2s	^{207}Pb/ ^{235}U
ZA	1 pale br, 2-3:1 pr	1.1	191	102.30	0.44	0.88	14147	0.503515	0.001165	12.48246
ZB	1 pale br, 2-3:1 sm pr	0.6	85	25.30	0.54	0.85	2534	0.500420	0.001593	12.40232
ZC	1 pale br, 2-3:1 pr	1.9	145	169.07	0.44	0.82	21505	0.511712	0.000973	12.67888

	± 2s	^{207}Pb/ ^{206}Pb	± 2s	^{206}Pb/ ^{238}U	± 2s	^{207}Pb/ ^{235}U	± 2s	^{207}Pb/ ^{206}Pb	± 2s	Disc. (%)
						Ages (Ma)				
ZA	0.03213	0.179799	0.000196	2628.9	5.0	2641.4	2.4	2651.0	1.8	1.0
ZB	0.04594	0.179749	0.000260	2615.6	6.8	2635.4	3.5	2650.6	2.4	1.6
ZC	0.02930	0.179703	0.000145	2663.9	4.1	2656.1	2.2	2650.1	1.3	-0.6

Notes:

All analyzed fractions represent best optical quality zircon present in the least magnetic recovered concentrate. All fractions underwent chemical abrasion pretreatment.

Abbreviations: br - brown; pr - prism; el - elongate; sm - small.

Pb^T is total amount (in picograms) of Pb.

Pb$_C$ is total measured common Pb (in picograms) assuming the isotopic composition of laboratory blank: 206/204 - 18.221; 207/204 - 15.612; 208/204 - 39.360 (errors of 2%).

Pb/U atomic ratios are corrected for spike, fractionation, blank, and, where necessary, initial common Pb; 206Pb/204Pb is corrected for spike and fractionation.

Th/U is model value calculated from radiogenic 208Pb/206Pb ratio and 207Pb/206Pb age, assuming concordance.

Disc. (%) - per cent discordance for the given 207Pb/206Pb age.

Appendix B
Table B1. Detrital zircon U-Pb data of the greywacke at Goose Lake

Goose Lake greywacke (RH18140)

	Ratios						Ages (Ma)						
Grain #	$^{207}Pb/^{206}Pb$	2 σ (Ma)	$^{207}Pb/^{235}U$	2 σ (Ma)	$^{206}Pb/^{238}U$	2 σ (Ma)	$^{207}Pb/^{206}Pb$	2 σ (Ma)	$^{207}Pb/^{235}U$	2 σ (Ma)	$^{206}Pb/^{238}U$	2 σ (Ma)	% discord.
1	0.18942	0.00212	13.60919	0.53199	0.52109	0.01952	2737	18	2723	36	2704	82	1.5
3	0.19113	0.00189	14.16757	0.55129	0.53759	0.02024	2752	16	2761	36	2773	84	-1.0
5	0.18198	0.00172	12.83213	0.46715	0.51142	0.01798	2671	16	2667	34	2663	76	0.4
6	0.18640	0.00207	12.56461	0.44770	0.48887	0.01656	2711	18	2648	33	2566	71	6.5
9	0.18140	0.00169	12.94636	0.50311	0.51762	0.01953	2666	15	2676	36	2689	82	-1.1
11	0.18091	0.00169	12.29370	0.44198	0.49287	0.01711	2661	15	2627	33	2583	73	3.6
13	0.18134	0.00170	12.27537	0.48040	0.49095	0.01865	2665	15	2626	36	2575	80	4.1
14	0.18127	0.00170	12.84473	0.48243	0.51391	0.01869	2665	15	2668	35	2673	79	-0.4
15	0.18499	0.00171	13.16334	0.50603	0.51607	0.01926	2698	15	2691	36	2682	81	0.7
16	0.18783	0.00177	13.63804	0.49685	0.52659	0.01854	2723	15	2725	34	2727	78	-0.2
17	0.19237	0.00183	13.22927	0.47237	0.49877	0.01717	2763	15	2696	33	2609	73	6.8
18	0.18247	0.00170	12.95228	0.50248	0.51481	0.01938	2675	15	2676	36	2677	82	-0.1
24	0.18252	0.00197	12.31751	0.49997	0.48945	0.01915	2676	18	2629	37	2568	82	4.9
25	0.18350	0.00175	12.55755	0.53293	0.49632	0.02053	2685	16	2647	39	2598	88	3.9
26	0.19717	0.00187	14.10865	0.56239	0.51898	0.02009	2803	15	2757	37	2695	85	4.7
28	0.20284	0.00197	15.39453	0.75772	0.55043	0.02656	2849	16	2840	46	2827	109	1.0
29	0.18428	0.00176	12.65817	0.58237	0.49819	0.02242	2692	16	2655	42	2606	96	3.9
30	0.19088	0.00183	13.23980	0.51349	0.50306	0.01891	2750	16	2697	36	2627	81	5.4
32	0.18505	0.00174	13.33013	0.50302	0.52246	0.01909	2699	15	2703	35	2710	80	-0.5
33	0.18894	0.00182	13.22793	0.51832	0.50778	0.01928	2733	16	2696	36	2647	82	3.8
37	0.19231	0.00178	14.01790	0.69212	0.52866	0.02564	2762	15	2751	46	2736	107	1.2
41	0.18437	0.00179	12.41300	0.47590	0.48829	0.01811	2693	16	2636	35	2563	78	5.8
42	0.18222	0.00172	12.31759	0.50869	0.49025	0.01971	2673	16	2629	38	2572	85	4.6
43	0.18606	0.00175	12.55885	0.46102	0.48954	0.01737	2708	15	2647	34	2569	75	6.2
46	0.18728	0.00177	12.59031	0.52722	0.48757	0.01989	2718	15	2649	39	2560	86	7.1
47	0.18356	0.00177	12.45813	0.51268	0.49222	0.01969	2685	16	2640	38	2580	85	4.7
48	0.18699	0.00175	12.55629	0.57226	0.48703	0.02173	2716	15	2647	42	2558	93	7.0
49	0.18629	0.00179	12.65954	0.60675	0.49288	0.02315	2710	16	2655	44	2583	99	5.7
50	0.19924	0.00193	15.30263	0.62176	0.55705	0.02198	2820	16	2834	38	2854	90	-1.5
51	0.18190	0.00178	11.78468	0.49672	0.46988	0.01926	2670	16	2587	39	2483	84	8.4
53	0.18373	0.00174	12.65774	0.53079	0.49965	0.02041	2687	16	2655	39	2612	87	3.4
54	0.18442	0.00175	12.27578	0.50249	0.48277	0.01922	2693	16	2626	38	2539	83	6.9
55	0.18697	0.00181	12.55079	0.58756	0.48684	0.02230	2716	16	2647	43	2557	96	7.1
56	0.18599	0.00176	12.89525	0.57078	0.50284	0.02174	2707	16	2672	41	2626	93	3.6
60	0.18908	0.00181	13.36932	0.54721	0.51280	0.02041	2734	16	2706	38	2669	86	2.9
61	0.18639	0.00177	12.41966	0.58483	0.48325	0.02229	2711	16	2637	43	2541	96	7.5
62	0.18459	0.00204	13.12870	0.60131	0.51582	0.02293	2695	18	2689	42	2681	97	0.6
63	0.19847	0.00192	15.39598	0.73074	0.56263	0.02614	2814	16	2840	44	2877	107	-2.8
64	0.18644	0.00178	13.42167	0.81606	0.52211	0.03135	2711	16	2710	56	2708	131	0.1
65	0.18647	0.00180	12.86268	0.55820	0.50028	0.02117	2711	16	2670	40	2615	90	4.3
66	0.19078	0.00181	13.00062	0.57155	0.49424	0.02121	2749	16	2680	41	2589	91	7.1
67	0.18522	0.00177	12.72418	0.52865	0.49824	0.02014	2700	16	2659	38	2606	86	4.2
68	0.18966	0.00188	12.98242	0.59354	0.49646	0.02216	2739	16	2678	42	2599	95	6.2
71	0.18227	0.00217	11.95335	0.71087	0.47564	0.02772	2674	20	2601	54	2508	120	7.5
73	0.18591	0.00176	12.20247	0.51155	0.47604	0.01944	2706	16	2620	39	2510	84	8.8
75	0.18120	0.00174	12.43858	0.60281	0.49786	0.02365	2664	16	2638	45	2605	101	2.7
77	0.18432	0.00178	12.31643	0.58934	0.48462	0.02271	2692	16	2629	44	2547	98	6.5
78	0.18837	0.00179	12.82240	0.58286	0.49368	0.02194	2728	16	2667	42	2587	94	6.3
79	0.23319	0.00225	17.85423	0.63497	0.55531	0.01901	3074	15	2982	34	2847	78	9.1
80	0.18513	0.00173	12.63702	0.51434	0.49508	0.01961	2699	15	2653	38	2593	84	4.8
81	0.18564	0.00177	12.12132	0.48397	0.47356	0.01836	2704	16	2614	37	2499	80	9.1
82	0.18609	0.00180	12.64095	0.51560	0.49268	0.01952	2708	16	2653	38	2582	84	5.6
83	0.18612	0.00176	12.43632	0.52067	0.48462	0.01977	2708	16	2638	39	2547	85	7.2
84	0.18653	0.00185	12.61714	0.49684	0.49058	0.01870	2712	16	2651	36	2573	80	6.2
85	0.18306	0.00205	11.72174	0.56432	0.46441	0.02174	2681	18	2582	44	2459	95	9.9
87	0.18230	0.00174	11.99939	0.48960	0.47740	0.01894	2674	16	2604	38	2516	82	7.1
89	0.17660	0.00190	12.05581	0.63401	0.49512	0.02549	2621	18	2609	48	2593	109	1.3
90	0.18365	0.00171	12.75848	0.52334	0.50385	0.02013	2686	15	2662	38	2630	86	2.5
92	0.18544	0.00178	12.35606	0.48110	0.48325	0.01823	2702	16	2632	36	2541	79	7.2
93	0.18712	0.00183	12.70359	0.52874	0.49237	0.01992	2717	16	2658	38	2581	85	6.1
98	0.18277	0.00177	11.74090	0.49026	0.46590	0.01893	2678	16	2584	38	2466	83	9.5

214

Appendix C
Table C1. Detrital Zircon U-Pb data of the at Courageous Lake

Courageous Lake greywacke (13AB2206A)

	Ratios						Ages (Ma)							
Grain #		207Pb/206Pb	2 σ (Ma)	207Pb/235U	2 σ (Ma)	206Pb/238U	2 σ (Ma)	207Pb/206Pb	2 σ (Ma)	207Pb/235U	2 σ (Ma)	206Pb/238U	2 σ (Ma)	% discord.
1	7660	0.18626	0.00153	12.25680	0.58527	0.47727		2709	13	2624	44	2515	97	8.6
2	6723	0.18389	0.00151	13.18891	0.55996	0.52018		2688	14	2693	39	2700	91	-0.5
3	24916	0.18652	0.00157	12.70134	0.54284	0.49388		2712	14	2658	39	2587	89	5.6
4	7972079	0.18686	0.00169	12.64077	0.62948	0.49063		2715	15	2653	46	2573	103	6.3
5	23640	0.18453	0.00150	13.32340	0.68022	0.52367		2694	13	2703	47	2715	111	-0.9
6	1220	0.19135	0.00395	13.14500	0.62676	0.49822		2754	34	2690	44	2606	91	6.5
7	19095	0.17797	0.00144	12.04248	0.54182	0.49075		2634	13	2608	41	2574	93	2.8
8	44064	0.18101	0.00147	12.64693	0.51931	0.50672		2662	13	2654	38	2643	87	0.9
9	5905	0.18533	0.00149	12.11448	0.49295	0.47408		2701	13	2613	37	2501	82	8.9
10	23479	0.18060	0.00155	12.27892	0.45380	0.49311		2658	14	2626	34	2584	76	3.4
12	4436	0.18178	0.00150	11.78148	0.47347	0.47007		2669	14	2587	37	2484	81	8.4
13	4235	0.18840	0.00208	12.91112	0.74793	0.49704		2728	18	2673	53	2601	121	5.7
14	13766	0.18126	0.00148	12.29115	0.48093	0.49180		2664	13	2627	36	2578	81	3.9
15	11306	0.18497	0.00160	12.67397	0.56889	0.49695		2698	14	2656	41	2601	94	4.4
16	7420	0.18362	0.00159	13.16812	0.57894	0.52011		2686	14	2692	41	2700	94	-0.6
17	15991	0.18168	0.00151	12.34627	0.67783	0.49285		2668	14	2631	50	2583	114	3.9
18	7731	0.18268	0.00158	11.84727	0.51684	0.47035		2677	14	2592	40	2485	88	8.6
19	5927	0.18381	0.00152	12.99672	0.62566	0.51282		2688	14	2679	44	2669	103	0.9
20	1762	0.18418	0.00159	12.62944	0.56396	0.49733		2691	14	2652	41	2602	93	4.0
21	2539	0.18772	0.00171	12.35038	0.63410	0.47716		2722	15	2631	47	2515	104	9.2
22	15025	0.18366	0.00152	12.45741	0.56606	0.49193		2686	14	2640	42	2579	94	4.8
23	4967	0.18210	0.00150	12.37433	0.57911	0.49286		2672	14	2633	43	2583	97	4.0
24	7382	0.17876	0.00153	12.20590	0.54099	0.49523		2641	14	2620	41	2593	92	2.2
25	5216	0.18205	0.00150	12.58566	0.47278	0.50140		2672	14	2649	35	2620	78	2.4
26	6018	0.18217	0.00157	12.27938	0.48791	0.48887		2673	14	2626	37	2566	82	4.8
27	6148	0.18456	0.00151	12.18463	0.57014	0.47881		2694	13	2619	43	2522	95	7.7
29	5632	0.18070	0.00145	12.51172	0.46752	0.50218		2659	13	2644	35	2623	78	1.7
30	10639	0.18087	0.00167	11.98176	0.50305	0.48044		2661	15	2603	39	2529	85	6.0
31	3989	0.18823	0.00151	13.58498	0.51229	0.52343		2727	13	2721	35	2714	81	0.6
32	2499	0.18191	0.00147	12.44583	0.75041	0.49620		2670	13	2639	55	2597	126	3.3
33	3228	0.18504	0.00155	12.64242	0.56025	0.49553		2699	14	2653	41	2595	92	4.7
34	1343	0.18363	0.00154	12.38215	0.47044	0.48905		2686	14	2634	35	2567	78	5.4
35	656	0.18858	0.00169	13.11523	0.56295	0.50440		2730	15	2688	40	2633	90	4.3
36	2889	0.18660	0.00153	12.75903	0.58150	0.49592		2712	13	2662	42	2596	95	5.2
37	4225	0.18487	0.00154	12.57033	0.53075	0.49316		2697	14	2648	39	2584	88	5.1
38	4349	0.18199	0.00148	11.86367	0.45831	0.47278		2671	13	2594	36	2496	78	7.9
39	6253	0.18420	0.00151	12.65429	0.52686	0.49824		2691	13	2654	38	2606	87	3.8
40	2167	0.18314	0.00151	12.17298	0.55339	0.48208		2681	14	2618	42	2536	93	6.5
41	6914	0.17708	0.00146	11.08528	0.42854	0.45403		2626	14	2530	35	2413	76	9.7
42	5059	0.18434	0.00154	12.72873	0.59988	0.50079		2692	14	2660	43	2617	99	3.4
43	2473	0.18460	0.00152	12.56651	0.61828	0.49373		2695	14	2648	45	2587	103	4.9
44	5693	0.18139	0.00146	11.99944	0.47808	0.47977		2666	13	2604	37	2526	81	6.3
45	3392	0.18354	0.00150	11.86888	0.50961	0.46902		2685	13	2594	39	2479	86	9.2
47	2923	0.18094	0.00148	11.94892	0.49044	0.47896		2661	13	2600	38	2523	83	6.3
48	1601	0.18794	0.00153	12.38975	0.55427	0.47812		2724	13	2634	41	2519	91	9.1
51	1750	0.18243	0.00149	12.24292	0.61175	0.48672		2675	13	2623	46	2556	103	5.4
52	4956	0.18339	0.00151	12.19087	0.53154	0.48213		2684	14	2619	40	2537	89	6.6
53	5906	0.17865	0.00143	11.74729	0.57264	0.47691		2640	13	2584	45	2514	99	5.8
54	2039	0.18141	0.00148	12.13860	0.47917	0.48529		2666	13	2615	36	2550	81	5.2
55	2818	0.18070	0.00148	12.19085	0.46938	0.48931		2659	14	2619	36	2568	79	4.2
57	2805	0.18860	0.00194	12.82777	0.56692	0.49330		2730	17	2667	41	2585	91	6.4
58	1790	0.19198	0.00160	13.40374	0.69608	0.50637		2759	14	2709	48	2641	110	5.2
60	20761	0.18259	0.00150	11.65523	0.44519	0.46296		2677	14	2577	35	2453	76	10.0
62	62314	0.18731	0.00159	13.27871	0.69400	0.51414		2719	14	2700	48	2674	112	2.0
65	76385	0.18297	0.00149	12.89500	0.51261	0.51114		2680	13	2672	37	2662	84	0.8
66	89550	0.19838	0.00160	14.20963	0.55313	0.51951		2813	13	2764	36	2697	83	5.0
67	5640	0.18570	0.00154	12.48970	0.48764	0.48780		2704	14	2642	36	2561	80	6.4
68	23346	0.18112	0.00147	12.17426	0.55023	0.48750		2663	13	2618	42	2560	93	4.7
69	97593	0.18100	0.00145	12.57226	0.56008	0.50376		2662	13	2648	41	2630	94	1.5
71	39674	0.18293	0.00153	12.14431	0.66189	0.48148		2680	14	2616	50	2534	112	6.6
72	12494	0.18702	0.00182	12.53556	0.54743	0.48613		2716	16	2645	40	2554	89	7.2
74	3274	0.19293	0.00157	12.91085	0.57931	0.48535		2767	13	2673	41	2551	92	9.5
75	13954	0.18425	0.00152	12.53906	0.55657	0.49357		2692	14	2646	41	2586	92	4.8
76	52843	0.18096	0.00148	12.02849	0.54542	0.48209		2662	14	2607	42	2536	93	5.7
78	8365	0.18293	0.00149	12.36044	0.53199	0.49005		2680	13	2632	40	2571	89	4.9
79	9474	0.18815	0.00158	12.58010	0.57044	0.48493		2726	14	2649	42	2549	93	7.9
80	3315	0.18142	0.00162	12.16523	0.81124	0.48633		2666	15	2617	61	2555	138	5.0
17b	11537	0.18180	0.00150	12.72038	0.52308	0.50745		2669	14	2659	38	2646	87	1.1
8b	98134	0.18036	0.00144	12.53868	0.49206	0.50420		2656	13	2646	36	2632	82	1.1

Appendix D

Table D1. Detrital zircon U-Pb data of the ferruginous clastic sediment at Point Lake

Point Lake ferruginous clastic sediment (RHNWT-29C)

Grain #	Ratios $^{207}Pb/^{206}Pb$	2 σ (Ma)	$^{207}Pb/^{235}U$	2 σ (Ma)	$^{206}Pb/^{238}U$	2 σ (Ma)	Ages (Ma) $^{207}Pb/^{206}Pb$	2 σ (Ma)	$^{207}Pb/^{235}U$	2 σ (Ma)	$^{206}Pb/^{238}U$	2 σ (Ma)	% discord.
RHNWT29(1)-1	0.18919	0.00163	12.33226	0.64830	0.47277	0.02452	2735	14	2630	48	2496	106	10.5
RHNWT29(1)-10	0.17606	0.00162	12.12911	0.66869	0.49964	0.02716	2616	15	2614	50	2612	116	0.2
RHNWT29(1)-2	0.18605	0.00162	12.69677	0.78316	0.49494	0.03022	2708	14	2657	56	2592	129	5.2
RHNWT29(1)-3	0.18241	0.00157	12.78044	0.45350	0.50816	0.01749	2675	14	2664	33	2649	74	1.2
RHNWT29(1)-4	0.18349	0.00164	12.68776	0.61852	0.50149	0.02403	2685	15	2657	45	2620	102	2.9
RHNWT29(1)-5	0.18385	0.00163	10.55468	0.90633	0.41638	0.03556	2688	15	2485	77	2244	160	19.5
RHNWT29(1)-6	0.18674	0.00163	12.62971	0.49407	0.49053	0.01871	2714	14	2652	36	2573	80	6.3
RHNWT29(1)-7	0.18606	0.00167	12.27014	0.50318	0.47831	0.01914	2708	15	2625	38	2520	83	8.4
RHNWT29(1)-8	0.18320	0.00160	11.84606	0.53711	0.46898	0.02087	2682	14	2592	42	2479	91	9.1
RHNWT29(1)-9	0.17457	0.00155	10.98532	0.46570	0.45639	0.01892	2602	15	2522	39	2424	83	8.2
RHNWT29(1)-11	0.17558	0.00152	11.09778	0.44137	0.45842	0.01779	2612	14	2531	36	2433	78	8.2
RHNWT29(1)-13	0.18281	0.00158	11.45369	0.47391	0.45442	0.01839	2678	14	2561	38	2415	81	11.8
RHNWT29(1)-14	0.17500	0.00156	8.50150	0.50632	0.35233	0.02075	2606	15	2286	53	1946	98	29.3
RHNWT29(1)-15	0.18622	0.00163	11.31716	0.53106	0.44076	0.02032	2709	14	2550	43	2354	90	15.6
RHNWT29(1)-16	0.18386	0.00163	12.28813	0.50290	0.48474	0.01936	2688	15	2627	38	2548	84	6.3
RHNWT29(1)-17	0.17416	0.00157	10.91443	0.40199	0.45451	0.01623	2598	15	2516	34	2415	72	8.4
RHNWT29(1)-18	0.18547	0.00160	11.79560	0.62162	0.46125	0.02398	2702	14	2588	48	2445	105	11.4
RHNWT29(1)-19	0.18309	0.00159	11.90614	0.60066	0.47164	0.02344	2681	14	2597	46	2491	102	8.5
RHNWT29(1)-20	0.18335	0.00159	12.14002	0.46762	0.48022	0.01802	2683	14	2615	36	2528	78	7.0
RHNWT29(1)-21	0.18709	0.00175	12.80772	0.53346	0.49650	0.02015	2717	15	2666	38	2599	86	5.3
RHNWT29(2)-12	0.18364	0.00160	12.62798	0.53422	0.49873	0.02065	2686	14	2652	39	2608	88	3.5
RHNWT29(2)-13	0.19118	0.00175	12.95213	0.50309	0.49136	0.01855	2752	15	2676	36	2577	80	7.7
RHNWT29(2)-14	0.17965	0.00156	10.90418	0.44042	0.44022	0.01737	2650	14	2515	37	2352	77	13.4
RHNWT29(2)-15	0.18370	0.00163	12.08663	0.43843	0.47719	0.01678	2687	15	2611	33	2515	73	7.7
RHNWT29(2)-16	0.18212	0.00158	11.65629	0.50731	0.46421	0.01980	2672	14	2577	40	2458	87	9.6
RHNWT29(2)-17	0.18450	0.00158	12.44103	0.64752	0.48905	0.02511	2694	14	2638	48	2567	108	5.7
RHNWT29(2)-18	0.18593	0.00162	12.06372	0.46736	0.47058	0.01776	2706	14	2609	36	2486	77	9.8
RHNWT29(2)-19	0.18272	0.00169	9.11604	0.53012	0.36183	0.02077	2678	15	2350	52	1991	98	29.7
RHNWT29(2)-20	0.18492	0.00164	12.51261	0.48302	0.49075	0.01844	2697	15	2644	36	2574	79	5.6
RHNWT29(2)-22	0.18417	0.00160	12.62843	0.56459	0.49731	0.02181	2691	14	2652	41	2602	93	4.0
RHNWT29(2)-23	0.18523	0.00160	12.05344	0.55730	0.47194	0.02143	2700	14	2609	42	2492	93	9.3
RHNWT29(2)-24	0.18101	0.00157	12.18281	0.47056	0.48815	0.01837	2662	14	2619	36	2563	79	4.5
RHNWT29(2)-26	0.18692	0.00163	12.92918	0.50644	0.50167	0.01916	2715	14	2675	36	2621	82	4.2
RHNWT29(2)-27	0.18935	0.00174	12.94039	0.57632	0.49567	0.02160	2736	15	2675	41	2595	92	6.3
RHNWT29(2)-28	0.18016	0.00154	12.43150	0.48022	0.50044	0.01885	2654	14	2638	36	2616	80	1.8
RHNWT29(2)-29	0.19316	0.00170	13.12770	0.49115	0.49291	0.01792	2769	14	2689	35	2583	77	8.1
RHNWT29(2)-30	0.18049	0.00156	11.84278	0.47765	0.47588	0.01875	2657	14	2592	37	2509	81	6.7
RHNWT29(2)-31	0.18474	0.00160	12.23775	0.49027	0.48044	0.01879	2696	14	2623	37	2529	81	7.5
RHNWT29(2)-33	0.17917	0.00351	11.43545	0.50564	0.46290	0.01835	2645	32	2559	40	2452	80	8.8
RHNWT29(2)-35	0.18442	0.00159	12.37369	0.47175	0.48663	0.01807	2693	14	2633	35	2556	78	6.2
RHNWT29(2)-10	0.18033	0.00157	12.10299	0.54790	0.48677	0.02162	2656	14	2612	42	2557	93	4.5
RHNWT29(2)-2	0.18465	0.00165	12.20191	0.63784	0.47926	0.02468	2695	15	2620	48	2524	107	7.7
RHNWT29(2)-36	0.18205	0.00162	12.15111	0.58208	0.48408	0.02279	2672	15	2616	44	2545	98	5.7
RHNWT29(2)-38	0.18337	0.00159	12.25008	0.45196	0.48451	0.01737	2684	14	2624	34	2547	75	6.2
RHNWT29(2)-39	0.18367	0.00162	12.19969	0.43636	0.48174	0.01670	2686	14	2620	33	2535	72	6.8
RHNWT29(2)-4	0.18520	0.00160	12.11517	0.49755	0.47445	0.01905	2700	14	2613	38	2503	83	8.8
RHNWT29(2)-41	0.17540	0.00150	11.23215	0.42504	0.46444	0.01712	2610	14	2543	35	2459	75	6.9
RHNWT29(2)-42	0.18661	0.00161	12.46813	0.47906	0.48459	0.01814	2712	14	2640	35	2547	78	7.4
RHNWT29(2)-5	0.17569	0.00152	10.60083	0.42055	0.43761	0.01694	2613	14	2489	36	2340	76	12.4
RHNWT29(2)-6	0.18136	0.00161	12.62220	0.56367	0.50478	0.02209	2665	15	2652	41	2634	94	1.4
RHNWT29(2)-7	0.18079	0.00157	11.88240	0.45681	0.47669	0.01785	2660	14	2595	35	2513	77	6.7

Appendix E
Table E1.

Zircon U-Pb data on the OG1 standard with known (TIMS) age of 3465.4 ± 0.6 Ma (Stern et al., 2009). The boxes underneath the Table are the weighted mean $^{207}Pb/^{206}Pb$ age.

	Grain #	^{206}Pb (cps)	^{204}Pb (cps)	$^{207}Pb/^{206}Pb$	2 σ (Ma)	$^{207}Pb/^{235}U$	2 σ (Ma)	$^{206}Pb/^{238}U$	2 σ (Ma)	$^{207}Pb/^{206}Pb$	2 σ (Ma)	$^{207}Pb/^{235}U$	2 σ (Ma)	$^{206}Pb/^{238}U$	2 σ (Ma)	% discord.
				Ratios						Ages (Ma)						
Point Lake ferruginous clastic sediment	OG1-1	304115	155	0.29630	0.00257	29.51760	1.64821	0.72253	0.03985	3451	13	3471	53	3506	147	-2.0
Goose Lake greywacke	OG1-2	244822	213	0.29792	0.00262	29.29302	1.70442	0.71311	0.04101	3459	14	3463	56	3470	153	-0.4
Courageous Lake greywacke	OG1-3	331914	163	0.29865	0.00257	29.66143	1.67617	0.72032	0.04023	3463	13	3476	54	3497	149	-1.3
Slemon Lake tuff	OG1-4	342977	146	0.29875	0.00258	29.13758	1.27529	0.70737	0.03035	3464	13	3458	42	3449	114	0.6
	OG1-5	386672	145	0.30001	0.00260	29.81720	1.38504	0.72083	0.03289	3470	13	3481	45	3499	122	-1.1
	OG1-1	867873	176	0.29658	0.00285	29.21116	1.23987	0.71434	0.02953	3452	15	3461	41	3475	110	-0.8
	OG1-2	922056	190	0.29592	0.00275	29.88370	1.05854	0.73241	0.02503	3449	14	3483	34	3542	92	-3.5
	OG1-3	891604	184	0.29578	0.00277	29.78059	1.14417	0.73024	0.02721	3448	14	3480	37	3534	101	-3.2
	OG1-4	1081667	295	0.29602	0.00280	29.14195	1.15081	0.71400	0.02737	3450	15	3458	38	3474	102	-0.9
	OG1-5	1118434	310	0.29731	0.00287	29.06448	1.22305	0.70900	0.02904	3456	15	3456	40	3455	109	0.1
	OG1-6	1022593	274	0.29662	0.00276	29.67735	1.23773	0.72564	0.02950	3453	14	3476	40	3517	109	-2.4
	OG1-7	661052	336	0.29762	0.00278	29.34022	1.24496	0.71499	0.02959	3458	14	3465	41	3477	110	-0.7
	OG1-8	474805	81	0.30016	0.00288	28.96945	1.21925	0.69999	0.02869	3471	15	3452	40	3421	108	1.9
	OG1-9	339229	12	0.30094	0.00279	29.43172	1.29977	0.70931	0.03063	3475	14	3468	42	3456	114	0.7
	OG1-10	591339	169	0.30074	0.00279	30.03626	1.38782	0.72436	0.03279	3474	14	3488	44	3512	121	-1.4
	OG1-1	523645	2	0.29824	0.00242	27.06341	1.04696	0.65814	0.02489	3461	13	3386	37	3260	96	7.4
	OG1-2	528247	5	0.29791	0.00244	28.91981	1.50753	0.70405	0.03624	3459	13	3451	50	3436	136	0.9
	OG1-3	393879	0	0.29690	0.00242	29.83608	1.31150	0.72884	0.03148	3454	13	3481	42	3529	116	-2.8
	OG1-4	475893	3	0.29641	0.00240	28.70065	1.38638	0.70225	0.03344	3452	13	3443	46	3429	125	0.8
	OG1-5	279000	9	0.29613	0.00242	29.04111	1.15105	0.71127	0.02759	3450	13	3455	38	3463	103	-0.5
	OG1-6	380704	26	0.29619	0.00239	28.22968	1.13494	0.69125	0.02722	3450	12	3427	39	3387	103	2.3
	OG1-7	347427	84	0.29787	0.00240	29.16792	1.09751	0.71019	0.02610	3459	12	3459	36	3459	98	0.0
	OG1-8	569657	102	0.29765	0.00244	28.58146	1.12810	0.69642	0.02689	3458	13	3439	38	3407	101	1.9
	OG1-1	456495	122	0.29893	0.00245	28.66064	1.17415	0.69537	0.02791	3465	13	3442	39	3403	105	2.3
	OG1-2	308694	10	0.29906	0.00240	27.65838	1.35117	0.67076	0.03232	3465	12	3407	47	3309	124	5.8

Mean $^{207}Pb/^{206}Pb$ = 3465.0±8.7 [0.25%] 95% conf.
Wtd by data-pt errs only, 0 of 2 rej.
MSWD = 0.0058, probability = 0.94

Mean $^{207}Pb/^{206}Pb$ = 3455.5±4.3 [0.13%] 95% conf.
Wtd by data-pt errs only, 0 of 8 rej.
MSWD = 0.51, probability = 0.83

Mean $^{207}Pb/^{206}Pb$ = 3458.7±7.7 [0.22%] 95% conf.
Wtd by data-pt errs only, 0 of 10 rej.
MSWD = 2.2, probability = 0.020

Mean $^{207}Pb/^{206}Pb$ = 3461.6±5.9 [0.17%] 95% conf.
Wtd by data-pt errs only, 0 of 5 rej.
MSWD = 1.12, probability = 0.35

Appendix F - Preliminary study of the detrital chromite in the fuchsitic quartzite from the Central Slave Cover Group

Figure F1. (A, B) Hand sample images of the fuchsite bearing quartzite at Dwyer Lake (A) and Bell Lake (B). Note the black chromite-rich laminae. (C) Thin section image (PPL) showing the heavy mineral laminae containing chromite, rutile and zircon surrounded by cr-rich mica (fuchsite). (D) A chromite grain engulfed by fuchsite (XPL).
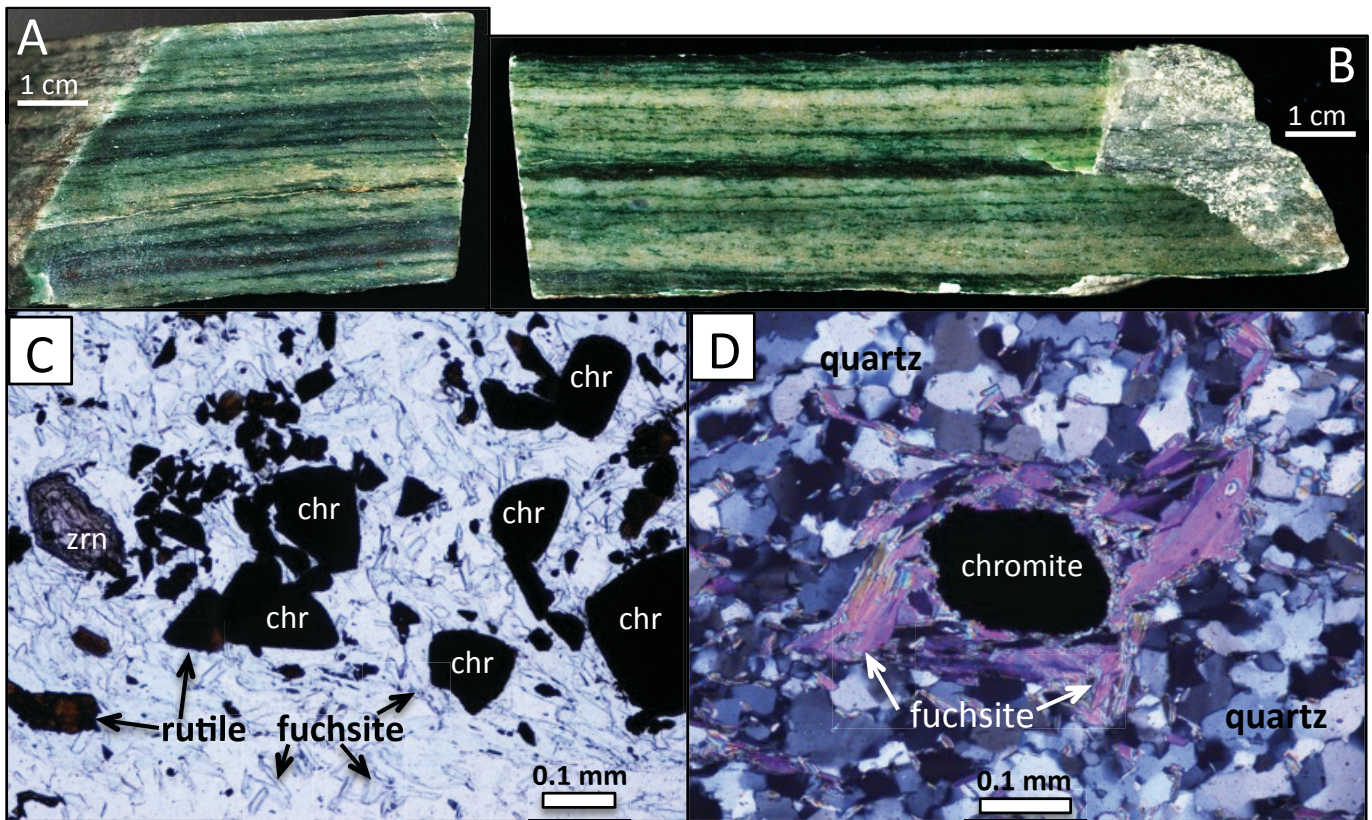
Table F1.

Detrital chromite grains from Bell and Dwyer Lake
-electron microprobe analysis

Bell Lake
n=52

	SiO2	TiO2	Al2O3	FeO	Fe2O3calc	Cr2O3	MgO	MnO	NiO	ZnO	CaO	Total
Average	0.10	0.37	16.06	21.45	4.62	42.94	0.41	1.59	0.04	12.20	0.00	99.76
Min	0.02	0.12	13.33	19.92	0.11	39.27	0.31	1.29	0.01	8.89	0.00	99.26
Max	0.37	2.26	20.75	23.93	7.09	45.84	0.50	1.83	0.07	14.94	0.02	100.44

Dwyer Lake
n=38

	SiO2	TiO2	Al2O3	FeO	Fe2O3calc	Cr2O3	MgO	MnO	NiO	ZnO	CaO	Total
Average	0.20	0.36	16.58	20.95	2.22	44.10	0.34	1.63	0.04	12.69	0.00	99.10
Min	0.09	0.09	13.54	18.13	0.00	40.10	0.20	1.33	0.00	10.62	0.00	94.29
Max	2.30	3.60	19.68	22.70	4.16	48.29	0.53	1.82	0.07	15.89	0.03	99.77

◆ The chromite from Bell and Dwyer are substantially more iron-rich and Mg-poor than the igneous precursors which likely is due to Fe-Mg exchange during prograde metamorphism.
◆ They are enriched in Zn and depleted in Ni.
◆ The activity of Zn has exchanged with Fe^{2+}, Mn and also partly Mg.
◆ The trivalent ions Cr, Al, and ferric-iron seems to be less modified.

These features are in good agreement with other metamorphosed chromites worldwide. In general, and when reading the literature, especially work by Barnes (2000), Barnes and Roeder (2001) and Rollinson et al. (2002), the Bell and Dwyer detrital chromite seems to show very typical element behavior during metamorphism. However, the only two exceptions are: (1) Extensive magnetite replacement (in form of rims or zones) are not evident within Bell and Dwyer chromite grains. This is a feature that are common in many amphibolite facies metamorphosed chromite grains (Barnes and Roeder, 2001), (2) The zinc values are a bit on the heavy side although comparable zinc concentration has been found in other detrital chromites (e.g., Figueiras and Waerenborgh, 1997; Pownceby and Bourne, 2006), values between 2-8 wt.% ZnO are more typically for amphibolite grade chromites whilst < 0.5 wt.% are normally for greenschist grade chromites (Barnes, 2000).

Figure F2. Electron microprobe data showing a transect of the chromite grains in the backscatter image. Note Zn substitution for Fe and partly Mg which is related to the amphibolite facies metamorphism.

Chromite transect
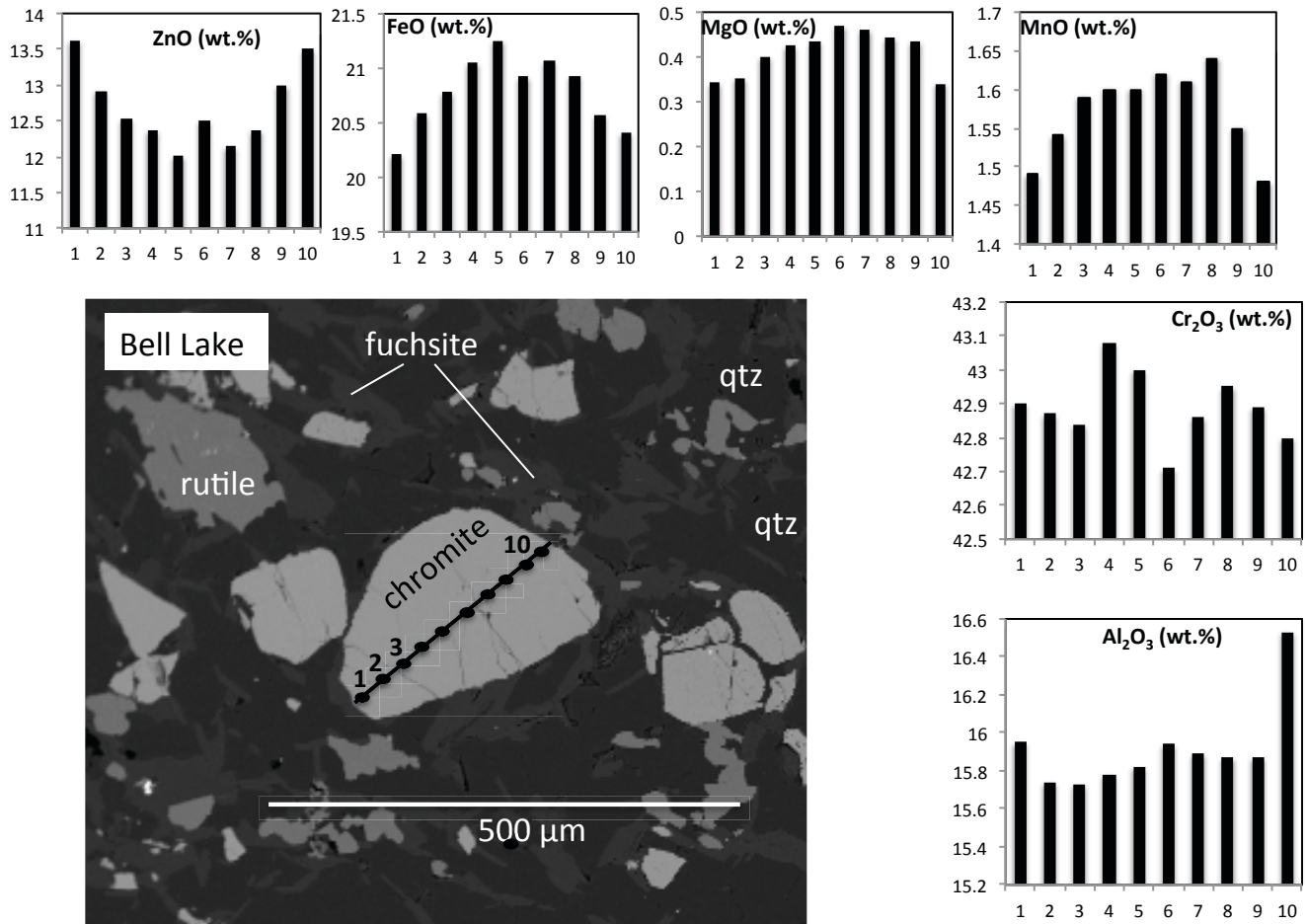
Figure F3. Some plots showing the genral elemental trends in the chromite grains from Bell and Dwyer Lake quartzite. Note the very low Mg# which is due to Mg-Fe^{2+} exchange. This, along with Zn enrichment, is one of the main difference between greenschist and amphibolite facies chromite (e.g., Barnes, 2000).
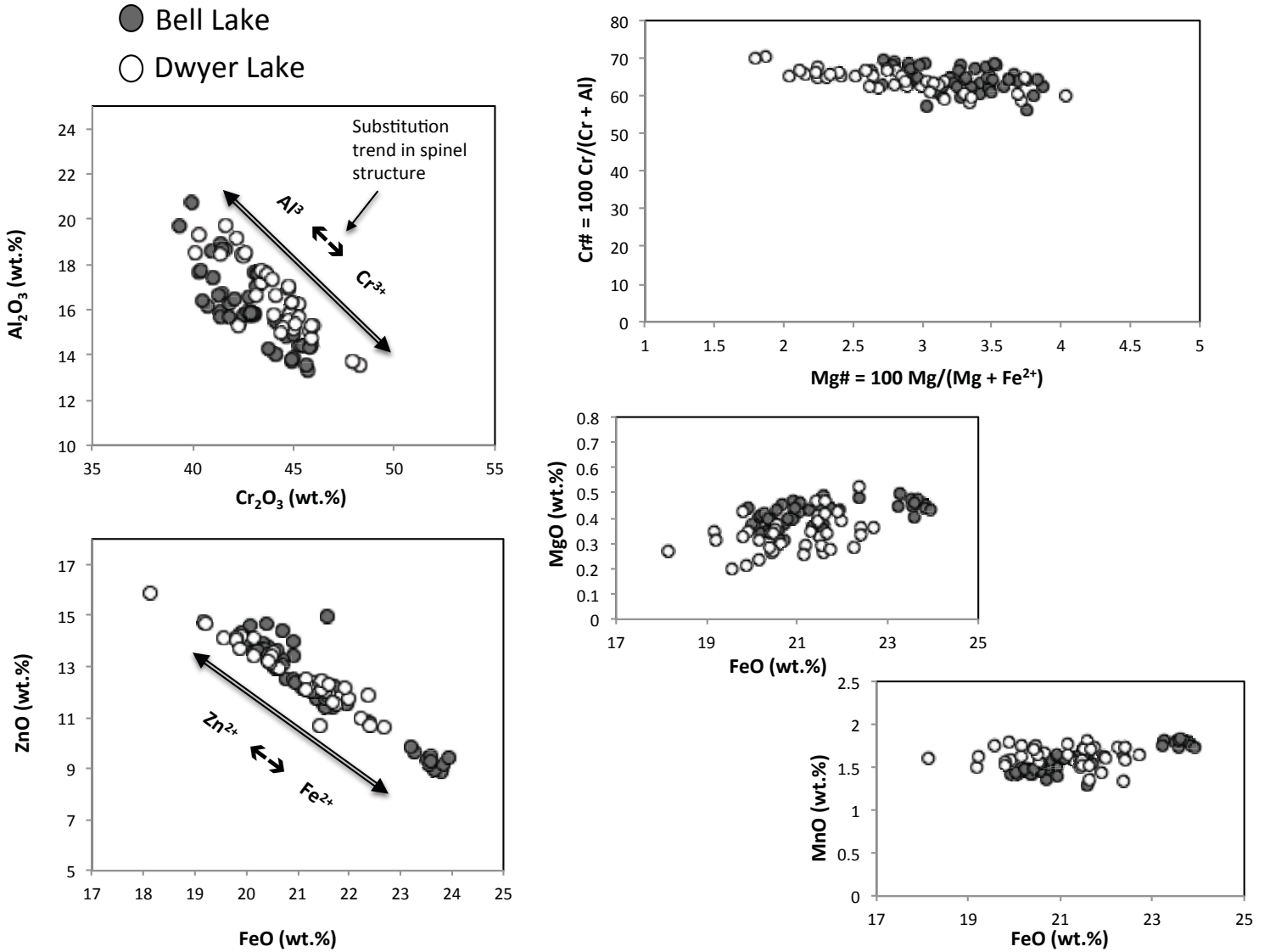
Figure F4. Discrimination diagrams showing the likeliness of the chromite grains to have been derived from an Al-undepleted komatiitic source. This source is no longer exposed in the Slave craton.
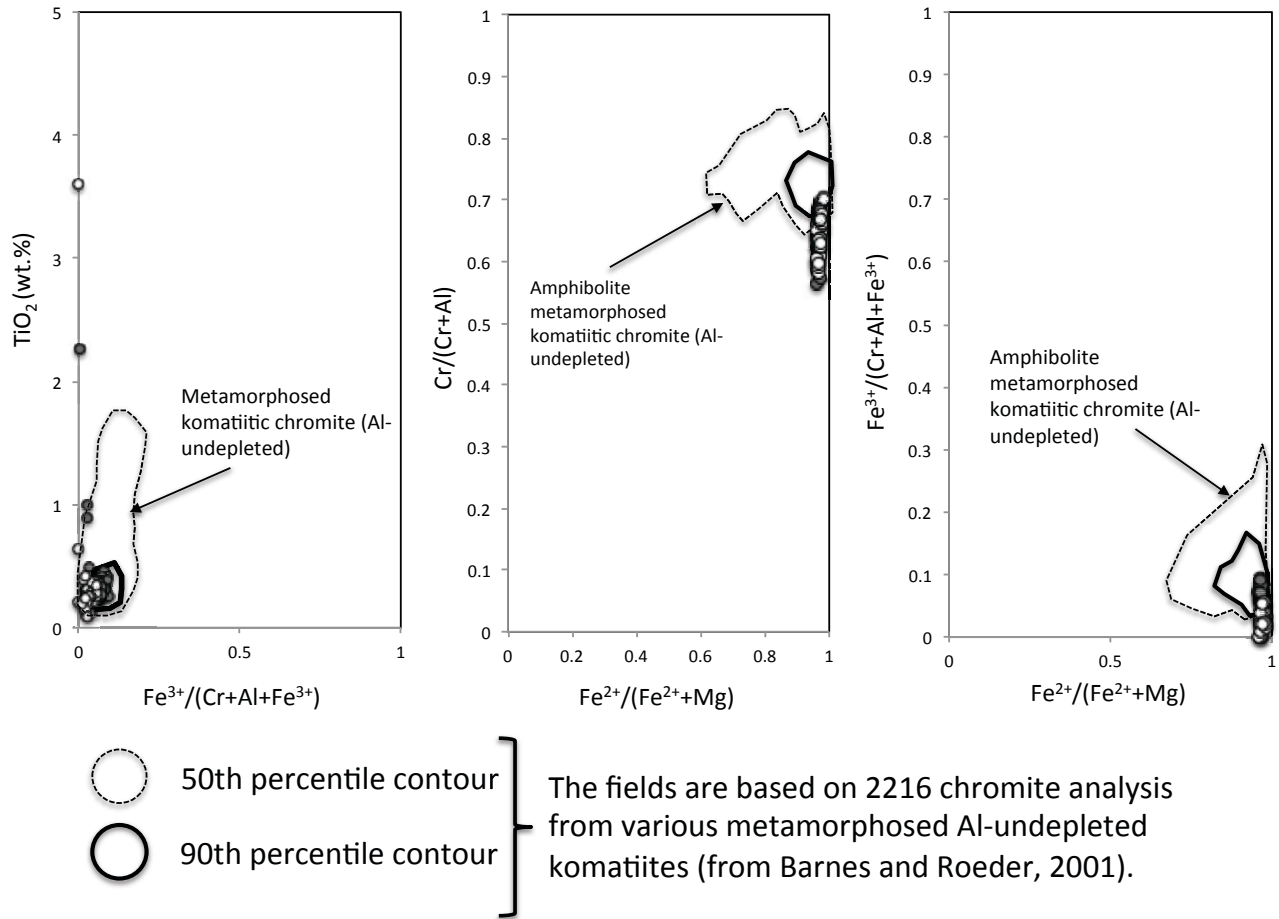
Figure F5. Triangular plot comparing the Bell and Dwyer Lake detrital chromites with those reported from komatiites and from the Witwatersrand conglomerate. Compositional fields from Barnes and Roeder (2001).
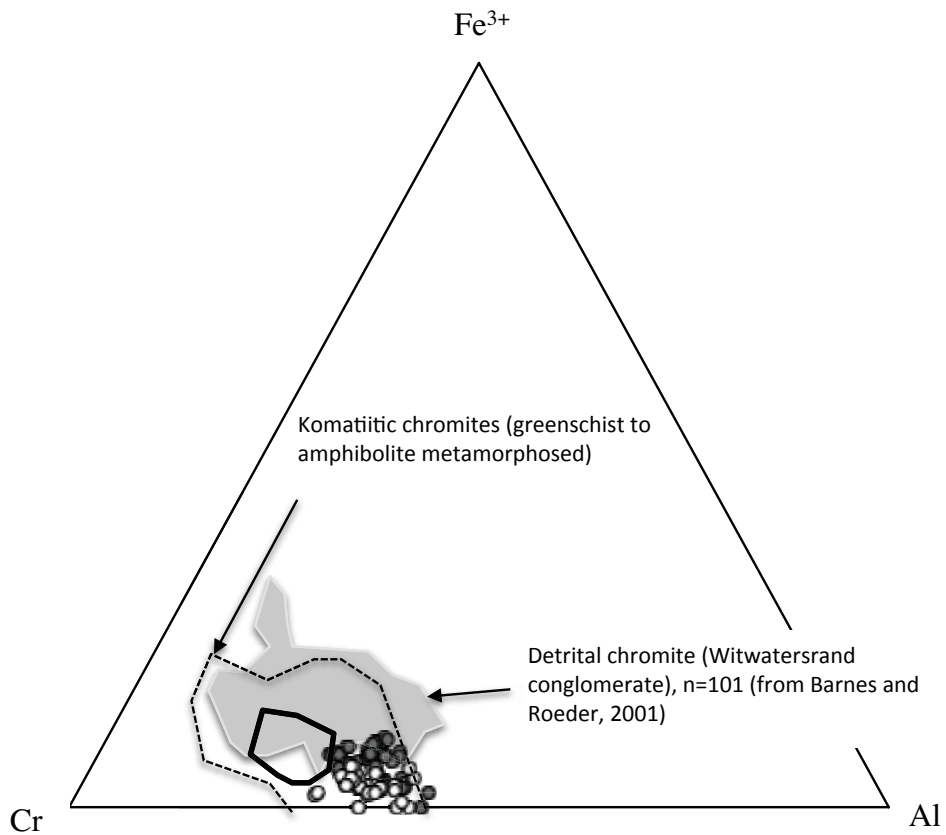
Table F2. Re-Os isotopic data from the bulk chromites at Bell and Dwyer Lake. TRD = rhenium depletion model ages, TMA = osmium isotope model ages.

Sample Name	TRD Age (Ma) O-chondrite	Abs. 2σ	TMA Age (Ma) O-chondrite	Abs. 2σ	PGE Os	Abs. 2σ	Ir	Abs. 2sd	Pt	Abs. 2sd	Pd	Abs. 2sd	Re
Bell Lake	2215.7	532.6	2600.5	651.5	13.18	0.07	12.28	0.27	0.81	0.03	2.58	0.07	0.17
Dwyer Lake	1574.6	568.3	1743.1	636.5	19.09	0.26	12.95	0.27	1.65	0.06	5.89	0.17	0.16

Figure F6. The chondrite normalized PGE patterns for the Bell Lake and Dwyer Lake chromite grains. The relative similar pattern suggests a common source for both portion of chromite grains.
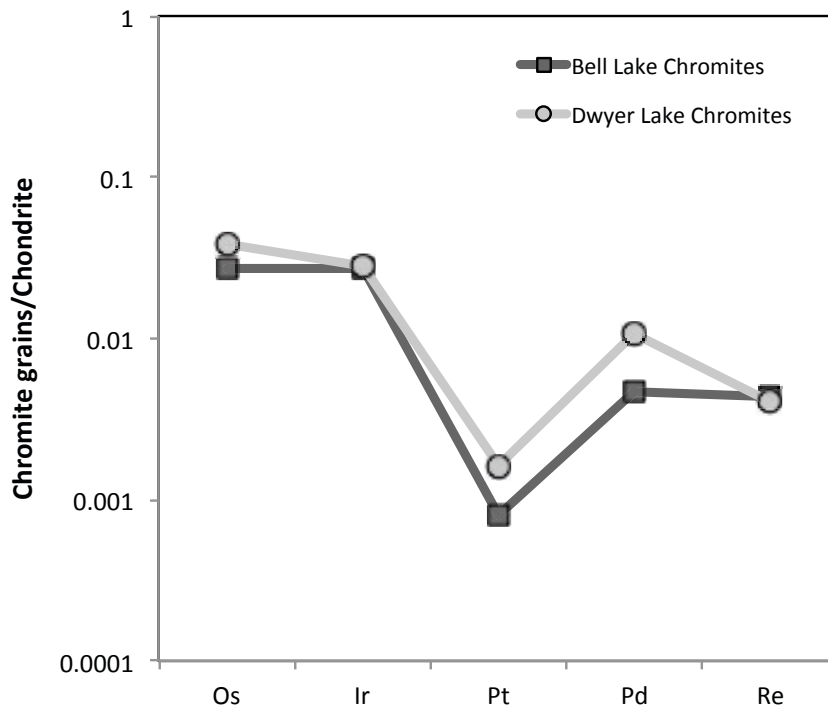
Appendix G - A metamorphosed weathering profile?

Figure G1. Brown Lake basal unconformity. The contact between the basement and the cover sequence shows a cobble conglomerate (A, B) directly overlying mylonitized tonalitic basement rocks. A closer look reveal that the cobbles have an outer crust of almost 100 % quartz and an inner core (C) that is likely of basement origin having an igneous texture and similar grain size. As such, they may represent rip-up clasts of the basement. (D, E) Fine-grained laminae of acicular sillimanite occur in the matrix of the cobble conglomerate.
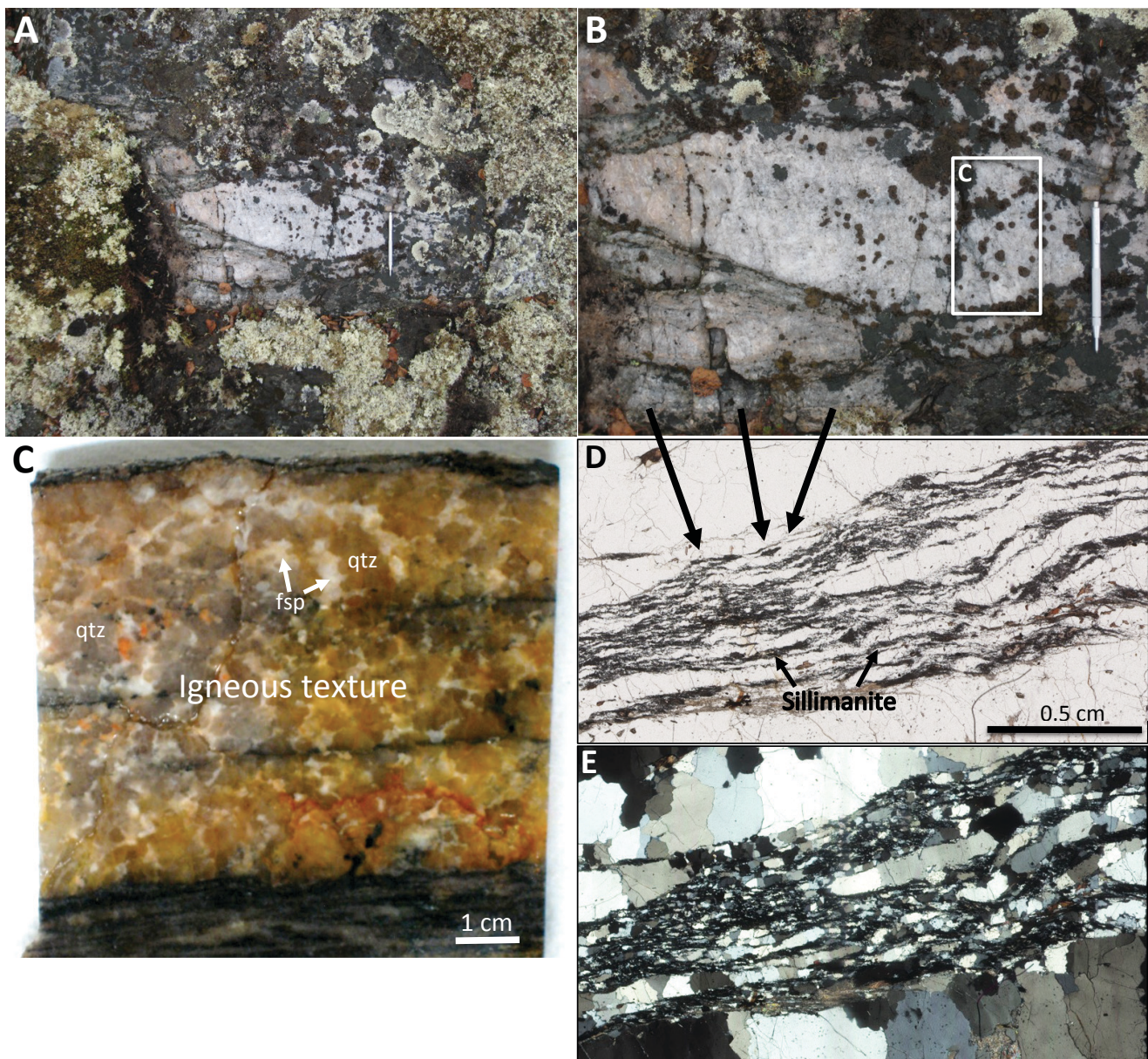
Figure G2. The Dwyer Lake basal contact. This contact can be seen as a change from a more igneous tonalitic texture into a more bedded transition zone that ends in fuchsite bearing quartzite (A, B). This transition locally contains small quartz rich pebbles. (C, D) Transect of the saw cut channel sampling conducted on the contact.
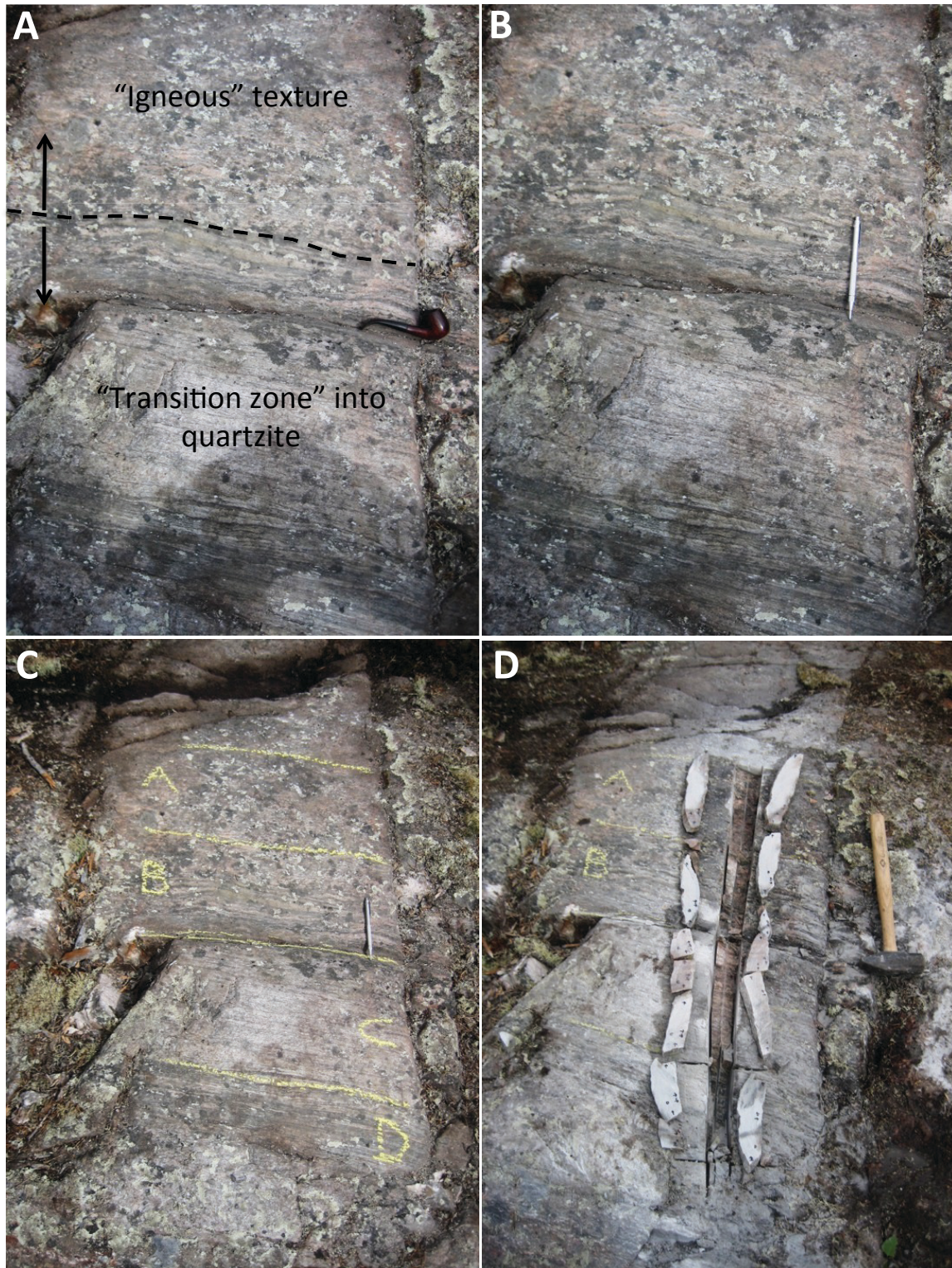
Figure G3. Selected elemental map images from the basement rock near the contact in Figure G2. Many of the muscovite grains contain very fine-grained fibrous sillimanite often in association with margarite (A, B, C, D, E). Also very fine-grained Al spinel is found throughout (F). These Al rich phases indicate a high Al rich protolith.